Aerodynamic Design Optimization and Flow Separation Control of the UAS-S45 using Wing Morphing Technology

by

Musavir BASHIR

MANUSCRIPT-BASED THESIS PRESENTED TO ÉCOLE DE TECHNOLOGIE SUPÉRIEURE IN PARTIAL FULFILLEMENT FOR THE DEGREE OF DOCTOR OF PHILOSOPHY
Ph.D.

MONTREAL, APRIL 4TH, 2023

ÉCOLE DE TECHNOLOGIE SUPÉRIEURE
UNIVERSITÉ DU QUÉBEC

BOARD OF EXAMINERS

THIS THESIS HAS BEEN EVALUATED

BY THE FOLLOWING BOARD OF EXAMINERS

Mrs. Ruxandra Mihaela Botez, Thesis Supervisor
Department of Systems Engineering at École de technologie supérieure

Mr. Tony Wong, Thesis Co-supervisor
Department of Systems Engineering at École de technologie supérieure

Mr. Philippe Bocher, President of the Board of Examiners
Department of Mechanical Engineering at École de technologie supérieure

Mr. Georges Ghazi, Member of the jury
Department of Systems Engineering at École de technologie supérieure

Mr. Rosario Pecora, Member of the jury
Department of Aerospace Engineering at University Federico II, Naples, Italy

THIS THESIS WAS PRENSENTED AND DEFENDED

IN THE PRESENCE OF A BOARD OF EXAMINERS AND PUBLIC

ON MARCH 28TH

AT ÉCOLE DE TECHNOLOGIE SUPÉRIEURE

ACKNOWLEDGMENT

First, I am particularly grateful to my supervisor, Prof. Ruxandra Mihaela Botez, for her technical support, leadership and professional guidance, encouragement, and mentoring during my research. I especially appreciate her patience and understanding.

Special thanks are extended to Prof. Tony Wong for his advice, guidance, and valuable suggestions throughout the research work.

Many thanks you to the Hydra Technologies team in Mexico for their continuous support, especially Mr. Carlos Ruiz, Mr. Eduardo Yakin, and Mr. Alvaro Gutierrez Prado.

Then, I would like to thank Jérémy Laliberté and Salman Shafi for allowing me to join and be funded by the CREATE UTILI program. This program allowed me to enhance my knowledge of Unmanned Aerial Systems by working with Tri-Star multi-copters company team. I also met people from the drone industry through meetings, workshops, and internships, which was very fulfilling.

I want to thank Alessandro Ceruti for the opportunity to work on my research. This collaboration was enriching and allowed us to share our knowledge and culture to conduct very good research. Thank you also for your support in revising our papers, that was very helpful.

I want to thank my colleagues at the LARCASE, Simon Longtin-Martel, Seyed Mohammad Hashemi, Mir Hossein Negahban, Nicola Zonzini, and the internship students with whom I worked with during this thesis: Mohamed Greinch, Maxime Soule, Alexandre Chanas, Ludivine May and Clément Cuartero. We have shared very good moments despite the COVID-19 crisis.

Last but not least, I would like to extend my gratitude to the persons who always give moral support to me throughout my career and research. This journey would have never been possible

without their support. I would like to mention my mother, Rafiqa Bano; my father, Bashir Ahmed; my wife, Sadaf Aleem; my son, Zahran Musavir and my brothers, Maqsood Ahmad and Basharat Bashir, and my sisters, Afeeda Bashir, Tahira Bashir and Fatima Bashir. Thank you very much to all of you for your moral support, and without all of you, maybe I could not finish this project by the given time.

I am deeply grateful to my family for their ever-lasting love and support. I dedicate this work to them.

Optimisation de Design Aérodynamique et Contrôle de Séparation de Flux sur le UAS-S45 en Utilisant des Ailes Déformables

Musavir BASHIR

RÉSUMÉ

La conception des avions modernes est grandement influencée par des considérations environnementales, telles que le bruit et les émissions de carbone, l'amélioration de l'efficacité énergétique et la croissance neutre en carbone, et la hausse des prix du carburant a également fait de l'efficacité énergétique un élément essentiel de la conception des avions. Le secteur de l'aviation a utilisé de nombreuses stratégies pour atteindre ces objectifs, et cette thèse vise à développer un concept d'aile déformable basé sur le Morphing Leading Edge (MLE) et le Morphing Trailing Edge (MTE) pouraugmenter l'efficacité aérodynamique d'un avion. Par conséquent, une optimisation aérodynamique et structurelle pour le profil UAS-S45 à l'aide de la technologie d'aile déformante a été réalisée au Laboratoire de recherche en contrôles actifs, avionique et aéroServoÉlasticité (LARCASE).

Cela inclut un cadre d'optimisation, qui combine un algorithme d'optimisation, des techniques de paramétrage de profil aérodynamique et un solveur aérodynamique. Pour obtenir les formes d'ailes optimisées, différentes méthodes de paramétrage, telles que les méthodes de Bézier-Parsec (BP), de transformation de forme de classe (CST) et de Makima, ainsi que des algorithmes d'optimisation, tels que la recherche de motifs d'optimisation en essaim de particules couplée (PSO), l'algorithme génétique et l'optimisation de la fenêtre noire (BWO). Les effets de diverses techniques de paramétrage et de choix d'algorithmes sur le temps de calcul et les résultats de l'optimisation aérodynamique sont étudiés. Plusieurs fonctions objectives, telles que la minimisation de la traînée, la maximisation de la portance à la traînée et la maximisation des performances d'endurance aérodynamique, ont été utilisées pour optimiser les arbres de profil aérodynamique. Un solveur aérodynamique a été couplé à une optimisation interne basée sur MATLAB. Les méthodes de paramétrage ont été intégrées au solveur aérodynamique bidimensionnel connu sous le nom de XFoil, et le modèle de turbulence Transition ($\gamma - Re_\theta$) a été utilisé pour valider les résultats.

Les résultats de l'optimisation ont révélé que les ailes déformables de type Morphing Leading Edge (MLE) et Morphing Trailing Edge (MTE) améliorent leurs performances aérodynamiques dans différentes conditions de vol. Par exemple, le coefficient de portance du profil MLE a été augmenté de 21 % et le coefficient de portance maximal a été porté à 9.6 %. De plus, un retard de 3 degrés pour l'angle d'attaque du décrochage a été observé. Les configurations MTE ont également montré une amélioration significative des performances aérodynamiques. Les profils MTE ont augmenté le coefficient de portance maximal à 8.13%, et l'endurance a été maximisée en augmentant $C_L^{3/2}/C_D$ de 10.25%. Dans l'ensemble, l'aile déformante peut augmenter le coefficient de portance maximal, retarder la séparation de la couche limite et augmentant l'angle d'attaque de décrochage.

De plus, une optimisation structurelle préliminaire a été effectuée pour aider à la conception et à l'analyse d'une structure de bord d'attaque déformable à l'aide de l'analyse de sensibilité paramétrique. La corrélation entre les variables de conception, telles que l'épaisseur du stratifié composite, les propriétés du matériau, l'orientation des plis, le nombre de plis, etc., et les paramètres de deux critères de défaillance, la rupture de contrainte maximale et la défaillance de Tsai-Wu, ont été évaluées. L'étude a permis d'obtenir les variables importantes qui sont significatives pour la conception de l'aile déformable. Les matrices de corrélation et de détermination ainsi que les nuages de points ont été obtenus pour tous les paramètres de conception et, par conséquent, ces résultats ont été utilisés pour concevoir l'aile au bord d'attaque déformable en composite.

En outre, l'utilisation de la technologie des ailes déformables comme technique de contrôle du décrochage a été étudiée parce quela commande de décrochage dynamique se produit dans toutes les applications aérospatiales. La nécessité d'un contrôle dynamique du décrochage est cruciale pour les UAV et les avions militaires, car ils nécessitent un haut niveau de manœuvrabilité. La conception et la mise en œuvre de la technologie DMLE (Dynamically Morphing Leading Edge) ont été étudiées de manière exhaustive pour différents paramètres de déformation, tels que la fréquence et l'amplitude de déviation, et moment du début de déformation. Il s'est avéré efficace pour contrôler la formation et le développement du vortex de pointe et la séparation des flux, empêchant ainsi le profil de connaître un décrochage dynamique.

Mots-clés : aile déformable, optimisation aérodynamique, PSO, BWO, CFD, déformation de bord d'attaque, déformation de bord de fuite, décrochage dynamique, bord d'attaque à déformation dynamique

Aerodynamic Design Optimization and Flow Separation Control of the UAS-S45 using Wing Morphing Technology

Musavir BASHIR

ABSTRACT

Modern aircraft design is greatly impacted by environmental considerations, such as noise and carbon emissions, fuel efficiency improvement, and carbon-neutral growth, and the rise of fuel prices has also made fuel efficiency a vital element in aircraft design. The aviation sector has used many strategies to meet these goals, and this thesis aims to develop a morphing wing concept based on the Morphing Leading Edge (MLE) and Morphing Trailing Edge (MTE) to increase the aerodynamic efficiency of an aircraft. Therefore, an aerodynamic and structural optimization for the UAS-S45 airfoil using morphing wing technology was performed at the Research Laboratory in Active Controls, Avionics, and AeroServoElasticity (LARCASE).

This includes an optimization framework, which combines an optimization algorithm, airfoil parameterization techniques, and an aerodynamic solver. To obtain the optimized wing shapes, different parameterization methods, such as the Bezier-Parsec (BP), Class Shape Transformation (CST), and Makima methods, and optimization algorithms, such as the Coupled Particle Swarm Optimization (PSO)-Pattern search (PS), Genetic Algorithm, and Black Window Optimization (BWO) were implemented. The effects of various parameterization techniques and algorithm choices on computing time and the results of aerodynamic optimization are investigated. Several objective functions, such as drag minimization, lift-to-drag maximization, and maximizing aerodynamic endurance performance, were used to optimize the airfoil shapes. An aerodynamic solver was coupled with an in-house MATLAB-based optimization framework. The parameterization methods were integrated with the two-dimensional aerodynamic solver known as XFoil, and the Transition ($\gamma - Re_\theta$) turbulence model was used to validate the results.

The optimization results revealed that Morphing Leading Edge (MLE) and Morphing Trailing Edge (MTE) wings improve their aerodynamic performance at different flight conditions. Such as, the lift coefficient of the MLE airfoil was increased by 21%, and the maximum lift coefficient was increased to 9.6%. In addition, a 3-degree delay for the stall angle of attack was observed. The MTE configurations also showed a significant improvement in aerodynamic performance. The MTE airfoils increased the maximum lift coefficient to 8.13%, and the endurance was maximized by increasing $C_L^{3/2}/C_D$ by 10.25%. Overall, the morphing wing potentially increased the maximum lift coefficient, delayed the separation of the boundary layer, and increased the stall angle of attack.

In addition, a preliminary structural optimization was conducted to assist in the design and analysis of a morphing leading-edge structure using the parametric sensitivity analysis. The correlation among the design variables, such as composite laminate thickness, material properties, ply orientation, number of plies, etc., and the parameters for two failure criteria, maximum stress failure, and Tsai-Wu failure, were evaluated. The investigation helped in

obtaining the important variables which are significant for the morphing wing design. The correlation and determination matrices along with scatter plots were obtained for all the design parameters, and therefore, these results were used to design the composite morphing leading-edge wing.

Furthermore, the use of morphing wing technology as a stall control technique was studied because dynamic stall control occurs in all aerospace applications. The need for dynamic stall control is crucial for UAVs and military aircraft, as they require a high level of maneuverability. The design and implementation of the Dynamically Morphing Leading Edge (DMLE) technology were comprehensively investigated for different morphing parameters, such as deflection frequency and amplitude, and the morphing starting time. It was effective in controlling the formation and development of leading-edge vortex and flows separation, thus preventing the airfoil from experiencing dynamic stall.

Keywords: morphing wing, aerodynamic optimization, PSO, BWO, CFD, Morphing Leading Edge (MLE), Morphing Trailing Edge (MTE), Dynamic Stall, Dynamically Morphing Leading Edge (DMLE)

TABLE OF CONTENTS

Page

LIST OF TABLES

Page

LIST OF FIGURES

Page

LIST OF ABREVIATIONS

ATAG	Air Transport Action Group
BWO	Black Widow Optimization
CFD	Computational Fluid Dynamics
CST	Class Shape Transformation
DLR	German Aerospace Research Center (Deutsches Zentrum fur Luft und Raumfahrt)
DNLE	Droop Nose Leading Edge
DSV	Dynamic Stall Vortex
EADS	European Aeronautic Defence and Space Company
ETS	École de Technologie Supérieure
FishBAC	Fishbone Active Camber
GA	Genetic Algorithm
ICAO	International Civil Aviation Organization
LARCASE	Laboratory of Applied Research in Active Control, Avionics and Aeroservoelasticity
LEV	Leading Edge Vortex
LSB	Laminar Separation Bubble
NACA	National Advisory Committee for Aeronautics
NASA	National Aeronautics and Space Administration
NOVEMOR	Novel Air Vehicles Configurations: Fluttering Wings to Morphing Flight project
NURBS	Non-uniform Rational B-Splines
PS	Pattern Search
PSO	Particle Swarm Optimization
RANS	Reynold Average Navier-Stokes equations

SADE	Smart High Lift Devices for Next Generation Wings project
SARISTU	Smart Intelligent Aircraft Structures project
SST	Shear Stress Transport
TEV	Trailing Edge Vortex
UAS	Unmanned Aerial System
UAV	Unmanned Aerial Vehicle
UDF	User Defined Function
VMLE	Variable Morphing Leading Edge

LIST OF SYMBOLS

α	Angle of attack
α_{te}	Trailing edge direction
α_{amp}	oscillating amplitude
α_{mean}	mean angle of attack
c_l	Lift force per unit span
c_d	Drag force per unit span
C_L	Lift coefficient
$C_{L,MAX}$	Max Lift Coefficient
C_D	Drag coefficient
$C_{L,MAX}$	Max Drag Coefficient
c	Chord
c_p	Specific fuel consumption
C_f	Skin friction coefficient
D	Drag force
D_k	Destruction term (Turbulent kinetic energy)
D_ω	Destruction term (Specific Dissipation Rate)
dz_{te}	Trailing edge thickness
e	Non-dimensional Oswald efficiency number
E	Endurance
E_a	Aerodynamic Endurance Efficiency
E_γ	Source terms (Vortex)
f	Function
H	Shape factor

XXX

k_T	Turbulent kinetic energy
k	Reduced Frequency
L	Lift force
M	Mach number
P_k	Production term (kinetic energy)
r_{le}	Leading edge radius
Re_θ	Reynolds number with respect to the momentum thickness
S	Wing planform area
t	Thickness
$\theta(k)$	Camber Line Slope
U	Boundary layer edge velocity
v_i^n	Velocity vector
V_∞	Free stream velocity
W_i	Initial weight of the aircraft
W_f	Final weight of the aircraft
W_{le}	maximum leading edge downward displacement
y^+	Distance In Wall Coordinate
x_i^n	Position vector
x_c	Upper crest position in horizontal coordinates
y_c	Upper crest position in vertical coordinates
z_{te}	Trailing edge offset in the vertical direction
β_{te}	Trailing edge wedge angle
η_{pr}	Propeller efficiency
ρ	Free stream density

∂	Differential operator
θ	Momentum thickness
ξ	Streamwise coordinate
μ	Dynamic viscosity coefficient
σ	Source
ω	Specific Dissipation Rate
γ	Vortex
c_l	Lift force per unit span
$C_{N_2}^{N_1}$	CST class function
c_p	Specific fuel consumption
C_f	Skin friction coefficient
E	Endurance
E_a	Aerodynamic Endurance Efficiency
K_i^n	Binomial coefficient K
X_{tu}	Translation variable in x for the upper surface
X_{tl}	Translation variable in x for the lower surface
ρ	Air density
Θ	Morphing deflection angle

INTRODUCTION

Environmental and operational constraints have significantly influenced the design of modern aircraft. A significant component of a green economy strategy is the promotion and adoption of sustainable aircraft technology. Environmental issues, including noise and carbon emissions, are gaining increasing importance in the development and use of commercial aircraft. In addition, fuel efficiency has also become a crucial component in aircraft design because of the unpredictability of its costs. These difficulties are even more critical when the present predictions regarding the increase in aviation traffic are considered.

The Advisory Council for Aeronautics Research in Europe (ACARE) 2020 targets are among the most well-known in the academic and industrial communities (Sébastien et al., 2008). They call for cutting emissions of nitrogen oxides (NOx) by 80% and carbon dioxides (CO_2) by half. However, it is obvious that meeting most of these targets will require substantial R&D investment in innovative technologies in multiple fields, including materials, engines, systems, structure, and aerodynamics.

Researchers are investigating the design of new aircraft technologies that would be more climate-friendly and fuel efficient. For example, modern aircraft utilize traditional hinged flight control surfaces that can be optimized for particular levels, but they cause a lot of noise due to vibrations and drag provoked by the gap between the wing's main body and its adjacent control surfaces. This unnecessary drag on conventional wings reduces aircraft performance and increases fuel burn levels, thus adding CO_2 emissions. The targets set by the International Air Transport Association (IATA) to reduce carbon emissions were reported in detail (Hileman, 2022).

Since conventional aircraft remained fundamental in design and performance, nature provides an elegant and efficient flight to get birds off the ground. Some species of birds have been observed flying on trajectories as far as Alaska to New Zealand over eight days without stopping, while others have been observed soaring as high as 37,000 feet. But how do birds

seem to be aerodynamically efficient and how can we use these solutions to enhance aircraft performance?

For example, during bird flight, the wing will be extended and straightened during the downstroke while it will be bent inward and twisted up during the upstroke. Thus, drag is reduced while thrust is increased, therefore increasing energy efficiency. Initially, these principles may seem difficult to realistically utilize in an aircraft, and researchers have attempted to mimic bird flight to improve the aerodynamic performance for a broader flight envelope. However, such an attempt requires a high Level of Technology Readiness (LTR), which allows it to be installed on UAVs because of safety and weight concerns. This possibility of meeting the desired aerodynamic efficiency by mimicking the bird flight is known as the "morphing wing technology". The early years of aeronautical research focused on biomimetic techniques based on flexible and highly deformable wing structures by adjusting their shapes for different flight conditions (Bar-Cohen, 2006; Harvey et al., 2021; Jiakun et al., 2021).

"Morphing Wing Technology" is the ability to change specific aspects of a wing shape so that it could accomplish higher aerodynamic performance (Barbarino et al., 2011). Currently, aircraft are developed for certain flight conditions, and they can perform well over their flight envelope; however, their performance is suboptimal for multi-point flight conditions. Morphing can improve aircraft performance by adapting an aircraft's geometry to changing flight conditions. Figure 0.1 compares some of the pros and cons of morphing by type. Each morphing type's advantages are presented in red boxes and its drawbacks are in blue boxes.

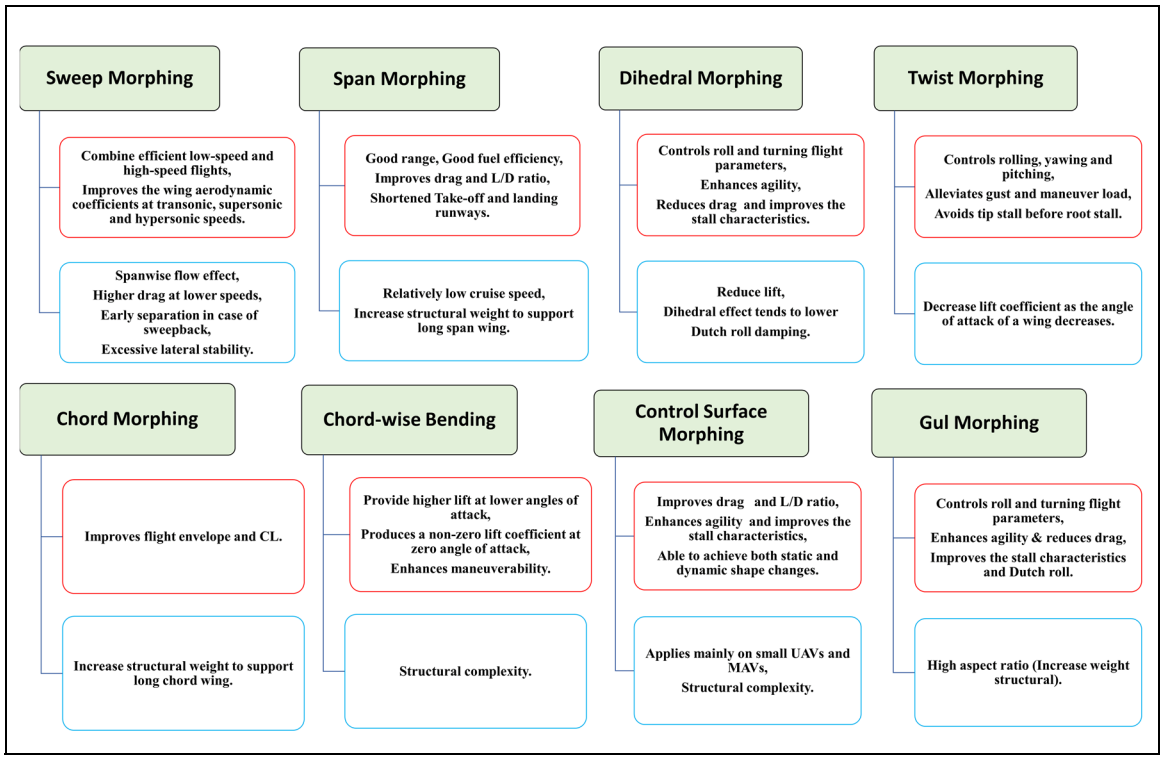

Figure 0.1 Different morphing types with their advantages and disadvantages

Several significant collaborations have been established between industry, academia, and research institutions to design, manufacture, and test innovative morphing technologies with the aim of reducing fuel and greenhouse gas emissions (Frota, 2010; Kintscher et al., 2011; Papadopoulos, 2016). Therefore, several morphing wing projects were carried out at our Research Laboratory in Active Controls, Avionics, and AeroServoElasticity (LARCASE) (R. Botez, 2018a; Koreanschi et al., 2017b; Koreanschi, et al., 2016b; Popov et al., 2008).

In addition, an UAV may experience a sudden pitch attitude variation following maneuvers or unexpected external disturbances (W. McCroskey et al., 1975; Saeed et al., 2018). Consequently, an abrupt and sudden change in the angle of attack may develop non-linear unsteady aerodynamic effects such as dynamic stall. (Cummings et al., 2008; Shyy et al., 2010). At the stall angle of attack, the wing cannot produce as much lift as expected or intended because the airflow over it spreads and no longer follows its normal path. Therefore, the angle of attack needs to be lowered rapidly to avoid a stall state.

In a static stall, the angle of attack changes very little while the flow separates from the wing. However, in a dynamic stall, the angle of attack increases more rapidly, and the flow over the wing is drastically altered. The lift suddenly drops off under such conditions, and the aircraft stops flying. This situation quickly leads to dangerous negative pitching moments and thus causing accidents.

Since the morphing wing technology mimics bird flight, it can help to control or significantly reduce the adverse effects of dynamic stall. The potential benefits of controlling and further delaying this nonlinear aerodynamic stall effect could be achieved by employing a Morphing Leading Edge (MLE) wing. An in-depth understanding of the unsteady flow physics characterizing this class of morphing wings would be helpful. Therefore, investigating the dynamic stall phenomenon over morphing airfoils is important, and developing suitable numerical approaches to such unsteady CFD analysis will contribute to novel morphing wing technologies advancement for green aircraft.

CHAPTER 1

STATE-OF-THE-ART AND RESEARCH CONTRIBUTIONS

1.1 Problem statement

Modern Modern Unmanned Aerial Vehicles (UAVs) offer several advantages, including low operating costs, the ability to fly in risky conditions, long flight endurance, etc., and therefore are used for fire detection, search and rescue, wildlife monitoring, security surveillance, and so on. Depending on their mission objectives, UAVs can be handheld or massive autonomous systems. Figure 1.1 presents the various performance parameters of UAVs according to their mission specifications.

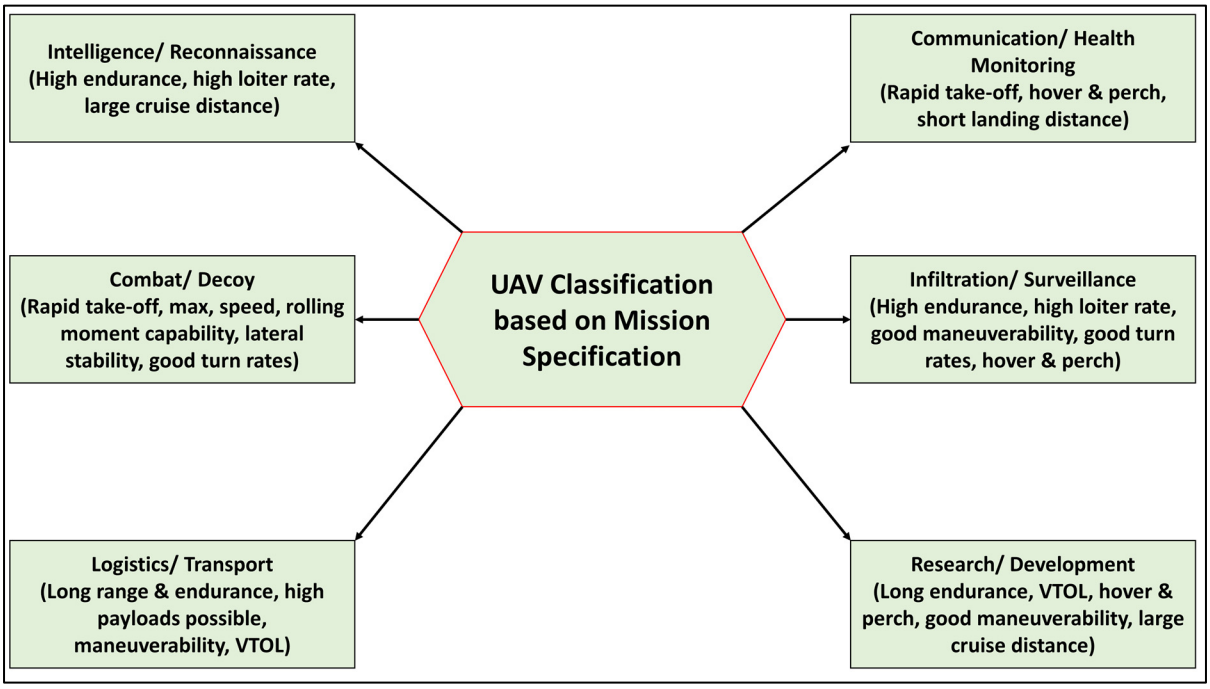

Figure 1.1 UAV performance parameters with their associated mission objectives.

UAVs are generally designed, developed and manufactured as per their mission specification. Therefore, they are developed to fly optimally for certain situations, and they can perform very well over those flight conditions; however, their performance is suboptimal for multi-point

flight envelopes. Morphing Wing Technology can improve the UAV's overall performance by adapting their wing geometry to changing flight conditions.

The aviation industry has implemented various solutions to achieve enhanced aerodynamic performance. Smart material, laminar flow, and air traffic management technologies are some of the solutions that the aviation industry has explored (Abbas et al., 2013; Ranasinghe et al., 2019). Morphing wing technology is a bio-inspired technology that enables an aircraft to modify its design configuration at different speeds and altitudes, and to optimize its performance over the entire flight envelope. However, morphing technology has not yet been applied in a real aircraft in a way that allows it to realize its full potential. Most studies emphasize single flight condition optimization, which is insufficient to represent the operating flight envelope; such designs for optimum performance at one specific flight condition cause serious performance degradation under off-design conditions. An optimized morphing design for the entire flight operating envelope with experimental validation is a challenging task, that would result in high aerodynamic performance.

In addition, the conventional hinged high lifting devices and trailing edge surfaces used in present-day aircraft create surface discontinuities, increasing the drag, causing noise, and possibly contributing to the creation of a turbulent boundary layer. Numerous researchers believe that laminarization technology has the maximum potential to reduce drag and avoid flow separation, but it requires thin airfoils and smooth, seamless surfaces (Abbas et al., 2013; Concilio, et al., 2019; Carossa et al., 2016; Kintscher et al., 2011). Morphing wing technology can solve these issues by providing seamless wing surfaces that can adapt its shape to different conditions. Therefore, this thesis presents the implementation of morphing wing technology on the Hydra Technologies UAS- S45 wing and optimize it for aerodynamic and structural performances.

Although many investigations were done into the aerodynamic optimization of morphing wings, most of them focus on examining the optimization framework (Sugar-Gabor et al., 2013; Gamboa et al., 2009; Lyu et al., 2015; Magrini et al., 2018). This limited focus

underscores the importance of studying the impact of algorithm selection for obtaining the optimal aerodynamic optimization results and reduced computing time. In addition, the choice of different shape parameterization techniques in the optimization framework is also significant because it generates a design space where the optimizer searches for the optimal solution. Therefore, the studies for comparative analysis of optimization algorithms and the shape parameterization techniques should be conducted.

Furthermore, several active and passive flow control techniques for dynamic stall control can be found in the literature, however, the use of morphing wing technology, such as dynamically morphing leading edge and trailing edge can barely be found in the literature. That includes dynamic meshing with time-dependent geometry parametrization. This unsteady morphing airfoil motion represents the true nature of the problem because the leading and trailing edge deflections cause unsteady flow effects. The use of morphing wing technology as a stall control mechanism, and the unsteady flow behavior analysis of pitching airfoils are both significant in the field of aerodynamics.

The research presented in this thesis was mainly divided into two areas: 1) a morphing optimization approach that combines aerodynamic and structural performances with the aim to find the optimal airfoil shapes for the UAS-S45 to increase its overall performance for different flight conditions; and 2) the application of morphing wing technology to delay the formation and development of leading-edge vortex, and flow separation, thereby controlling the dynamic stall.

1.1.1 Optimization of an UAS-45 Morphing Wing

An aerodynamic and structural optimization by use of different parameterization methods and optimization algorithms was performed at the LARCASE for the UAS-S45 airfoil using Morphing Leading Edge (MLE) and Morphing Trailing Edge (MTE) approaches. An aerodynamic design of morphing wing surfaces with continuous camber variation was aimed to replace traditional discrete control surfaces, such as flaps, ailerons, or slats. A camber

morphing wing helps an aircraft to fly at its optimal aerodynamic efficiency for multiple flight conditions by altering its wing geometry and allowing smooth flow behavior.

Optimization in aircraft design, specifically in morphing wing technology, is a key to satisfy the required mission, flight operation, and performance needs. This optimization requires the selection of the most appropriate optimization algorithm and parameterization method, which can be obtained by carrying out the comparison analysis. While gradient-based techniques usually have faster convergence rates than metaheuristic algorithms, the latter has the advantages of high solution accuracy, flexibility, and obtaining global optimum results. Furthermore, implementing morphing wing technology in an UAV increases the number of design variables, so that optimization is performed at different mission segments, thus making it likely to find the global optimal solution.

In this research, three parameterization methods: the Bezier-Parsec (BP), Class Shape Transformation (CST), and Makima, and three optimization algorithms: the Coupled Particle Swarm Optimization (PSO)-Pattern Search (PS), the Genetic Algorithm, and Black Window Optimization (BWO) are analyzed. Different objective functions, such as drag minimization, lift-to-drag and aerodynamic endurance maximization are employed to optimize the aerodynamic shape of the UAS-S45 airfoil.

These optimization results using the above-mentioned optimization algorithms and the impact of the fitness function on solution quality were evaluated. The optimization was carried out at Mach numbers of 0.08, 0.1 and 0.15 for the cruise and climb flight conditions. All these optimization algorithms obtained comparable lift-to-drag ratio results with differences of less than 0.03 % as well as similar airfoil geometries and pressure distributions.

The Morphing Leading Edge (MLE) optimization was studied to improve the aerodynamic performance of the UAS-S45 at the cruise condition at the angle of attack of 2°. This MLE optimization resulted in the drag coefficient reduction by 12.18% in comparison to the reference airfoil drag coefficient. An aerodynamic improvement of the lift-to-drag ratio was

obtained by 15.22%. Furthermore, the aerodynamic endurance, expressed by $\frac{C_L^{3/2}}{C_D}$ increased from 29.52 to 32.48, representing a 10% better performance for the UAS-S45 MLE optimized airfoil configuration than that of its reference airfoil.

The aerodynamic performance also showed a significant improvement for the MTE configurations with respect to the reference airfoils. An increase of the maximum lift coefficient ($C_{L,max}$) of up to 8.13% and of the aerodynamic endurance efficiency of $\frac{C_L^{3/2}}{C_D}$ of up to 10.25% were obtained, for the UAS-S45 MTE airfoils.

Furthermore, a study of the design and analysis of a morphing leading-edge (MLE) structure for the UAS-S45 wing integrated with an actuation mechanism was done. Parametric optimization and sensitivity analysis are effective solutions to obtain optimized structural design. Several design parameters were compared by using the "correlation" and the parameters affecting the wing model were explored to predict failure indices for the wing.

The wing model input parameters included the composite material properties, ply angles, ply stacking sequences, etc. The correlation and determination matrices were then computed using the parameter sets' results by identifying the parameters with the highest correlation coefficients. These findings were then used to adapt the composite MLE for its target droop nose optimization and to design a demonstrator.

1.1.2 Dynamic Stall Control of an UAS Morphing Wing

Unsteady aerodynamic analysis plays an essential role in translating morphing concepts into designs. Dynamic stall is an aerodynamic phenomenon that occurs when the flow over wings and aerodynamic bodies separate rapidly due to changes in relative freestream conditions. Dynamic stall is marked by increased flow-field instability, resulting in increased airframe vibration and reduced aerodynamic performance (Gupta et al., 2019; Wei et al., 2021). A thin and reversed flow region forms at the trailing edge before a dynamic stall, and a reverse

pressure gradient moves the separation area to the leading edge. However, the flow remains attached to the airfoil. The leading-edge vortex produces a powerful suction. A Leading-Edge Vortex (LEV) progressively splits from the airfoil surface to generate a Dynamic Stall Vortex (DSV). The DSV develops near the trailing edge as the angle of attack increases, resulting in significant force variations. At a higher angle of attack, the DSV separates from the airfoil's trailing edge. Figure 1.2 shows the various stages of the recirculating flow regions.

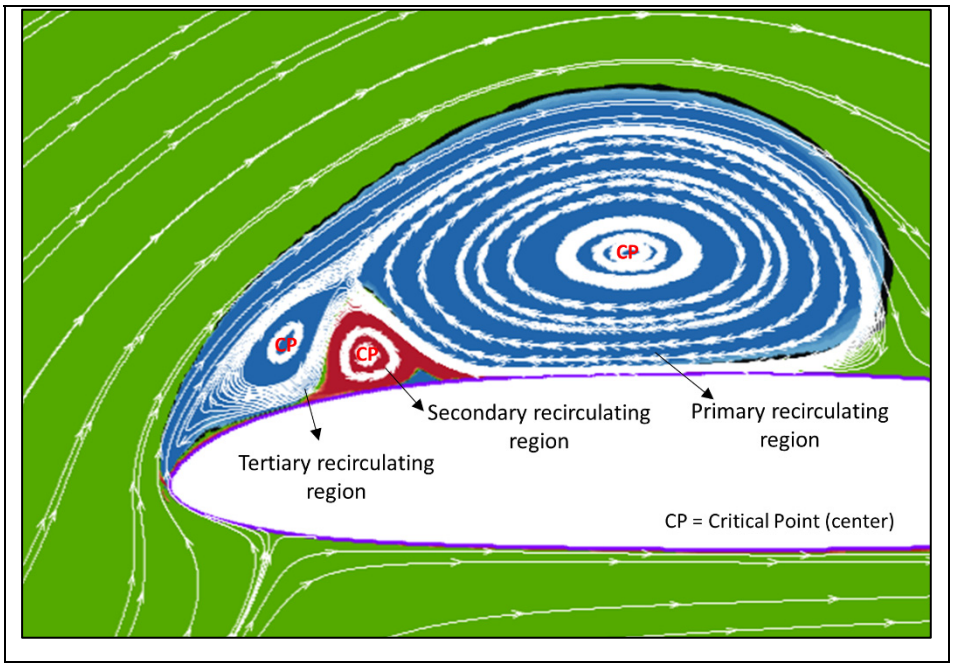

Figure 1.2 Various phases of the recirculating flow regions

The use of morphing wing technology as a flow control technique has resulted in efficient aerodynamic designs (Ignazio Dimino et al., 2017; Sugar-Gabor et al., 2014; Sinapius et al., 2014; Vu et al., 2005). Dynamic stall control is especially significant because it occurs in all aerospace applications, such as on UAVs (Mathisen et al., 2021; Sekimoto et al., 2022), helicopter rotors (Liiva, 1969; Richez, 2018), wind turbines (Larsen et al., 2007; Zhu et al., 2021), and military aircraft (Brandon, 1991; Nguyen et al., 2022). Dynamic stall is caused by a rapidly pitching airfoil. The LEV is a critical component of dynamic stall, as it increases the lift coefficient. However, the lift is lost when the vortex sheds into the wake, thus increasing drag and shifting the pitching moment. Since the discovery of dynamic stall, researchers have

tried to understand LEV mechanics and to modify its formation. Altering the LEV formation may increase an aircraft's operational envelope.

The research findings mentioned above have shown that different methods can be implemented to alleviate the dynamic stall of a pitching airfoil. In this thesis, we are implementing the MLE technology to control the dynamic stall. However, dynamic morphing phenomena impose a significant amount of complexity in the structure and control system of a morphing wing.

Therefore, firstly the statically MLE airfoils design obtained from the optimization approach is analyzed in this thesis to enhance the overall aerodynamic performance. The obtained optimized airfoils are then implemented to investigate dynamic stall phenomena. Relatively few numerical studies have used optimized airfoils to mimic the dynamic stall phenomenon associated with a moderate Reynolds number (Re = 10^6) turbulence flow regime. The $\gamma - Re_\theta$ transition model's capacity to appropriately depict dynamic stall and to contribute to a better understanding of the flow physics of dynamic stall will thus aid in the design optimization for dynamic stall alleviation.

Secondly, the design and implementation of the Dynamically Morphing Leading Edge (DMLE) technology are investigated for different morphing parameters, such as deflection frequency and amplitude, and the morphing starting time, and which is hardly found in the literature. This research investigates the formation and control of LEV and flows separation, thus preventing the airfoil from experiencing dynamic stall. Systematic research is performed for dynamic stall control with DMLE technology on an oscillating UAS-S45 airfoil.

1.2 Research Objectives

1.2.1 Morphing Wing Design Optimization

The main objective of this research is to provide an accurate optimization framework for the performance improvements that can be obtained for the UAS-S45 wings by using the

Morphing Leading-Edge (MLE) and Morphing Trailing Edge (MTE) wing technologies and to determine their shape changes required to obtain these results. The analysis is performed for several airspeeds and for a wide range of angles of attack with the aim to cover a large part of the UAV's flight envelope. To achieve the proposed global objective, the following sub-objectives were established:

a) Geometrical Parameterization and Optimization of the UAS-S45 Wing

- Optimal solutions can be found by exploring the physical domain using parameterization. Before beginning the optimization process, the suitable parameterization approach should be considered because it impacts the geometry shape and the design space exploration. The study's first goal was to find an appropriate parameterization technique in order to manage the morphing wing geometry;
- Since parameterization defines the design space, which is later used by the optimization algorithm, therefore, it is essential for it to allow the optimizer to thoroughly examine and search for the optimal solution. In this context, the Bezier-Parsec (BP) parameterization was implemented for the design exploration due to its level of flexibility and closeness to the airfoil parameters;
- Implementation of the modified Class Shape Parameterization (CST) for reconstructing the smooth airfoils for the morphing shape design and for ensuring superior performance due to its convergence rate, flexibility, and robustness. The CST function controls the airfoil's leading-edge shape and provides accurate shapes by respecting the leading edge radius;
- Implementation of different global optimization algorithms, such as coupled Particle Swarm Optimization (PSO)/Pattern Search (PS), a Genetic Algorithm (GA), and Black Widow Optimization (BWO) in different optimization frameworks with the aim to compare their results, and, to choose an appropriate optimization algorithm;

b) **Application of coupled Particle Swarm Optimization-Pattern Search (PSO-PS) for the Performance improvement of the UAS-S45 Morphing Airfoil**

- Aerodynamic optimization of the Morphing Leading Edge (MLE) and Morphing Trailing Edge (MTE) wing technology for the UAS-S45 airfoil by implementing drag minimization objective function for different flight conditions;
- Aerodynamic analysis of the morphing UAS-S45 airfoil for the increase of the aerodynamic endurance of the UAS-S45for cruise flight conditions;
- The understanding of the underlying flow mechanism triggered by MLE and MTE technology to improve the boundary layer behavior, and its impact on the laminar-turbulent transition.

c) **Application of the Black Widow Optimization (BWO) Algorithm and its Comparison with other Algorithms for the Performance improvement of the UAS-S45 Morphing Airfoil**

- Aerodynamic optimization of a Droop Nose Leading Edge (DNLE) airfoil for the UAS-S45 by implementing lift-to-drag maximization and aerodynamic endurance maximization objective functions for different flight conditions;
- Aerodynamic optimization of the UAS-S45 airfoil for the increase of the maximum lift coefficient and boundary layer separation delay at various stall angles of attack;
- The comparison of three algorithms, such as Particle Swarm Optimization (PSO), a Genetic Algorithm (GA), and Black Widow Optimization (BWO) for analysis of their convergence rates and results for the Droop Nose Leading Edge (DNLE) airfoil.

d) **Structural Optimization of an UAS-S45 Droop Nose Leading Edge (DNLE) Wing**

- Design and development of a Droop Nose Leading Edge (DNLE) morphing wing structure and mechanism for the UAS-S45 wing to optimize its aerodynamic performance in flight;

- Development of the flexible composite skin, modeled using laminate characteristics (thickness, material, and plies orientation) using Ansys Composite PrepPost (ACP) from the ANSYS software package;
- Sensitivity analysis of a DNLE morphing composite wing to obtain the parameters with the highest correlation coefficients. These parameters with their high values will affect the morphing wing design and help to predict the possible failures.

1.2.2 Dynamic Stall Control of a Morphing Leading-Edge (MLE) Wing

Developing an unsteady aerodynamic model for the UAS-S45 morphing airfoil with the aim to analyze its transient aerodynamic coefficients is another major objective of this thesis. The first step is to investigate a numerical approach to study the dynamic stall phenomenon, followed by the study of the effect of the Dynamically Morphing Leading Edge (DMLE) on controlling this unsteady flow phenomenon. Several sub-objectives were targeted to achieve this goal and they are summarized in the following order:

- Obtain the hysteresis cycles of lift, drag, and moment coefficients for a pitching UAS-S45 airfoil at different reduced frequencies. A relationship between various parameters, such as reduced actuation frequency, amplitude, and flow conditions (Reynolds number, airfoil pitching rate) are presented;
- Analyses of optimized Morphing Leading Edge (MLE) and Morphing Trailing Edge (MTE) airfoils for dynamic stall control, given that the dynamic airfoil morphing phenomena imposes a significant amount of complexity in the structure and control systems of a morphing wing;
- Development of an unsteady parameterization method for the Dynamically Morphing Leading Edge (DMLE) airfoil geometry that can account for unsteady deformations during the morphing wing process, followed by its implementation in the commercial software Ansys – Fluent using an in-house User Defined Function (UDF);

- Analyses of the Dynamically Morphing Leading Edge (DMLE) airfoil at different morphing parameters, such as deflection frequency and amplitude, and morphing starting time. The objective is to control the formation and development of LEV and flow separation, thus preventing the airfoil from experiencing dynamic stall.

1.3 Research Methodology and Models

In this work, numerical analyses (2D and 3D) of a morphing wing system were carried out using an in-house MATLAB optimization framework consisting of both originally developed and commercially available tools. The framework is a multi-objective, constrained airfoil optimization tool, and supports different geometry parameterization methods and algorithms. The user can select and modify the parameterization method, after which the geometrical and aerodynamic constraints, optimization method, analysis conditions, and type of aerodynamic solver for each condition can be selected. The user then develops the objective function in terms of the aerodynamic coefficients of the airfoil.

In this research, three parameterization methods: the Bezier-Parsec (BP) and Class Shape Transformation (CST), and Makima, and three optimization algorithms: the coupled Particle Swarm Optimization-Pattern search (PSO/PS), Genetic Algorithm (GA), and Black Window Optimization (BWO) were used. XFoil solver was used for performing the two-dimensional airfoil analysis, and Ansys-Fluent solver was used for validation and to perform 3D flow analysis. ICEM-CFD for generating high-quality meshes around the morphing wings. In addition, Ansys and Hypermesh were used for a composite design and optimization. The following subsections will briefly present and explain these codes and models.

1.3.1 Bezier-PARSEC (BP) Parameterization

A mathematical formulation is necessary for parameterizing the airfoil shapes, and it plays an important role in the overall optimization process. Many studies have demonstrated that the overall optimization process's accuracy, resilience, and computational time are all significantly

impacted by the choice of shape parameterization technique. This technique needs to have a wide design space, be resilient for the control of all parameters, and be directly related to the airfoil geometry in order to provide the best aerodynamic result.

Addressing the two above-mentioned concerns inspired the coupling of two well-known methods, thus creating Bezier-PARSEC (BP) parameterization, which combines the benefits of both the Bezier and PARSEC methods. The BP parameters are aerodynamically related to an airfoil shape, and therefore, it facilitates the Bezier control point within four different curves. These four curves help to determine the leading and trailing edges of the camber line, and the leading and trailing edge parts of the thickness distributions. The BP parameters are representing the physical characteristics of a given airfoil. Moreover, to develop new airfoil shapes based on this specific representation, it would be necessary to have the description of basis functions for each parameter to recreate the new ones. One of these combinations is known as BP3333 and it uses 12 parameters to determine the control points of a Bézier curve. These parameters are:

Parameter	
r_{le}	the radius at the leading edge;
β_{te}	the angle at the trailing edge;
x_t	the position in x of the apex of the thickness curve;
y_t	the position in x of the apex of the thickness curve;
dz_{te}	the thickness of the trailing edge of the thickness curve
α_{te}	the angle of the trailing edge
z_{te}	the y position of the trailing edge of the camber curve
γ_{le}	the radius at the leading edge;
x_c	the position in x of the apex of the camber curve
y_c	the position in y of the apex of the camber curve
κ_t	the curvature at the top of the curve
κ_c	the curvature at the top of the curve

This combined parameterization offers 4 control points for the leading-edge thickness curve and 4 points for the trailing-edge thickness curve. The leading-edge camber curve and the trailing-edge camber curve also have 4 control points each. Note that this parametrization is called BP3333 because each of these Bézier curves is of degree 3.

The thickness curve, i.e., the difference between the y-value of the upper surface and the y-value of the lower surface gives 2 other curves which are symmetrical for the upper and lower surface. Added to the camber curve, the resulting profile becomes non-symmetric. Unfortunately, the BP3333 parametrization does not offer sufficient accuracy at the trailing edge and is generally not recommended for wing parameterization.

Another combined parameterization similar to BP3333 is the one called BP3434 (Derksen et al., 2010). This technique offers 10 aerodynamic parameters and 5 Bezier parameters. It uses Bézier curves of degree 4 for the trailing edge thickness and its camber. Figure 1.3 shows the control points used for this parameterization.

A fourth-degree Bezier curve is given by:

$$x(u) = x_0(1-u)^2 + 4x_1u(1-u)^3 + 6x_2u^2(1-u)^2 + 4x_3u^3(1-u) + x_4u^4 \quad (1.1)$$

and

$$y(u) = y_0(1-u)^2 + 4y_1u(1-u)^3 + 6y_2u^2(1-u)^2 + 4y_3u^3(1-u) + y_4u^4 \quad (1.2)$$

.

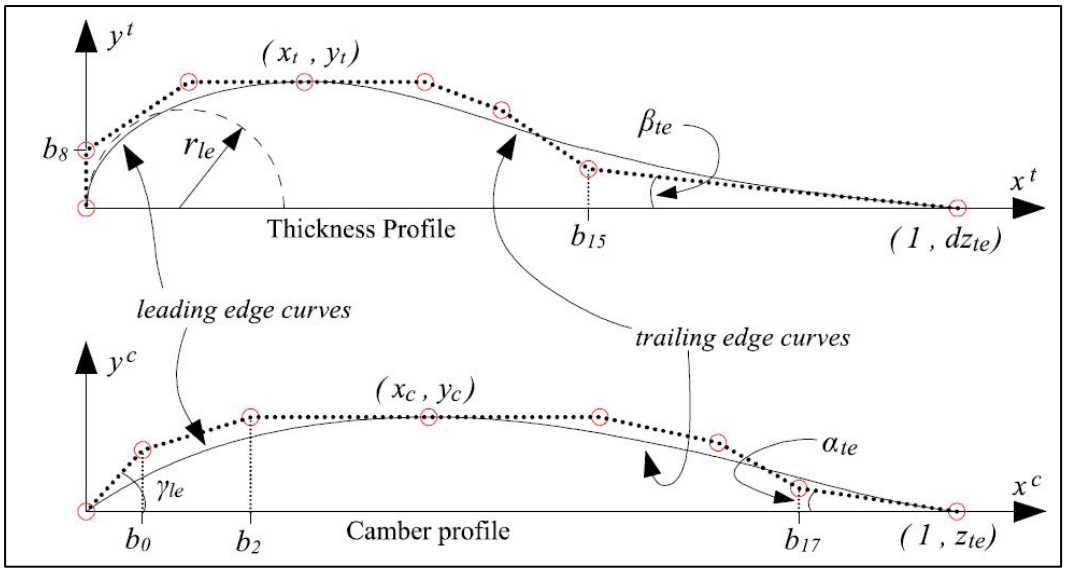

Figure 1.3 BP3434 method parameter definition

1.3.2 The CST Airfoil Parameterization

Class Shape Transformation (CST) is a powerful parameterization technique for modeling two-dimensional and three-dimensional shapes (Kulfan, 2007). The general two-dimensional CST equations can represent any smooth airfoil. One airfoil can be differentiated from another in the CST method by two arrays of coefficients considered into the defining equations. These coefficients control the curvatures of the upper and lower surfaces of the airfoil. This parameterization method captures the entire design space of smooth airfoils and is thus especially useful for any application requiring a smooth airfoil.

Most general CST leading edge morphing can only occur by adding a y-axis deflection to control the points, which may be constrained to maintain a constant skin length. However, that y-axis deflection neglects the x-axis deflection in a Droop Nose Leading Edge (DNLE) morphing. Therefore, DNLE morphing also needs to be constrained. To this end, new parameters are added to impose where the deflection of the LE on the wing ($Morph_{length}$) begins and to assess a specific deflection angle (θ). This approach assumes that there is an axis located on the $\frac{x}{c}$ axis that serves as a basis for the morphing. An arc that is a tangent to the $\frac{x}{c}$

axis on one side and tangent to the deflection angle on the other side begins at $\frac{x}{c} = Morph_{length}$. The length of the arc is the $Morph_{length}$. The skin keeps its relative position to the closest point on the morphing mechanism, meaning that it keeps the same distance perpendicular to the arc. Figure 1.4 illustrates the setup by showing the axis and the arc's neutral unmorphed position and then its variation of $\frac{y}{c}$ with $\frac{x}{c}$ while morphing occurs. For example, the Morph 0.2, 30° figure shows that its morphing begin at $\frac{x}{c} = 0.2$, and the tangent of the end of the arc that is not at $\frac{y}{c} = 0$ has a 30° angle to the $\frac{x}{c}$ axis. More details are presented in Section 4.3.1.

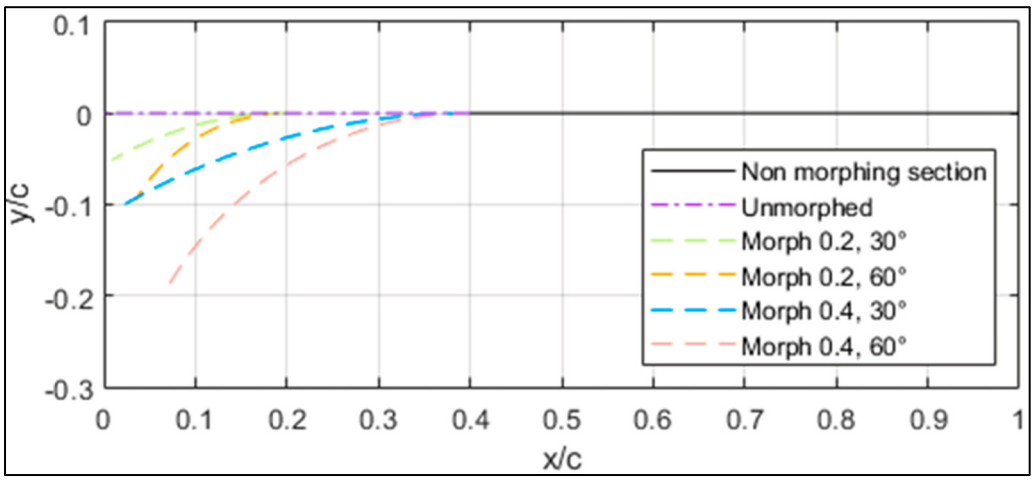

Figure 1.4 Deflection arcs for different morphing conditions

1.3.3 PSO algorithm

The Particle Swarm Optimization (PSO) belongs to the class of gradient-free algorithms. The main motivation of using these algorithms is to use an objective function that acts as an input and returns the optimal value and location of the specific function. However, in some cases, the input function can be noisy, non-differentiable, and computationally costly. An algorithm that employs derivate to optimize such a function would be practically infeasible.

PSO is a meta-heuristic global optimization algorithm, that explores a function's search space to find its global minimum, using approaches that allow it to escape local minima. Gradient-based optimization algorithms cannot guarantee the discovery of a global minimum due to their tendency to become trapped at local minima; these algorithms focus on exploring the search space to maximize the chance of finding the global minimum.

PSO explores the search space through the use of particles by spreading out several particles across the search space, and by evaluating the function value at each particle. It moves these particles around the search space iteratively, through a combination of inertial, personal, and social vectors. These vectors are partially stochastic, which encourages even higher discovery of the search space, while the personal and social vectors help to guide the particles toward more promising locations. PSO has become one of the most widely used global optimization algorithms due to its high accuracy and efficiency.

A global minimum can be found in the context of three major components: an 'inertial' component that is responsible for handling the particle in the previous direction; a 'personal' component that is used to point the particle toward the personal best location; and a 'social' component which directs the particle toward the global best location. The termination conditions associated with such an algorithm are depending on the desired level of convergence. The parameter selection must include a guaranteed convergence of the velocities of the particles, which needs to be zero, such that;

$$v_i^n\,(k) = \left[v_i^n(k-1) + c_1 r_1\left(pbest_i^n - x_i^n(k-1)\right) + c_2 r_2\left(pbestg_i^n - x_i^n(k-1)\right)\right] \tag{1.3}$$

where x_i^n is the position vector; v_i^n is a randomly generated velocity vector of the particles at search initialization, $pbest_i^n$ is a vector representing the best solution achieved by the particle, $pbestg_i^n$ is a vector representing the "global best solution" collectively achieved by the swarm, c_1 and c_2 are stochastic acceleration terms that pull each particle toward $pbest_i^n$ and $pbestg$ positions, respectively, and r_1 and r_2 are random numbers in the uniform range [0, 1].

The update of the position vector at the k^{th} iteration gives the following equation:

$$x_i^n(k) = x_i^n(k-1) + v_i^n(k) \tag{1.4}$$

In comparison, the Pattern Search (PS) algorithm belongs to the local optimization algorithm, which measures the points available within a particular proximity to a specific location. The PS algorithm employs the search direction around the existing point, utilizing the pattern and size of the current mesh size. A key objective of this work is to construct a hybrid algorithm that combines PS and PSO algorithms to overcome their respective shortcomings and thus more quickly to determine global minimum. Figure 1.5 illustrates one of the optimization strategies employed in this thesis.

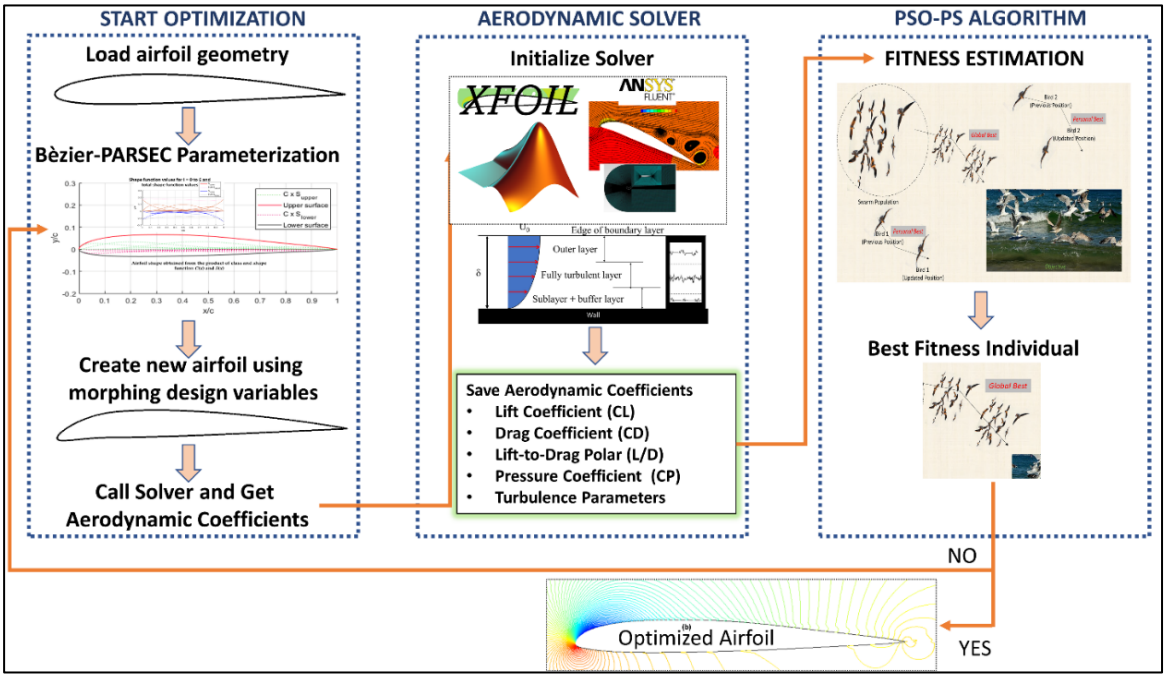

Figure 1.5 Schematics of the optimization framework with a Hybrid Optimizer/PSO algorithm combined with a Pattern Search algorithm

1.3.4 Black Widow Optimization (BWO)

It is well known that nature-inspired algorithms can solve a range of scientific and engineering optimization problems due to their flexibility and ease of use. Moreover, meta-heuristic algorithms does not require structural changes in optimization problems. For example, the Black Widow Optimization (BWO) algorithm is inspired by the unique mating behavior of the black widow spider (Hayyolalam et al., 2020). The BWO algorithm differs from other methods, as it offers effective performance in both its exploration and exploitation phases. The BWO thus seems to be an ideal approach that helps to solve various optimization problems, including finding of the different local optima. This method includes a unique stage, called cannibalism. With the introduction of such a phase, species (or individuals) get eliminated due to their lack of fitness, leading to early convergence.

Black widows are generally nocturnal, the female spins her web at night. When the female black widow wants to mate, she makes particular spots on her net that captivate the male's attention. When the initial male crosses the entry, the web is altered, making the web less attractive to rivals by its reduction. The female will consume the male during or post-mating. After hatching, the offspring participate in sibling cannibalism but stay on their mother's web for a short period, during which they possibly even consume the mother. This complete cycle leads to the survival of strong and fit individuals. It is considered to be the global optimum of the objective function. The pictorial chart in Figure 1.6 illustrates the BWO's main phases.

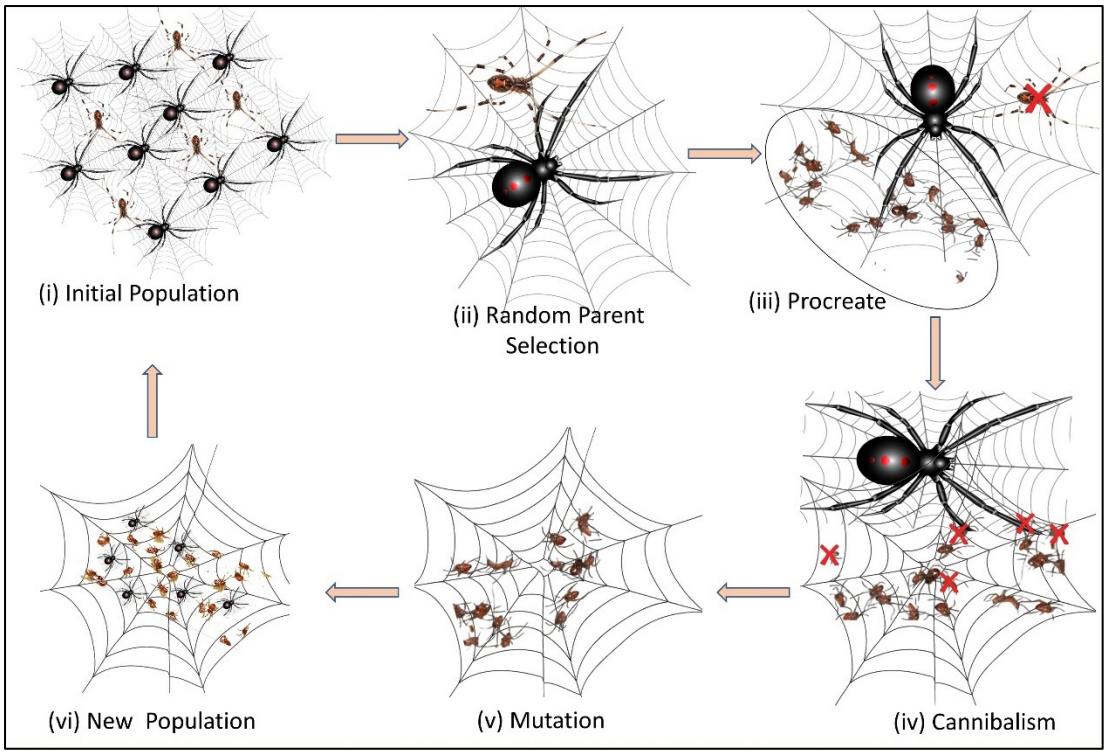

Figure 1.6 Black Widow Optimization (BWO) algorithm

The BWO's detailed outline is presented in Section 4.3.2.

1.3.5 XFoil

XFoil, one of the well-established and effective panel codes developed by M. Drela (Drela, 1989), employs the 2-equations method. It has been determined that the viscous-inviscid interaction plays a crucial role in an integral 2-equation model of boundary layers, specifically in cases of weak separation regions and transition areas.

The XFoil code uses a very sophisticated and reliable method for simultaneously solving boundary layer and potential flow equations. However, it has the drawback of severely limiting the structure of the panel code solver. Alternate or substitute methods for handling viscous inviscid interaction must be investigated, as this study's objective is to create a boundary layer

computation that can be "plugged in" and used in various applications, such as 2D airfoil analysis and cascade analyses.

A viscous formulation can be employed to measure free or imposed flow transition as a way to control transitional separation bubbles and to manage the trailing edge separation. The flow transition is calculated using the e^N approach, allowing the control of different turbulence level parameters.

$$\frac{d\theta}{d\xi} + (2 + H - M_e^2)\frac{\theta}{u_e}\frac{du_e}{d\xi} = \frac{C_f}{2} + \left\{\frac{v_0}{u_e}\right\} \tag{1.5}$$

$$\theta\frac{dH^*}{d\xi} + \left(2H^{**} + H^*(1-H)\right)\frac{\theta}{u_e}\frac{du_e}{d\xi} = 2C_D - H^*\frac{C_f}{2} + \left\{(1-H^*)\frac{v_0}{u_e}\right\} \tag{1.6}$$

Where shape factors H^* and H^{**} are defined in the following equations

$$xH^* = \frac{\int_0^{\propto}\frac{u}{U}\left(1-\left(\frac{u}{U}\right)^2\right)dy}{\int_0^{\propto}\frac{u}{U}\left(1-\left(\frac{u}{U}\right)\right)dy} \tag{1.7}$$

and

$$H^{**} = \left(\frac{0.064}{H_k - 0.8} + 0.251\right)M_e^2 \qquad \text{with} \qquad H_k = \frac{H - 0.290M_e^2}{1 + 0.113M_e^2} \tag{1.8}$$

Non-converged solutions are given a high penalty through the penalty function to obtain convergence solutions; that can eventually be eliminated during the design process.

1.3.6 High-fidelity Computational Fluid Dynamics (CFD) solver

Ansys Fluent is used to accurately solve viscous boundary layer and flow separation problems. The turbulence study model used here is called Transition ($\gamma - Re_\theta$); and consists in the

incorporation of SST k-ω together with intermittency γ and transition onset Reynolds number. Re_θ is the critical Reynolds number where intermittency begins. The four transport equations of the Transition ($\gamma - Re_\theta$) SST are;

$$\frac{\partial(\rho k)}{\partial t} + \frac{\partial(\rho U_j k)}{\partial x_j} = P_k - D_k + \frac{\partial}{\partial x_j}\left[(\mu + \sigma_k \mu_t)\frac{\partial k}{\partial x_j}\right] \tag{1.9}$$

$$\frac{\partial(\rho\omega)}{\partial t} + \frac{\partial(\rho U_j \omega)}{\partial x_j} = P_\omega - D_\omega + \frac{\partial}{\partial x_j}\left[(\mu + \sigma_\omega \mu_t)\frac{\partial \omega}{\partial x_j}\right] + 2(1 - F_1)\frac{\rho\sigma_{\omega 2}}{\omega}\frac{\partial k}{\partial x_j}\frac{\partial \omega}{\partial x_j} \tag{1.10}$$

$$\frac{\partial(\rho\gamma)}{\partial t} + \frac{\partial(\rho U_j \gamma)}{\partial x_j} = P_\gamma - E_\gamma + \frac{\partial}{\partial x_j}\left[\left(\mu + \frac{\mu_t}{\sigma_\gamma}\right)\frac{\partial \gamma}{\partial x_j}\right] \tag{1.11}$$

$$\frac{\partial(\rho\overline{Re_{\theta t}})}{\partial t} + \frac{\partial(\rho U_j \overline{Re_{\theta t}})}{\partial x_j} = P_{\theta t} + \frac{\partial}{\partial x_j}\left[\sigma_{\theta t}(\mu + \mu_t)\frac{\partial \overline{Re_{\theta t}}}{\partial x_j}\right] \tag{1.12}$$

1.3.7 Dynamic Mesh and UDF

One of the most important aspects while solving numerical simulations is the discretization of the computational domain. It is important to analyze and verify the grid generation to find a grid-independent solution. In addition, a very good compromise between accuracy and computational cost has to be found. The selection of the correct size and shape of the computational domain is crucial for the quality of the results. The computational size should be large enough to make sure that the boundary conditions assigned to the outer domain do not alter the flow around the airfoil, and are small enough to guarantee a reasonable computational power consumption

To obtain a meaningful prediction of the flow field around an oscillating airfoil, the use of the sliding mesh method for rotating grid is one of the most precise approaches. This technique,

currently employed, results in the creation of two separate cell zones. By choosing the internal circular domain, it was possible to obtain a uniform rigid mesh motion and an airfoil's pitching motion without affecting the quality of the cells. Both the outer steady and inner rotating zone are characterized by two matching interface zones that were merged to create the mesh interface. At each time step, the intersection of the two zones will be evaluated, and a new non-conformal grid interface was designed. The mesh motion should allow the connection of every zone through non-conformal interfaces, and should remain in contact with each other by allowing an accurate evaluation of the fluid flowing across the interface (Geng et al., 2018; Matsson, 2022).

The physical problem of a deforming airfoil/wing involves the motion of its boundaries and the consequent adjustment of the computational domain to a geometry change. To obtain an accurate solution for the unsteady flow, reliable methods for moving and deforming the computational grids are necessary. The CFD software ANSYS-Fluent provides a framework capable of establishing transient mesh motion. However, the desired boundary motion and cell zone adaption are possible by employing an User Defined Function (UDF).

Three dynamic mesh motion methods, namely Smoothing, Layering, and Remeshing, are the available models, already implemented in ANSYS - Fluent, used to update the surface/volume mesh in the deforming region. These three schemes can be used separately or in combination, depending on specific characteristics of the approached problem to be solved, such as deformation amplitudes and grid structure. Fundamentally, mesh smoothing, and layering provides instant mesh deformation capabilities. At the same time, remeshing is used when the boundary motion produces significant changes in the moving mesh. Therefore, pre-tuned mesh quality criteria cannot be respected anymore (Batina, 1991).

The grid is changed locally if the new cells pass the skewness test. The old cells survive if the new ones are discarded. A maximum cell skewness value and a maximum and minimum cell length scale must be established to effectively employ dynamic mesh. In this study, both unstructured and structured hybrid meshes were considered, as illustrated in Figure 1.7, with a

structured quadrilateral layer mesh around the airfoil and unstructured triangle mesh elsewhere. With a blunt trailing edge, it was possible to obtain O-shaped block layers surrounding the airfoil and thereby minimize any instabilities caused by sharp trailing-edge corners. Wall y^+ parameters defines a dimensionless height of the first grid point measured from a wall, utilized to evaluate the near-wall mesh requirements. To appropriately represent the near-wall mesh, a grid was modelled that satisfied the turbulence model's wall y^+requirements. In the current investigation, the $\gamma - Re_\theta$ turbulence model required that the first airfoil cells should be located in the viscous sublayer; thus, a y^+ close to 1 was targeted.

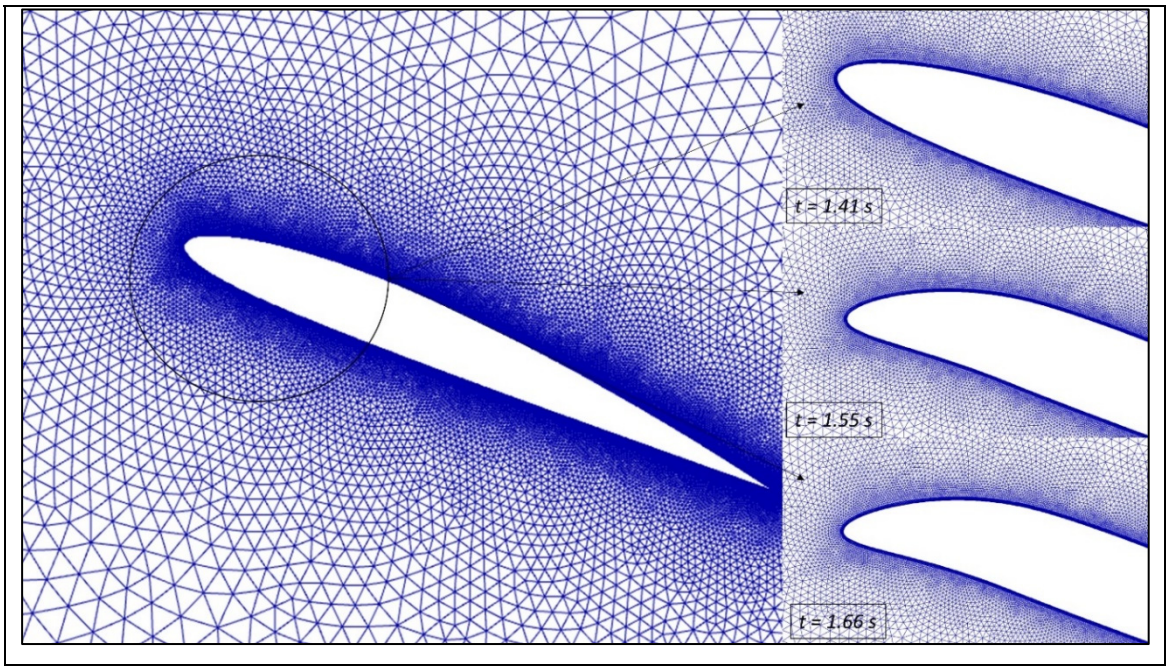

Figure 1.7 Hybrid Mesh of Baseline UAS-S45 Airfoil

Lastly, we define the model's dynamic zone motion. Any zone or boundary can be stiff, deforming, or stationary. If the zone is a rigid body, an UDF or 6 DOF solver can be used to define the grid's motion. Boundaries and cell zones are stiff. If these zones deform, the affected regions can be determined using smoothing and remeshing settings. A user-defined function can specify the geometry and zone motion over time for a deforming and moving zone, i.e., an airfoil's morphing leading edge.

UDFs are C-language functions that can be dynamically inserted into the ANSYS-Fluent solver to enhance or personalize system functionalities. Using these functions makes it possible to alter computational grids and set custom boundary conditions, cell zone motions, material properties, flow regimes, etc. In addition, ANSYS-Fluent provides macros and functions to access solver data. Every UDF must therefore include udf.h in the beginning of the code file to compile DEFINE macros and other functions. UDF-containing source files can be compiled or interpreted. Source files are analyzed and loaded at runtime for interpreted UDFs. which are compiled in two steps. First, ANSYS-Fluent loads a common object code library. After their interpretation or compilation, UDFs can be connected to a solver by selecting the function name.

1.3.8 Hypermesh Finite Element Modelling code

Hypermesh is a high-fidelity Finite Element modeling software. This pre- and post-processing software from Altair facilitates the use of complex CAD models. It enables efficient product development through multiphysics simulation and optimization. For example, Hypermesh uses zero-dimensional (0D) elements such as mass points and 1D elements such as springs, as well as on 2D and 3D models such as shell elements, plates, and hexahedral or tetrahedral elements.

The advantages of Hypermesh also lie in its ability to manage any mesh parameter, use morphing tools, use and manage assemblies, and fully parameterize simulations and optimization. The pre-processing includes model design, discretization and/or meshing, elements selection, the application of their physical properties, the selection of a material and its parameters, constraints and boundary conditions, the loads, and finally, the selection of the type of analysis. Figure 1.8 shows the different plies and leading-edge stringers with a skin mesh generated in Hypermesh.

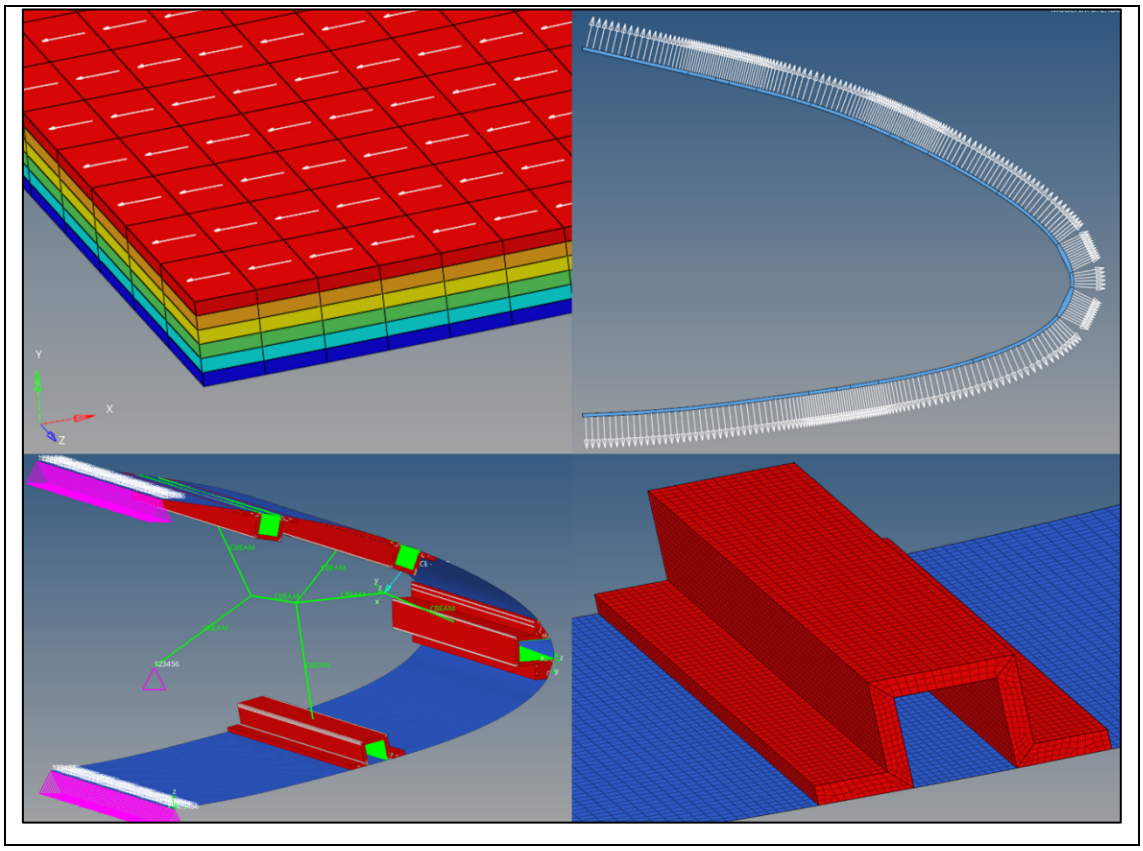

Figure 1.8 Grid generation of a Droop Nose Leading Edge (DNLE) with composite layers

CHAPTER 2

RESEARCH APPROACH AND THESIS ORGANIZATION

The research performed on the improvement of aerodynamic characteristics through a morphing wing approach presented in the current thesis was divided into several phases:

- Problem statement and design of the morphing concept;
- Development and validation of the tools needed for the analysis;
- Two-dimensional aerodynamic optimization and validation performed on the UAS-S45;
- Three-dimensional structural optimizations and high-fidelity analysis performed on the UAS-S45 wing.
- Unsteady aerodynamic analysis of a pitching UAS-S45 airfoil for the dynamic stall study.

Each phase was needed to achieve the desired objectives and to provide further knowledge on the morphing wing concept's performance, application range, and limitations.

2.1 Thesis Research Approach

The increase in aerodynamic performance gives many advantages, such as low fuel consumption, high flight endurance, etc. The morphing wing approach is one way to obtain the desired performance improvements. As discussed in previous sections, a morphing wing can increase the aircraft's performance at different flight conditions by changing its shape.

2.1.1 Morphing Wing Optimization Project

The morphing wing optimization is one of LARCASE's ongoing projects to develop methodologies for aerodynamic and structural performance improvements of the UAS-S45.

The projects consists in embraces aerodynamics, structure, and composite optimization development, which will continue to be used in future research areas.

The comparison of three different optimization algorithms: Black Widow Optimization (BWO), a Genetic Algorithm (GA), and Particle Swarm Optimization/Pattern Search (PSO/PS), for optimizing the UAS-S45 airfoil should be performed. The optimal algorithm will then be applied to optimize the UAS-S45 morphing wing for different flight conditions.

The aerodynamic optimization is performed for Morphing Leading Edge (MLE) and Morphing Trailing Edge (MTE) airfoils of the UAS-S45 at different flight conditions. The PSO is coupled with the Pattern Search (PS) algorithm, a new hybrid optimization technique. The objectives of this aerodynamic optimization are to minimize the drag, maximize the lift-to-drag (L/D) ratio, and maximize the endurance of the UAS-S45 for different flight conditions. For the airfoil parametrization, Bezier-PARSEC (BP) technique was used to generate the baseline airfoil, and to obtain its various morphing configurations by defining various constraints on the trailing and leading edges of the wing. The low-fidelity aerodynamic solver XFoil and the high-fidelity CFD solver Ansys-Fluent were used for the optimization, and their results were compared. Menter's Transition ($\gamma-Re_\theta$) SST turbulence model was used to predict the flow transition.

The MLE and MTE optimization improved the aerodynamic performance of the UAS-S45 airfoil. Overall, the lift coefficients were increased for the range of angles of attack. Compared to the unmorphed (baseline) wing configuration, the lift coefficient of the morphing airfoil was increased by 21%, and the maximum lift coefficient was increased to 9.6%. In addition, a 3-degree delay for the stall angle of attack was observed. Three different Mach numbers (0.08, 0.1, and 0.15) and two flight conditions (cruise and climb) were chosen for the optimization process, and they gave the same results, with a variation of less than 0.03 %. Furthermore, the optimized shapes, as well as pressure distributions were found to be very close to each other.

The MTE configurations showed a significant improvement in aerodynamic performance. The MTE airfoils increased the maximum lift coefficient to 8.13% and maximized the endurance ($C_L^{3/2}/C_D$) to 10.25%. In addition, the DNLE airfoils showed promising potential in delaying flow separation and reducing noise. The DNLE airfoil also has low weight, as it has less number of discrete parts.

In addition, a preliminary structural optimization was conducted for the design and analysis of a Droop Nose Leading Edge (DNLE) structure. By use of the Ansys parametric analysis optimization, correlation' or 'dependency' among the design variables was carried out and the relationship between these variables was determined. The parameters of the wing model, such as composite laminate thickness, material properties, ply orientation, number of plies, etc., and two failure criteria such as the maximum stress failure and Tsai-Wu failure, were evaluated. The number of design variables were reduced in the final optimization process and only those parameters that correlate with the goals of optimization, and the ability to estimate the failure indices for the wing were considered. The failure criteria for each Finite Element was calculated using the Ansys Composite PrepPost (ACP) in the Ansys software. The correlation and determination matrices along with scatter plots were obtained for all design parameters, and therefore, this output data will be used to adapt the composite morphing leading edge for target droop nose optimization, and, ultimately, to design a demonstrator.

2.1.2 Dynamic Stall Control Project

In the literature, several strategies have proven to show the potential to reduce dynamic wing stall. Integration of a morphing wing for stall delay is one of these strategies. However, due to the added complexity of the wing's structure and control system, a detailed analysis of the design is needed. Therefore, studying dynamic stall on optimized airfoils with Morphing Leading Edge (MLE) and Morphing Trailing Edge (MTE) is the first goal of this research.

The effects of the optimized Morphing Leading Edge (MLE) and Morphing Trailing Edge (MTE) on dynamic stall vortex (DSV) around a pitching airfoil through numerical simulations

were investigated. A Reynolds number of 2.4 x 10^6 and five different reduced frequencies of k = 0.05, 0.08, 0.12, 0.16, and 0.20 were chosen for this study. The aerodynamic coefficients were compared, such as the lift, drag, and moment coefficients of the baseline airfoil with those of the morphing airfoils. The effect of reduced frequency on the pitching airfoil are analyzed. The $C_{l,max}$ increases with the reduced frequency: from $C_{l,max}$= 2.674 at k = 0.05 to $C_{l,max}$= 3.016 at k = 0.2 and from $C_{l,max}$= 0.2.862 at k = 0.08 to $C_{l,max}$= 2.996 at k = 0.16. A similar pattern for drag coefficients was observed; however, 'k' had a mixed effect on the drag coefficients ($C_{d,max}$). Therefore, the value of ($C_{d,max}$) changes from 1.53 at k = 0.05 to 1.435 at k = 0.2 and from ($C_{d,max}$) = 1.48 at k= 0.08 to ($C_{d,max}$) = 1.51 at k = 0.16. The downstroke shows that different types of vortices are created near the trailing edge, and these vortices increase the lift force after their formation, and the lift reduces again when they separate and shed into the downstream wake.

The results also showed that a highly reduced frequency stabilizes the LEV and reduces the lift variation in the dynamic stall stage. The $C_{l,max}$, $C_{d,max}$ and the stall angles of attack are obtained for all reduced frequencies. The new radius of curvature of the MLE airfoil minimizes the streamwise adverse pressure gradient and delays the formation of the Dynamic Stall Vortex (DSV). Furthermore, a 14.26 % delay in stall angle was obtained for the morphing airfoil compared to the reference airfoil, and $C_{l,max}$ increased from 2.49 to 3.04. However, the MTE airfoil does not affect the dynamic stall. Vorticity behavior during DSV formation showed that the MTE can change vortices' formation and increase vorticity flux from the leading-edge shear layer, thus increasing DSV circulation.

This study also presented the effect of the Dynamically Morphing Leading Edge (DMLE) airfoil on the structure and behavior of DSV around the UAS-S45 pitching airfoil. Firstly, the parametrization framework was developed to dynamically morph the leading edge of the airfoil by camber line deformation. This framework was developed using an unsteady parametrization model of the NACA asymmetric airfoil equations, adapted to model the morphing motion of the leading edge. This scheme was then integrated within the commercial software ANSYS-Fluent using an UDF for dynamically deflecting the airfoil boundaries and controlling the mesh

motion. Finally, dynamic and sliding mesh techniques were used to simulate unsteady flow across the sinusoidally pitching UAS-S45 airfoil, and $\gamma - Re_\theta$ turbulence model was used because of its ability to capture the unsteady flow behaviour. The aerodynamic coefficients, hysteresis cycles, LEV-dominant flow patterns, and dynamic stall were obtained. The mesh quality and the choice of appropriate time steps are important in the simulation process. A $y^+ < 1$ was used and the adopted time step of $t = 10^{-4}$ captured all variable gradients in the turbulent boundary layer with high precision.

Two detailed studies were performed: i) Firstly, the DMLE of an oscillating airfoil was studied, for which its pitching motion was defined, while the droop nose amplitude and its starting time were evaluated. In this study, the impact of droop nose amplitude variation and morphing starting time on the aerodynamic performance for three different amplitude cases were analyzed. ii) Secondly, the DMLE of an airfoil was analyzed at stall angles of attack. The DMLE analysis provides further details on the dynamic lift and drag forces values for pre-defined deflection frequencies of 1 Hz, 2 Hz, 5 Hz, and 10 Hz. The detailed account of significant is presented in Chapter 7.

2.2 Thesis Organization

2.2.1 First journal paper

The research paper entitled "Aerodynamic Design Optimization of a Morphing Leading Edge and Trailing Edge Airfoil – Application on the UAS-S45" was published in The Applied Science Journal, Special Issue: in November 2019. This paper presents the optimization and numerical results obtained for the UAS-S45 morphing wing.

This work presents an aerodynamic optimization method for a Droop Nose Leading Edge (DNLE) and Morphing Trailing Edge (MTE) of a UAS-S45 root airfoil by using Bezier-PARSEC parameterization. The method is performed using a hybrid optimization technique based on a Particle Swarm Optimization (PSO) algorithm combined with a Pattern Search

algorithm. This is needed to provide an efficient exploitation of the potential configurations obtained by the PSO algorithm. The drag minimization and the endurance maximization were investigated for these configurations individually as two single-objective optimization functions. The aerodynamic calculations in the optimization framework were performed using the XFOIL solver with flow transition estimation criteria, and these results were next validated with a Computational Fluid Dynamics solver using the Transition ($\gamma-Re_\theta$) Shear Stress Transport (SST) turbulence model. The optimization was conducted at different flight conditions. Both the DNLE and MTE optimized airfoils showed a significant improvement in the overall aerodynamic performance, and MTE airfoils increased the efficiency of $C_L^{3/2}/C_D$ by 10.25%, indicating better endurance performance. Therefore, both DNLE and MTE configurations show promising results in enhancing the aerodynamic efficiency of the UAS-S45 airfoil.

2.2.2 Second journal paper

The research paper "Optimization and Design of a Flexible Droop Nose Leading Edge Morphing Wing based on a Novel Black Widow Optimization (BWO) Algorithm-Part I" was published in The Designs Journal, Special Issue: in November 2020. This paper presents the aerodynamic and structural optimization results obtained for the UAS-S45 morphing wing.

An aerodynamic optimization for a Droop Nose Leading Edge (DNLE) morphing of a well-known UAV, the UAS-S45, is proposed, using a novel Black Widow Optimization (BWO) algorithm. This approach integrates the optimization algorithm with a modified Class Shape Transformation (CST) parameterization method to enhance aerodynamic performance by minimizing drag and maximizing aerodynamic endurance at the cruise flight condition. The CST parameterization technique is used to parameterize the reference airfoil by introducing local shape changes and provide skin flexibility to obtain various optimized morphing airfoil configurations. The optimization framework uses an in-house MATLAB algorithm, while the aerodynamic calculations use the XFoil solver with flow transition estimation criteria. These results are validated with a CFD solver utilizing the Transition ($\gamma-Re_\theta$) Shear Stress

Transport (SST) turbulence model. Numerical studies verified the effectiveness of the optimization strategy, and the optimized airfoils have shown a significant improvement in the overall aerodynamic performance, by up to 12.18% drag reduction compared to the reference airfoil, and an increase of aerodynamic endurance of up to 10% for the UAS-S45 optimized airfoil configurations over its reference airfoil. These results indicate the importance of leading-edge morphing in enhancing the aerodynamic efficiency of the UAS-S45 airfoil.

2.2.3 Third journal paper

The research paper "Optimization and Design of a Flexible Droop Nose Leading Edge Morphing Wing based on a Novel Black Widow Optimization (BWO) Algorithm-Part II" was accepted for publication in The Designs Journal in October 2022. This work presents the aerodynamic and structural optimization results obtained for the UAS-S45 morphing wing.

This work presents an aerodynamic and structural optimization for a Droop Nose Leading Edge Morphing airfoil as a high lift device for the UAS-S45. The results were obtained using three optimization algorithms: coupled Particle Swarm Optimization-Pattern Search, Genetic Algorithm, and Black Widow Optimization algorithm. The lift-to-drag ratio was used as the fitness function, and the impact of the choice of optimization algorithm selection on the fitness function was evaluated. The optimization was carried out at various Mach numbers of 0.08, 0.1, and 0.15, respectively, and at the cruise and take-off flight conditions. All these optimization algorithms obtained effectively comparable lift-to-drag ratio results with differences of less than 0.03% and similar airfoil geometries and pressure distributions. In addition, an unsteady analysis of a Variable Morphing Leading Edge airfoil with a dynamic meshing scheme was carried out to study its flow behaviour at different angles of attack and the feasibility of leading-edge downward de-flection as a stall control mechanism. The numerical results showed that the variable morphing leading edge reduces the flow separation areas over an airfoil and in-creases the stall angle of attack. Furthermore, a preliminary investigation was conducted into the design and sensitivity analysis of a morphing leading-edge structure of the UAS-S45 wing integrated with an internal actuation mechanism. The

correlation and determination matrices were computed for the composite wing geometry for sensitivity analysis to obtain the parameters with the highest correlation coefficients. The parameters include the composite material qualities, thickness, ply angles, and the ply stacking sequence. These findings can be utilized to design the flexible skin optimization framework, obtain the target droop nose deflections for the morphing leading edge, and design an improved model.

2.2.4 Forth journal paper

The research paper "Numerical investigation of dynamic stall reduction on the UAS-S45 airfoil using an optimized airfoil method" was submitted for publication in The Aeronautical Journal in September 2022. This paper evaluates dynamic stall control using MLE and MTE results for the UAS-S45 morphing wing.

This paper investigates the effect of the optimized Morphing Leading Edge (MLE) and the Morphing Trailing Edge (MTE) on Dynamic Stall Vortices (DSV) for a pitching airfoil through numerical simulations. In the first stage of the methodology, the optimization of the UAS-S45 airfoil was performed using a morphing optimization framework. The mathematical model used Bezier-Parsec parametrization, and the Particle Swarm Optimization algorithm was coupled with a Pattern Search with the aim of designing an aerodynamically efficient UAS-45 airfoil. The $\gamma - Re_{\theta}$ transition turbulence model was firstly applied to predict the laminar to turbulent flow transition. The morphing airfoil increased the overall aerodynamic performances while delaying boundary layer separation. Secondly, the unsteady analysis of the UAS-S45 airfoil and its morphing configurations was carried out and the unsteady flow field and aerodynamic forces were analyzed at the Reynolds number of 2.4 x 10^6 and five different reduced frequencies of k = 0.05, 0.08, 1.2, 1.6 and 2.0. The lift (C_L), drag (C_D) and moment (C_M) coefficients variations with the angle of attack of the reference and morphing airfoils were compared. It was found that a higher reduced frequencies of 1.2 to 2 stabilized the leading-edge vortex that provided its lift variation in the dynamic stall phase. The maximum lift $\left(C_{L,max}\right)$ and drag ($C_{D,max}$) coefficients and the stall angles of attack are evaluated for all

studied reduced frequencies. The numerical results have shown that the new radius of curvature of the MLE airfoil can minimize the streamwise adverse pressure gradient and prevent significant flow separation and suppress the formation of the DSV. Furthermore, it was shown that the morphing airfoil delayed the stall angle of attack by 14.26% with respect to the reference airfoil, and that the $C_{L,max}$ of the airfoil increased from 2.49 to 3.04. However, while the MTE airfoil was found to increase the overall lift coefficient and the $C_{L,max}$, it did not control the dynamic stall. Vorticity behavior during DSV generation and detachment has shown that the MTE can change the vortices' evolution and increase vorticity flux from the leading-edge shear layer, thus increasing DSV circulation. The conclusion that can be drawn from this study is that the fixed drooped morphing leading edge airfoils have the potential to control the dynamic stall. These findings contribute to a better understanding of the flow analysis of morphing airfoils in an unsteady flow.

2.2.5 Fifth journal paper

The research paper titled "Stall Delay and Laminar Separation Bubble Dynamics over a Dynamically Morphing UAS-S45 airfoil" was submitted for publication in The Biomimetics Journal: Special Issue in December 2022. The research on dynamic stall control using Dynamically Morphing Leading Edge (DMLE) results for the UAS-S45 morphing wing is presented in this paper.

This paper investigated the effect of the Dynamically Morphing Leading Edge (DMLE) on the flow structure and behavior of vortices for dynamic stall around a pitching UAS-S45 airfoil with the aim to control the dynamic stall. The unsteady parametrization framework was developed specifically to model the morphing motion of the leading edge with time. This scheme was then integrated within the numerical solver by developing a User-Defined-Function (UDF), which served to dynamically deflect the airfoil boundaries and control the dynamic mesh algorithm used to deform and adapt the surrounding mesh. Both the dynamic and sliding mesh techniques were used to simulate unsteady flow across the sinusoidally pitching UAS-S45 airfoil. $\gamma - Re_\theta$ turbulence model is good for capturing the flow structures

of dynamic airfoils associated with leading edge vortex formations for a wide range of Reynolds numbers. Two broader studies are considered: i) Firstly, the DMLE of an oscillating airfoil is investigated. In this part, the pitching-oscillation motion of an airfoil is defined and the parameters such as droop nose amplitude (A_D) and its starting time are evaluated. The effect of variation of A_D and starting time of morphing leading edge on the aerodynamic performance will be studied, and three different amplitude cases are considered in this paper; ii) secondly, the DMLE of an airfoil at stall angles of attack is investigated. In this part, the analysis of the dynamically morphing leading edge is performed to provide further insights into the dynamic lift and drag forces during the motions at for pre-defined morphing frequencies of 1 Hz, 2 Hz, 5 Hz and 10 Hz, respectively. It was found that the DMLE of an oscillating airfoil at all the A_D values of 0.01, 0.005 and 0.075 and different morphing times respectively, lift coefficient for the airfoil increases almost linearly until 28°, after which a sudden surge in the C_l is observed as compared to the reference airfoil. In terms of drag coefficient, there is 17.70 % decrease in drag coefficient. It was found that the morphing airfoil delayed the stall angle of attack with respect to the stall of the reference airfoil by 11.63 %, and $C_{L,max}$ of the airfoil increased by 21.87 %. The numerical results have shown that the new radius of curvature of the DMLE airfoil can minimize the streamwise adverse pressure gradient and prevent significant flow separation by delaying the Dynamic Stall Vortex (DSV) occurrence.

2.3 Concluding Remarks

Following the results obtained in Section 2.2, the aerodynamic and structural performance of the UAS-S45 wing was improved using morphing wing optimization. This work utilized the concept of the MLE and the MTE to improve the aerodynamic performance and to control the dynamic stall.

CHAPTER 3

AERODYNAMIC DESIGN OPTIMIZATION OF A MORPHING LEADING EDGE AND TRAILING EDGE AIRFOIL–APPLICATION ON THE UAS-S45

Musavir Bashir [a], Simon Longtin-Martel [b], Ruxandra Mihaela Botez [c] and Tony Wong [d]

[a, b, c, d] Department of System Engineering, École de Technologie Supérieure,
1100 Notre-Dame West, Montréal, Québec, Canada H3C 1K3

Paper published in *Applied Sciences*, February 2021.
DOI: https://doi.org/10.3390/app11041664

Résumé

Ce travail présente une méthode d'optimisation aérodynamique pour un bord d'attaque de type "Droop Nose" (DNLE) et un bord de fuite déformable (MTE) d'un profil d'UAS-S45 en utilisant une paramétrisation Bézier-PARSEC. La méthode est réalisée à l'aide d'une technique d'optimisation hybride basée sur un algorithme d'optimisation en essaim de particules (PSO) combiné à un algorithme de recherche de traces. Ceci est nécessaire pour permettre une utilisation efficace des configurations potentielles obtenues par l'algorithme PSO. La minimisation de la traînée et la maximisation de l'endurance ont été étudiées pour ces configurations individuellement en tant que deux fonctions d'optimisation à objectif unique. Les calculs aérodynamiques dans le cadre de l'optimisation ont été effectués à l'aide du solveur Xfoil avec des critères d'estimation de transition d'écoulement et ces résultats ont ensuite été validés avec un solveur de dynamique des fluides numériques en utilisant le modèle de turbulence "Transition ($\gamma - Re_\theta$) Shear Stress Transport (SST) ". L'optimisation a été réalisée dans des conditions de vol différentes. Les profils optimisés DNLE et MTE ont montré une amélioration significative de la performance aérodynamique globale, et les profils MTE ont augmenté l'endurance $C_L^{3/2}/C_D$ par 10.25%. Par conséquent, les configurations DNLE et MTE montrent des résultats prometteurs exprimés par l'amélioration de l'efficacité aérodynamique du profil UAS-S45.

Abstract

This work presents an aerodynamic optimization method for a Droop Nose Leading Edge (DNLE) and Morphing Trailing Edge (MTE) of a UAS-S45 root airfoil by using Bezier-PARSEC parameterization. The method is performed using a hybrid optimization technique based on a Particle Swarm Optimization (PSO) algorithm combined with a Pattern Search algorithm. This is needed to provide an efficient exploitation of the potential configurations obtained by the PSO algorithm. The drag minimization and the endurance maximization were investigated for these configurations individually as two single-objective optimization functions. The aerodynamic calculations in the optimization framework were performed using the XFOIL solver with flow transition estimation criteria, and these results were next validated with a Computational Fluid Dynamics solver using the Transition ($\gamma-Re_\theta$) Shear Stress Transport (SST) turbulence model. The optimization was conducted at different flight conditions. Both the DNLE and MTE optimized airfoils showed a significant improvement in the overall aerodynamic performance, and MTE airfoils increased the efficiency of $C_L^{3/2}/C_D$ by 10.25%, indicating better endurance performance. Therefore, both DNLE and MTE configurations show promising results in enhancing the aerodynamic efficiency of the UAS-S45 airfoil.

3.1 Introduction

3.1.1 Outline of the Research

The goal of reducing global fuel consumption and fuel-related emissions has placed tremendous pressure on the aviation industry. In 2018, the aviation industry was responsible for 895 million tons of CO_2 emissions globally emitted into the atmosphere (BBC News, 2019). Reducing fuel consumption will benefit both the world environment and the air transport industry. According to the Aviation Transport Action Group (ATAG), a reduction in fuel burning will have a significant impact on the aviation industry because the largest operating cost of this industry is fuel (BBC News, 2019). Drastic measures are still required even though

some steps have already been taken to reduce these emissions. Various solutions have been implemented by the aviation industry, including smart material technology, laminar flow technology, air traffic management technologies, advanced propulsion techniques and sustainable fuels (R. Botez, 2018b; Gerhards et al., 2001; Valasek, 2012). Morphing wing technology is one of the technologies showing high potential in decreasing aircraft fuel consumption (S Ameduri et al., 2020; Barbarino et al., 2011; R Botez et al., 2018; Communier et al., 2020). Even though there is no settled definition for "morphing", this term is borrowed in Aviation Technology from avian flight to describe the ability to modify maneuvers at certain flight characteristics in order to obtain the best possible performance. This type of application requires morphing structures capable of adapting to changing flight conditions. Morphing systems include several wing shape modifications, span or sweep changes, changes in twist or dihedral angle (Salvatore Ameduri et al., 2020) and variations of the airfoil camber (Communier et al., 2020) or of the thickness distribution (R. Botez, 2018b). In the design phase, both military and civilian aircraft traditionally fly at a single or few optimum flight conditions; morphing, however, is envisioned to increase the number of optimum operational points for a given aircraft (Barbarino et al., 2011).

The morphing strategy scope is broad in the sense that an optimal solution can be generated in various ways with respect to a wide spectrum of mission profiles and types, and flight regimes. Novel technologies need to be part of recent efforts to produce environmentally sustainable and efficient aircraft. To meet environmental guidelines, including those of the International Civil Aviation Organization's (ICAO's) Committee on Aviation Environmental Protection (CAEP), innovative technologies such as "morphing" are fascinating as they provide advantages over conventional wing configurations (Marino et al., 2014b). Additionally, "morphing" is more practically applied in Unmanned Aerial Vehicles (UAVs) because of their reduced scale and lower complexity in terms of wing design structure and energy consumption expressed in terms of actuation power (S Ameduri et al., 2020; I Dimino et al., 2020; Noviello et al., 2019), in addition to the advantages that morphing designs are lighter and less noisy than their conventional designs. Some morphing opportunities with potential benefits for increasing aerodynamic performance of the UAS-S45 are shown in Figure 3.1.

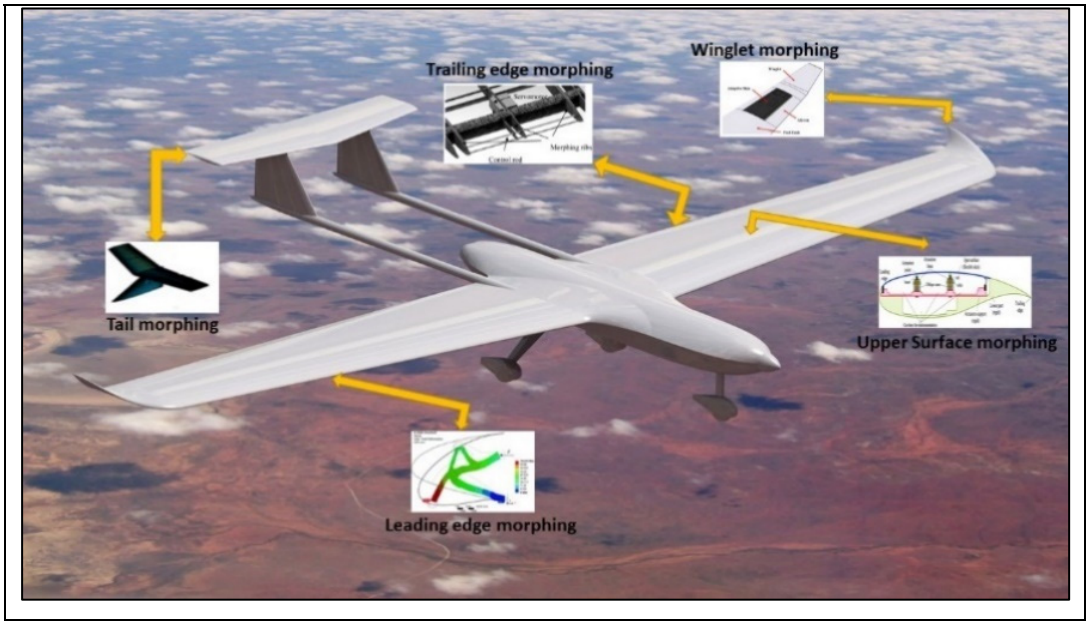

Figure 3.1 UAS-S45 with Potential Morphing Configuration Capabilities

Aircraft are designed to achieve optimal aerodynamic performance (maximum lift-to-drag ratio) for a mission specification and for an extended range of flight conditions. Nevertheless, these mission specifications change continuously throughout the different flight phases, and an aircraft often flies at non-optimal flight conditions. Although the conventional hinged high lifting devices and trailing edge surfaces (discrete control surfaces) in aircraft are effective in controlling the airflow for different flight conditions, they create surface discontinuities, which increase the drag (Carossa et al., 2016; Pantelakis et al., 2011). The disadvantages of these hinged surfaces are found in both their deployed and retracted configurations (Y. Li et al., 2013). When deployed, the gaps between the high lifting surface and the wing can cause noise and turbulence, and therefore can produce a turbulent boundary layer and thus increase drag. Even when retracted, the trailing edge hinges still produce a turbulent boundary layer. Numerous researchers believe that the laminar flow technology has the maximum potential to reduce drag and to avoid flow separation (Abbas et al., 2013; Arena, Nagel, et al., 2019). For this goal, the wings require the design of thin airfoils, seamless high-quality surfaces and variable droop leading edges. The use of these high continuous smooth lifting devices in UAVs will further broaden their flight envelope and extend their endurance. These challenges can be addressed by using morphing technology in the current aviation industry.

The aim of this study is thus to investigate the aerodynamic optimization by employing constrained shape parameterization for UAS-S45 root airfoil using Droop Nose Leading Edge (DNLE) and Morphing Trailing Edge (MTE) technologies. The aerodynamic design of continuous morphing wing surfaces employed to replace traditional discrete control surfaces, such as flaps, ailerons or sometimes slats, to adjust the camber of the wing, are discussed in this paper along with the parameterization strategy and the optimization algorithm.

3.1.2 Littérature Survey

The potential in the field of aircraft morphing is evident as hundreds of research groups worldwide have been dedicated to studying the different aspects of morphing. Two of the earliest groups were launched by NASA, and they worked within the "Active Flexible Wing program" and the "Mission Adaptive Wing program" (RW DeCamp et al., 1981; Perry III et al., 1995). In these programs, flutter suppression, load alleviation and load control during rapid roll maneuvers were investigated.

One of the potential consequences of flexible morphing structures is that both dynamic properties and aerodynamic loads of the wing are affected. Hence, the aeroelastic effects arising from interactions between the configuration-varying aerodynamics and the morphing structure are significant. Li et al. have presented important morphing studies in terms of aeroelastic, control and optimization aspects (Li et al., 2018). The nonlinear aeroelastic behaviour of a composite wing with morphing trailing-edge has been studied (D. Li et al., 2013). Moreover, the nonlinear aeroelastic behaviour of a composite wing with morphing trailing-edge has been studied.

Aero-elastically stable configurations of a morphing wing trailing edge driven by electromechanical actuators have been investigated (Pecora et al., 2014). The effects induced by trailing-edge actuators stiffnesses on the aeroelastic behaviour of the wing were simulated using different approaches. The results revealed that flutter could be avoided if sufficient stiffness was provided by these actuators. An analytical sensitivity calculation platform for flexible wings has been studied (Hang et al., 2020; Su et al., 2019). This platform has been

used to perform wing aeroelastic optimization and stability analysis. In another study, a low-fidelity model of an active camber aero-elastic morphing wing was developed to investigate the critical speed values by varying its chord-wise dimension (Jiaying Zhang et al., 2021). A wide range of configurations was explored to predict the dynamic behaviour of these active camber morphing wings.

The combined flutter behaviour and gust response of a series of flexible airfoils has been investigated (Berci et al., 2013). Rayleigh's beam equation was used to model this series of flexible airfoils. The effect of chordwise flexibility of a compliant airfoil was investigated numerically to demonstrate its dynamical stability (Cook et al., 2014; Murua et al., 2010). An actuated two-dimensional membrane airfoil was investigated experimentally and numerically, and it was found that membrane flexibility decreased the drag and delayed the stall. These aeroelastic studies are significant in understanding the flexible morphing wing and its potentially relevant effects. However, our study does not consider the structural effects of morphing, and therefore the optimization is aimed to improve the aerodynamic drag performance and endurance in the given range of angles of attack.

Other research projects in the US and Canada include the "Smart Materials and Structures Demonstration" program initiated to develop new affordable smart materials to establish the performance gains by investigating smart rotors, the smart aircraft and the marine propulsion system; the "Aircraft Morphing" program (Sanders et al., 2004); the "Advanced Fighter Technology Integration" (AFTI) program, aimed to develop and demonstrate in flight a smooth variable camber wing and flight control system capable of adjusting the wing's shape in response to flight conditions to maximize aerodynamic efficiency; the "Active Aeroelastic Wing" program, demonstrated to improve aircraft roll control through aerodynamically induced wing twist on a full-scale high-performance aircraft at transonic and supersonic speeds; the "Morphing Aircraft Structures" program (Pendleton et al., 2000); the "Mission Optimized Smart Structures" (MOSS), in which aerodynamic optimization was performed with the stretching of the leading edge using a novel skin material developed with a nanocomposite at the National Research Council of Canada (Fortin, 2019); and the "Controller

Design and Validation for Laminar Flow Improvement on a Morphing Research Wing–Validation of Numerical Studies with Wind Tunnel Tests—CRIAQ MDO 7.1" (Koreanschi, Oliviu, et al., 2016; Koreanschi, Sugar-Gabor, et al., 2016a). The CRIAQ 7.1 project took place at our Laboratory of Applied Research in Active Controls, Avionics and AeroServoElasticity LARCASE.

The European Union has conducted several projects, including the "Active Aeroelastic Aircraft Structures" (3AS) project, to develop novel active aeroelastic control strategies to improve aircraft performance (structural weight, better control effectiveness) by controlling structural deformations to modulate the desired aerodynamic deformations (Arena, Palumbo, et al., 2019); the "Aircraft Wing Advanced Technology Operations" (AWIATOR) project, in which novel fixed wing configurations were introduced aimed at reducing the vortex hazard by implementing larger winglets and further improving aircraft efficiency and reducing farfield impact (Oliviu et al., 2016); the "New Aircraft Concepts Research" (NACRE) project, in which Powered Tails and Advanced Wings were studied to obtain high environmental performance (noise and CO2 emissions)—both high aspect ratio low-sweep wings and forward-swept wings (with natural laminar flow) contributed to achieving good fuel efficiency (Frota, 2010); the "Smart Leading Edge Device" (SmartLED) project (Pantelakis et al., 2011); the "Smart High Lift Devices for Next Generation Wings" (SADE) project (Schweiger et al., 2002). Both SmartLED and SADE were aimed to develop and investigate the morphing high lift devices, "smart leading edge" to enable seamless high lift devices and therefore enable laminar wings and "smart single-slotted flap", for the next generation aircraft of high surface quality for drag reduction. Projects by the European Union also included the "Smart Fixed Wing Aircraft" (SFWA) project (Sawyers, 2008) and the "Smart Intelligent Aircraft Structures" (SARISTU) project to address the physical integration of smart intelligent structural concepts. The SARISTU included a series of research collaborations to addresses aircraft weight and operational cost reductions as well as an improvement in the flight profile specific aerodynamic performance (Hans Monner et al., 2009). Other projects by the European Union were the "Novel Air Vehicle Configurations" (NOVEMOR) project, in which morphing wing solutions (span and camber strategies and wing-tip devices) were proposed to enhance lift capabilities

and maneuvering (König et al., 2010); the “Clean-Sky 1 and 2” projects (Arena, Concilio, et al., 2019; Wölcken et al., 2015); the “Combined Morphing Assessment Software Using Flight Envelope Data” (CHANGE) project, which developed a modular software architecture capable of determining and achieving optimum wing shape (Suleman et al., 2014); and the “Sustainable and Energy Efficient Aviation” (SE2A) project aimed to investigate the Morphing structures for the 1g-wing to exploit the nonlinear structural behavior of wing design components to achieve passive load alleviation (Ameduri, Dimino, et al., 2018).

The “Morphing Architectures and Related Technologies for Wing Efficiency Improvement-CRIAQ MDO 505” was also realized at the LARCASE in the continuation of the CRIAQ 7.1 project mentioned above. The achievements of the international Canadian-Italian CRIAQ MODO 505 project are mentioned in various publications (Grigorie et al., 2012; Andrei Vladimir Popov et al., 2010).

The aircraft optimization process has evolved dramatically over the past decades. The design of new intelligent algorithms and computational solvers has substantially impacted the overall design process, including the “morphing aircraft optimization”. The verification and validation of aircraft design using optimization techniques has reduced its huge experimental costs and has been achieved by the use of efficient algorithms and computational solvers (J. Hicken, 2009; Skinner et al., 2018). An optimization process is initiated by minimizing or maximizing an objective function for the target design concept with respect to design variables subjected to given constraints, which were applied to limit the search space and therefore to yield physically feasible optimization results. Both gradient-based and gradient-free intelligent algorithms have been used in these optimization processes, and their results are dependent on the type of optimization problem to be solved (Skinner et al., 2018). These algorithms are discussed in the following sections. Many optimization techniques based on bioinspired processes and Surrogate-Assisted natural methods have been formulated, and mathematical and statistical analysis of these algorithms has been performed (Chugh et al., 2020; D.-S. Lee et al., 2008; Safari et al., 2013; Junhao Zhang et al., 2017). The comparative performance study based on convergence trends was performed with different geometry parameterization

techniques. Both advantages and disadvantages can be found in these optimization algorithms for complex shape functions. However, the goal of this study is to perform aerodynamic design optimization of morphing airfoil using Particle Swarm Optimization (PSO) algorithm combined with Pattern Search technique.

Similarly, various computational solvers are employed based on their desired solution accuracy and computational cost (Martinelli et al., 2013). Researchers have conducted various aerodynamic and structural optimization studies, including design studies of different surfaces (components) of the wing, such as its upper surface, trailing edge or leading edge. Adjoint-based airfoil optimization has been studied using Euler equations (Jameson et al., 2008), while other researchers have implemented extensive gradient-based aerodynamic shape optimization methodologies for transonic wing design using high-fidelity RANS solvers (Lyu et al., 2014). Many other optimization studies have been performed using different optimization techniques. Some of the most notable works are summarized in Table 3.1.

Table 3.1 Airfoil optimization research carried out by using different techniques

Authors	**Category**	**Optimization Techniques**
(Sugar-Gabor, et al., 2016)	Several Morphing Geometries	Artificial Bee Colony Algorithm and a Classical Gradient-Based Search Routine
(Lyu et al., 2014)	Camber Morphing	Gradient-Based Optimization Algorithm with an Adjoint Method
(Hashimoto et al., 2014)	High Wing Configuration	Kriging Surrogate-Assisted Genetic Algorithm
(Ganguli et al., 2009)	Preliminary UAV Design	Kriging Surrogate-Optimization Model
(Koreanschi, Oliviu, et al., 2016)	Wing Tip	Artificial Bee Colony and a Gradient Method
(Fincham et al., 2015)	Camber Morphing	Pareto Frontiers with a Genetic Algorithm
(Murugan et al., 2015)	Camber Morphing	Pareto Frontiers with a Genetic Algorithm
(Albuquerque, 2017)	Several Morphing Geometries	Multidisciplinary Design Optimization with Gradient-Based Optimization Algorithm
(Manas Khurana et al., 2008b)	Several UAV Geometries	Particle Swarm Optimization (PSO) Algorithm

Authors	Category	Optimization Techniques
(Kao et al., 2019)	Several Morphing Geometries	Gradient-Based Optimization
(Magrini et al., 2019)	Leading Edge Morphing	Multi-Objective Optimization with a Genetic Algorithm
(Gong et al., 2019)	Variable Sweep, Span and Chord Morphing	Genetic Algorithm in conjunction with a Surrogate Model

The study presented in this paper analyses the aerodynamic optimization of the Hydra Technologies S45 Balaam UAS airfoil. This unmanned aerial surveillance (UAS) system is needed to provide security and surveillance capabilities for the Mexican Air Forces, as well as civilian protection in dangerous situations. This study of Morphing Wing Technology has the aim to enhance the aerodynamic efficiency and the effective range of the UAS S45, as well as to extend the flight time. The next section of this paper presents the optimization framework of the overall methodology, which includes two objective functions' formulations ("drag minimization" and "endurance maximization"). The parameterization technique is also presented in Section 3 and has the aim to obtain the "optimal aerodynamic shapes"; the computational solvers for calculating aerodynamic coefficients and the optimization algorithms employed are also presented. The results obtained by these solvers and algorithms for the UAS-S45 optimized designs are compared with the baseline UAS-S45 model results.

3.2 Methodology

This optimization framework study performs the aerodynamic optimization of the leading edge and trailing edge of a morphing airfoil by using an intelligent and iterative process based on user-defined aerodynamics and constraints. The methodology involves the objective function formulation integrated with a geometrical shape parameterization model, an aerodynamic flow solver and the optimization algorithm.

For this study, an optimization framework is designed to allow the integration of shape generation using the direct manipulation of the airfoil shape variables while respecting the geometrical constraints. The optimization procedure framework is described in Figure 3.2, and

it consists of a parameterization block based on the Bezier–Parsec (BP) parameterization airfoil shape technique and an aerodynamic solver, such as the panel solver XFOIL (Version 6.99, MIT, USA, 2013). The validation of its results is done using high-fidelity solver in Fluent based on Reynolds-averaged Navier–Stokes (RANS) equations in the Transition SST model. A hybrid optimizer based on Particle Swarm Optimization (PSO) algorithm combined with the Pattern Search technique is also used. The optimization procedure is shown in Figure 3.2 and is described in detail in Sections 3.1–3.4.

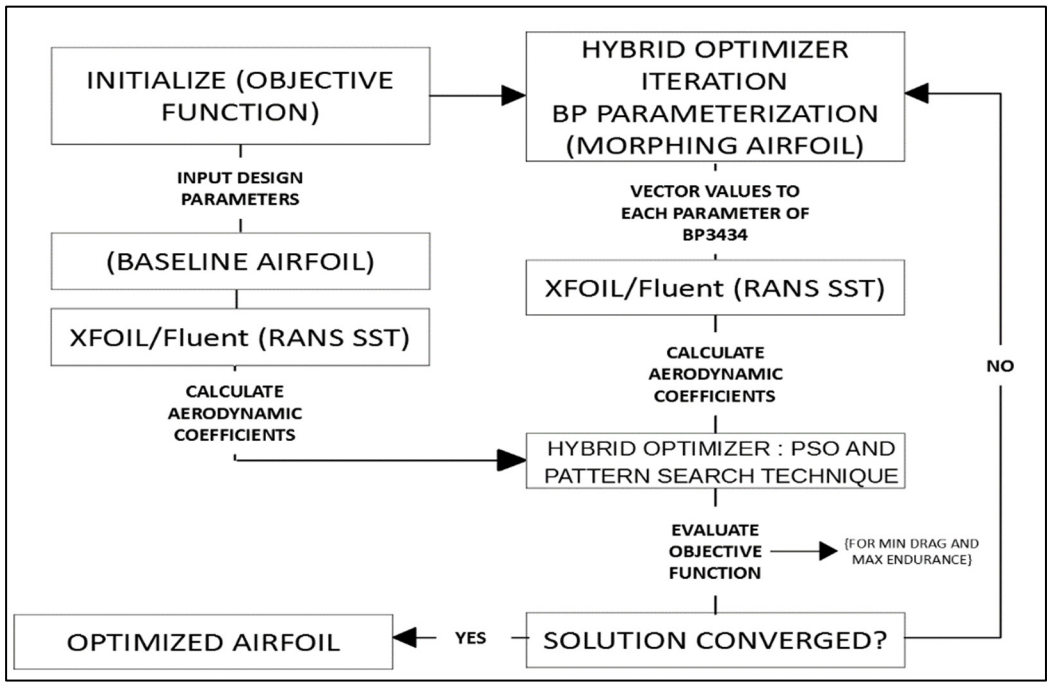

Figure 3.2 Schematics of the optimization procedure

3.2.1 Objective Function Definition

Numerous researchers have stated that there is always a trade-off between aerodynamic coefficients and performance parameters in aerodynamic design problems (Buckley et al., 2010). A difficult balance exists between increasing aircraft performance and meeting design constraints efficiently in practical aerodynamic design problems. For example, the objective of aerodynamic optimization is lift maximization, drag minimization or maximization of the

lift-to-drag ratio while keeping C_L and/or C_D constant as constraints. Likewise, various airfoil shapes are optimized for their morphing by considering an increased lift-to-drag ratio and, at the same time, for meeting the given constraints. Other airfoil shape optimizations may involve those of multiple aerodynamic coefficients based on performance parameters such as range, loiter and control. Such optimization techniques can be applied to solve complex aerodynamic design problems for a broad range of flight conditions.

In addition, the design problem shown in this paper must consider the extended range of flight operating conditions that a UAV is expected to encounter within its flight envelope. As mentioned above, this study considers the optimization of the airfoil shape for drag minimization and for endurance maximization as individual target objective functions.

The mathematical formulation of the drag minimization objective function is the following.

$$minimize\ C_D(x); x\ \epsilon\ (airfoil\ set) \tag{3.1}$$

Subject to

$$C_{L_{max}}\ (x, \alpha, M\ \geq) 1 \cdot 608$$

$$C_{L_{morph}} \geq C_{L_{min,baseline}(x,\alpha,M)}$$

where

$$x \in (airfoil\ set, the\ vector\ of\ airfoil\ shape\ function\ design\ variables)$$

The lift coefficients of the UAS-S45 are calculated for each angle of attack using design parameters mentioned in a previous paper of our team (Segui et Botez, 2019). The constraints implemented are both maximum lift coefficient and lift coefficient of baseline airfoil at each angle of attack. The optimization runs are executed with a minimum lift coefficient at each angle of attack. Constraints are applied by penalty functions to the objective function to ensure optimum performance is obtained at each given angle of attack.

For the design of a long-endurance UAV, Equations (3.2) and (3.3), which are needed to determine the endurance (E) of a propeller-powered UAV, are well established using the Breguet formula (J. Okrent, 2017).

$$E = \frac{\eta_{pr}}{c_p}\frac{C_L^{\frac{3}{2}}}{C_D}\sqrt{2\rho S}\left(\frac{1}{\sqrt{W_f}} - \frac{1}{\sqrt{W_i}}\right) \tag{3.2}$$

where c_p is the specific fuel consumption, η_{pr} is the propeller efficiency, ρ is the free stream density, S is the wing planform area, W_i is the initial weight of the aircraft, W_f is the final weight of the aircraft and C_L and C_D are the lift and drag coefficients, respectively.

The parameters that do not affect the airfoil shape design in the endurance performance can be neglected in Equation (3.2), and the parameters that can affect the airfoil shape design are only the two aerodynamic coefficients C_L and C_D; therefore, (3.2) can be reformulated as

$$E_a = \frac{C_L^{\frac{3}{2}}}{C_D} \tag{3.3}$$

Therefore, an optimized airfoil maximizes the lift and minimizes the drag coefficients in the above Equation (3.3); therefore, the overall endurance aerodynamic efficiency is maximized. The weighted average of the flight envelope is used to find out the time that the UAV would have to spend in different flight regimes. Since the present study concerns the surveillance UAS-S45 optimization, it is assumed that 80% of total flight time is spent in loiter flight conditions, which require maximum endurance. Therefore, the objective function to maximize the endurance aerodynamic efficiency with the same constrained optimization is given by the following equation:

$$\text{maximize } E_a(x) = \frac{C_L^{\frac{3}{2}}}{C_D} \tag{3.4}$$

where

$$x \in (airfoil\ set, the\ vector\ of\ airfoil\ shape\ function\ design\ variables$$

3.2.2 Parameterization Strategy

Parameterization of the airfoil shapes for the UAS design and optimization requires a mathematical formulation, and it becomes an important part of the overall optimization process. Studies have shown that the choice of shape parameterization technique has a strong influence on the solution accuracy, robustness and computational time of the overall optimization process (Manas Khurana et al., 2008a). In order to obtain an optimal aerodynamic solution, the shape function must be directly related to the airfoil geometry, have a flexible design space, and be robust for the control of all parameters. Some of the well-known methods are the Discrete Based Approach, the Bezier curves, the B-Spline or NURBS curves, the Cubic Spline and the Free-Form Representation (Manas Khurana et al., 2008a; Trad et al., 2020). The drawbacks of these methods are that they do not use airfoil shape parameters, they require a large number of design variables, and they often provide inaccurate shapes for the leading edge and trailing edge of an airfoil.

These limitations have been partly removed by using the polynomial-based functions, such as PARSEC and CST. “PARSEC” is characterized by eleven design coefficients that control airfoil shape parameters, and they are the: (a) edge radius, (b) upper crest abscissa, (c) upper crest ordinate, (d) upper crest curvature, (e) lower crest abscissa, (f) lower crest ordinate, (g) lower crest curvature, (h) trailing edge ordinate, (i) trailing edge thickness, (j) trailing edge direction and (k) trailing edge wedge angle. Several studies have shown PARSEC method’s superior performance with respect to the Discrete Based Approach, based on their convergence rate, flexibility and epistasis, which is due to the nonlinear dependency of the objective function on the design parameters (Derksen et al., 2009). However, it has also been found that the leading edge and trailing edge design coefficients in this parameterization method do not provide accurate airfoil shape; therefore, implementing morphing design using only these PARSEC design coefficients might further increase the airfoil shape complexity.

Therefore, a combined approach, the Bezier-PARSEC (BP) parameterization method, was developed (Derksen et al., 2010) that included the advantages of Bezier with PARSEC combination, and it was found to be suitable for this study. The BP parameterization was implemented in this paper with the aim to increase the solution accuracy, flexibility and efficiency of morphing leading edge and trailing edge optimizations. More significantly, this technique provides the large search space needed for morphing leading edge and trailing edge design, and it reduces the computational time.

The BP method has been further divided into two parameterization sub-methods: BP3333 and BP3434. Four third-order Bezier curves are used to represent the airfoil shape in the BP3333 parameterization sub-method. The BP3434 parameterization has a 3rd-degree edge thickness curve, a 4th-degree trailing edge thickness curve, a 3rd-degree leading edge camber curve and a 4th-degree trailing edge camber curve. Due to the smaller number of degrees of freedom in the BP3333 method with respect to those of the BP3434 method, specifically at the trailing edge and at the leading edge, the BP3434 method was chosen in this research.
A fourth-degree Bezier curve is given by:

$$x(u) = x_0(1-u)^2 + 4x_1u(1-u)^3 + 6x_2u^2(1-u)^2 + 4x_3u^3(1-u) + x_4u^4 \quad (3.5)$$

and

$$y(u) = y_0(1-u)^2 + 4y_1u(1-u)^3 + 6y_2u^2(1-u)^2 + 4y_3u^3(1-u) + y_4u^4 \quad (3.6)$$

The parameterization is controlled by 15 parameters: 10 aerodynamic and 5 Bezier parameters. Figure 3.3 shows the graphical representations of these parameters.

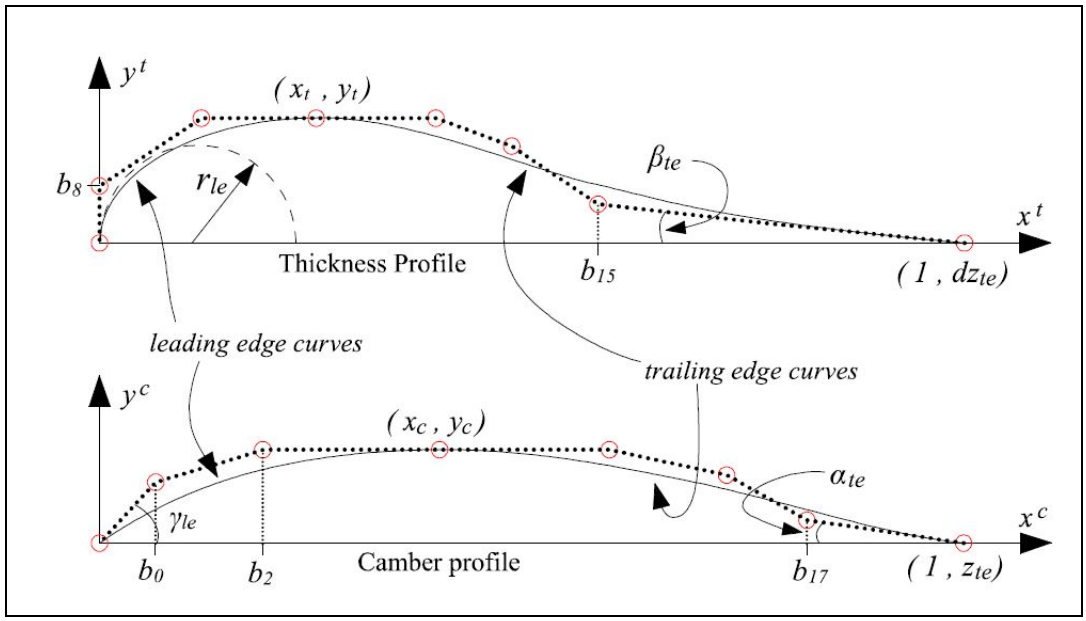

Figure 3.3 BP3434 method parameter definition. The BP3434 parameterization has a 3rd-degree edge thick-ness curve, a 4th-degree trailing edge thickness curve, a 3rd-degree leading edge camber curve and a 4th-degree trailing edge camber curve

The control points definitions for the leading and trailing edge Bezier curves are given in Table 3.2 for the thickness profile curve, and in Table 3.3 for the camber profile curve (Kharal et Saleem, 2012). The upper and lower bound values of the parameters used in the BP parameterization optimization method calculated in this study for the UAS-S45 are presented in Table 3.4.

Table 3.2 Thickness profile curve control points definition

Leading Edge		**Trailing Edge**	
$x_0 = 0$	$y_0 = 0$	$x_0 = x_t$	$y_0 = y_t$
$x_1 = 0$	$b_1 = b_8$	$x_1 = (7x_t + 9b_8^2/2r_{le})/4$	$y_1 = y_t$
$x_2 = {-3b_8^2}/{2r_{le}}$	$y_2 = y_t$	$x_2 = 3x_t + 15b_8^2/4r_{le}$	$y_2 = (y_t + b_8)/2$
$x_3 = x_t$	$y_3 = y_t$	$x_3 = b_{15}$	$y_3 = dz_{te} + (1 - b_{15})\tan(\beta_{te})$
-	-	$x_4 = 1$	$y_4 = dz_{te}$

Table 3.3 Camber profile curve control points definition

Leading Edge		**Trailing Edge**	
$x_0 = 0$	$y_0 = 0$	$x_0 = x_c$	$y_0 = y_c$
$x_1 = b_0$	$y_1 = b_0 \tan(\gamma_{te})$	$x_1 = \frac{1}{2}(3x_c - y_c cot(\gamma_{le}))$	$y_1 = y_c$
$x_2 = b_2$	$y_2 = y_c$	$x_2 = \frac{1}{6}(-8y_c cot(\gamma_{le}) + 13x_c)$	$y_2 = \frac{5}{6}y_c$
$x_3 = x_c$	$y_3 = y_c$	$x_3 = b_{17}$	$y_3 = z_{te} + (1 - b_{17})\tan(\alpha_{te})$
-	-	$x_4 = 1$	$y_4 = z_{te}$

Table 3.4 Values of the upper and lower bounds of parameters used in the BP method

Parameter	r_{le}	β_{te}	x_t	y_t	dz_{te}	b_8	b_{15}	α_{te}
Lower	−0.036	0.0009	0.0009	0	0.045	0.18	0	0.135
Upper	−0.003	0.3	0.9	0.03	0.6	1.5	0.6	1.2
Parameter	z_{te}	γ_{le}	x_c	y_c	b_0	b_2	b_{17}	-
Lower	0.045	0	0.009	0.09	0	0	0	-
Upper	0.45	0.003	1.5	1.8	2.1	2.7	2.7	-

3.2.3 Description of Flow Solvers

Various solvers have been employed in aerodynamic optimization studies, such as the Fully Potential Flow, Coupled Boundary-Layer, Euler and Viscous Navier–Stokes solvers (Khurana, 2011). The type of solver chosen by a user depends upon the type of optimization problem. Results obtained with the flow solver must be consistently accurate in order for the optimization to be considered highly adequate.

For this aerodynamic research, incompressible flow solvers are needed as they can perform fast computation, and also can provide high accuracy results. Therefore, in this paper, two types of aerodynamic solvers are used for the aerodynamic optimization: a Panel-based method

and a Reynolds-Averaged Navier–Stokes equations (RANS) solver. The choice to keep the computational cost low for an airfoil analysis leads directly to the use of the XFOIL code, which is known for its very good combination of execution speed and accuracy of results. Furthermore, in order to obtain higher accuracy results for solving the viscous boundary layer and the flow separation than the XFoil solver, a well-established high-fidelity Computational Fluid Dynamics (CFD) solver, Ansys Fluent was also used in this morphing airfoil analysis.

3.2.3.1 XFoil

XFoil is a code for airfoil design and analysis consisting of inviscid, inverse and viscous formulations (Drela et al., 2015). The viscous formulation can be used to calculate free or imposed forced flow transition to handle transitional separation bubbles, to calculate aerodynamic coefficients and to cope with moderately trailing edge separation. It uses an approximate e^N envelope method to calculate the flow transition. The turbulence level settings are kept as default with free transition features. Both the boundary layer and the wake parameters are calculated with a two-equation integral boundary layer formulation as shown in Equations (3.7) and (3.8), respectively (Van de Wal, 2010).

$$\frac{d\theta}{d\xi} + (2 + H - M_e^2)\frac{\theta}{u_e}\frac{du_e}{d\xi} = \frac{C_f}{2} + \left\{\frac{v_0}{u_e}\right\} \tag{3.7}$$

$$\theta\frac{dH^*}{d\xi} + \left(2H^{**} + H^*(1-H)\right)\frac{\theta}{u_e}\frac{du_e}{d\xi} = 2C_D - H^*\frac{C_f}{2} + \left\{(1-H^*)\frac{v_0}{u_e}\right\} \tag{3.8}$$

where shape factors H^* and H^{**} are defined in the following equations

$$xH^* = \frac{\int_0^{\propto}\frac{u}{U}\left(1-\left(\frac{u}{U}\right)^2\right)dy}{\int_0^{\propto}\frac{u}{U}\left(1-\left(\frac{u}{U}\right)\right)dy} \tag{3.9}$$

and

$$H^{**} = \left(\frac{0.064}{H_k - 0.8} + 0.251\right) M_e^2 \text{ with } H_k = \frac{H - 0.290 M_e^2}{1 + 0.113 M_e^2} \tag{3.10}$$

At high angles of attack where stall occurs, XFoil has difficulties in giving a converging solution for the airfoil analysis. To obtain the convergence of the solution, non-converged solutions are given a high penalty by setting the fitness function arbitrarily large via a penalty function, and thus they are eventually eliminated during the design process. The solver tolerance value used for this penalty function calculation is 0.002.

Many researchers have employed XFoil software in morphing airfoil studies. In one of these studies, the results obtained using XFoil were compared with those obtained using the Reynolds-Averaged Navier–Stokes (RANS) solvers for camber morphing, and only a slight difference between the results was observed (Woods, Fincham et al., 2014).

3.2.3.2 CFD Fluent Solver

The validation of solvers and mesh settings is needed before carrying out the optimization studies. The validation studies were performed at a Reynolds number of 2.4×10^6 and a Mach number of 0.10. The range of angles of attack was considered from 0° to 16° to include the stall angle. The aerodynamic coefficients and the pressure distribution were obtained and further used for solution validation. A C-shaped computational domain with structured grids, as seen in Figure 3.4, was used in domain discretization after the performance of the mesh convergence test. The turbulence model used in this study was the Transition $(\gamma - Re_\theta)$ SST. This model uses a combination of SST K-ω coupled with intermittency γ and transition onset Reynolds number. Re_θ is the critical Reynolds number where the intermittency starts (Langtry et al., 2005). Four transport equations of the Transition $(\gamma - Re_\theta)$ SST model are given below:

$$\frac{\partial(\rho k)}{\partial t} + \frac{\partial(\rho U_j k)}{\partial x_j} = P_k - D_k + \frac{\partial}{\partial x_j}\left[(\mu + \sigma_k \mu_t)\frac{\partial k}{\partial x_j}\right] \tag{3.11}$$

$$\frac{\partial(\rho\omega)}{\partial t} + \frac{\partial(\rho U_j \omega)}{\partial x_j} \tag{3.12}$$
$$= P_\omega - D_\omega + \frac{\partial}{\partial x_j}\left[(\mu + \sigma_\omega \mu_t)\frac{\partial \omega}{\partial x_j}\right]$$
$$+ 2(1 - F_1)\frac{\rho\sigma_{\omega 2}}{\omega}\frac{\partial k}{\partial x_j}\frac{\partial \omega}{\partial x_j}$$

$$\frac{\partial(\rho\gamma)}{\partial t} + \frac{\partial(\rho U_j \gamma)}{\partial x_j} = P_\gamma - E_\gamma + \frac{\partial}{\partial x_j}\left[\left(\mu + \frac{\mu_t}{\sigma_\gamma}\right)\frac{\partial \gamma}{\partial x_j}\right] \tag{3.13}$$

$$\frac{\partial(\rho\overline{Re_{\theta t}})}{\partial t} + \frac{\partial(\rho U_j \overline{Re_{\theta t}})}{\partial x_j} = P_{\theta t} + \frac{\partial}{\partial x_j}\left[\sigma_{\theta t}(\mu + \mu_t)\frac{\partial \overline{Re_{\theta t}}}{\partial x_j}\right] \tag{3.14}$$

The spatial discretization used in the solution is of the second order for all the turbulence statistical parameters, including the momentum, the turbulent kinetic energy, the specific dissipation rate, the intermittency and the Reynolds momentum thickness.

ANSYS Fluent was used in this study to carry out the numerical analysis. The meshing was done using ANSYS Mesher, as shown in Figure 3.4. The rectangular computational domain was designed around the airfoil geometries. The outlet length was selected to be 30c, which was adequate to allow for the full development of the wake flow, based on the size of the computational domain adopted in previous studies. The distance from the domain inlet to the airfoil was 10c to prevent the inlet boundary from unphysically impacting the induction field upstream of the airfoil. The high-quality grids were generated with dense grids in the boundary layer of the airfoil with a gradual decrease of grid cells away from the airfoil surface. The first layer's thickness was calculated based on inlet velocity and adopted accordingly to capture the laminar and transitional boundary layer regions. Furthermore, the grid sensitivity analysis was performed according to the number of cells in the computational domain.

A freestream velocity of 34 m/s with a turbulence rate of 0.01 percent was imposed at the inlet. The surface of the airfoil was modelled as a zero-roughness no-slip wall, and its values were executed on the grid domain, which prescribed its motion relative to the rest of the computational domain. A symmetry boundary condition was applied to achieve a parallel flow

at the top and bottom of the domain by assuming zero normal velocity and zero normal gradients of the flow quantities. A zero static gauge pressure was applied at the exit of the domain. Iterations were finalized when all scaled residuals were below 1×10^6.

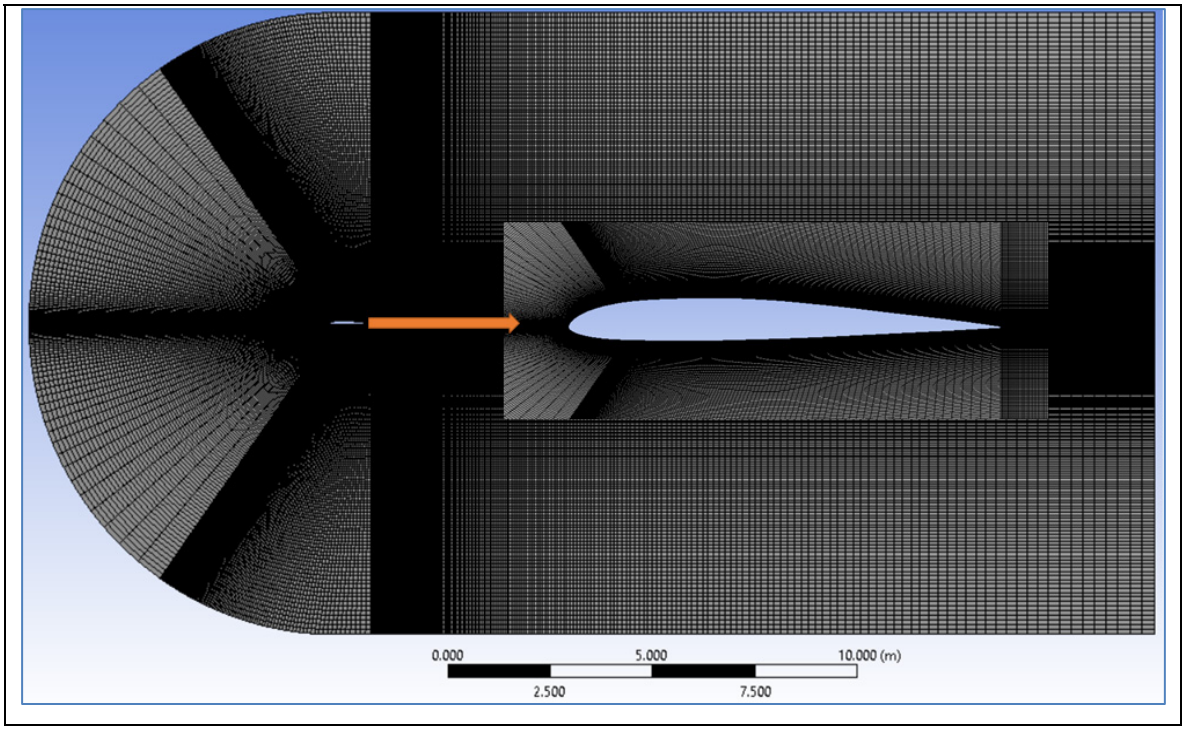

Figure 3.4 Grid around the airfoil used in Reynolds-averaged Navier–Stokes (RANS) simulations

3.2.4 Optimization Algorithm

An intelligent search algorithm is essential for the direct numerical optimization of airfoil design. This algorithm operates iteratively and utilizes the inputs of the shape parameterization method to define the airfoil shape, and then it uses the flow solver to calculate the aerodynamic coefficients. Its efficiency is assessed according to its ability to provide a global optimal solution with reasonable computational resources. Therefore, the choice of such an algorithm influences the solution convergence and its feasibility.

Researchers have implemented various algorithms, such as the Gradient-Based, Adjoint-Based and Evolutionary algorithms with the aim to investigate and solve various optimization problems (M Khurana, 2011). These algorithms have been considered to solve different aerodynamic optimization problems based on their advantages and disadvantages. The hybrid optimizer based on the Particle Swarm Optimization (PSO) algorithm was used in this paper for the UAS-S45 optimization, and it was further combined with the Pattern Search algorithm in order to enhance the solution convergence and its refinement.

Evolutionary algorithms have attracted the attention of shape designers due to their characteristics, such as their suitability for modelling discontinuous shape functions, obtaining global optimal solutions, ease of parallel computing, etc. During morphing airfoil optimization, gradient-based algorithms converge fast, but they only cover a small area out of a large airfoil search space, and thus a local minimum solution instead of global minimum solution is found. It is also difficult to find the gradient of the non-linear flow fields for gradient-based optimizers.

Therefore, a PSO algorithm is used, based on a simplified social behavior closely related to the swarming theory, where the solutions are represented by a set of particles that heuristically navigate through a design space (Khan et al., 2020). The efficiency of PSO algorithms over genetic algorithms is due to their independence from parameters, such as crossovers and mutations; instead, the solution is updated by sharing its information amongst its populations of particles.

3.2.4.1 PSO Algorithm

In the PSO algorithm, each particle is a solution to a given optimization problem and is composed of two vectors: “position” and “velocity”. A position vector x_i^n is used to store the positioning of the particles in the given dimensional space. The velocity vector v_i^n is updated using the following equation for each iteration k:

$$v_i^n\ (k) = \left[v_i^n(k-1) + c_1 r_1\left(pbest_i^n - x_i^n(k-1)\right)\right. \\ \left. + c_2 r_2\left(pbestg_i^n - x_i^n(k-1)\right)\right] \tag{3.15}$$

where x_i^n = position vector; v_i^n= randomly generated velocity vector of the particles at search initialization; $pbest_i^n$ = vector representing the best solution achieved by the particle; $pbestg_i^n$ = vector representing the "global best solution" collectively achieved by the swarm; c_1 and c_2 = stochastic acceleration terms that pull each particle toward $pbest_i^n$ and $pbestg$ positions respectively; r_1 and r_2 = random numbers in the uniform range [0, 1];

The update of the position vector at the k^{th} iteration is given by the following equation:

$$x_i^n(k) = x_i^n(k-1) + v_i^n(k) \tag{3.16}$$

The PSO procedure can be outlined as follows:

1. Generate an initial swarm with arbitrary values of the particle position and arbitrary initial velocities in the n-dimensional search space;
2. Evaluate the fitness of each particle of the swarm by searching a new velocity vector applied to each individual particle; the new velocity vector is influenced by its best position, the swarm's best position and its previous velocity;
3. Update the velocity of the particles as shown in Equation (3.15) and the position of the particles as shown in Equation (3.16) and evaluate the new fitness function;
4. Repeat steps 2 and 3 until the maximum number of iterations is reached or until the results no longer improve for a given number of iterations.

Pattern Search (PS) is a direct search optimization method that is used to minimize a function by comparing its value at each iteration with its value at its previous iteration in a finite set of trial points. The method is outlined as follows:

1. Select the initial solution;
2. Explore the direction search by evaluating each objective function value, one at a time;
3. Evaluate the objective function. If the objective function is minimized, then update it; otherwise, do not update it;
4. Evaluate the next values of the objective function following the previous steps 2 to 3;
5. After exploring the search of all possible values of the objective function and the minimization of the overall objective function, the PS method follows a pattern move; and
6. If the overall objective function has not been minimized, repeat the process.

3.2.4.2 Hybrid Optimization Scheme

A hybrid optimizer is used in this study, as shown in Figure 3.5. In this figure, the hybrid optimization implies that the PSO-based optimization process is applied firstly to its variables to obtain their optimized values. Since the first optimization process may not be accurate as it would result in low variations of values to be optimized, a second optimization process would then be applied to the results of the first optimization process. In this case, PSO, a non-elitist algorithm, is then followed by Pattern Search, using hybrid optimization. The PSO and Pattern Search can then be used to find a local optimum in a limited search area; the use of both PSO and PS algorithms through hybrid optimization ensures better results than a single optimization process. The independent variables given as inputs to the optimization process are also limited due to their upper and lower bounds. These bounds ensure that the search space for both the PSO and Pattern Search algorithms remains within them. During the PSO algorithm execution, if a solution is found outside the bounds of the search space, any such solution outside these bounds will have its value replaced by that of its given upper and/or lower bounds, without any influence on other solutions. The hybrid optimizer's procedure is shown in Figure 3.5.

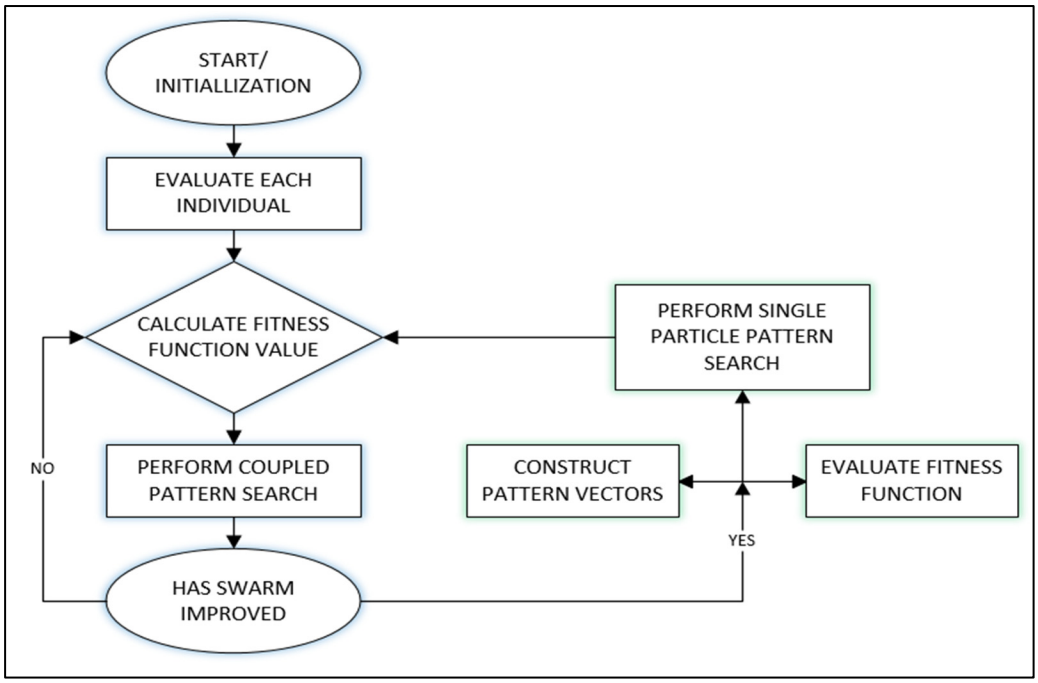

Figure 3.5 Schematics of the Hybrid Optimizer/ Particle Swarm Optimization (PSO) algorithm combined with the Pattern Search algorithm

3.3 Discussion and Results

The aerodynamic optimization considered in this study applies to both Droop Nose Leading Edge Morphing (DNLE) and Morphing Trailing Edge (MTE) configurations. To utilize the full potential of the "morphing" concept, a baseline shape optimization was carried out followed by its morphing shape design at various flight conditions given in Table 3.5. These cases are based on various altitudes and Reynolds numbers that are computed for the airspeed of 34 m/s. These given flight conditions are chosen because of the fact that the UAS-S45 can reach altitudes of 20,000 ft and a stall speed of 34 m/s. The design framework uses endurance maximization as an optimization function to enhance the performance of the UAS-S45 over a large part of its flight regimes. Figure 3.6 shows the flight envelope of UAS-S45. From a physical standpoint, every flight condition is defined by a specific Mach number, altitude (Reynolds number and temperature are calculated according to ISO standard atmosphere) and a fixed lift coefficient. The present study considered the optimization of the leading edge and trailing edge of the UAS S45 conventional wing that could be both morphed. The difference

of performances obtained between the baseline airfoil and the morphed one demonstrate the overall benefits of morphing airfoil design. Figure 3.7 shows the design of Droop Nose Leading Edge (DNLE) and Morphing Trailing Edge (MTE) airfoil configurations versus the baseline airfoil. Figure 3.7 (a) shows the basic concept of the morphing wing with combined morphing leading and trailing edge deflections and Figure 3.7 (b) shows two cases of MTE designs.

Table 3.5 Operating conditions for design problem of UAS-S45 at the airspeed of 34 m/s

Flight Condition	**Altitude (Feet)**	**Reynolds Number**
Flight Condition I	0	2.40×10^6
Flight Condition II	10,000	1.88×10^6
Flight Condition III	20,000	1.45×10^6

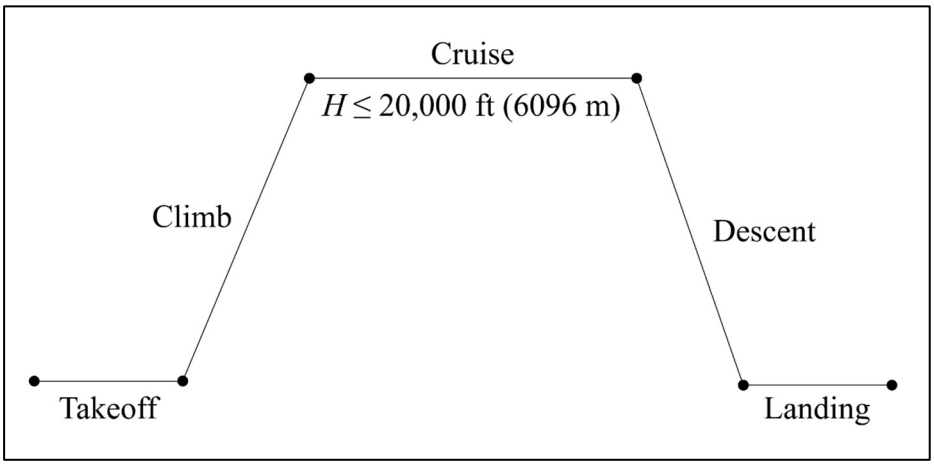

Figure 3.6 Schematic of the flight regimes of UAS-S45

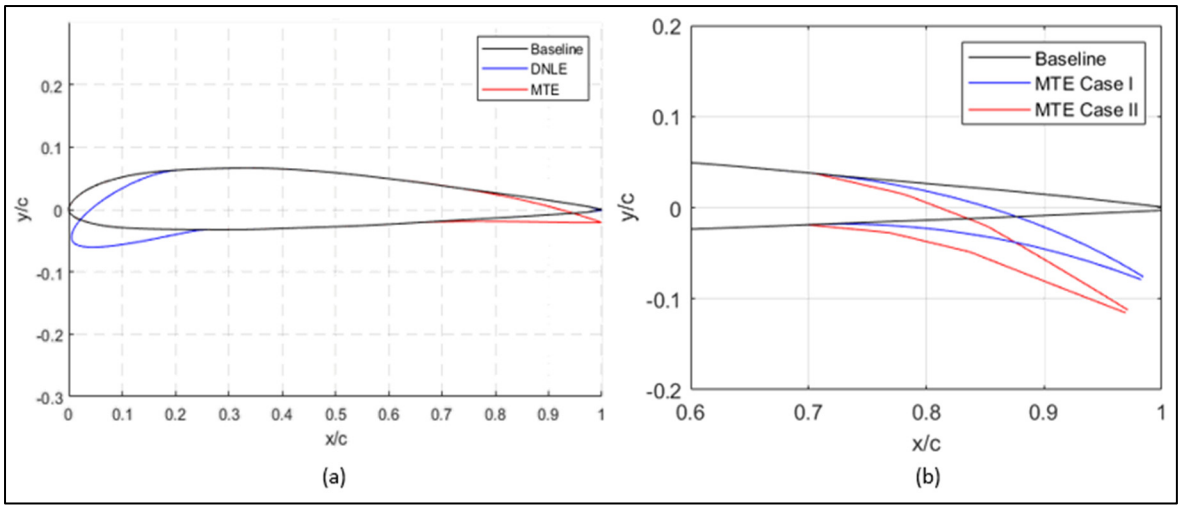

Figure 3.7 Design of Droop Nose Leading Edge (DNLE) and Morphing Trailing Edge (MTE) airfoil configurations versus the baseline airfoil. (a) the basic concept of the morphing wing with combined morphing leading and trailing edge de-flections; (b)the two cases of MTE designs

Figure 3.8 shows the aerodynamic coefficients C_L and C_D variations of the baseline UAS-S45 root airfoil for two Reynolds numbers Re = 1.2×10^6 and Re = 2.4×10^6, which were calculated using the XFoil and the Transition $(\gamma - Re_\theta)$ SST in Ansys/Fluent software. As seen in Figure 3.8, the lift coefficients' variations with the angle of attack were predicted accurately, while small differences were found in drag coefficient variations with the angle of attack. These differences in the drag coefficients' variations are found largely at angles of attack higher than 4° because the pressure-based drag coefficient becomes the dominant component of the total drag coefficient and flow separation conditions result in a decreased friction-based drag coefficient. This result implies that drag forces are very sensitive to turbulence effects and the Transition $(\gamma - Re_\theta)$ SST model can solve the turbulence problems more accurately than the XFoil solver.

Figure 3.9a shows the friction coefficient variations with the chord for the angles of attack of 0°, 2° and 6° obtained by use of the Transition $(\gamma - Re_\theta)$ SST model; this figure indicates very good accuracy in predicting the flow separation phenomena as the skin friction coefficient increases slightly with the increase in angle of attack. Figure 3.9 (a,b) also shows the initial

flow separation, the separated region and its reattachment. It is seen in Figure 3.9a that the laminar-to-turbulent transition region is located at 18% of the chord (0.18c) at an angle of attack of 6° and at 43% of the chord (0.43c) at an angle of attack of 2°. The variations of the skin friction coefficient along the chord were assessed at different angles of attack using the Transition ($\gamma - Re_\theta$) SST model in Figure 3.9.

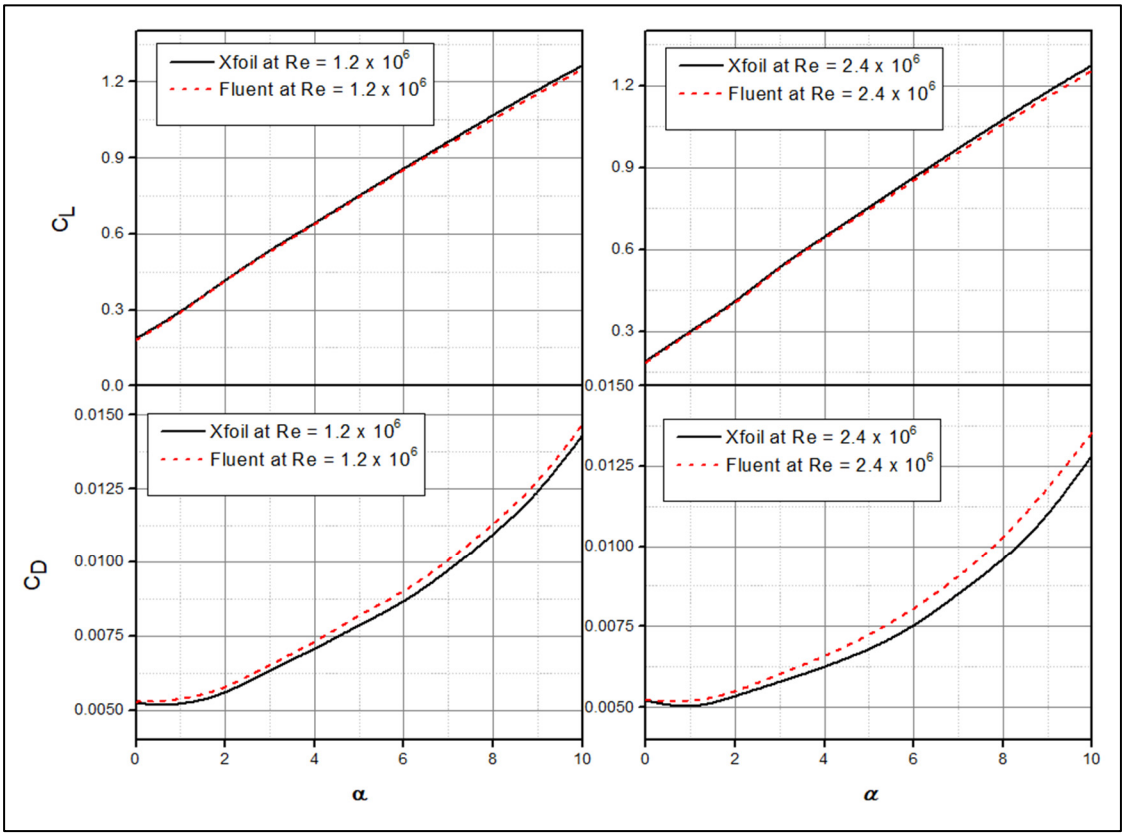

Figure 3.8 Aerodynamic lift and drag coefficient variations using the XFoil and Fluent solvers

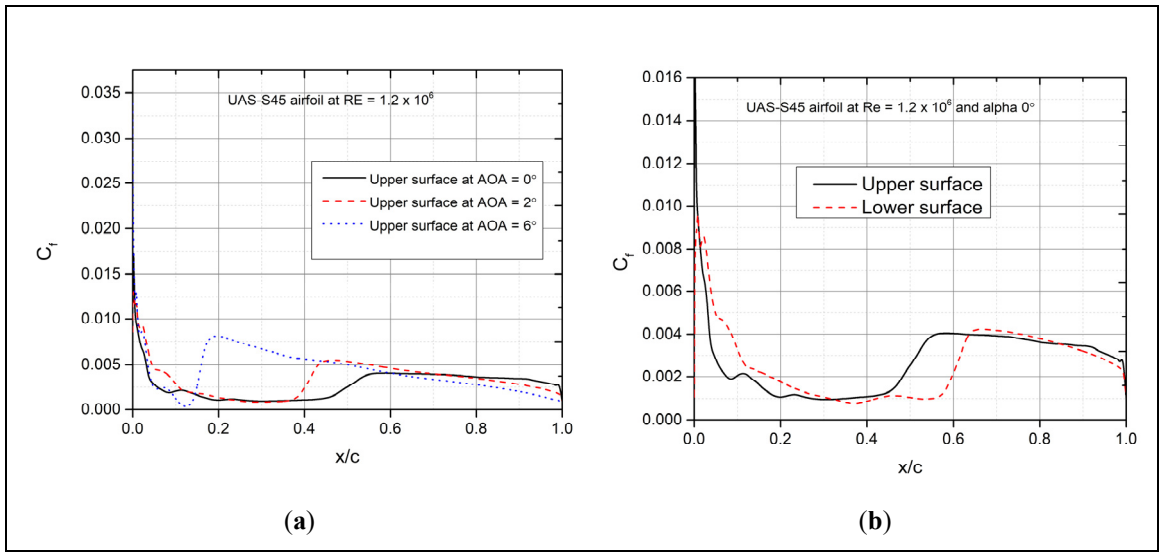

Figure 3.9 Skin friction coefficients variations with the chord obtained at different angles of attack. (a) the friction coefficient variations with the chord for the angles of attack of 0°, 2° and 6°; (b) the initial flow separation, the separated region and its reattachment for upper and lower surface

The velocity magnitude contours plots at three angles of attack (4°, 10°, 16°) at Re = 2.4×10^6 are shown in Figure 3.10. The turbulent intensities play an important role in understanding the flow behavior over an airfoil, and they are shown in Figure 3.10 for the angles of attack of 4° and 10°.

The contour lines remain attached to the airfoil at low angles of attack such as 4°, as shown in Figure 3.10a; the flow starts to separate at the trailing edge of the airfoil at an angle of attack of 10° as shown in Figure 3.10b and changes into a fully separated flow at the angle of attack of 16° as shown in Figure 3.10c. It is important to understand that boundary layer separation takes place at an angle of attack of approximately 10°. The separation region shown in Figure 3.10c causes increased drag as it induces a large wake that completely changes the flow downstream of the point of separation. It is clear that the turbulent intensity is minimal at the airfoil leading edge at a low angle of attack of 4°, as seen in Figure 3.11a, while at the angle of attack of 10°, the turbulent intensity increases over the airfoil surface, including at its leading edge.

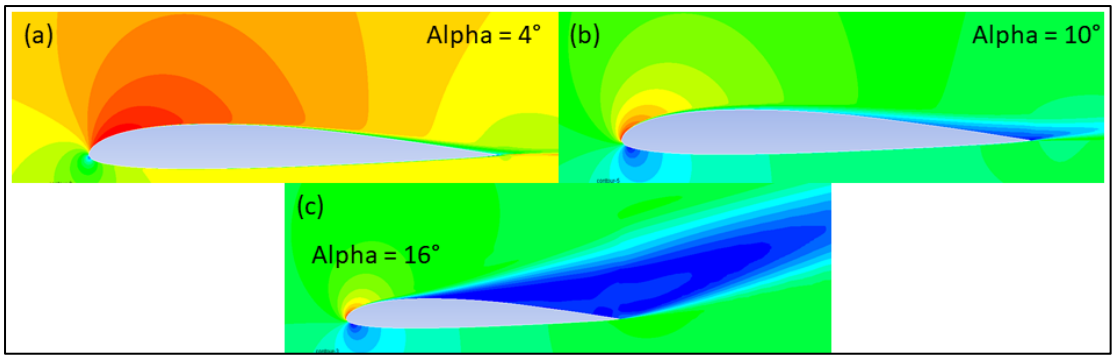

Figure 3.10 Velocity magnitude contour plots at three angles of attack at Re = 2.4 × 106. (a) the contour lines at low angles of attack such as 4°; (b) the contour lines at low angles of attack such as 10°; (c) a fully separated flow at the angle of attack of 16°

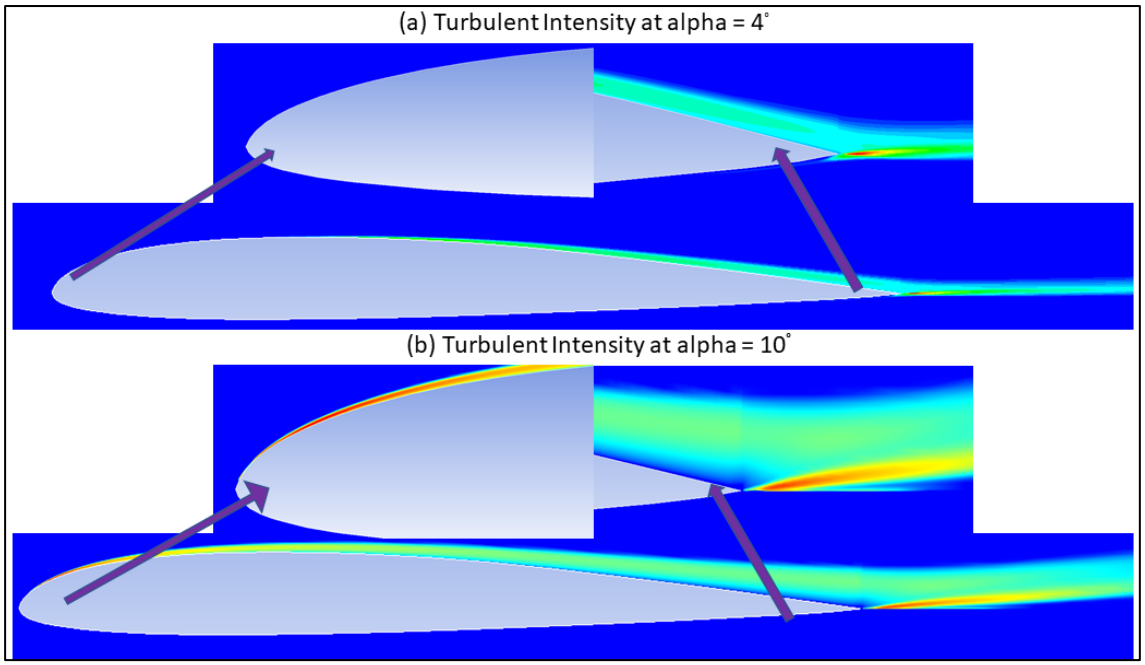

Figure 3.11 Contour plots of turbulent intensity comparison for baseline airfoil at the airspeed of 34 m/s. (a) the turbulent intensity at a low angle of attack of 4°; (b) the turbulent intensity at a low angle of attack of 10°

3.3.1 Optimization of Morphing Leading Edge

The Droop Nose Leading Edge (DNLE) optimization was performed to satisfy the objective functions defined in Equation (1) for drag minimization and in Equation (5) for endurance

maximization. The optimization processes were carried out for two cases of DNLE control point deflections, defined as “Opt. Case I” and “Opt. Case II”.

In “Opt. Case I”, a morphing DNLE is a smooth single structural layout with a morphing leading edge starting location fixed at 22% of the chord. The trailing-edge is not allowed to move, while the leading-edge points are only allowed to move in the vertical direction to effectively adapt the chord-length variation of the baseline airfoil.

In “Opt. Case II”, the morphing DNLE is free to change its shape anywhere from 0 to 22% of the chord. The starting point and the end point of the leading edge are used to represent the morphing DNLE shape. The parameterization of the DNLE shape was obtained by using the Bezier–PARSEC (BP) method, in which the leading-edge radius of the airfoil and 5 Bezier control points were used to maintain the slope continuity within the airfoil shape.

The XFoil software was used to efficiently investigate the aerodynamics of the optimized morphing geometries. The aerodynamic performance of the DNLE was evaluated to determine its best airfoil design shape for each flight condition. The computations were performed for the three flight conditions listed in Table 3.5. The results were obtained in terms of aerodynamic lift and drag coefficients variations with angle of attack and pressure distributions versus the airfoil chord locations for the optimized airfoil geometries.

Figure 3.12a illustrates the initial (reference) versus the final (optimized or morphed) airfoil shape, while Figure 3.12b shows the convergence trend for the minimum drag optimization function for an optimized airfoil shape with DNLE at an angle of attack of 50. The algorithms PSO with Pattern Search converge to the optimal solution after 90 iterations. The x-axis indicates the number of function evaluations, and the y-axis shows the value of the fitness. The fitness value is the objective function value of each particle of the algorithm, expressing the performance of any airfoil shapes.

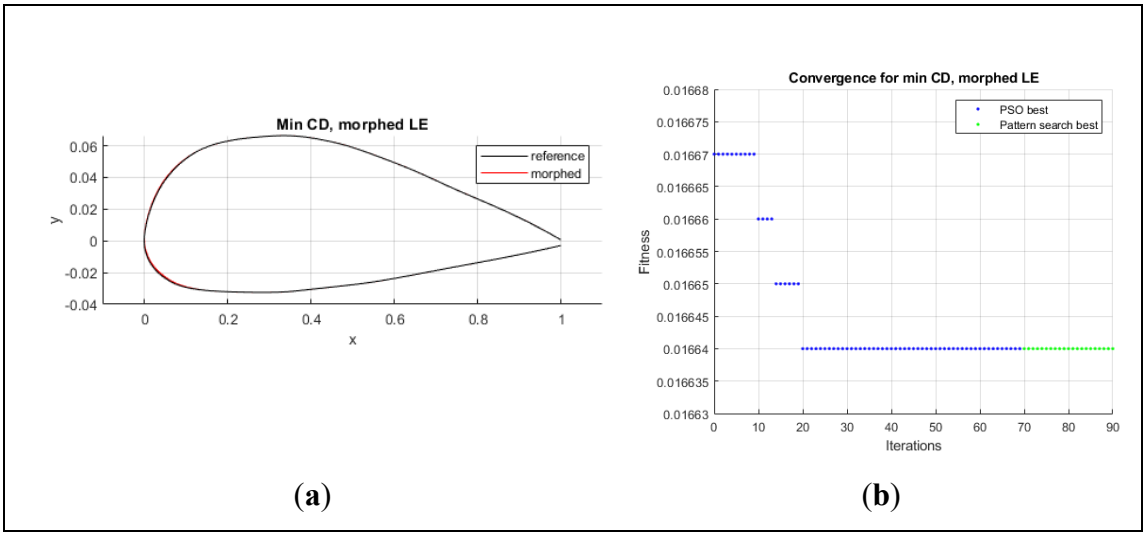

Figure 3.12 Optimized airfoil and convergence history for drag minimization function; (a) the initial (reference) versus the final (optimized or morphed) airfoil shape, (b) the convergence trend for the minimum drag optimization function

These results for the droop nose leading edge (DNLE) optimization are shown in Figures 3.13 and 14, and the UAS-S45 baseline airfoil aerodynamic coefficients were compared to those of the optimized airfoils. Figure 3.13a–d show the variations of lift coefficients with the angles of attack. The lift coefficient variations for all three flight conditions for Opt. Case I and Opt. Case II and the baseline airfoil in Figure 3.13a–c show that higher lift coefficients were obtained for Opt. Cases I and II than those of the baseline airfoil. Figure 3.13d shows that the DNLE designs for Opt. Case I at three different flight conditions. It is found that Opt. Case I DNLE design is the best at Flight Condition III. These optimal shapes revealed that maximum increment of the lift coefficient with respect to the baseline airfoil of up to almost 21% was found for Opt. Case I design seen in Figure 3.13c. In addition, an increase of 9.6% was obtained for the maximum lift coefficient, associated with a stall angle delay of 3° as seen in Figure 3.13c. Therefore, it was found that both Opt. Case I and Opt. Case II results are better than the baseline airfoil results. These better results can be explained by the pressure distribution change around the airfoil. The DNLE design does not cause an adverse pressure gradient as the flap configuration, but instead, it decreases the maximum speed at the airfoil leading edge, which is similar to the findings (Burnazzi et al., 2014).

Figure 3,14 presents the evaluation of the lift vs. drag polar of the baseline airfoil and of the optimized airfoils for three different flight conditions. Therefore, the increased aerodynamic performance of optimized airfoils in terms of their lift versus drag variation for all three flight conditions can be seen in Figure 3.14a–d.

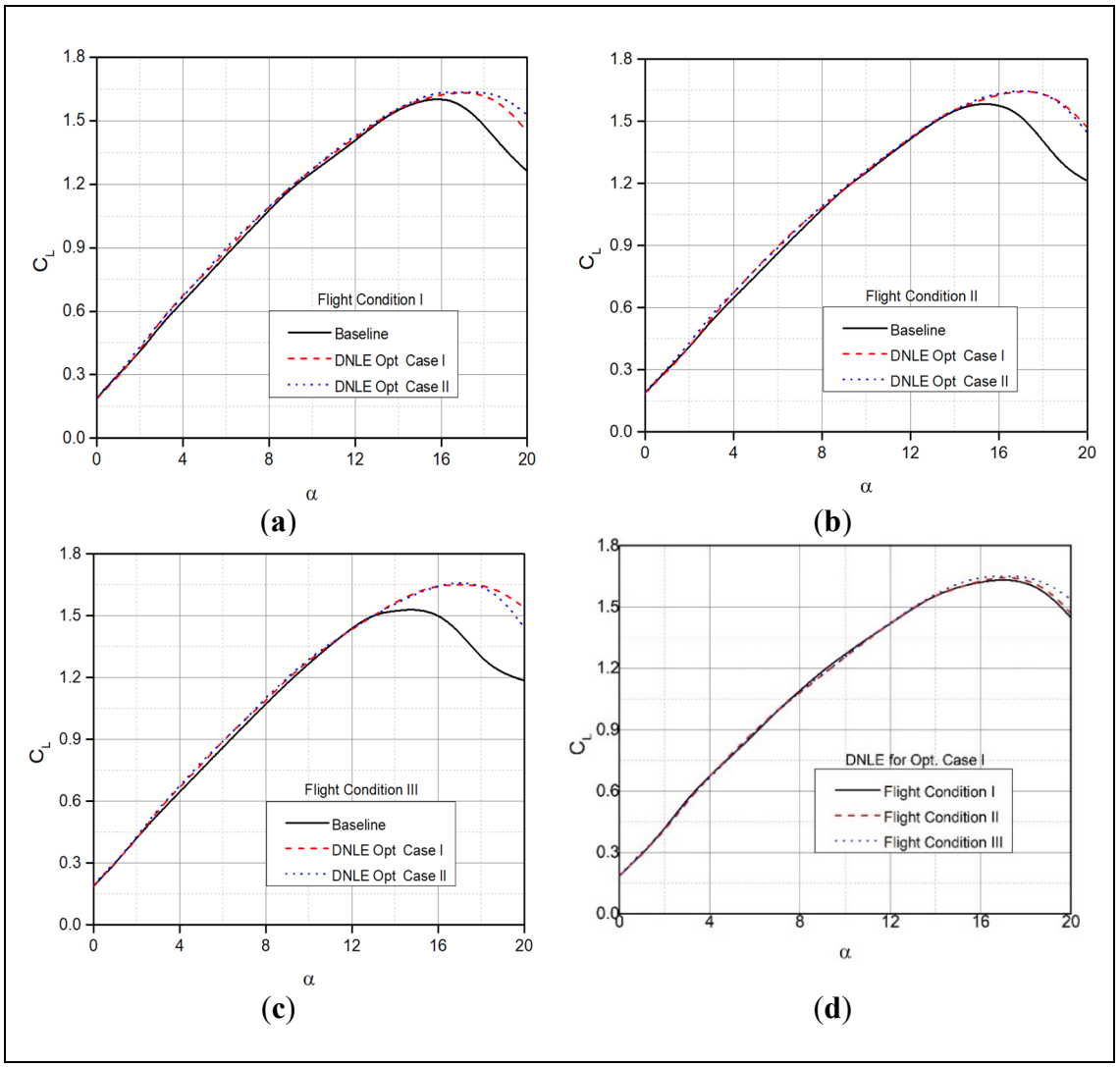

Figure 3.13 Lift coefficients versus angle of attack at two optimized design configurations; (a) Figure 13a show the variations of lift coefficients with the angles of attack at Flight Condition I (b) the variations of lift coefficients with the angles of attack at Flight Condition II; (c) the variations of lift coefficients with the angles of attack at Flight Condition III; (d) the lift co-efficient variations for all three flight conditions for Opt. Case I

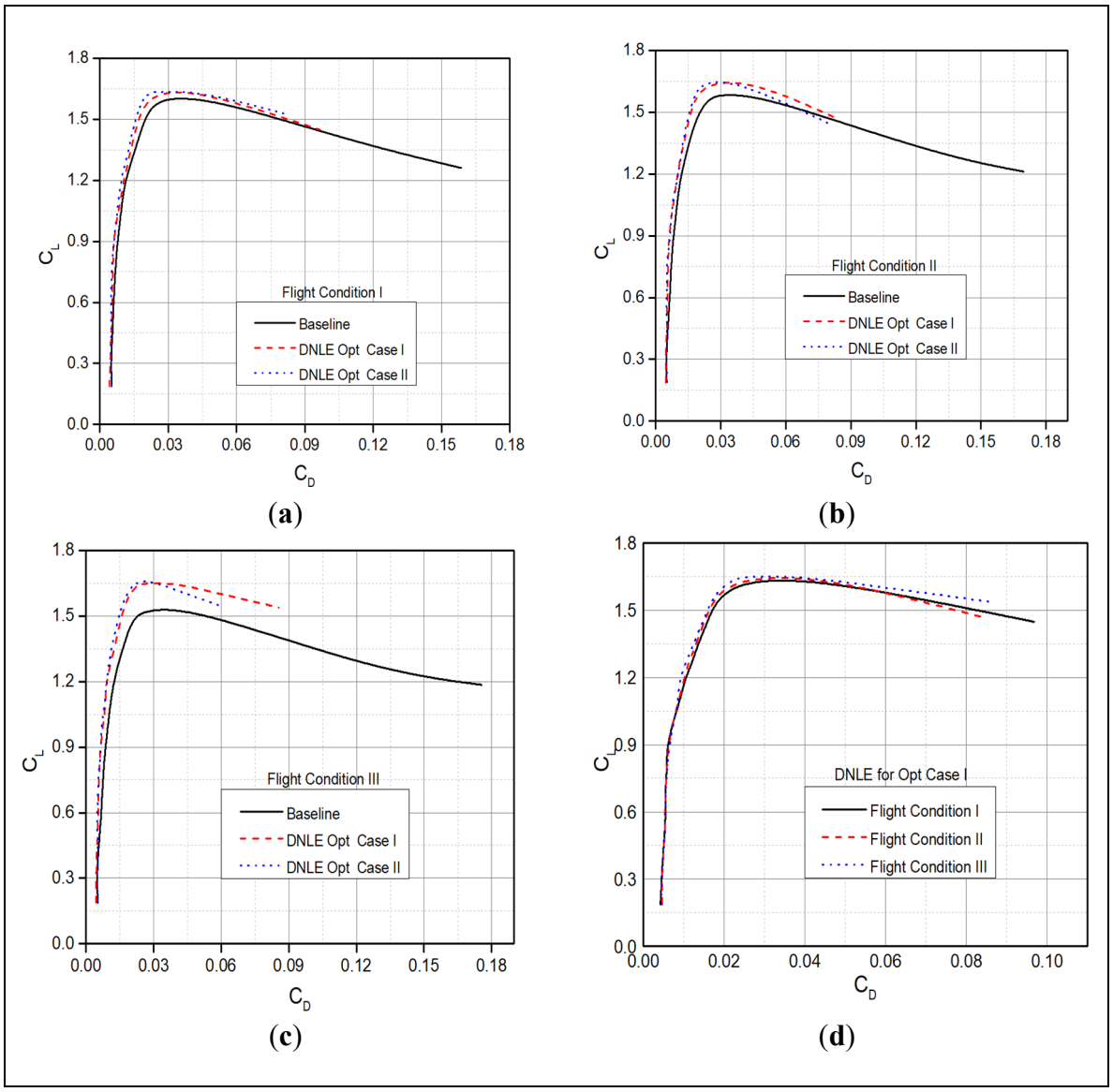

Figure 3.14 Aerodynamic performance for two optimized design configurations. (a) Figure 13a show the drag polar at Flight Condition I; (b) drag polar at Flight Condition II; (c) drag polar at Flight Condition III; (d) drag polar for all three flight conditions for Opt. Case I

The pressure coefficients' variations with the chord of optimized airfoils for three flight conditions are shown in Figure 3.15. It is clear that the major changes in pressures take place near the leading edge at its upper surface, and that the pressure peaks then remain smooth on the rest of the airfoil for all configurations in Figure 3.15a for an angle of attack of 4° and in Figure 3.15b for an angle of attack of 10°. The chord-wise pressure distribution reveals that increased performance was obtained for DNLE configurations. By comparing the chord-wise

pressure distributions for different configurations at angles of attack of 10° for the baseline versus optimized airfoils, it is found that a kink in the suction peak is followed by a constant pressure distribution. The DNLE-optimized configuration at flight condition III undergoes flow separation, and reattaches shortly on the airfoil surface, as seen in Figure 3.15b.

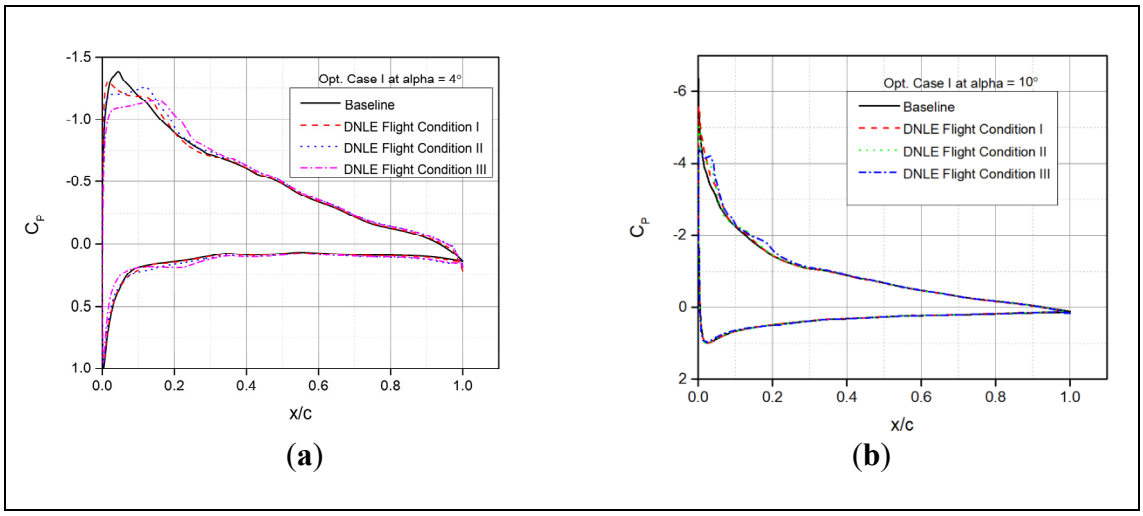

Figure 3.15 Pressure coefficients variations with the airfoil chord for Opt. Case I (a) at angles of attack of 4°; (b) at angles of attack of 10°

Figure 3.16a illustrates the initial (reference) versus the final (optimized or morphed) airfoil shape, while Figure 3.16b presents the convergence for aerodynamic endurance optimization while utilizing the PSO algorithm with Pattern Search for the DNLE-optimized airfoil at an angle of attack of 50°. A downward trend followed by constant values is clearly visible for the function, thus indicating the approach to the global optimum.

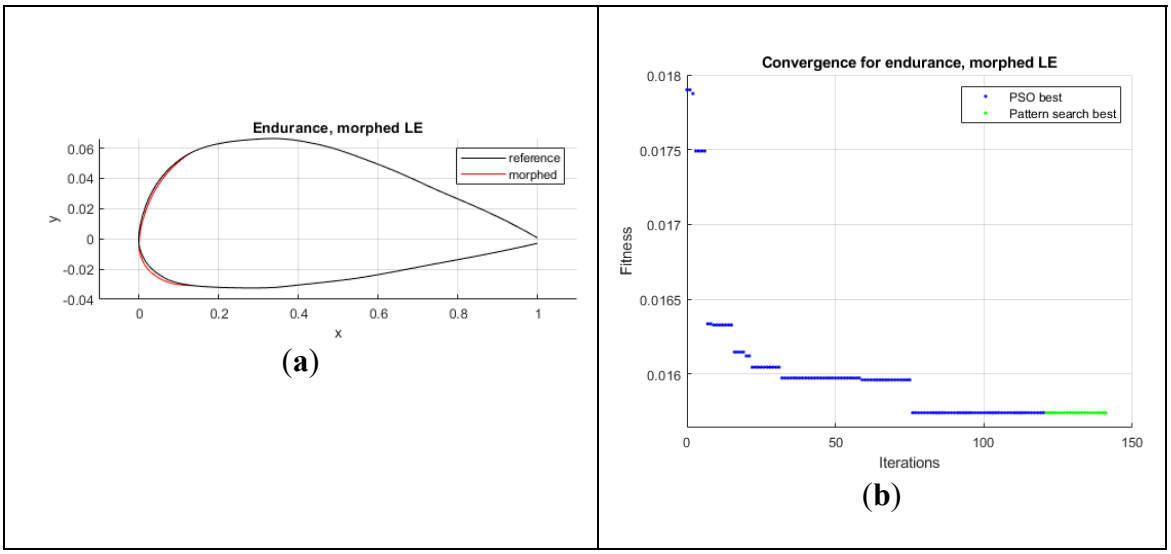

Figure 3.16 Optimized airfoil and convergence history for endurance maximization function. (a) the initial (reference) versus the final (optimized or morphed) airfoil shape; (b) the convergence for aerodynamic endurance optimization

Figure 3.17 shows that the optimization process led to an increase in endurance maximization characterized by $C_L^{3/2}/C_D$ in the optimized DNLE airfoils for three different flight conditions. The maximum endurance capability given by $C_L^{3/2}/C_D$ for the same lift coefficient of the baseline airfoil to the lift coefficient of the morphing DNLE configuration Opt. Case I was found to be 1.17 and 1.21, respectively. Furthermore, the values of $C_L^{3/2}/C_D$ increased from 117 to 132, thus indicating better endurance performance for the UAS-S45 DNLE airfoil configurations than for its baseline airfoil at three flight conditions.

The flow transition behavior can be seen in the velocity contour plots of one of the DNLE airfoils, as shown in Figure 3.18a for an angle of attack of 4° and in Figure 3.18b for an angle of attack of 10°. The comparison of baseline airfoil and DNLE configurations at a 10° angle of attack shows that higher gradients are formed for the DNLE airfoil in comparison with those of the baseline airfoil, illustrated in Figure 3.10. However, the trailing edge flow separation region remains the same for both airfoils. In addition, the Turbulent Kinetic Energy (TKE) for the baseline airfoil and for the DNLE airfoils by use of the Transition ($\gamma - Re_\theta$) SST turbulence model are shown in Figure 3.18 (c, d). It is evident that the leading edge is propagating the energy towards the downstream; thus, a considerable decrease is observed in the wake

turbulence. The TKE occurring in the baseline airfoil, which starts from the upper surface and moves towards the trailing edge was not observed in the DNLE-optimized airfoil at an angle of attack of 4°, as seen in Figure 3.18c.

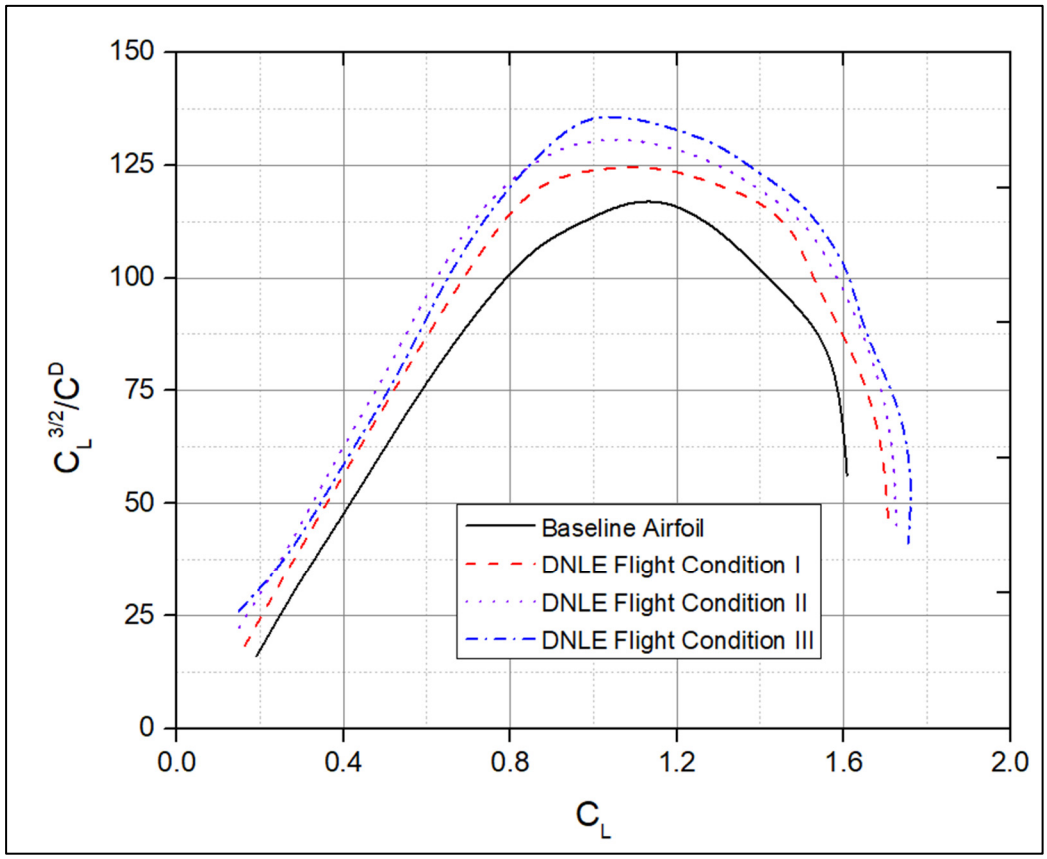

Figure 3.17 Comparison of the endurance for baseline and DNLE airfoils

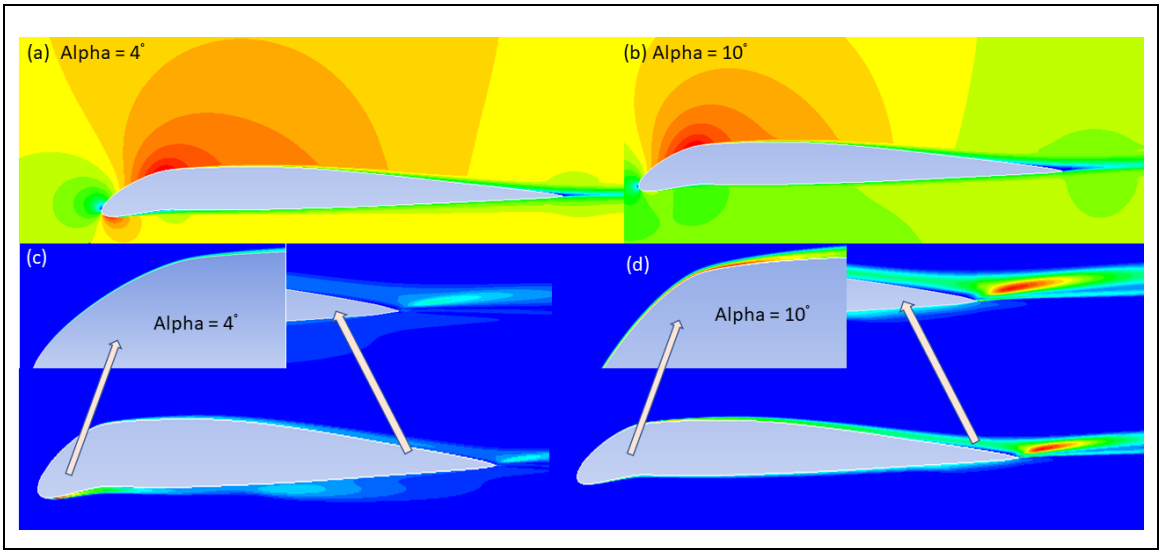

Figure 3.18 Velocity magnitude and turbulent kinetic energy contour plots. (a) Velocity contour lines at low angles of attack such as 4°; (b) Velocity contour lines at low angles of attack such as 10°; (c) the turbulent intensity at a low angle of attack of 4°; (d) the turbulent intensity at a low angle of attack of 10°

3.3.2 Morphing Trailing Edge Optimization

The optimization process defined in Section 3.1 was implemented on the MTE airfoil by using the same two optimization functions defined by Equation (3.1) for drag minimization and by Equation (3.4) for endurance maximization. The optimization of the Morphing Trailing Edge (MTE) airfoil shape for the three flight conditions given in Table 3.5 was performed.

The optimization processes were carried out for two types of MTE control points. In the first type, referred to as Opt. Case I, MTE is a smooth single shape with a morphing starting point and trailing edge end point. The leading edge is not allowed to move, while the trailing edge points are only allowed to move in the vertical direction with respect to the baseline airfoil.

In the Opt. Case II, the MTE is a three-segmented finger-like configuration. The points are outlined to represent the morphing trailing edge starting location, the length of the first segment and the length of the second segment. The morphing location was kept at x/c = 0.60, so that enough space was provided for the actuation mechanism, and which is where its upper and lower limits were given as constraints. The upper bounds and the lower bounds were chosen

to prevent the generation of morphing airfoil shapes with no likelihood of having very good aerodynamic efficiency. XFoil was used as an aerodynamic solver and therefore as a powerful tool that allowed obtaining fast convergence solutions. The results were later validated by the use of a RANS models in Ansys/Fluent solver.

Figure 3.19a illustrates the initial (reference) versus the final (optimized or morphed) airfoil shape, while Figure 3.19b illustrates the convergence trend for the minimum drag optimization function for an optimized airfoil shape with MTE at an angle of attack of 50. It is seen that the graph in Figure 3.19b trends to a constant after some iteration steps, which shows convergence to its optimal solution.

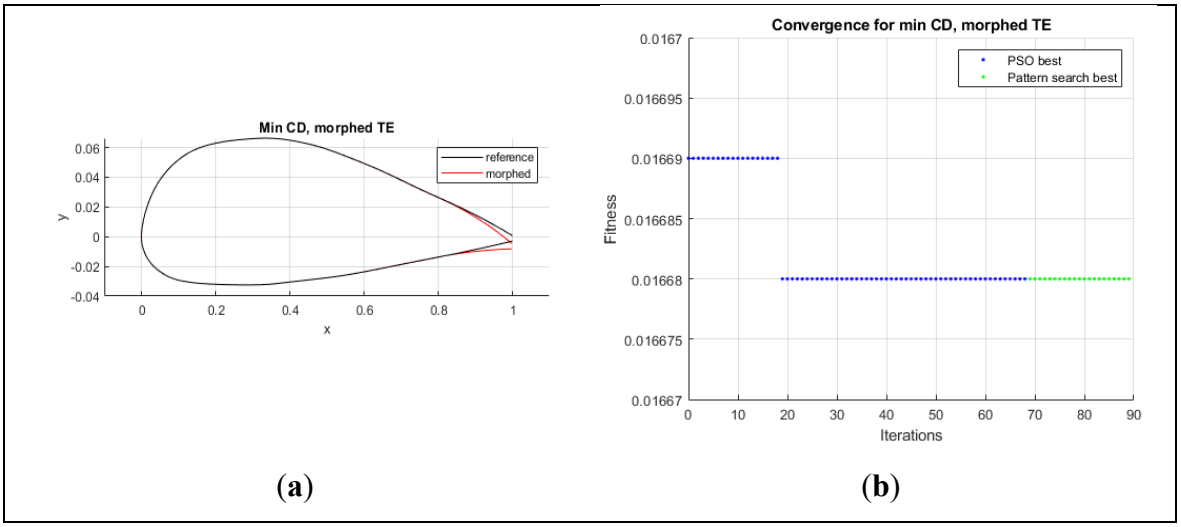

Figure 3.19 Optimized airfoil and convergence history for drag minimization function. (a) the initial (reference) versus the final (optimized or morphed) airfoil shape, (b) the convergence trend for the minimum drag optimization function

The first set of results obtained for MTE for different flight conditions are shown in Figure 3.20a–d. The lift coefficients are presented for the three different flight conditions in the two different cases of Opt. Case I and Opt. Case II. The lift coefficients of the optimized airfoil design have higher values than those of the baseline airfoil; therefore, the optimized shapes produce an improvement of the lift coefficient with respect to the baseline airfoil of up to

almost 26%, as seen in Figure 3.20c for Opt. Case I. In addition, an increase of 8% is obtained for the maximum lift coefficient for the optimized airfoils with respect to the baseline airfoil.

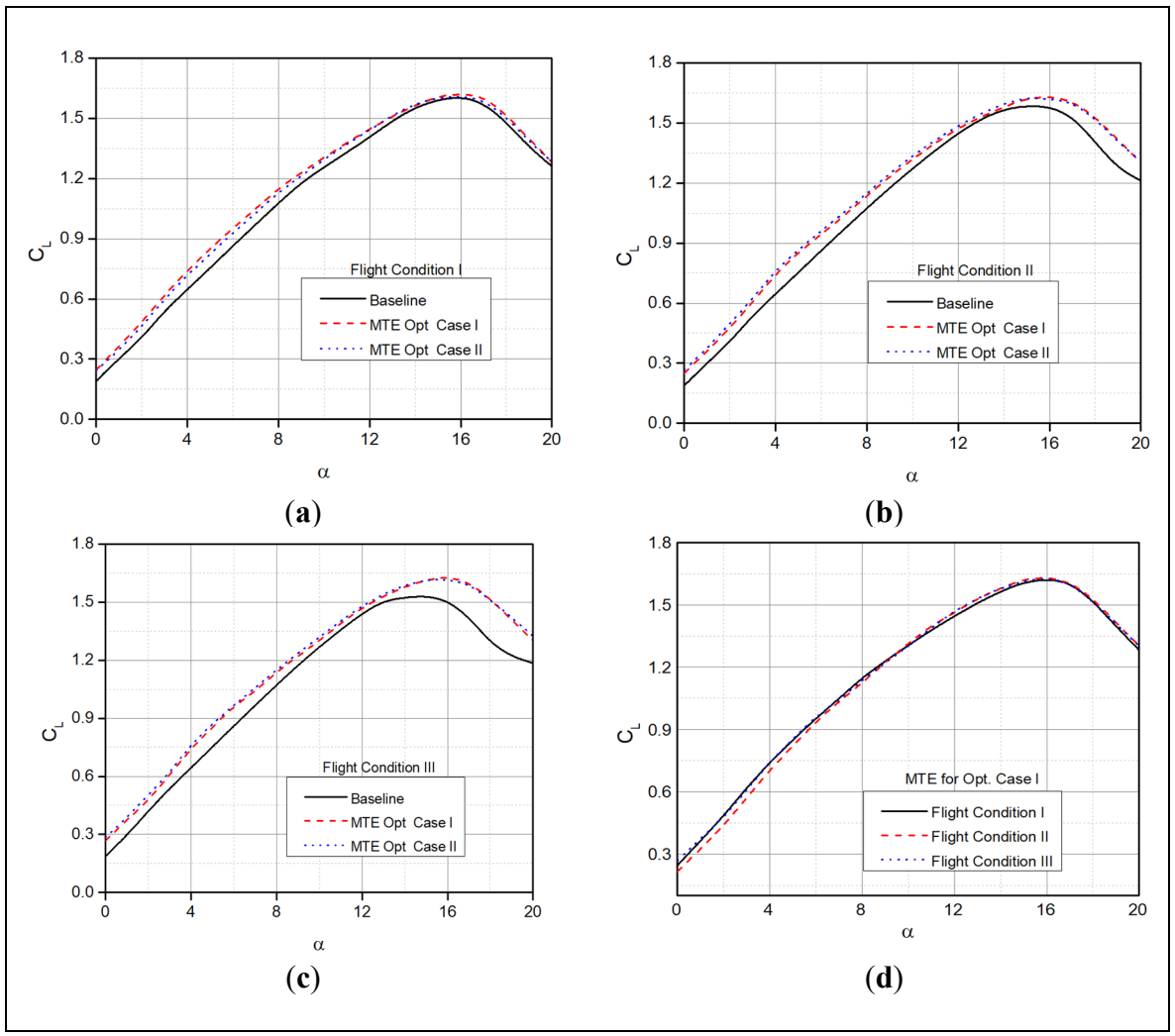

Figure 3.20 Lift coefficients versus angle of attack at two optimized design configurations; (a) the variations of lift coefficients with the angles of attack at Flight Condition I (b) the variations of lift coefficients with the angles of attack at Flight Condition II; (c) the variations of lift coefficients with the angles of attack at Flight Condition III; (d) the lift coefficient variations for all three flight conditions for Opt. Case I

Figure 3.21 presents the evaluation of the lift versus drag variation (polar) of the baseline airfoil and the optimized airfoils for different flight conditions. The increased aerodynamic performance of optimized airfoils for all three flight conditions can be seen in Figure 3.21a–d.

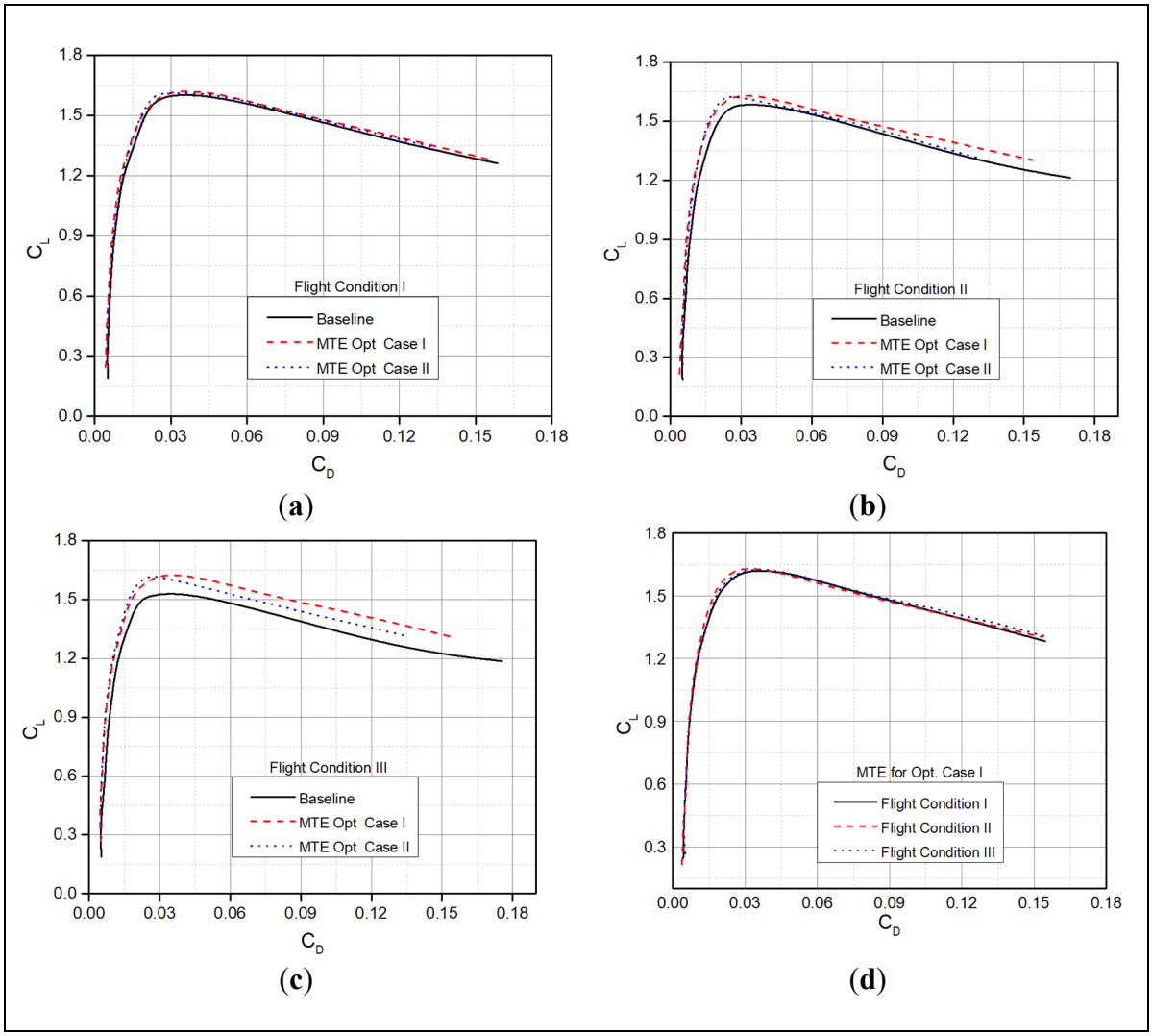

Figure 3.21 Lift coefficients versus drag coefficients for various optimized design configurations. (a) the drag polar at Flight Condition I; (b) drag polar at Flight Condition II; (c) drag polar at Flight Condition III; (d) drag polar for all three flight conditions for Opt. Case I

The pressure coefficients of the MTE airfoil cases at three different flight conditions are shown in Figure 3.22. It can be observed that the suction peaks of the optimized airfoils are higher than those of the baseline airfoil. The MTE airfoil results expressed in terms of "effective camber change" lead to a significant increase in the negative pressure value at the trailing edge surface. The low performance of the baseline airfoil compared to that of the optimized airfoils can be related to the unfavorable pressure gradient on its upper surface near the leading edge,

thereby causing an earlier laminar–turbulent transition of the boundary layer by slightly increasing the drag.

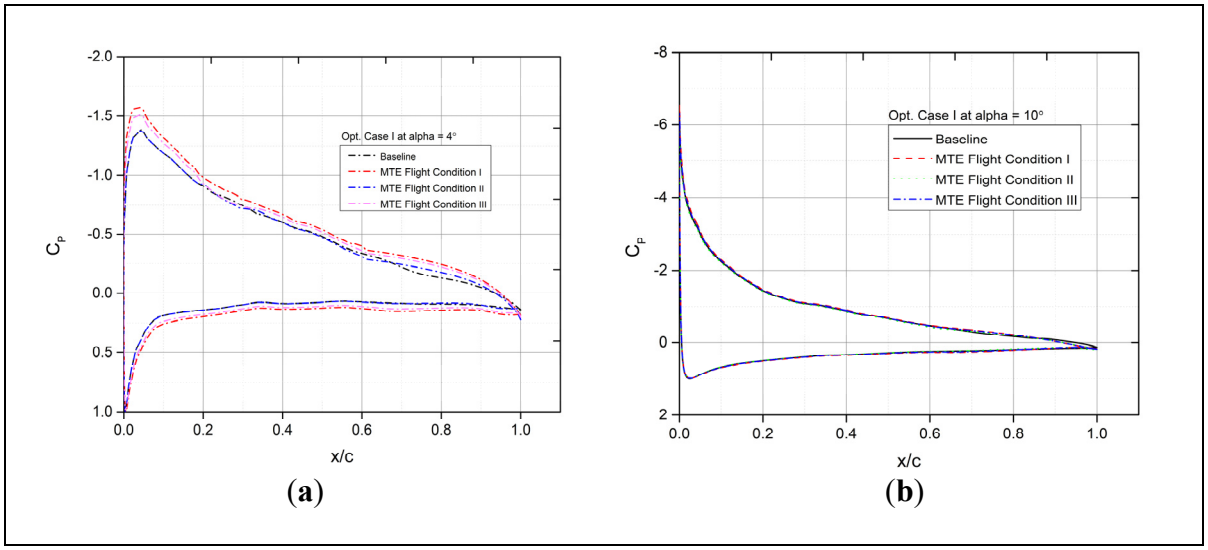

Figure 3.22 Pressure coefficients for different MTE design configurations. (a) at angles of attack of 4°; (b) at angles of attack of 10°

Figure 3.23a illustrates the initial (reference) versus the final (optimized or morphed) airfoil shape, while Figure 3.23b presents the convergence graph of the aerodynamic endurance optimization for the given MTE optimized airfoil while utilizing the PSO algorithm with pattern search. Figure 3.23b shows that the algorithm performs well and improves the airfoil shape to maximize the endurance.

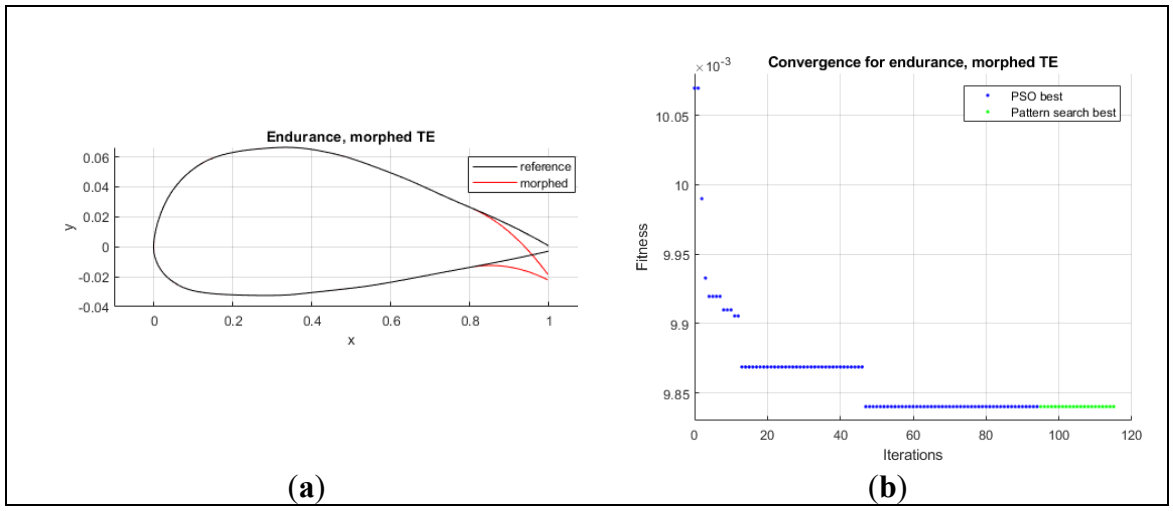

Figure 3.23 Optimized airfoil and convergence history for endurance maximization function. (a) the initial (reference) versus the final (optimized or morphed) airfoil shape; (b) the convergence graph of the aerodynamic endurance optimization

The optimization process using the endurance maximization objective function led to improved endurance performance in the optimized airfoils with respect to the endurance performance of the baseline airfoil. The performance measured in terms of $C_L^{3/2}/C_D$ variation with C_L is shown for three different flight conditions in Figure 3.24. The endurance performance of each optimized airfoil shows a higher value in the MTE Opt. Case I with respect to its baseline airfoil configurations. For the same endurance performance defined by the $C_L^{3/2}/C_D$ ratio, the lift coefficients were found to be 1.17 for the baseline airfoil and 1.45 for the MTE airfoil configuration for the optimized flight condition II, respectively. Furthermore, as seen in Figure 3.24, the efficiency of $C_L^{3/2}/C_D$ increased by approximately 10.25% for flight condition III; this finding indicates the improved endurance performance of the UAS-S45 airfoil.

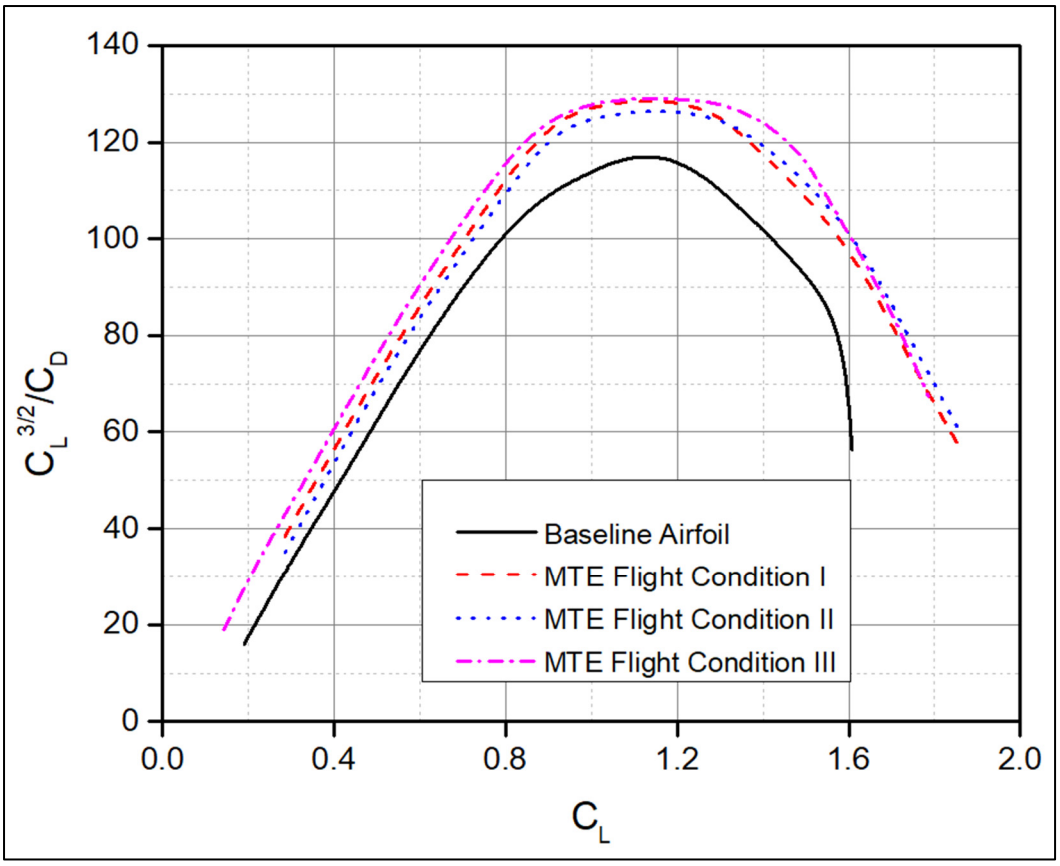

Figure 3.24 Comparison of the endurance performance for baseline and MTE airfoils

The difference between the results obtained by the two objective functions of drag minimization and endurance maximization to obtain optimal airfoil configurations was determined. The optimized airfoil geometrical shapes were obtained for drag minimization and endurance maximization as shown in Figure 3.25. The main difference observed in the airfoil geometries, as shown in Figure 3.25, is that the trailing edge obtained with the drag minimization objective function gave a smaller deflection than the baseline airfoil. Likewise, the endurance maximization objective function requires higher airfoil deflection with a continuous trailing edge.

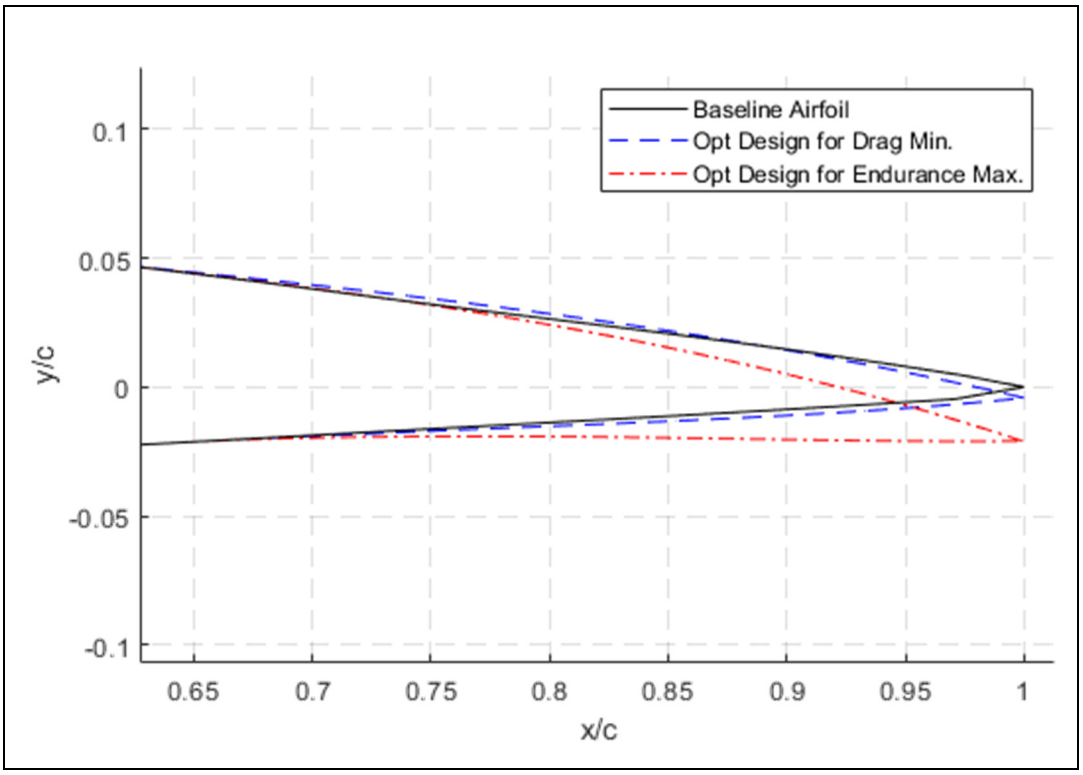

Figure 3.25 Comparison of MTE airfoil shapes based on different performance objectives

The contour plots of the velocity magnitude and of the turbulent kinetic energy are visualized for the baseline airfoil and for the airfoils optimized by the Transition ($\gamma-Re_\theta$) SST turbulence model in Figure 3.26. These contour plots reveal that for a given MTE deflection, larger TE separation regions are found at 4° angles of attack than at 10° angles of attack. Similarly, the vertex of turbulent kinetic energy (TKE) originating from the MTE at an angle of attack of 40° has more strength than the vertex and the angle of attack of 10°. The TKE contour plot of the baseline airfoil at an angle of attack of 4° is approximately comparable to the TKE contour plot of the MTE airfoil at an angle of attack of 10°. Therefore, the MTE-optimized airfoils can provide increased aerodynamics performance with respect to the performance of the original airfoils.

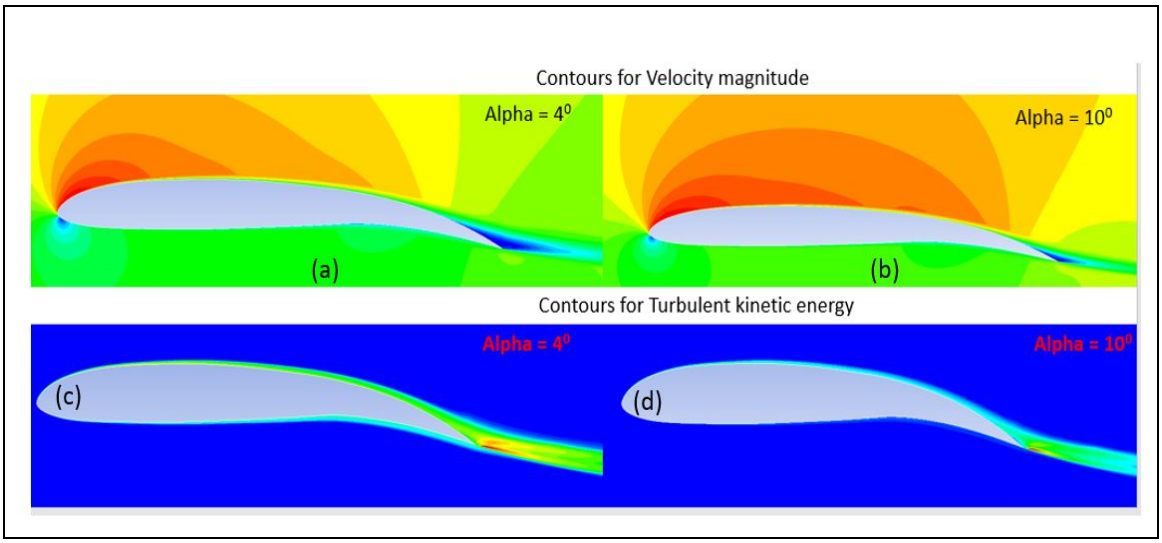

Figure 3.26 Velocity magnitude and Turbulent Kinetic Energy (TKE) contour plots. (a) Velocity contour lines at low angles of attack such as 4°; (b) Velocity contour lines at low angles of attack such as 10°; (c) the turbulent intensity at a low angle of attack of 4°; (d) the turbulent intensity at a low angle of attack of 10°

3.4 Conclusions

This study was conducted to perform aerodynamic optimization of Morphing Trailing Edge (MTE) and Droop Nose Leading Edge (DNLE) airfoils for the UAS-S45 at different flight conditions. A new hybrid optimization technique was chosen by coupling the Particle Swarm Optimization (PSO) with the Pattern Search (PS) algorithms. The optimization function was designed to minimize drag with respect to given constraints such as airfoil lower and upper bounds, as well as to increase endurance in given flight conditions. The Bezier–PARSEC (BP) technique was used to parameterize the baseline airfoil shape, as well as to obtain its various optimized morphing configurations by using different constraints on the morphing of both the Morphing Trailing Edge (MTE) and the Droop Nose Leading Edge (DNLE) of the wing.

Within the aerodynamics optimization framework, the low-fidelity solver XFoil and the high-fidelity CFD solver Ansys Fluent were used. The results obtained using both solvers were compared for their validation. Specifically, the flow transition was predicted using Menter's Transition ($\gamma - Re_\theta$) SST turbulence model. In addition, the optimization framework was done

from an aerodynamics perspective, and therefore, no structural studies were taken into consideration.

Both DNLE and MTE airfoil optimizations were aimed to increase the aerodynamic performance of the UAS-S45 for a wide range of angles of attack. For each of the three considered flight conditions, enhanced aerodynamic efficiency was obtained by optimizing the morphing airfoil design with respect to its UAS-S45 baseline airfoil. The optimization results have shown an increase of lift coefficients in DNLE airfoils until the stall angle of attack and thus a delay in the stall angle. An improvement in the lift coefficient was produced for the DNLE airfoils with respect to the baseline airfoil of up to 21%. In addition, an increase of 9.6% was obtained for the maximum lift coefficient, and the stall angle was also delayed by 3 degrees. Similarly, the aerodynamic performance showed a significant improvement for the MTE configurations. An increase in the maximum lift coefficient of up to 8.13% and of the efficiency of $C_L^{3/2}/C_D$ by 10.25% was obtained, thus indicating an increased endurance performance for the MTE airfoils of the UAS-S45. The delay of the leading-edge separation by use of DNLE airfoils was another interesting result.

The flight conditions were chosen from the UAS-S45 manufacturer Hydra Technology user manual. These conditions do not cover aircraft maneuvers or gust responses. UAS-S45 maneuvers and gust response studies could be done in the future. Other objectives of this morphing optimization study will include the three-dimensional analysis of a UAS-S45 wing with a combined droop nose leading edge (DNLE) and continuous morphing trailing edge (MTE). The improvements at the performance level, such as the typical fuel savings with the optimized morphing concepts for a given flight mission, will also be studied in the future. Based on the aero-structural studies, various configurations will be analyzed, and the internal actuation mechanism will be implemented. Wind tunnel and flight tests could be further performed to validate the optimized UAS-S45 model.

CHAPTER 4

OPTIMIZATION AND DESIGN OF A FLEXIBLE DROOP NOSE LEADING EDGE MORPHING WING BASED ON A NOVEL BLACK WIDOW OPTIMI-ZATION ALGORITHM-PART I

Musavir Bashir [a], Simon Longtin-Martel [b], Ruxandra Mihaela Botez [c] and Tony Wong [d]

[a, b, c, d] Department of System Engineering, École de Technologie Supérieure,
1100 Notre-Dame West, Montréal, Québec, Canada H3C 1K3

Paper published in *Designs*, January 2021.
DOI: https://doi.org/10.3390/designs6010010

Résumé

Une optimisation aérodynamique pour un bord d'attaque déformable de type "Droop Nose" (DNLE) d'un UAV bien connu, l'UAS-S45, est proposée en utilisant un nouvel algorithme d'optimisation intitulé Black Widow (BWO). Cette approche intègre l'algorithme d'optimisation à une méthode de paramétrage CST ("Class Shape Transformation") modifiée pour améliorer les performances aérodynamiques en minimisant la traînée et en maximisant l'endurance dans les conditions de vol de croisière. La technique CST est utilisée pour paramétrer le profil de référence en utilisant des changements de forme locaux pour offrir une flexibilité de la peau du matériel de l'aile pour obtenir diverses configurations de profils déformés optimisées. L'optimisation utilise un algorithme Matlab développé interne (dans notre laboratoire), tandis que les calculs aérodynamiques sont réalisés en utilisant le solveur XFoil avec des critères d'estimation de transition d'écoulement. Ces résultats sont validés avec un solveur CFD en utilisant le modèle de turbulence "Transition ($\gamma-Re_\theta$) Shear Stress Transport (SST) ". Des études numériques ont vérifié l'efficacité de la stratégie d'optimisation et les profils optimisés ont montré une amélioration significative de la performance aérodynamique globale jusqu'à 12.18% de réduction de la traînée par rapport au profil de référence et une augmentation de l'endurance aérodynamique allant jusqu'à 10% pour les configurations de profils optimisées de l'UAS-S45 par rapport à son profil de référence. Ces

résultats indiquent l'importance de la déformation du nez du profil pour améliorer l'efficacité aérodynamique du profil de l'UAS-S45.

Abstract

An aerodynamic optimization for a Droop Nose Leading Edge (DNLE) morphing of a well-known UAV, the UAS-S45, is proposed, using a novel Black Widow Optimization (BWO) algorithm. This approach integrates the optimization algorithm with a modified Class Shape Transformation (CST) parameterization method to enhance aerodynamic performance by minimizing drag and maximizing aerodynamic endurance at the cruise flight condition. The CST parameterization technique is used to parameterize the reference airfoil by introducing local shape changes and providing skin flexibility to obtain various optimized morphing airfoil configurations. The optimization framework uses an in-house MATLAB algorithm, while the aerodynamic calculations use the XFoil solver with flow transition estimation criteria. These results are validated with a CFD solver utilizing the Transition $(\gamma - Re_\theta)$ Shear Stress Transport (SST) turbulence model. Numerical studies verified the effectiveness of the optimization strategy, and the optimized airfoils have shown a significant improvement in the overall aerodynamic performance, by up to 12.18% drag reduction compared to the reference airfoil, and an increase of aerodynamic endurance of up to 10% for the UAS-S45 optimized airfoil configurations over its reference airfoil. These results indicate the importance of leading-edge morphing in enhancing the aerodynamic efficiency of the UAS-S45 airfoil.

4.1 Introduction

Rising fuel prices and increased environmental concerns have driven the aircraft manufacturing industry to set new goals for the future. As a result, operational efficiency is becoming more crucial in future aircraft development. Before the COVID-19 pandemic, air traffic was expected to triple in the next few years, resulting in market demand for around 9000 new regional planes, which would increase global emissions even more (Overton, 2019).

Therefore, it is essential to reduce these emissions by using advanced techniques to improve aircraft performance.

Many methods have been used to improve the aircraft efficiency, notably the wing aerodynamic efficiency. Motivated researchers at the Research Laboratory in Active Controls, Avionics, and AeroServoElasticity (LARCASE) have been working on methods to reduce aircraft fuel consumption (Bashir et al., 2021; R. Botez, 2018a; Dancila et al., 2013; Félix Patrón et al., 2014; Hamy et al., 2016; Khan et al., 2020). Morphing is a way to adapt wings to a variety of flight situations to improve their overall performance. It has the potential to significantly enhance an aircraft's lift, drag, and noise characteristics by improving the flow behavior over the wing by removing unnecessary discontinuities and gaps in its surface. Morphing wing technology could potentially save energy and help reduce greenhouse gas emissions to meet the standards set by the ICAO (Wölcken et al., 2015). Additionally, “morphing” is more practically applied to Unmanned Aerial Vehicles (UAVs) because of their reduced scale, and lower complexity in terms of wing design structure and energy consumption expressed in terms of actuation power (S Ameduri et al., 2020; I Dimino et al., 2020; Noviello et al., 2019). Figure 4.1 shows the leading-edge morphing wing mechanism consisting of flexible skin. Morphing is achieved with compliant hinges connected to a linear actuator to realize the desired optimized airfoil shapes, obtained in a preliminary aerodynamic study.

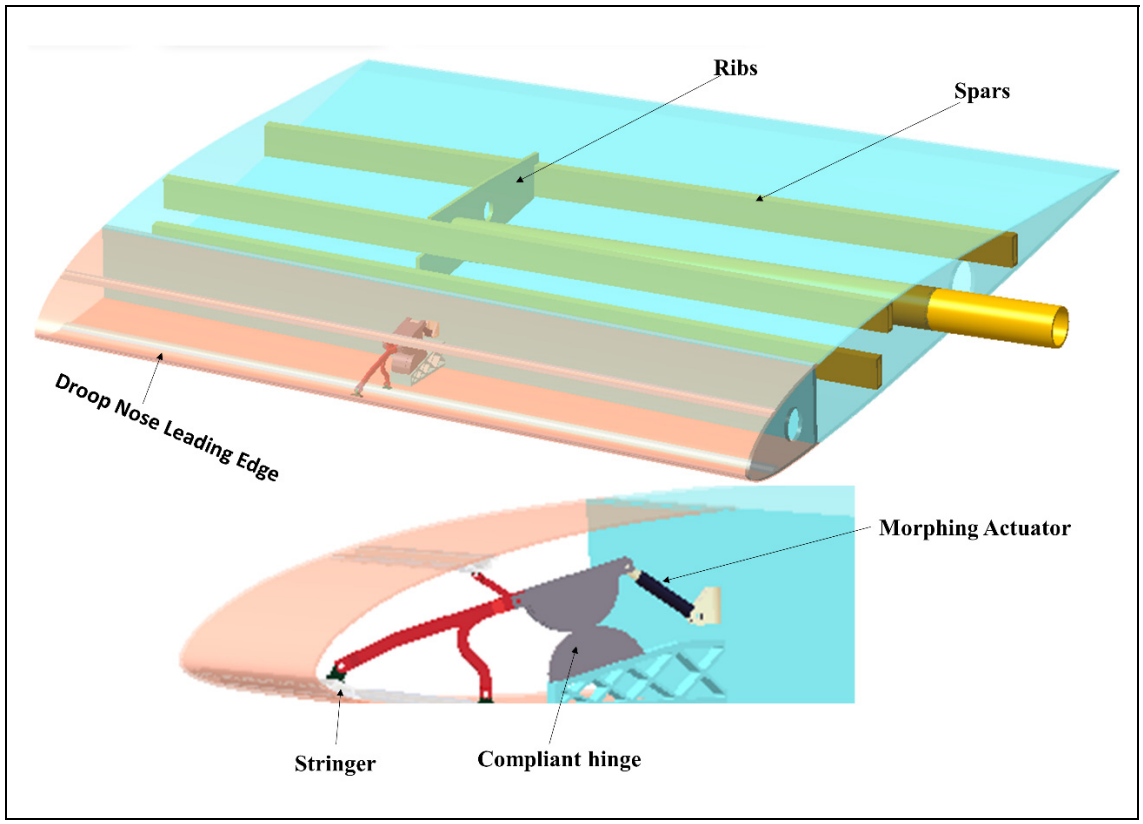

Figure 4.1 DNLE Morphing wing model

Morphing-based wing geometries resulting in very high lift coefficients, reduced drag, and reduced noise may be able to solve some of aviation's present problems (Ruxandra Mihaela Botez et al., 2007; D Communier et al., 2019; Eguea et al., 2020; Sugar-Gabor, et al., 2016; Koreanschi et al., 2017b; Marino et al., 2014a; Pecora, 2021). Furthermore, the development of gapless morphing leading-edge technology enables the improvement of critical performance parameters, such as aerodynamic coefficients, maximum speed, fuel consumption, maneuverability, range, and stability, and therefore a key for attaining the desired environmental goals (Fereidooni et al., 2021; May et al., 2021; Peter et al., 2013; Sodja et al., 2019). Performance can thus be increased by replacing the conventional flaps and slats with morphing wing devices.

Aircrafts with typical wing pivoted flaps and slats, and trailing edge surfaces regulate airflow and hence increase performance. However, when deployed and retracted, these hinged surfaces have several downsides. Noise, turbulence, and increased drag can all be caused by openings

between the high lifting surface and the wing (Burnazzi et al., 2014; Kintscher et al., 2011; Y. Li et al., 2013; Moens, 2019).

A leading-edge morphing device is a gapless flexible droop nose capable of undergoing significant shape and curvature transformations. The use of this morphing device is essential for producing flow laminarization. When compared to standard high-lift configurations like leading-edge slats, the gap-less flexible leading-edge is unvarying with the rest of wing without a step or a slot and offers increased stability. In addition to the aerodynamic benefits at high-speed flight conditions, this technology can result in significant performance improvements when is used in low-speed conditions, such as take-off or landing (Moens, 2019).

Most studies have focused on morphing technology implemented by retrofitting current aircrafts with new devices, such as morphing leading and trailing edge systems (Arena et al., 2018; Carossa et al., 2016; Malik et al., 2021; Yu et al., 2021). However, aerodynamic optimization is also important in the definition of morphing shapes. Airfoil shape parameterization, optimization algorithms, and airfoil design analysis are all part of aerodynamic shape optimization. The shape parameterization method has a significant impact on the results of the optimization. Many studies have shown that the choice of shape parameterization technique strongly influences the solution accuracy, robustness, and computational time of the overall optimization process (Manas Khurana et al., 2008b). Some well-known techniques for geometrical parameterization are presented in the literature (Manas Khurana et al., 2008b; Trad et al., 2020). These methods have the disadvantages of not using airfoil shape parameters, requiring a large number of design variables, and frequently producing erroneous shapes for an airfoil's leading and trailing edges.

The use of polynomial-based functions, such as PARSEC (Della Vecchia et al., 2014) and Class Shape Transformation (CST) (Kulfan, 2010) contributed to overcome some of these constraints. The parameters employed in the PARSEC approach are closely related to those of the airfoil shape (e.g., thickness, curvature, maximum thickness, and abscises). They provide the designer with a realistic picture of the design. The geometry definition must be used

together in an optimization technique, that takes the airfoil parameterization into account. Another novel approach of parameterization, known as Class Shape Transformation (CST), is a highly effective parameterization method thanks to its simplicity, resilience, and capacity to categorize the aerodynamic shape in a variety of configurations. It is capable of generating a diverse range of aerodynamic shapes using only a few parameters.

The numerical optimization study on the UAV drooped wing concept focuses on the implementation of novel optimization algorithms and parameterization techniques. It will be interesting to see if the new optimization algorithm morphs the leading edge of the airfoil while ensuring enhanced aerodynamic performance. Using a morphing Droop Nose Leading Edge (DNLE) on a fixed-wing UAV will provide significant aerodynamic benefits, as UAVs frequently lack high lifting surfaces. The optimization also allows for reshaping the reference wing shape, improving UAV flight performance in all design phases. This modification enhances wing aerodynamics by allowing numerous external shapes to find the one that best suits the aerodynamic needs in particular flight conditions.

This paper investigates suitable methods for the aerodynamic design of a Droop Nose Leading Edge (DNLE) morphing by employing modified Class Shape Transformation (CST) for the aerodynamic shape optimization. The aerodynamic design optimization of a morphing airfoil is performed using the novel Black Widow Optimization (BWO) algorithm. This work is part of the LARCASE Morphing Wing project, which addresses methods for the UAS-S45 optimization.

4.2 Bibliographical Review

A wide range of concepts used for the morphing wing design are available in the literature. Research on this topic began in the United States in 1973, when Boeing presented an advanced variable–camber wing wind tunnel test in the NASA's transonic wind tunnel (Boeing, June 1973). Boeing engineers aimed to integrate a device capable of altering wing curvature via an automated control system onboard a military aircraft in the mid-1980s.

NASA, in partnership with the US Air Force, launched the Advanced Fighter Technology Integration (AFTI)/F–111A Aardvark project (Bonnema et al., 1988; R Decamp et al., 1984; Smith, 1992). Li et al. (Li et al., 2018) summarized the most well-known examples of morphing concepts and methods for modeling and analyzing morphing wings. Flexsys Inc. (Kota et al., 2008; Kota et al., 2009) published work on smooth wing aerodynamics by suggesting a functional, seamless, hinge–free morphing trailing and leading edges method for wing adaptation to changing flying conditions. It was validated in flight on a NASA Gulfstream aircraft during an extended flight.

Numerous universities and research institutions in Europe have also performed research on leading-edge and trailing-edge morphing. As part of the Adaptive Wing project (ADIF) and SmartLED initiatives, Monner (HP Monner et al., 2000; Hans Monner et al., 2009) contributed significantly to the design of leading-edge morphing concepts. Following Monner's work, several EU-funded projects, such as SADE (Schweiger et al., 2002) and SARISTU (Concilio et al., 2021; Liauzun et al., 2018), were completed, in which a full-scale wing section characterized by a flexible and compliant skin enabled the achievement of smoothed and significant leading-edge camber variations, whose performance was validated through wind tunnel testing.

One of the EU-funded Clean Sky 2 projects on Natural Laminar Wings were focused on the conceptual design of a morphing Leading Edge capable of satisfying high lift requirements (De Gaspari et al., 2019). In this project, researchers worked on the skin structure, the internal compliant structure, and a possible actuation mechanism. A morphing leading edge was presented as a flexible alternative to rigid and permanent ribs having a high degree of stiffness. The flexible skin plates were made by merging numerous plates with revolute joints molded to the airfoil section's shape. The skin was allowed to move relative to the skin joint by using sliding joints and stringers to maintain rigidity.

As part of the “Smart Leading-Edge Device” (SmartLED) project (Kintscher et al., 2011), Monner attempted to develop another cutting-edge morphing concept in partnership with DLR and EADS. As an alternative to the A380's droop nose mechanism, this project proposed a smart leading-edge device for a maximum angle of 20 degrees.

The Leading-Edge Actuation Topology Design and Demonstrator (LeaTop) project (Sodja et al., 2019) aimed to create a seamless morphing leading edge that could replace the slats, that have been employed as leading-edge high lift devices. The boundary layer could change from laminar to turbulent following to a minor discontinuity in the wing's surface by increasing the wing's overall drag. However, when the slats were deployed during landing, a gap between the slats and the wing occurs. This gap could cause considerable aerodynamic noise. A seamless morphing leading-edge addressed each of these difficulties concurrently.

Our team at the Research Laboratory in Active Controls, Avionics, and Aeroservoelasticity (LARCASE) collaborated on a morphing wing project called "Laminar Flow Improvement on an Aeroelastic Research Wing" from 2006 to 2009 the CRIAQ MDO 7.1 project (Koreanschi, Oliviu, et al., 2016; Koreanschi, Sugar-Gabor, et al., 2016a). The "Morphing Architectures and Related Technologies for Wing Efficiency Improvement - CRIAQ MDO 505" project was also completed at our LARCASE in the continuation of the CRIAQ 7.1 project. The achievements of the Canadian-Italian CRIAQ MODO 505 project are mentioned in various publications (Grigorie et al., 2012; Andrei Vladimir Popov et al., 2010). Koreanschi et al. (Koreanschi et al., 2017a) used the two-dimensional CFD method to study a morphing wingtip, and the results were validated by wind tunnel testing and numerical simulation data. (Koreanschi, Sugar-Gabor, et al., 2016b) developed a morphing wing equipped with a flexible upper surface and actuated aileron and they have found that CFD findings and an experimental wind tunnel tests for a morphing wing had a good agreement in the pressure distribution.

The following sections present our work, including an extensive literature review. An optimization framework outlines the overall optimization approach in Section 3, where the parameterization technique is done in order to obtain the optimal aerodynamic shapes, as well

as the computational solvers for calculating aerodynamic coefficients and the optimization algorithms employed. The optimization framework also includes the two objective function formulations ("drag minimization" and "endurance maximization"). The results obtained using these solvers and algorithms for the UAS-S45 optimized designs are compared with the reference UAS-S45 model results in Section 4. Our conclusions and recommendations for future work are presented in Section 4.5.

4.3 Optimization Framework Methodology

We use an optimization framework to define the Droop Nose Leading Edge (DNLE) morphing concept. This method requires the definition of the objective function, parametrization of the geometric shape, and an optimization algorithm. Figure 4.2 illustrates the optimization strategy employed in this investigation. It involves generating airfoil form variables using CST while conforming to geometric constraints. The outline used two solvers, XFoil and Ansys Fluent, and a unique optimization algorithm based on the Black Widow Optimization (BWO). Subsections 3.1, 3.2, 3.3, and 3.4 describe the optimization technique. A comparative methodology was implemented in some of our other works (Bashir, Longtin Martel, et al., 2022a, 2022b).

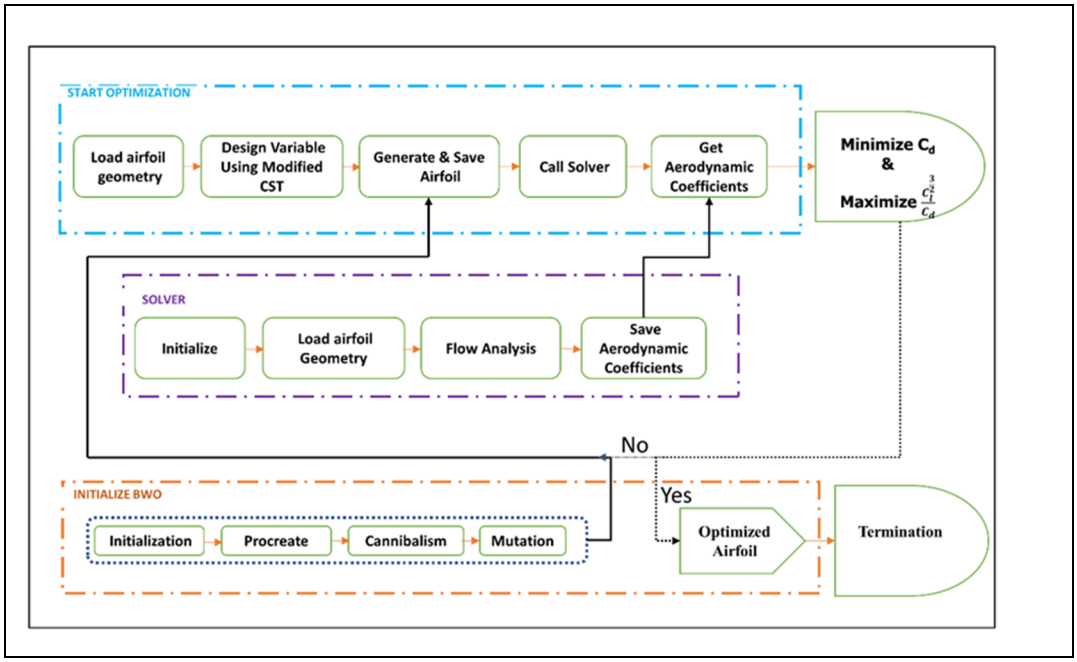

Figure 4.2 Flow chart for the code for airfoil shape optimization

The core optimization strategy is to write and execute a typical optimization loop in MATLAB. This optimization is launched by allowing the parametrization and solver information to be used to generate airfoil forms. The first block interfaces with both the solver and the BWO algorithm, allowing the modified CST to be used to illustrate airfoil shapes. Input is the airfoil's geometry, which is then used to compute the aerodynamic coefficients for the provided boundary conditions ANSYS Fluent, a commercial CFD programme, was used to validate the flow analysis. Geometric and aerodynamic limits are kept in the evaluation blocks, resulting in a penalised fitness value for an objective function. To improve the answer, the fitness values are examined and the decision variables are modified. In the loop, a Black Widow Optimization (BWO) method is applied until the optimal airfoil with the specified fitness cost is produced.

4.3.1 CST airfoil Parameterization

The airfoil parameterization is based on a modified class shape transformation (CST) method, whose equations are based on Kulfan's (Kulfan, 2010) work. First, the generalized CST equations are described as they are applied to the airfoil. Next, the upper and lower surfaces of y coordinates are defined individually, using a class function $C\left(\frac{x}{c}\right)$ and a shape function $S\left(\frac{x}{c}\right)$.

$$y_{upper} = C_{N_2}^{N_1}\left(\frac{x}{c}\right) S_{upper}\left(\frac{x}{c}\right) + y_{upperLE}\left(\frac{x}{c}\right) \tag{4.1}$$

$$y_{lower} = C_{N_2}^{N_1}\left(\frac{x}{c}\right) S_{lower}\left(\frac{x}{c}\right) + y_{lowerLE}\left(\frac{x}{c}\right) \tag{4.2}$$

where $\frac{x}{c}$ and $\frac{y}{c}$ are defined in percentage of the chord of the aircraft (therefore, $\frac{x}{c}$ has a value between 0 and 1) and N_1 and N_2 are 0.5 and 1, respectively.

The class function is defined as in equation (4.3);

$$C_{N_2}^{N_1}\left(\frac{x}{c}\right) = \left(\frac{x}{c}\right)^{N_1}\left(1-\frac{x}{c}\right)^{N_2} \tag{4.3}$$

The airfoil given by the class function is a primary airfoil and will be a basis for further airfoils by being multiplied by the value of the shape function. The class function values are shown in Figure 4.3.

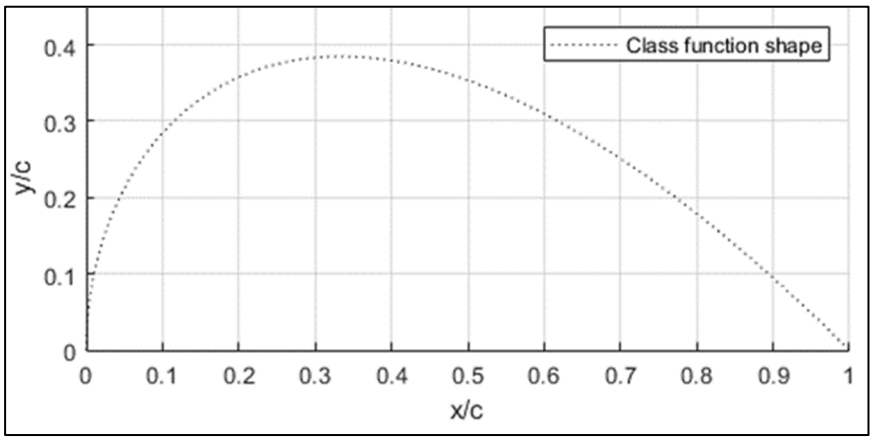

Figure 4.3 Class function shape with $N_1 = 0.5$ and $N_2 = 1$

The shape functions produce the specific shapes of the airfoil. The function is composed of various weights $W_{upper}(i)$ and $W_{lower}(i)$ defined as a real value, and is dependent of i, inside a Bernstein polynomial [55]. The equations for the upper and lower surfaces differ:

$$S_{upper}\left(\frac{x}{c}\right) = \sum_{i=0}^{N_{upper}} S_{upper}\left(\frac{x}{c}, i\right) = \sum_{i=0}^{N_{upper}} W_{upper}(i)\, B_{upper} \tag{4.4}$$

$$S_{lower}\left(\frac{x}{c}\right) = \sum_{i=0}^{N_{lower}} S_{lower}\left(\frac{x}{c}, i\right) = \sum_{i=0}^{N_{lower}} W_{lower}(i)\; B_{lower} \tag{4.5}$$

where

$$B_{upper} = K_i^{N_{upper}}\left(\frac{x}{c}\right)^i\left(1-\frac{x}{c}\right)^{N_{upper}-i} \tag{4.6}$$

and

$$B_{lower} = K_i^{N_{lower}} \left(\frac{x}{c}\right)^i \left(1 - \frac{x}{c}\right)^{N_{lower}-i} \tag{4.7}$$

are the Bernstein polynomials and K_i^N is the binomial coefficient K:

$$K_i^N = \frac{n!}{i!\,(n-i)!} \tag{4.8}$$

in which i is the value of the Bernstein polynomials' order.

The following graph shows both each individual S(x,i) value for i, as well as their sum to get S(x), when using the weights W(i) for the UAS S-45's airfoil (Figure 4.4). Those weights were determined by matching the S-45's airfoil to the weights that best fit the airfoil using Matlab's nonlinear programming solver.

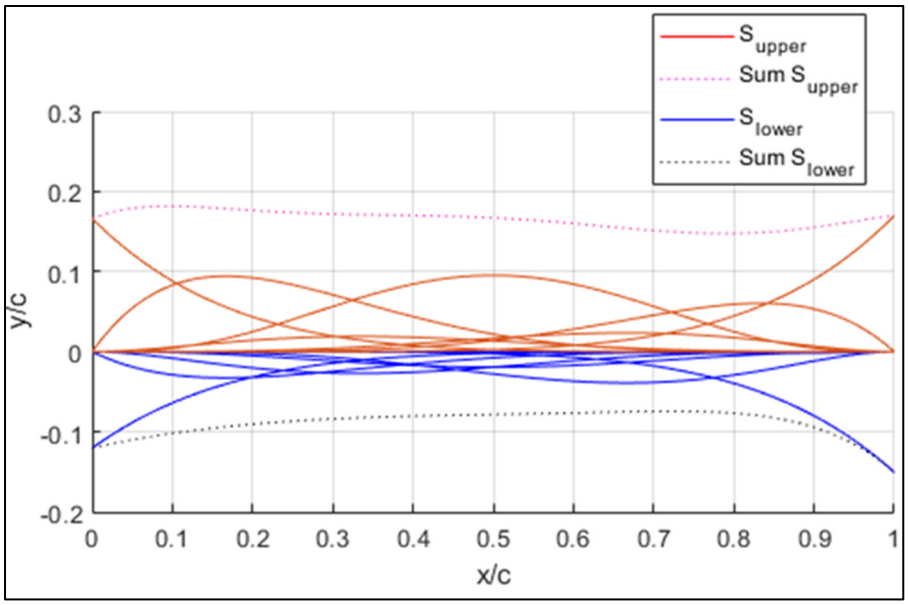

Figure 4.4 Shape function values for i=0 to 6 and total shape function values

When *C(x)* and *S(x)* are multiplied, and assuming both $y_{uppper_{LE}}$ and $y_{lower_{LE}} = 0$, the airfoil shapes shown in Figure 4.5 are obtained.

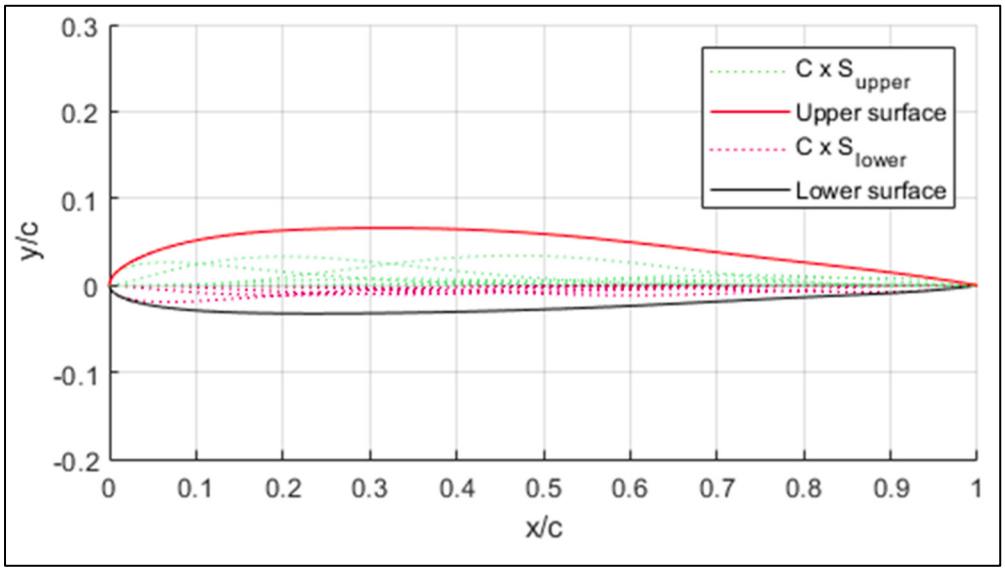

Figure 4.5 Airfoil shape obtained from the product of class and shape function $C(x)$ and $S(x)$

Most typical CST LE morphing can only occur by adding a y-axis deflection to control points and may have a constraint to maintain a constant skin length. However, that y axis deflection neglects the x-axis deflection that occurs in a droop nose leading edge morphing.

There is also a need to constraint the droop nose leading edge morphing. Therefore, new parameters are added to impose where the deflection of the LE on the wing ($Morph_{length}$) begins and impose a specific deflection angle (θ). The approach taken assumes that there is an axis located on the $\frac{x}{c}$ axis that serves as a basis for the morphing. An arc that is a tangent to the $\frac{x}{c}$ axis on one side and tangent to the deflection angle on the other side begins at $\frac{x}{c} = Morph_{length}$. The length of the arc is that of $Morph_{length}$. The skin keeps its relative position to the closest point on the morphing mechanism, meaning that it keeps the same distance that is perpendicular to the mechanism's arc. Figure 4.6 illustrates the setup by showing the axis and arc's neutral unmorphed position and then its variation of $\frac{y}{c}$ with $\frac{x}{c}$ while morphing occurs.

For example, the Morph 0.2, 30° figure has it's morphing begin at $\frac{x}{c} = 0.2$, and the tangent of the end of the arc that is not on $\frac{y}{c}$=0 has a 30° angle to the $\frac{x}{c}$ axis.

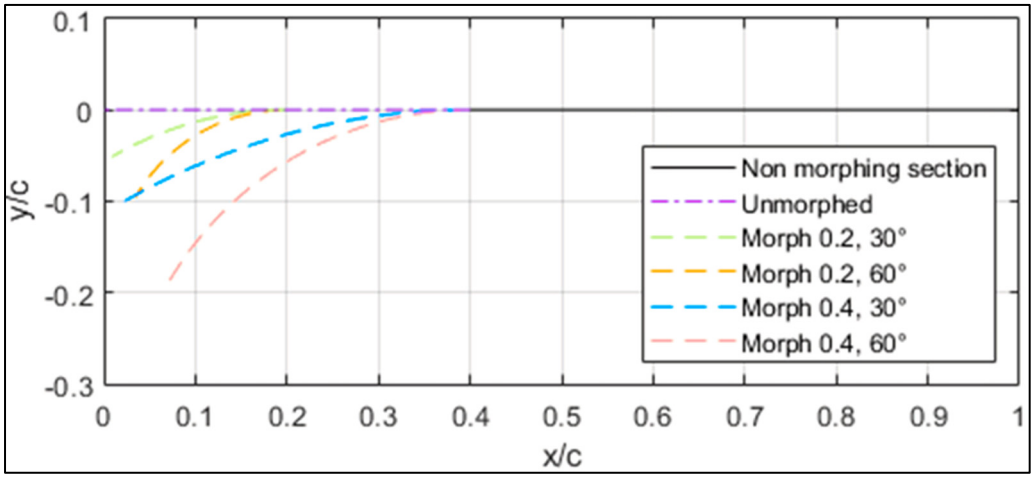

Figure 4.6 Deflection arcs for different morphing conditions

To calculate morphing position with the CST parameterization, the morphing process is done in two steps, the first process is considering y/c translation, and the second is considering $\frac{x}{c}$ translation. The translation itself is the sum of both the translation from the mechanism and the translation from the skin to the mechanism that is produced by the rotation of the mechanism. Figure 4.7 depicts the translation, with both axes from the deflection arc and skin movement in relation to the deflection arc. In (a), the deflection arc begins at $\frac{x}{c} = 0.4$, and the tangent to the free end of the arc is 60° from the $\frac{x}{c}$ axis. The movement of the airfoil skin follows the movement of the deflection arc, with both a $\frac{x}{c}$ and $\frac{y}{c}$ translation that follow the relative position on the arc from the unmorphed position. In (b), the relative skin movement from the arc is illustrated. While in the unmorphed position, the relative skin position is right above the selected $\frac{x}{c}$ axis point, when the arc has an angle with the $\frac{x}{c}$ axis, the relative skin position is changed, and is perpendicular to the tangent of the respective arc position, at the same distance as the respective $\frac{y}{c}$ distance between the relative skin position and $\frac{x}{c}$ axis. This translation will be most prominent when the difference between the $\frac{x}{c}$ axis and relative skin position are farther

on the unmorphed airfoil, and when the angle between the tangent of the arc and the $\frac{x}{c}$ axis are higher. When $\frac{x}{c} = \text{Morph}_{\text{length}}$, there is no difference in relative skin position since the tangent of the arc is 0°. When the unmorphed $\frac{x}{c} = 0$, there is no relative skin position difference since the distance between the relative skin position and $\frac{x}{c}$axis is 0 since it's the tip of the leading edge.

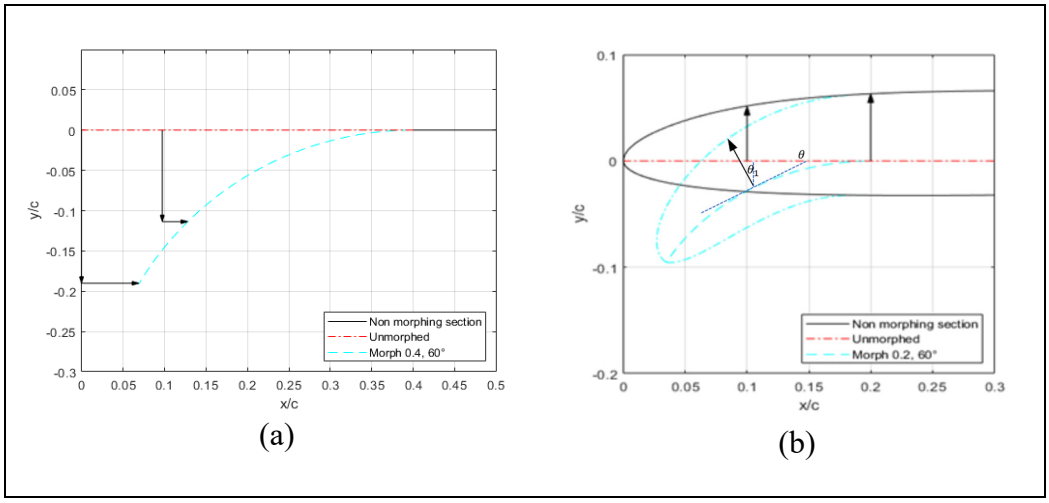

Figure 4.7 Translation from the deflection arc and relative skin position to the deflection arc

The equation to determine the arc center is:

$$\left(\frac{x}{c} - \frac{x}{c_{arc}}\right)^2 + \left(\frac{y}{c} - \frac{y}{c_{arc}}\right)^2 = \frac{y^2}{c_{arc}} \tag{4.9}$$

where $\frac{x}{c_{arc}}$ and $\frac{y}{c_{arc}}$ are the center position of the arc, and assuming $\frac{y}{c_{arc}}$ is the radius of the arc, and when using the fact that the center of rotation will be just under the beginning of the morphing section and that we know the position at which the morphing begins, we use

$$\frac{x}{c_{arc}} = Morph_{length} \tag{4.10}$$

so that the values for x/c and y/c can be calculated when $\frac{y}{c_{arc}}$ is known.

Since we can also know the arc length, as its value is $Morph_{length}$, it is possible to determine any other point on the arc. The Θ value is the same as the arc angle value. Therefore, since

$$Arclength = \Theta * r \tag{4.11}$$

$$Morph_{length} = Arclength \tag{4.12}$$

$$\frac{y}{c_{arc}} = r \tag{4.13}$$

$$\frac{y}{c_{arc}} = \frac{Morph_{length}}{\Theta} \tag{4.14}$$

Now the values of any $\left(\frac{x}{c_{arc}}, \frac{y}{c_{arc}}\right)$ point coordinates can be determined. The arc lengths $(arcl)$ from the $Morph_{length}$ position needed to obtain the angle of the morphing section are used to determine the $\frac{x}{c}$ and $\frac{y}{c}$ translared.

Since each skin section is attached to the closest section of the $\frac{x}{c}$ axis, it can be assumed that if the skin position is $\frac{x}{c_{skin}}$ and $\frac{y}{c_{skin}}$, and so the closest distance between the skin and the $\frac{x}{c}$ axis, y_{dist} is given as:

$$\frac{x}{c_{trans}} = \frac{x}{c_{trans1}} + \frac{x}{c_{trans2}} \tag{4.15}$$

$$\frac{y}{c_{trans}} = \frac{y}{c_{trans1}} + \frac{y}{c_{trans2}} \tag{4.16}$$

Where x_{trans1}, x_{trans2},y_{trans1} and y_{trans2} are the respective $\frac{x}{c}$ and $\frac{y}{c}$ translation from the deflection arc (1) and the relative skin movement in relation to the arc (2) which are included independently to the upper and lower surfaces. Finally, the following equation is obtained:

$$y_{upper} = C_{N_2}^{N_1}\left(\frac{x}{c}\right) S_{upper}\left(\frac{x}{c}\right) + y_{trans\ upper}\left(\frac{x}{c}\right) | \frac{x}{c} < Morph_{length} \quad (4.17)$$

$$y_{lower} = C_{N_2}^{N_1}\left(\frac{x}{c}\right) S_{lower}\left(\frac{x}{c}\right) + y_{trans\ lower}\left(\frac{x}{c}\right) | \frac{x}{c} < Morph_{length} \quad (4.18)$$

$$y_{upper} = C_{N_2}^{N_1}\left(\frac{x}{c}\right) S_{upper}\left(\frac{x}{c}\right) | \frac{x}{c} \geq Morph_{length} \quad (4.19)$$

$$y_{lower} = C_{N_2}^{N_1}\left(\frac{x}{c}\right) S_{lower}\left(\frac{x}{c}\right) | \frac{x}{c} \geq Morph_{length} \quad (4.20)$$

To translate the x, the function is no longer a function of $\frac{x}{c}$ but instead a function of $\frac{x}{c} - x_{trans}\left(\frac{x}{c}\right)$ while $\frac{x}{c} < Morph_{length}$ for a fixed Θ and a fixed $Morph_{length}$.

$$y_{upper} = C_{N_2}^{N_1}\left(\frac{x}{c} - X_{tu}\right) S_{upper}\left(\frac{x}{c} - X_{tu}\right) + y_{trans\ upper}\left(\frac{x}{c} - X_{tu}\right) | \frac{x}{c} - X_{tu} < Morph_{length} \quad (4.21)$$

$$y_{lower} = C_{N_2}^{N_1}\left(\frac{x}{c} - X_{tl}\right) S_{lower}\left(\frac{x}{c} - X_{tl}\right) + y_{trans\ lower}\left(\frac{x}{c} - X_{tl}\right) | \frac{x}{c} - x_{tl} < Morph_{length} \quad (4.22)$$

where

$$X_{tu} = x_{trans\ upper}\left(\frac{x}{c}\right) \quad (4.23)$$

$$X_{tl} = x_{trans\ lower}\left(\frac{x}{c}\right) \quad (4.24)$$

4.3.2 Black Widow Optimization (BWO)

Several nature inspired algorithms by biological systems, including particle swarm optimization (PSO), bee colony optimization (BCO), ant colony optimization (ACO), and genetic algorithm (GA) have been used for airfoil optimization (Sugar-Gabor, et al., 2014; Koreanschi et al., 2017b; Koreanschi, et al., 2016). Each of these methods optimizes globally. Recent work has proposed the use of Black Widow Optimization (BWO) to solve numerical

optimization problems (Hayyolalam et al., 2020). This algorithm was inspired by the black widow spider's life cycle. The black widow spider is well-known for its unusual mating behaviour, which served as the inspiration for the algorithm utilized in this study. Consider it a combination of evolutionary and swarm techniques. The BWO includes a phase that is unique, called "cannibalism." This phase has the advantage of excluding species with inadequate fitness from the circle, ensuing in algorithms converge faster. When compared to the other studied algorithms, the suggested BWO algorithm is capable of avoiding local optima. This algorithm makes no use of additional information, such as the objective function's gradient values.

The BWO algorithm is well-known for its staged implementation (Procreate, Cannibalism, and Mutation), as well as its various parameters such as procreating rate, cannibalism rate, and mutation rate. The more these parameters alter, the greater the possibility of jumping out of a local optimum and, thus, the greater the ability to explore the search space globally. This results in the equilibrium of these two stages of exploitation and exploration. This Procreate option can be used to regulate the transition of search agents from the global stage to the local stage, as well as to direct them toward the optimal solution. According to the literature, the procreate step aids the BWO algorithm solution in overcoming local optima by utilizing a large number of search agents to attain the global optima (Hayyolalam et al., 2020).

Black Widow Optimization (BWO) is a fascinating biomimetic for resolving difficult numerical optimization problems (Hayyolalam et al., 2020). BWO, like other evolutionary algorithms, incorporates conditions that emulate natural evolutionary processes such as selection, reproduction, and mutation. The flowchart in Figure 4.8 illustrates the BWO's primary steps in a concise manner.

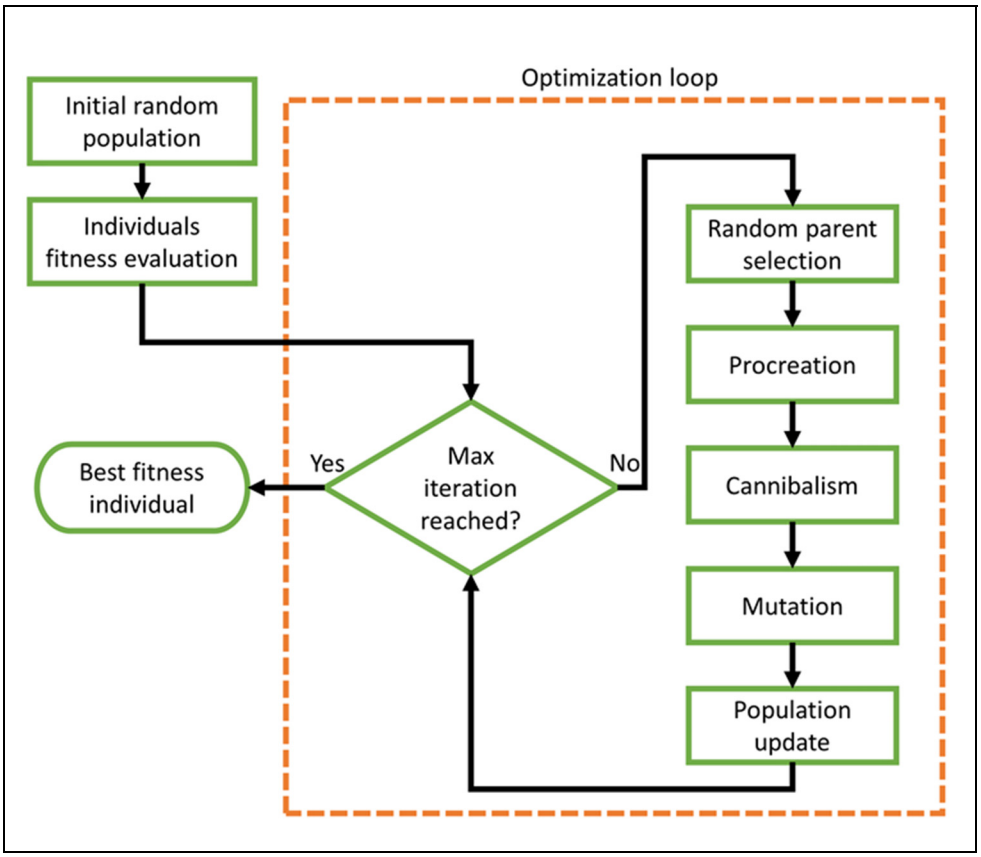

Figure 4.8 Black Widow Optimization (BWO) algorithm

The following are brief summaries of the BWO's primary steps:

In initial population phase, each spider represents a potential solution. These initial spiders, in pairs, try to reproduce the new generation. Female black widow eats the male during or after mating. As follows, this section of population can be defined as follows:

$$widow = (y_1, y_2 \dots, yPop_{var}) \tag{4.25}$$

where Pop_{var} is the optimization problem's dimension. Pop_{var} are also the number of threshold values the algorithm must obtain. Each set's fitness function f determines a widow's fitness given by $(y, y_2, \dots, yPop_{var})$. The widow fitness f(widow) can thus be written as:

$$Fitness = f(widow) = f(y_1, y_2 \dots, yP_{var}) \tag{4.26}$$

The initial spider population is used with the candidate matrix $(M_{pop} \times M_{var})$.

In Procreate phase, the new generations are produced by mating, in which only stronger offsprings survive. In nature, each pair mates in its own web, independently of the others. In reality, each pairing produces around 1000 eggs, but only a few of the spider infants survive. If an array called gamma contains random numbers, then children are formed by utilizing the following Equations 4.27 and 4.28, the offspring is formed.

$$x_1 = \gamma \times y_1 + (1 - \gamma) \times y_2 \quad (4.27)$$

$$x_2 = \gamma \times y_2 + (1 - \gamma) \times y_1 \quad (4.28)$$

where the parents are denoted by y_1 and y_2 and the offspring by x_1 and x_2. The process is reiterated Pop_{var} times. The fitness value is stored by adding the parents and offsprings. A cannibalism rating (CR) according to which the number of survivors is determined is set. Based on the CR, some of the best individuals are added to the newly created population.

In Cannibalism, there are three types: sexual, sibling, and cannibalism where newborn spiders eat their mothers. This process is then analyzed and documented in proportion to the number of survivors, yielding a cannibalism rating. These fitness ratings help distinguish weak from robust offspring.

In Mutation stage, the population is randomly picked from the population to be mutated throughout the mutation process. Each of the chosen solutions randomly flips two elements of the array. By integrating all populations, the new population is evaluated and stored. This procedure is used to determine the matrix's optimal widow.

Figure 4.9 illustrates the convergence plots of the cost function versus the number of iterations for the GA, PSO, and BWO algorithms. According to the convergence plot obtained from optimizing an airfoil for drag minimization at the same flight conditions and design variables

for all these algorithms, The GA method requires 14 iterations to attain the global minimum value of 0.019, the PSO algorithm requires 18 iterations, and the BWO algorithm requires only 11 iterations. As a result, the BWO algorithm surpassed the GA and PSO algorithms in terms of performance.

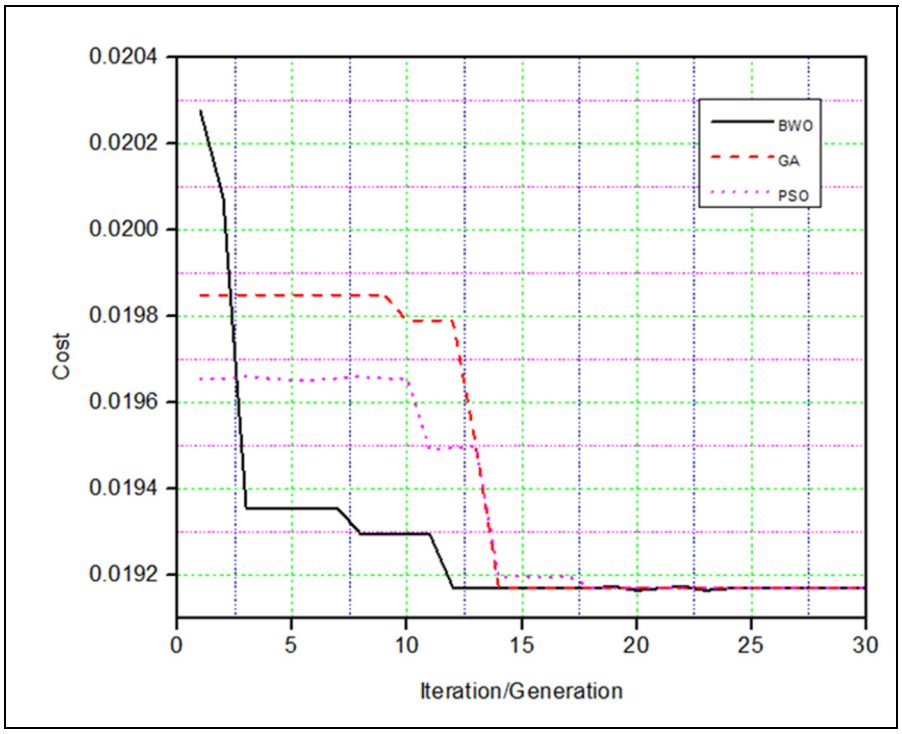

Figure 4.9 Cost convergence comparison of the BWO, PSO and GA

4.3.3 Aerodynamic solver

The aerodynamic solver is used to evaluate the performance of airfoil geometry in terms of aerodynamics. For evaluating aerodynamic performance, this study used two solvers, XFoil and Ansys Fluent. The selection of a turbulence model, the grid convergence for the mesh topology, and size were all part of the validation process.

4.3.3.1 XFoil Solver

External aerodynamics problems benefit significantly from panel approaches, which are based on the velocity potential flow theory. Panel methods result in reliable pressure and velocity distributions along an airfoil with little computational expense when the linearization hypothesis is valid. The velocity field can be represented as the gradient of a scalar potential. Linear methods can be used on thin bodies at modest angles of attack when there is no extensive separation, and the regime is subsonic. Drela's XFoil (Drela, 1989) is a popular program that predicts fixed or free transitions, mild trailing edge separation, and lift and drag prediction using linear flow and a viscous boundary layer (BL) interaction.

XFoil has difficulty providing a convergent solution for the airfoil analysis at high angles of attack where stall develops. To ensure solution convergence, non-converged explanations are penalized heavily by arbitrarily increasing the fitness function via a penalty function. As a result, they are finally omitted from the design process.

The findings obtained with XFoil were compared to those obtained with experimental data or with high fidelity solvers, and only a tiny difference was noted (Peerlings, 2018).

4.3.3.2 Transition SST Model

Aerodynamic data prediction needs precise recirculation of pressure drops, computation of boundary layers, and flow separation. While some studies incorporate the wall function of the flow model within the boundary layer into the RANS turbulence model, this sort of turbulent model is insufficient for effectively predicting the boundary layer, flow maintenance, pressure drop, and flow separation. Due to the fact that direct numerical simulations (DNSs) and other eddy resolved simulations are all extremely high computational techniques, the numerical analysis utilized the Transition SST turbulence model to generate highly precise and computationally efficient aerodynamic data.

The Transition ($\gamma-Re_\theta$) SST was employed in this investigation. This model uses SST K-ω, intermittency, and a transition onset Reynolds number. ($\gamma-Re_\theta$) is the crucial Reynolds number (Langtry et al., 2005). The intermittency of the boundary layer transition activates the turbulent kinetic energy generation term. Unlike the more usual use of intermittency to vary eddy viscosity, this method simulates higher laminar skin friction by modelling high freestream turbulence on laminar boundary layers. The fourth transport equation for Re is required for non-local turbulence strength. The additional transport equation also allows for numerous possibilities for different boundary conditions, creating a versatile and flexible tool.

4.3.3.3 Mesh Generation

ICEM was used to discretize the computational domain and solve each node using the governing equation. The airfoil geometries defined the C-shaped computational domain. The outlet boundary was established at 30c (c being the chord length) to agree for the full development of the wake flow. The distance was selected at 10c to prevent altering the flow field upstream of the airfoil. The dense grids formed in the airfoil's boundary layer, with smaller grid cells as they moved away from the surface. Laminar and transitional boundary layers can be captured using beginning layer thickness. Mesh topology surrounding the computational domain is shown in Figure 4.10.

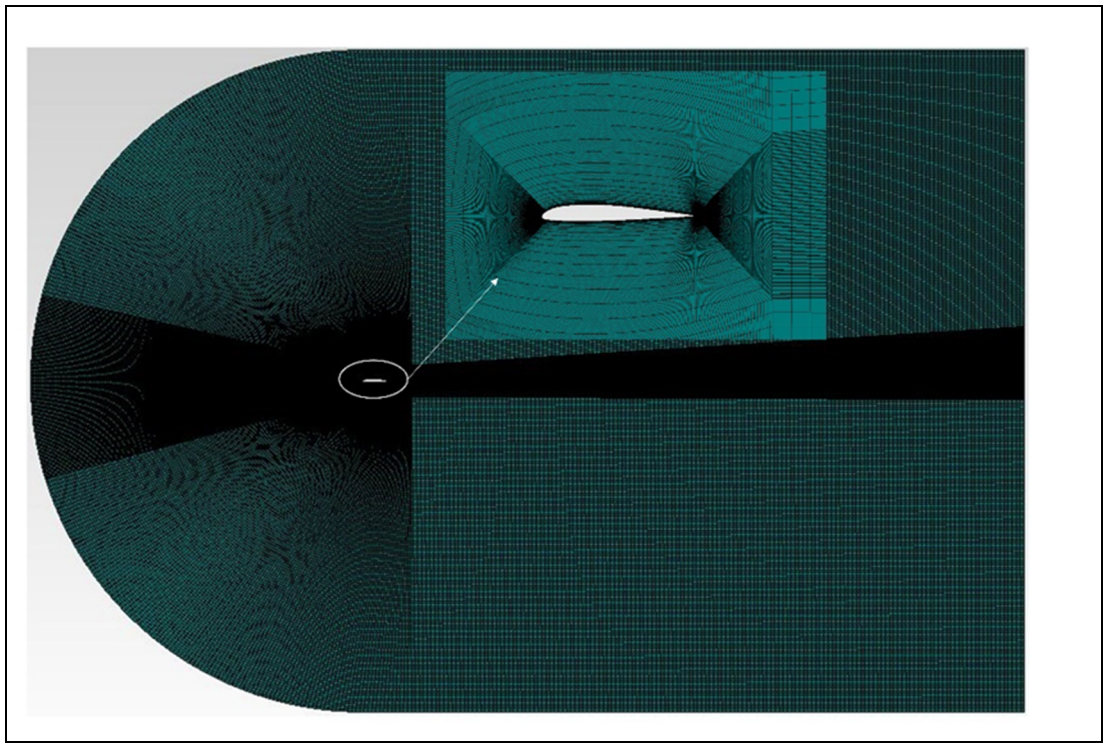

Figure 4.10 Grid generation of a morphing leading-edge airfoil

The intake was set at 34 m/s with a turbulence rate of 0.01 percent. The airfoil's surface was made non-slip and smooth. The outlet had a static gauge pressure of zero. The iterations ended when all scaled residuals were less than $1x10^6$.

The grid independence investigation was performed by altering the number of nodes in the dense mesh region. The drag coefficient was chosen as the mesh dependency criterion. Grid sizes of 100, 200 and 300 nodes were adequate to collect the results. The mesh size was then increased until additional increases in the mesh yielded very little difference in the values of drag coefficient.

4.4 Results & Discussion

The optimization results from coupling the CST parameterization methods with the Black Widow Optimization (BWO) algorithm for the UAS-S45 airfoil for the Droop Nose Leading Edge (DNLE) Morphing design were obtained. DNLE configurations consist of the focus of

this research. A reference airfoil shape optimization was performed to fully influence the "morphing" concept, followed by its morphing airfoil shape design. These scenarios are based on different altitudes and Reynolds numbers calculated for a 34 m/s airspeed, that was chosen because the UAS-S45 can reach altitude of 20,000 ft and has a stall speed of 34 m/s. The endurance maximization was chosen as an optimization function to improve the performance of the UAS-S45 over a large part of its flying regimes.

4.4.1 Optimization of Cruise Phase

The cruise flight condition was chosen because most of the flight time and fuel consumption occurs during the cruise phase. Accordingly, the objective functions were selected to maximize the aerodynamic endurance and to minimize the drag. The maximum lift coefficient and the lift coefficient of the reference airfoil at each angle of attack were implemented as constraints. Penalty functions applied constraints to the objective function to ensure that the optimum performance was obtained at each given angle of attack. The free-stream Mach number was 0.1, and the Reynolds number was 2.4 x 10^6. The general optimization problem is presented as follows:

The mathematical formulation of the drag minimization objective function is the following.

$$\begin{gathered} \text{Minimize } C_D\ (x); x\ \epsilon\ (airfoil\ set) \\ \text{subject to } C_{L_{max}}(x, \alpha, M\ \geq) 1 \cdot 608 \\ C_{L_{morph}} \geq C_{L_{min,baseline}(x,\alpha,M)}\ (x); x\ \epsilon\ \text{airfoil}\ set \end{gathered} \tag{4.29}$$

For the design of a long endurance UAV, the aerodynamic endurance (E) of a propeller powered UAV, as established by using the Breguet formula (J. B. Okrent, 2017), is used as an objective function

4.4.1.1 Drag Minimization

Drag minimization is achieved by optimizing the shape of a morphing Droop Nose Leading Edge (DNLE) to increase the aerodynamic efficiency during the cruise. The morphing location is kept as a variable and leading-edge morphing takes place within 30% chord to ensures that the rest of the airfoil remains as wing box without any changes. The performances of the reference and optimized airfoils are compared and presented in Table 4.1. The drag coefficient reduces to 0.00678, with 12% versus its initial value. An aerodynamic efficiency improvement of 15 % is achieved by optimizing the lift to drag ratio.

Table 4.1 Comparison of aerodynamic coefficients of the reference and optimized

	Angle of Attack (^{0})	**Reference Airfoil**	**Optimized Airfoil**	**Relative Difference in '%'**
C_D	2^0	0.00755	0.00663	-12
$\frac{C_L}{C_D}$	2^0	48.6887	56.1017	15

Figure 4.11(a) illustrates the initial (reference) versus the final (optimized or morphed) DNLE airfoil shape. Figure 4.11(b) shows the pressure coefficient calculated for the minimum drag optimized airfoil at an angle of attack of 2° versus its reference airfoil. Less unfavorable pressure gradient and smoother pressure peak than the original airfoil allows for longer laminar flow. Figure 4.11 compares the pressure coefficient fluctuations of optimized and reference airfoils with the chord (b). Pressure changes on the pressure side of the airfoil for a 2° angle of attack show the flow transition. By delaying turbulent flow towards the trailing edge, the DNLE optimized airfoil cruises better.

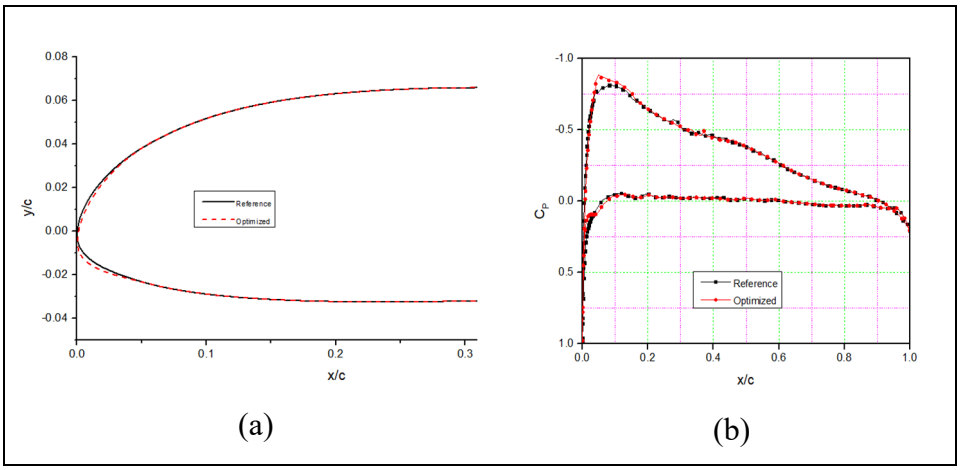

Figure 4.11 Assessment of results obtained for the UAS-S45 optimized airfoil for drag minimization (a) Airfoil shape and (b) Cp distribution versus the chord.

Figure 4.12 shows the pressure contours over the upper and lower surfaces of the reference and optimized airfoils at an angle of attack of 2°. The DNLE creates more negative pressure than the baseline airfoil. Hence, more lift was generated in the optimized airfoil.

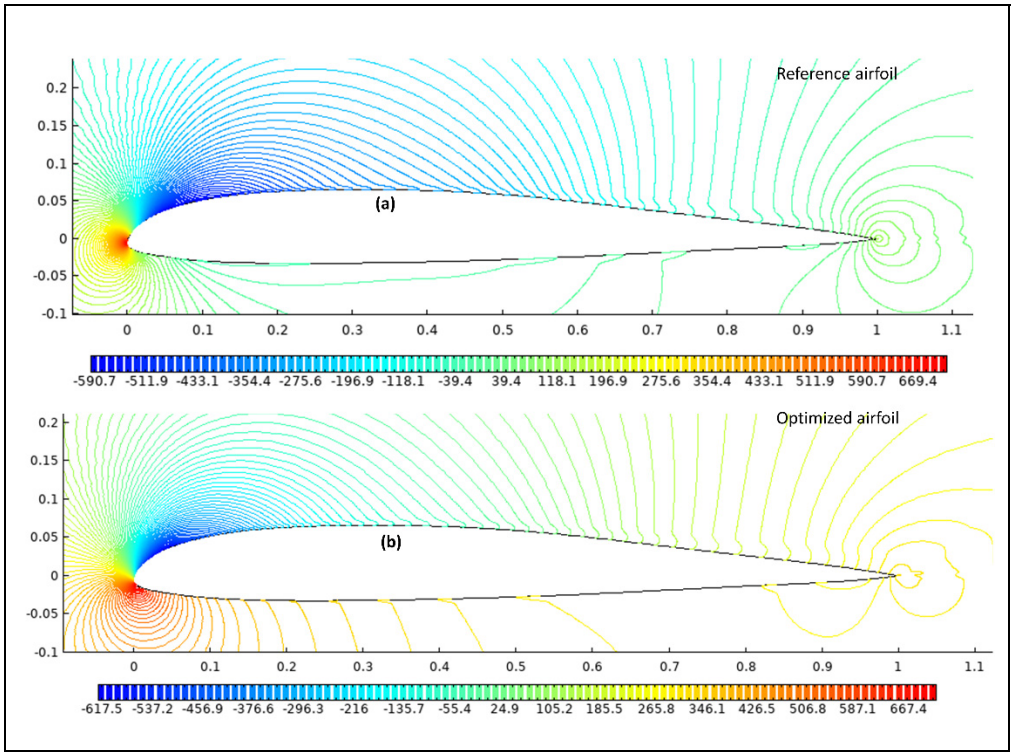

Figure 4.12 Comparison of pressure variations for the UAS-S45 optimized airfoil for drag minimization

The optimized airfoil's skin friction coefficient shows that the laminar-to-turbulent transition area is delayed by almost 10% of the chord, from 25% to 35% for the original airfoil. Increasing the angle of attack reduces the drag coefficient by increasing laminar flow and decreasing pressure drag.

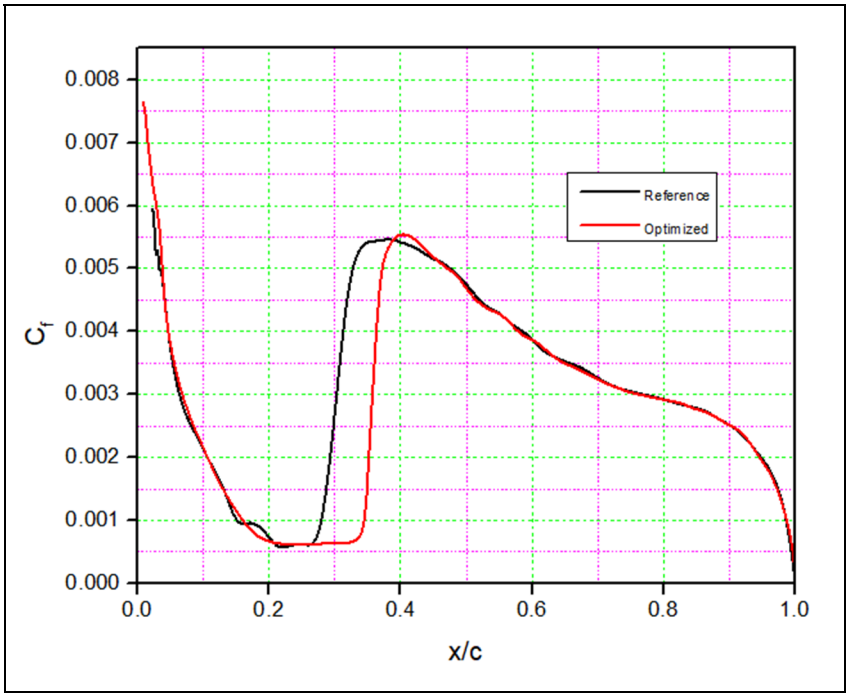

Figure 4.13 Comparison of the skin friction coefficient for the S45 optimized airfoil and for the reference airfoil for drag minimization

Figure 4.14 (a) shows the chordwise fluctuations of velocity magnitude contours at a 2° angle of attack. The lower surfaces of the reference and optimized airfoils have marginally lower velocities than the higher surfaces. The location of the airfoil's stagnation points changed between the optimized and reference airfoils. In Figure 4.14 (b), turbulence causes the intermittency factor to rapidly develop. As mentioned in section 3.2.2, on the upper surface, the intermittency rapidly increases from 0 to 1, showing the transition starting point. The beginning of the transition can be seen as an increase in intermittency near the surface, which then grows to unity at a certain distance. The intermittency's production is delayed in the optimized airfoil as compared to the baseline airfoil. The flow on the upper surface is laminar, but it reattaches and transforms into a turbulent flow.

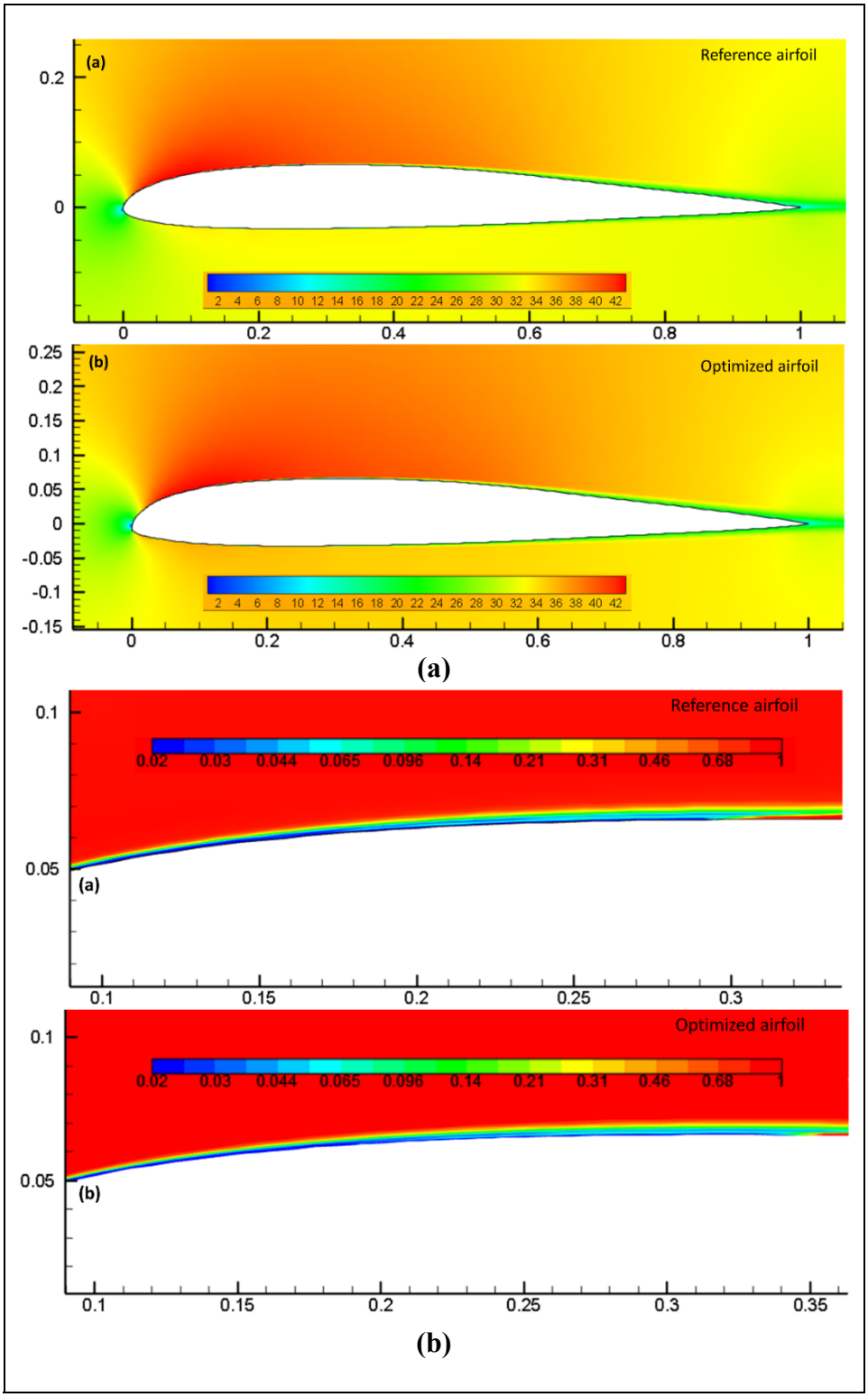

Figure 4.14 Comparison of the skin friction coefficient for the S45 optimized airfoil and for the reference airfoil for drag minimization

Table 4.2 presents a comparison between the drag coefficients for the reference airfoil and the optimized morphing airfoil. The drag coefficient reduction of the morphing optimized airfoil over the original reference airfoil was obtained for the range of angles of attack from 0° to 10°. At each angle of attack, the relative error describing the drag reduction is indicated. The best improvements in the drag reduction were found for the angle of attack between 2° and 6°.

Table 4.2 Optimized drag results for the reference and optimized morphing airfoils for a certain length of a flexible morphing section

Angle of attack	**Length of flexible section (m)**	**Reference airfoil C_D**	**Optimized airfoil C_D**	**Relative '%' difference**
0	0.05	0.0091	0.00691	-24.06
1	0.10	0.00801	0.00729	-8.98
2	0.07	0.00755	0.00663	-12.18
3	0.09	0.0093	0.00674	-27.52
4	0.23	0.00976	0.00643	-34.11
5	0.24	0.0102	0.00648	-36.47
6	0.23	0.00912	0.00678	-25.65
7	0.29	0.01016	0.0097	-4.52
8	0.29	0.01261	0.01143	-9.35
9	0.25	0.01251	0.01108	-11.43
10	0.29	0.01386	0.0129	-6.92

The drag minimization optimization increased the lift-to-drag ratio, as the lift coefficients remain relatively the same for the reference airfoil and the optimized airfoil. Figure 4.15 shows the lift-to-drag coefficient increments for the given drag coefficients for the optimized airfoil as compared to the original airfoil coefficients, for the Reynolds number of 2.4 x 10^6.

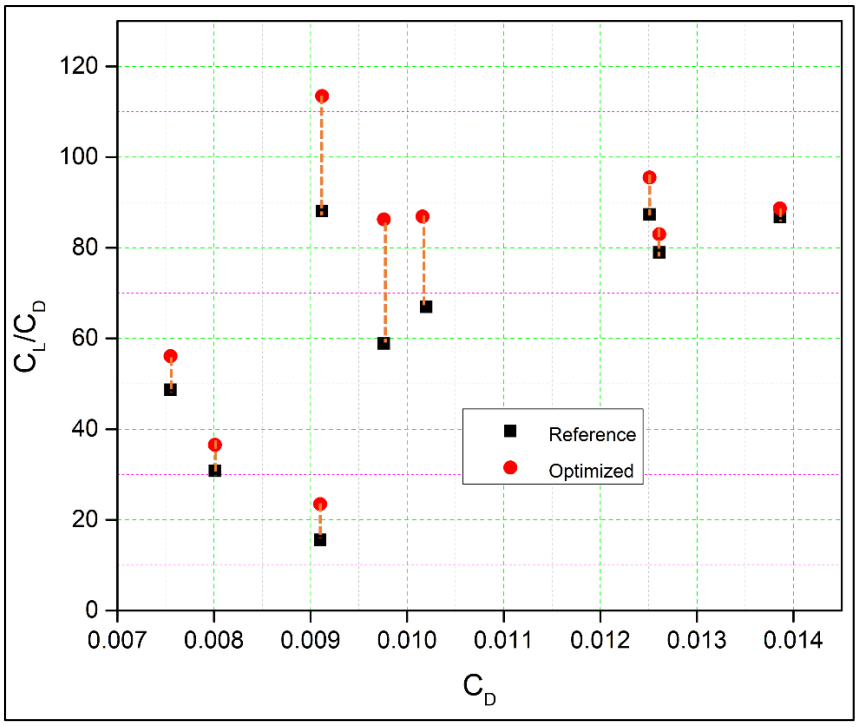

Figure 4.15 Increase in the lift-to-drag ratio at the same drag coefficient for the optimized airfoil versus the reference airfoil

4.4.1.2 Endurance Maximization

Another optimization case concerns optimizing the shape of an airfoil morphing Droop Nose Leading Edge (DNLE) with respect to the reference leading edge in order to increase aerodynamic efficiency during the cruise phase by maximizing its aerodynamic endurance. Table 4.3 shows that the optimization process led to an increase in endurance maximization, characterized by $CL^{\frac{3}{2}}/CD$ in the optimized DNLE airfoil. Furthermore, the values of $CL^{\frac{3}{2}}/CD$ increased from 29.52 to 32.48, indicating a 10% better endurance performance for the UAS-S45 DNLE airfoil configurations than that of its reference airfoil. At the same time, the drag coefficient for the optimized airfoil was smaller than CD obtained for the reference airfoil.

Table 4.3 Comparison of aerodynamic endurance and minimized drag of the reference and optimized airfoils

	Reference Airfoil	**Optimized Airfoil**	**Relative Difference in '%'**
$\frac{\left(C_L^{\frac{3}{2}}\right)}{C_D}$	29.52	32.48	10
C_D	0.00872	0.00796	-8

Figure 4.16(a) illustrates the initial (reference) versus the final (optimized or morphed) airfoil shape, while Figure 4.16(b) shows the pressure coefficients for the minimum drag optimized airfoil and the reference airfoil at an angle of attack of 2°. The change in the leading-edge shape of the optimized airfoil as compared to the reference airfoil is obtained by extending the flexible leading-edge section in the optimized airfoil. The optimized leading-edge deflection slightly drops around 12.58°. Similarly, on Figure 4.16(b), it can be observed that the optimized airfoil presents a smoother pressure peak and that the adverse pressure gradient is not as strong as the original airfoil pressure gradient, thus creating favorable conditions for an extended laminar flow. The pressure values variations with the chords of the optimized airfoils versus the reference airfoil are shown in Figure 4.16(c). It is clear that the most significant pressure fluctuations occur around the leading edge's upper surface. The chord-wise pressure distribution indicates the increased performance for the DNLE optimized airfoil at the cruise phase achieved by delaying the onset of turbulent flow towards the trailing edge.

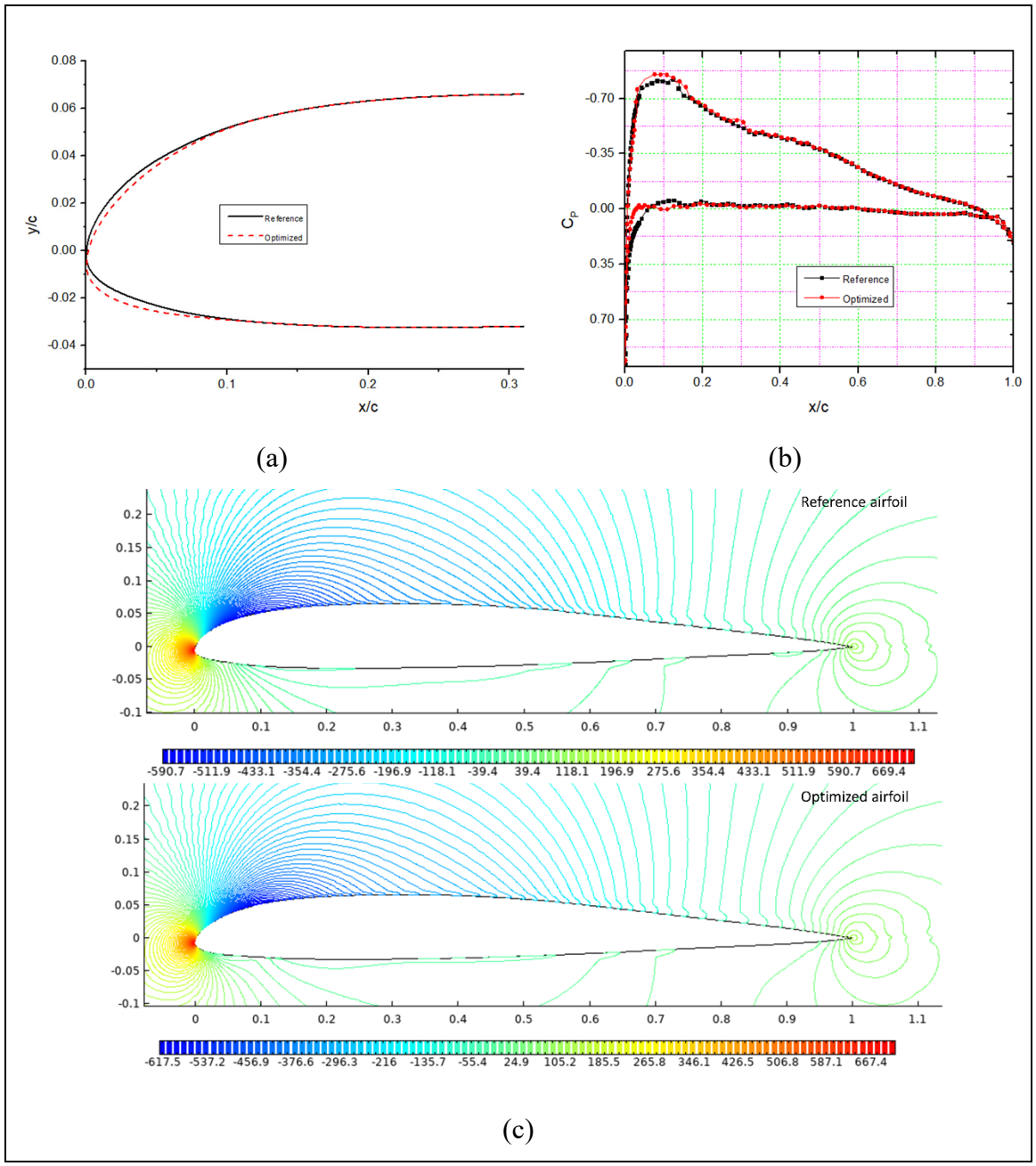

Figure 4.16 Comparison of results for the S45 optimized airfoil for maximized aerodynamic endurance: (a) Airfoil shape, (b) Cp distribution, (c) Pressure variation over the airfoil

The skin friction coefficient in Figure 4.17 shows that the laminar-to-turbulent transition zone is delayed by almost 10% of the chord, from 25% to 35% in the original airfoil. As the angle of attack increases, the laminar flow extent increases while the pressure drag decreases.

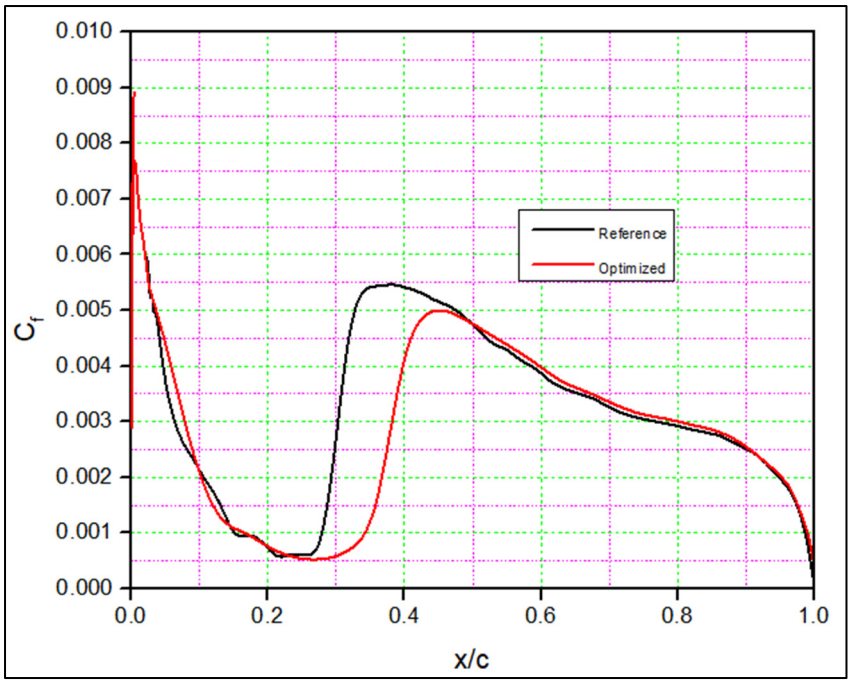

Figure 4.17 Increase in the lift-to-drag ratio at the same drag coefficient for the optimized airfoil versus the reference airfoil.

Figure 4.18 (a) shows the velocity contour plots of one of the DNLE airfoils for a 2° angle of attack. Comparing the reference and DNLE airfoils reveals that the DNLE airfoil has higher gradients than the reference airfoil. The improved airfoil's stagnation points were different. The improved airfoil showed a 15% increase in lift-to-drag coefficient ratio compared to the reference airfoil. Figure 4.18 (b) shows the separation-induced transition where turbulence rapidly increases the intermittency factor. The beginning of the transition can be seen as an increase in the intermittency near the surface, which then grows to unity at a certain distance. The intermittency's production is delayed from 0.3c in the reference airfoil to 0.37c in the optimized airfoil. The flow on the airfoil upper surface is laminar, but it reattaches and transforms into a turbulent flow.

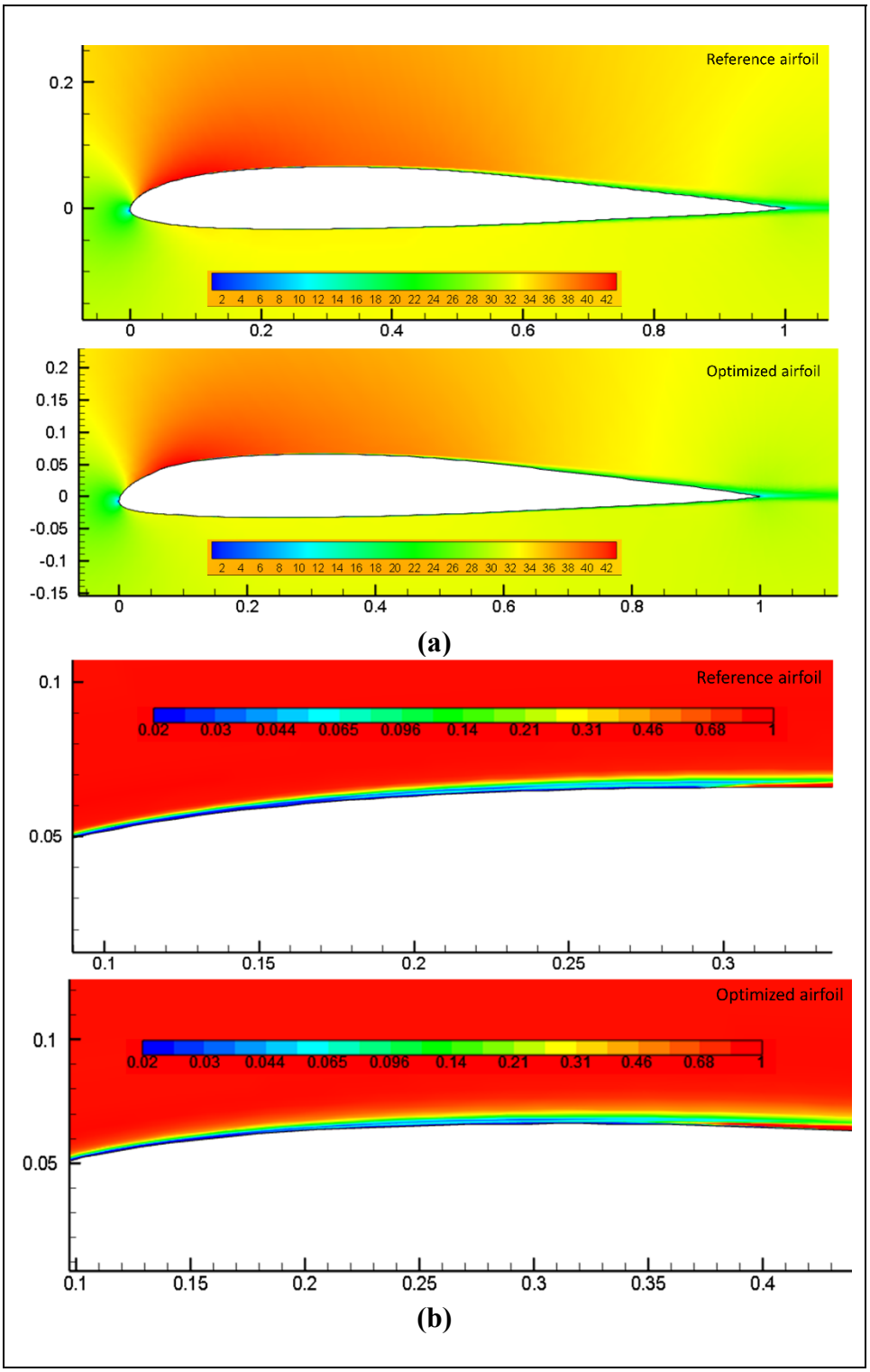

Figure 4.18 Assessment of the (a) velocity contours for the reference and optimized airfoil, and (b) intermittency contours the reference and optimized airfoil.

Table 4.4 presents a comparison between the aerodynamic endurance for the reference airfoil and for the optimized airfoil. The increase in the aerodynamic endurance of the optimized airfoil over the original reference airfoil was obtained for the range of angles of attack from 0^0 to 10^0. The improvement percentage is indicated for each angle of attack value.

Table 4.4 Optimized drag results for the reference and optimized morphing airfoils for a certain length of a flexible morphing section

Angle of attack (°)	Length of flexible section $\left(\frac{l}{c}\right)$	Reference $\frac{C_L^{\frac{3}{2}}}{C_D}$	Optimized $\frac{C_L^{\frac{3}{2}}}{C_D}$	Improvement '%'
0	0.19	5.86	9.06	54.51
1	0.06	15.28	19.54	27.86
2	0.12	29.52	32.48	10.05
3	0.06	34.68	49.78	43.55
4	0.24	44.63	65.67	47.13
5	0.18	55.30	93.42	68.94
6	0.21	78.94	114.83	45.45
7	0.19	81.90	130.02	58.75
8	0.22	78.81	142.62	80.96
9	0.23	91.34	154.41	69.05
10	0.20	95.11	160.50	68.74

The complete flight profile of a surveillance-based UAV mission consists mostly of takeoff, climb, cruise, standby, evacuation, return, descent, and landing phases, and the engine working states in different flight phases are varied. Therefore, all missions require improved performance, and they account for the different flight times and fuel consumption. A Simulink model of UAS-S45 was developed for fuel burn rate and specific fuel consumption in MATLAB, using the coefficient of thrust from both engines as well as their associated fuel consumption.

The fuel burn rate and specific fuel consumption were obtained for both the reference and optimized aerodynamic coefficients when the drag of the aircraft was equal to the thrust (in equilibrium uniform flight). A relationship between the lift and drag coefficients at various angles of attack was used to determine the drag for the weight of the aircraft in order to match the corresponding lift. The drag and lift were obtained from their corresponding aerodynamic coefficients using the next equations:

$$Lift = \frac{1}{2} * \ \rho * v^2 * S * CL \tag{4.30}$$

$$Drag = \frac{1}{2} * \ \rho * v^2 * S * CD \tag{4.31}$$

Where ρ is the air density, v the airspeed, S the wing surface (assumed to remain same), CL and CD are the lift and drag coefficients, respectively.

Figures 4.19 (a), (b), (c) and (d) show the DNLE morphing airfoil fuel burn for three different optimization functions expressed in terms of drag minimization, lift-to-drag maximization, and aerodynamic endurance maximization, and all of them indicate that the fuel consumption was reduced with respect to the reference airfoil. Figure 4.20 show the same results for the specific fuel consumption.

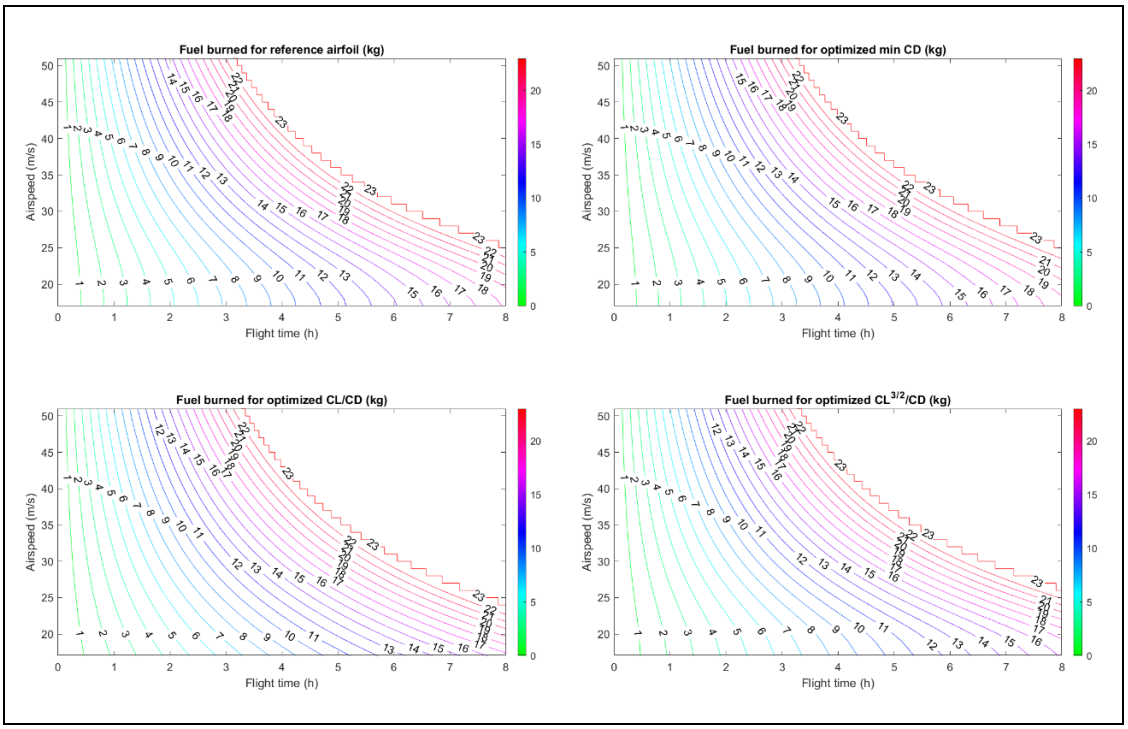

Figure 4.19 Comparison of fuel burn rate over flight time at different speeds for the reference and optimized configurations for the UAS-S45.

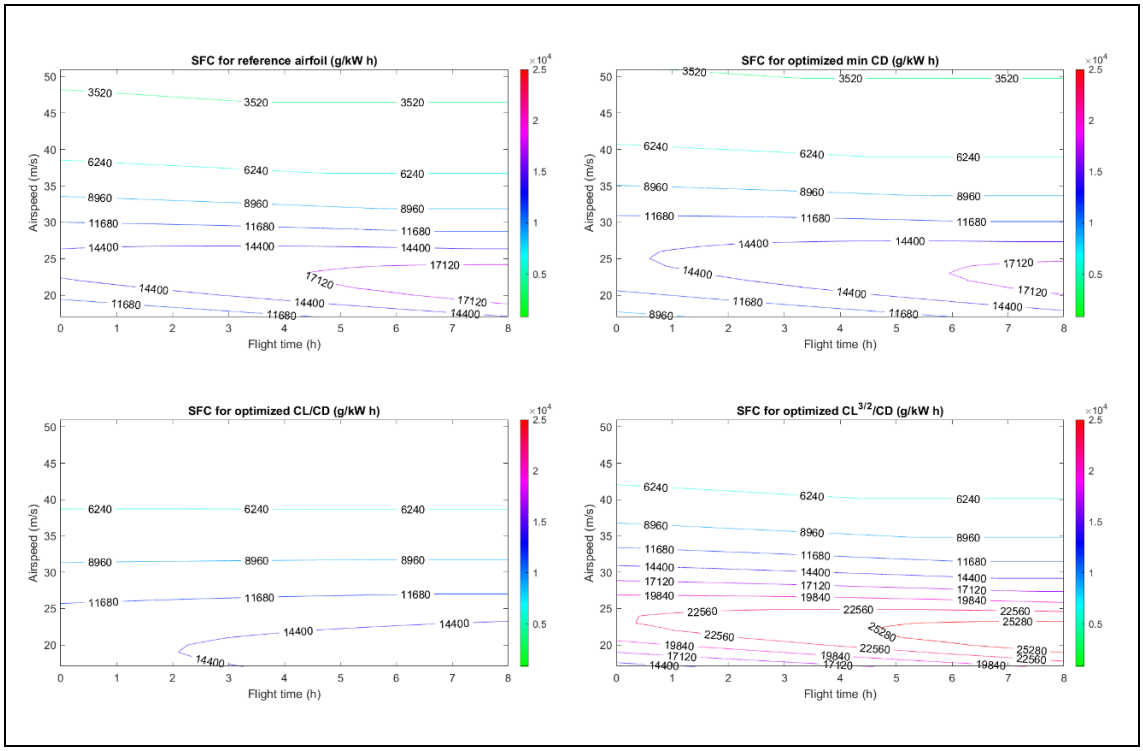

Figure 4.20 Comparison of specific fuel consumption with flight time at different speeds for the reference and optimized UAS-S45.

4.5 Conclusion

This work performed aerodynamic optimization of Droop Nose Leading Edge (DNLE) morphing airfoils for UAS-S45 at cruise flight conditions. A Black Widow Optimization (BWO) algorithm was coupled with a modified Class Shape Transformation (CST) parameterization method, and then it was employed to optimize the aerodynamic shape of a well-known UAS-S45 airfoil, to improve its drag and aerodynamic endurance performances. The CST parameterization technique was used to parameterize the reference airfoil by introducing local shape changes and providing skin length control to obtain its various optimized DNLE configurations. These included an in-house MATLAB method, an aerodynamic solver, and a high-fidelity CFD solver. Validity was assessed for both options. It was predicted by Transition ($\gamma - Re_\theta$) SST turbulence model.

The DNLE optimization was designed to increase the aerodynamic performance of the UAS-S45 at the cruise phase for an angle of attack of 2°. The DNLE optimized airfoil showed that the drag coefficient reduced to 0.00678, with a 12.18% drag reduction in comparison to the reference airfoil. In addition, an aerodynamic efficiency improvement of up to 15.22 % was achieved by increasing lift to drag ratio for the optimized UAS-S45 airfoil. A transition onset delay was also observed using the skin friction coefficients on the optimized DNLE airfoils. For the aerodynamic endurance objective function, the values of $CL^{\frac{3}{2}}/CD$ increased from 29.52 to 32.48, thus indicating a 10% better endurance performance for the UAS-S45 optimized airfoil configurations than for its reference airfoil. At the same time, the drag coefficient obtained using the aerodynamic endurance maximization objective function is reduced for the optimized airfoil as compared to the reference airfoil. In addition, it was observed that the DNLE morphing design will result in better fuel consumption when compared to the reference UAV.

In forthcoming work, this morphing optimization study will include the unsteady flow analysis on the DNLE airfoil. The transient behavior of the DNLE airfoil will be presented via a three-

dimensional analysis of the UAS-S45 wing with DNLE. Based on aero-structural studies, various configurations will be analyzed, and the actuation mechanism shown in Figure 4.1 will be implemented.

CHAPTER 5

OPTIMIZATION AND DESIGN OF A FLEXIBLE DROOP NOSE LEADING EDGE MORPHING WING BASED ON A NOVEL BLACK WIDOW OPTIMI-ZATION (B.W.O.) ALGORITHM-PART II

Musavir Bashir [a], Simon Longtin-Martel [b], Nicola Zonzini [c], Ruxandra Mihaela Botez [d], Alessandro Ceruti [e] and Tony Wong [f]

[a, b, d, f] Department of System Engineering, École de Technologie Supérieure, 1100 Notre-Dame West, Montréal, Québec, Canada H3C 1K3
[b, e] Department of Industrial Engineering, University of Bologna, Bologna, Italy Via Zamboni, 33, 40126 Bologna BO, Italy

Paper published in *Designs*, November 2022.
DOI: https://doi.org/10.3390/designs6060102

Résumé

Ce travail présente une optimisation aérodynamique et structurelle pour un profil avec un bord d'attaque déformable intitulé "Droop Nose Leading Edge (DNLE)" en tant que dispositif de haute portance pour l'UAS-S45. Les résultats ont été obtenus en utilisant trois algorithmes d'optimisation: l'optimisation couplée de l'essaim de particules-recherche de modèles, l'algorithme génétique et l'algorithme d'optimisation de la veuve noire. Le rapport portance/traînée (*L/D*) a été utilisé comme fonction d'aptitude et l'impact du choix de la sélection de l'algorithme d'optimisation sur la fonction d'aptitude a été évalué. L'optimisation a été réalisée à différents nombres de Mach de 0.08, 0.1 et 0.15, respectivement et aux conditions de vol de croisière et de décollage. Tous ces algorithmes d'optimisation ont donné des résultats avec des différences inférieures à 0.03% pour les rapports de portance/traînée, ainsi que des géométries de profils aérodynamiques et des distributions de pressions similaires. De plus, une analyse non-stationnaire d'un profil de bord d'attaque à déformation variable avec un schéma de maillage dynamique a été effectuée afin d'étudier son comportement d'écoulement à différents angles d'attaque et la faisabilité d'une déflexion vers le bas du bord d'attaque comme mécanisme de contrôle du décrochage. Les résultats numériques ont montré

que le bord d'attaque à déformation variable réduit les zones de séparation de l'écoulement sur le profil et augmente l'angle d'attaque de décrochage. De plus, une étude préliminaire a été menée sur la conception et l'analyse de sensibilité d'une structure de bord d'attaque déformable de l'aile de l'UAS-S45 intégrée à un mécanisme d'actionnement interne. Les matrices de corrélation et de détermination ont été calculées pour la géométrie en matériaux composites de l'aile pour l'analyse de sensibilité afin d'obtenir les paramètres avec les coefficients de corrélation les plus élevés. Ces paramètres comprennent les qualités du matériau composite, l'épaisseur, les angles de pli et la séquence d'empilement des plis. Ces résultats peuvent être utilisés pour concevoir l'optimisation de la peau flexible de l'aile, obtenir les déflections ciblées du nez de type "Droop Nose" pour le bord d'attaque déformable et concevoir un modèle amélioré.

Abstract

This work presents an aerodynamic and structural optimization for a Droop Nose Leading Edge Morphing airfoil as a high lift device for the UAS-S45. The results were obtained using three optimization algorithms: coupled Particle Swarm Optimization-Pattern Search, Genetic Algorithm, and Black Widow Optimization algorithm. The lift-to-drag ratio was used as the fitness function, and the impact of the choice of optimization algorithm selection on the fitness function was evalu-ated. The optimization was carried out at various Mach numbers of 0.08, 0.1, and 0.15, respectively, and at the cruise and take-off flight conditions. All these optimization algorithms obtained effectively comparable lift-to-drag ratio results with differences of less than 0.03% and similar airfoil geometries and pressure distributions. In addition, an unsteady analysis of a Variable Morphing Leading Edge airfoil with a dynamic meshing scheme was carried out to study its flow behaviour at different angles of attack and the feasibility of leading-edge downward de-flection as a stall control mechanism. The numerical results showed that the variable morphing leading edge reduces the flow separation areas over an airfoil and in-creases the stall angle of attack. Furthermore, a preliminary investigation was conducted into the design and sensitivity analysis of a morphing leading-edge structure of the UAS-S45 wing integrated with an internal actuation mechanism. The

correlation and determination matrices were computed for the composite wing geometry for sensitivity analysis to obtain the parameters with the highest correlation coefficients. The parameters include the composite material qualities, thickness, ply angles, and the ply stacking sequence. These findings can be utilized to design the flexible skin optimization framework, obtain the target droop nose deflections for the morphing leading edge, and design an improved model.

5.1 Introduction

Various environmental requirements have pushed the aircraft industry to design fuel-efficient and quieter aircraft (Overton, 2019). One possible strategy is improving an aircraft's aerodynamic efficiency, thus reducing the fuel needed for flights. However, the traditional approaches to further increase the aerodynamic efficiency (such as the lift-to-drag ratio) using the conventional wing configurations are facing limitations. Accordingly, researchers are introducing novel, cutting-edge technologies, such as adaptive morphing structures for flight optimization and flow management over the wing (S Ameduri et al., 2020; R. Botez, 2018a; Ruxandra Mihaela Botez et al., 2007; Hamy et al., 2016). Morphing structures have been investigated for several years, and the problems faced are mentioned in the literature (Ruxandra M Botez, 2022; Carossa et al., 2016; Carrier et al., 2012; Concilio et al., 2021; Kintscher et al., 2011; Li et al., 2018; Liauzun et al., 2018; Noviello et al., 2019; Peter et al., 2013). A wide range of morphing structures has been studied in the aviation industry on fighter aircraft (Smith, 1992), regional aircraft (Arena, Concilio, et al., 2019; De Gaspari et al., 2019; Moens, 2019), uncrewed air vehicles Sugar-Gabor, et al., 2014; Sugar-Gabor, et al., 2016), and General Aviation aircraft (Kintscher et al., 2011; Hans Monner et al., 2009; Pecora, 2021).

"Morphing" may be mainly used on uncrewed aerial vehicles due to their smaller scale and lesser complexity in terms of wing design structure and energy consumption, especially in terms of actuation power (UAVs) (RM Botez et al., 2018; D Communier et al., 2019; Communier et al., 2020; I Dimino et al., 2020; Elelwi et al., 2020; Khan et al., 2020). A telescoping spar and rib system was used to build an Unmanned Aerial Vehicle (UAV)

morphing wing capable of modifying its wing span and altering its chord (Gamboa et al., 2009). When compared to its non-morphing original base geometry, a numerical study revealed a drag reduction of up to 23%. Another survey of a medium-sized experimental UAV, ANTEX-M, in which wing morphing aerodynamic optimization of the wing's upper surface between its leading edge and 55% of its chord, as well as on the changing of the entire wing's geometry (Sugar-Gabor, et al., 2016). Similarly, a combat UAV's aerodynamic and structural multidisciplinary design optimization was carried out, and improved performances were obtained, as shown in (Tianyuan et al., 2009).

The Research Laboratory in Active Controls, Avionics, and AeroServoElasticity (LARCASE) participated in a morphing wing project called the "Morphing Architectures and Related Technologies for Wing Efficiency Improvement—CRIAQ MDO 505" (Koreanschi, Oliviu, et al., 2016; Koreanschi, Sugar-Gabor, et al., 2016a) and CRIAQ 7.1 project called " Laminar Flow Improvement on an Aeroelastic Research Wing" (Grigorie et al., 2012; Andrei Vladimir Popov et al., 2010).

There have been great successes in aircraft optimization processes in the past decade. New intelligent algorithms and computational solvers have completely re-formed the way aircraft design is thought, including through "morphing wing optimization." Proper analysis of aircraft design using optimization techniques has eliminated the hefty experimental costs of earlier methods and has resulted in improved algorithms and computational solvers (J. E. Hicken, 2009; Skinner et al., 2018). In addition, these optimization processes have utilized gradient-based and gradient-free algorithms (Skinner et al., 2018).

The optimization in aircraft design, specifically morphing technology, is significant because the optimized design is required to satisfy the required mission, flight operation, and performance needs. Thus, the choice of the optimization algorithm and the parameterization method is needed, and the comparative analysis makes it possible to obtain suitable outcomes. Although the gradient-based techniques usually have the fastest convergence rates than the metaheuristics, the metaheuristic algorithms have the advantages of solution accuracy,

flexibility, and obtaining global optimum solutions. Furthermore, implementing morphing wing technology in the UAV increases the number of design variables, and optimization is required at different mission segments; therefore, finding the optimal global solution becomes essential.

Such as metaheuristics (MHs) were implemented in the inverse problem-based optimization system identification method for small fixed-wing UAVs (Nonut et al., 2022). A flight test is undertaken to obtain data for the proposed scheme and MHs performance. Based on Freidman's statistical test, the L-SHADE method was optimal for longitudinal and lateral dynamics, with R-square errors of 0.5465 and 0.0487, respectively. Another study resulted in the design of a reliability optimization methodology based on double-loop optimization (D.O.) approach to solve a multiobjective conceptual design problem of a fixed-wing UAV (Champasak et al., 2022). Again, state-of-the-art meta-heuristics were employed, and the optimum dynamic parameter settings reduced runtime by 22.5% compared to the traditional metaheuristic run while keeping the competitive results.

A metaheuristic optimization based on a genetic algorithm was used for the UAS-S4 airfoil's upper surface (Koreanschi et al., 2017b). The genetic algorithm was coupled with three different optimization methods, and the optimal global solution was obtained for the wing tip demonstrator airfoil. In addition, the algorithm was proven to be robust as it converged to the optimal global region in less than 10 iterations or generations.

An Improved Fruit Fly Optimization Algorithm (IFOA) was developed and used with a C.F.D. solver to handle aerodynamic design optimization challenges (Tian et al., 2019). To minimize the drag coefficient, the IFOA was utilized to optimize three aerodynamic shape designs using a C.F.D. solver. In addition, the algorithm's convergence efficiency was shown for the inverse airfoil design.

The transient aerodynamic characteristics of a flexible leading edge need to be explored, and more research on optimization approaches in the field of morphing wings is required. Many

techniques have been used to reduce or eliminate dynamic stalls, including flap fluctuations, synthetic jet/periodic stimulation, and plasma actuators (Shmilovich et al., 2011; Stanewsky, 2001). Given that the local shape near the airfoil leading edge significantly affects the formation and evolution of dynamic stall vortices (Sankar et al., 2000) changing the leading edge shape could be a more efficient technique to reduce dynamic stall. Variable Droop Leading-Edge (VDLE) devices can provide active flow control to reduce the local Mach number and provide a better pressure distribution towards the leading edge, thereby delaying or eliminating the dynamic stall (Martin et al., 2003; Sahin et al., 2003).

The drooping of the leading edge of the FX63-137 airfoil at low Reynolds numbers was investigated in (Perry et al., 1987). The drooped leading edge has an effective angle of attack five degrees lower than the rest of the airfoil, which allows a higher maximum lift coefficient and a smaller stall angle. Such a leading-edge angle deflection could improve pressure distribution, reduce an unfavorable pressure gradient, and delay flow separation.
The integration of a leading-edge droop and a Gurney flap to improve rotor airfoil dynamic stall and post-stall was investigated (B.-s. Lee et al., 2005). The dynamic stall was delayed for a 20-degree leading-edge droop and 0.5 percent chord Gurney flap. Moreover, the maximum lift coefficient increased, but the negative pitching moment decreased, increasing the lift-to-drag ratio.

A variable droop leading edge was examined to analyze dynamic stall control (Chandrasekhara et al., 2004). The results demonstrated a high reduction in the dynamic stall. With suitable lift coefficients, considerable reductions in drag and pitching-moment coefficients were obtained, and positive damping revealed useful to remove torsional instabilities. The researchers demonstrated that the airfoil variable droop leading-edge reduced drag and increased the dynamic stall's pitching moment. These results were also obtained for the UH-60A rotor. A numerical technique based on loosely coupled C.F.D. and complete structural dynamics improved the rotor efficiency and performance.

Although there have been many investigations into the aerodynamic optimization of morphing wings, most studies focus on examining the optimization framework. First, it is significant to study the impact of metaheuristic selection on aerodynamic optimization outcomes and computing time because insufficient data was found in the literature. Second, the use of dynamic meshing with time-dependent morphing airfoil parametrization is hardly observed in the literature. It becomes imperative to analyze the unsteady flow behavior of morphing wings at various angles of attack and the possibility of leading-edge downward deflection as a stall control mechanism.

The research presented in this paper has two broader objectives: To compare three different optimization algorithms and identify the best method for the optimization technique. The optimization algorithms used are the Black Widow Optimization Algorithm, the Genetic Algorithm, and Particle Swarm Optimization. Firstly, the optimal algorithm will be used to optimize the aerodynamic Design of a morphing airfoil under various flight conditions. The second goal is to use a dynamic meshing approach to investigate the unsteady variable morphing leading edge to determine the flow physics and the practicality of leading-edge downward deflection as a stall control mechanism. In addition, a preliminary investigation on the design and sensitivity analysis of a morphing leading-edge structure coupled with an internal actuation system for the UAS-S45 wing will be conducted. Finally, the parameters affecting the wing model will be explored to improve further optimization studies and the prediction of possible failures for each finite element.

5.2 Methodology

5.2.1 Aerodynamic Design Optimization

An aerodynamic shape optimization framework defines the Droop Nose Leading Edge (DNLE) morphing. This morphing changes the leading edge to its required aerodynamic shape when actuated. The control of such a kind of morphing involves formulating an objective function for a model using a geometric shape parameterization, an aerodynamic flow solver,

and an optimization algorithm to implement the methodology. Figure 5.1 depicts the optimization framework that was employed in this study. It enables shape parameterization integration with an aerodynamic solver and optimization algorithm. The shape design and the managed control of airfoil shape variables, simultaneously respecting geometrical constraints, is carried out by a parameterization technique called C.S.T. (class/shape transformation), an aerodynamic solver (either XFoil or the Transition S.S.T. model) were used, and three different optimization algorithms to compare their convergence: the Genetic Algorithm (G.A.), Particle Swarm Optimization (PSO) and the Black Widow Optimization (B.W.O.). Our previous paper describes the optimization procedure in detail (Bashir, Longtin-Martel, et al., 2022).

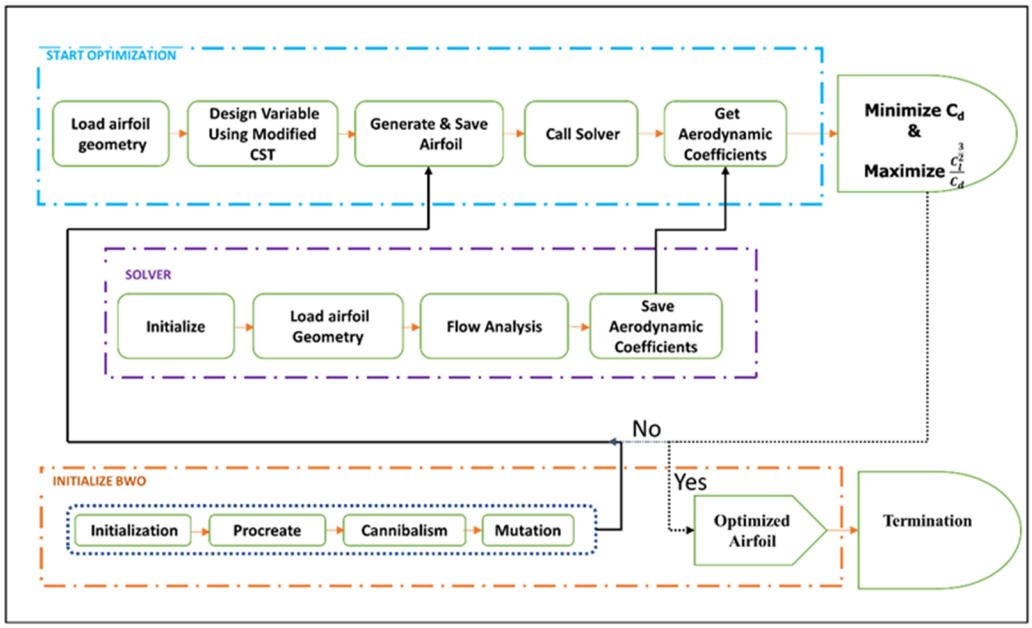

Figure 5.1 Flow chart for the airfoil shape optimization

5.2.2 Numerical Approach

5.2.2.1 Morphing Model and Method

In the computational framework, a numerical analysis tool is used to evaluate the performance of a dynamic morphing leading edge airfoil geometry in terms of its aerodynamics. A flexible

morphing leading edge can achieve a chord-wise and span-wise differential camber variation with the same structural system by providing a smooth shape with no additional gap. A numerical method with dynamic mesh and User-Defined Functions (UDFs) was adopted to study the aerodynamic characteristics of the morphing wing. The Variable Morphing Leading Edge (VMLE) process was obtained in Ansys Fluent.

The parametrization approach used for the leading-edge deflection is based on the third-order polynomial deformation, in which the surface nodes are moved according to the parameterization technique. For the UAS-S45 airfoil, this approach consists of its thickness distribution added to an unsteady shape parametrization of its camber line. The morphing wing section is located in the 0–16% chord of the airfoil, while the rest of the airfoil is fixed. Figure 5.2 illustrates the motion of the morphing leading edge, where δ is the maximum leading-edge deflection, indicating the vertical distance between the initial unmorphed leading-edge position and the maximum (final) position of the morphing leading edge.

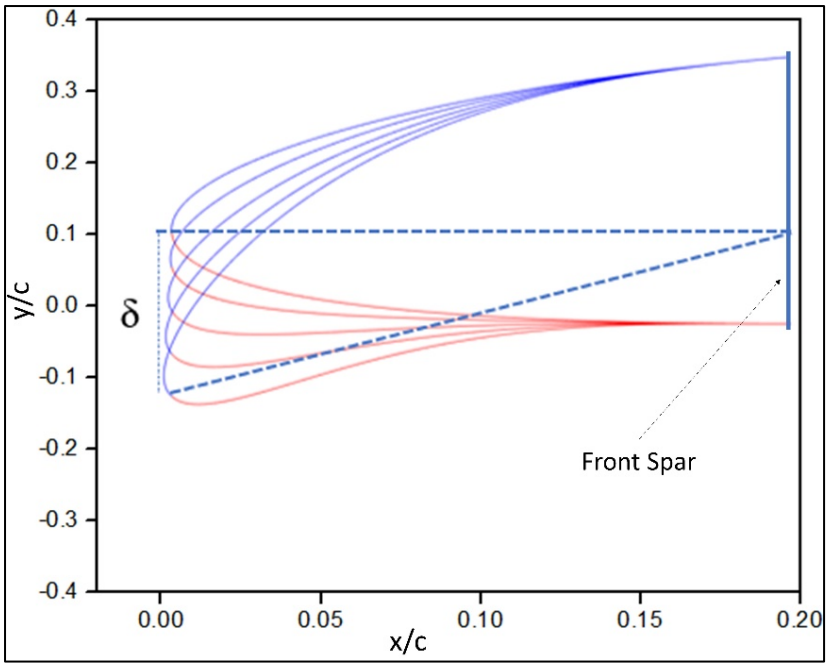

Figure 5.2 Variable morphing leading edge airfoil at different deflection angles

5.2.2.2 Computational Domain and Method

The C-shaped computational flow domain consists of a UAS-S45 airfoil with a morphing leading edge, as shown in Figure 5.3. In the present investigation, the $\gamma - Re_\theta$ turbulence model was used, and to keep the grids in the viscous sublayer; the first layer height in the wall required a y^+ less than one. All spatial terms in conservation equations are discretized using the second-order upwind approach. The solver manages the pressure-velocity coupled algorithm, and the gradient term is computed using the least-squares cell-based configuration. Four boundary conditions are a velocity inlet, a pressure outlet, symmetric faces with airfoils, and a no-slip condition on the wall. The inlet and pressure far field are located at 20-chord lengths (20 c) distance from the leading edge, and the outlet domain is 30 c away. All test cases are performed for a Reynolds number Re = 2.4×10^6 from chord data and a Mach number of 0.10 in a free steam flow velocity of 34 m/s at standard sea-level conditions.

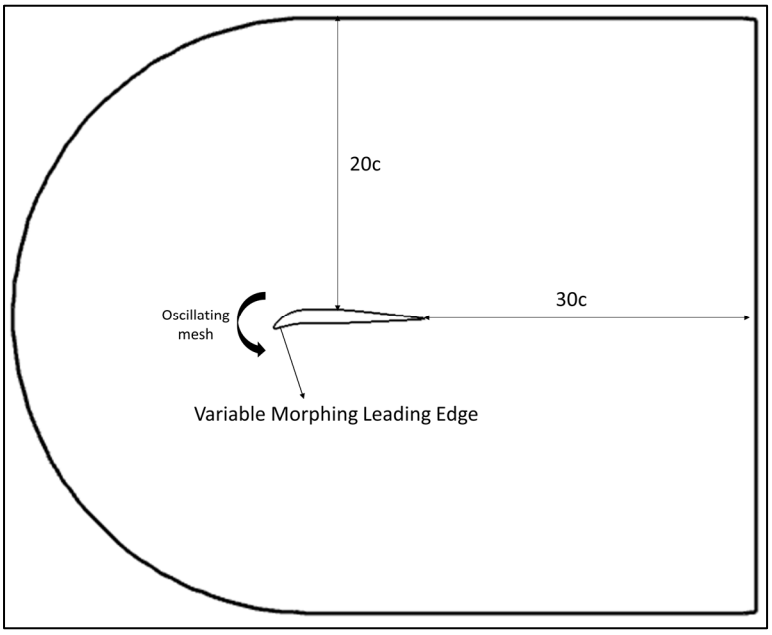

Figure 5.3 Computational region and boundary conditions

5.2.2.3 Dynamic Mesh Technique

The dynamic mesh update methods included in ANSYS Fluent were utilized to simultaneously deform the mesh and the geometry while maintaining a high-quality mesh. Diffusion-based smoothing was used because it is more robust at mesh quality preservation (as required for moving boundaries) than spring-based smoothing. The mesh grid is shown in Figure 5.4. In addition, a User-Defined Function (UDF) was created to include the unsteady parametrization method to use the dynamic meshing schemes in Ansys Fluent. The UDF uses the DEFINE_GRID_MOTION macro included in Ansys Fluent.

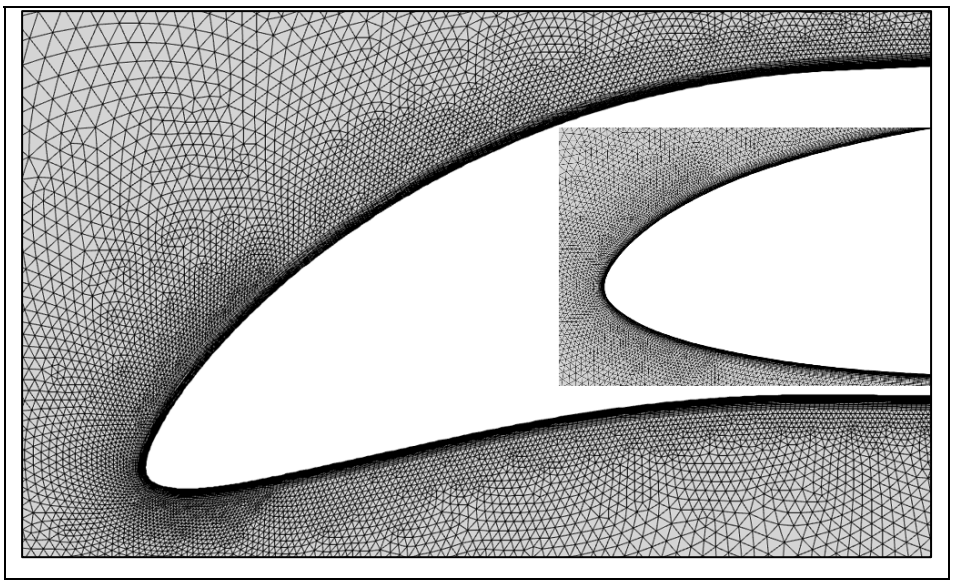

Figure 5.4 A dynamic mesh model of the variable morphing leading edge airfoil

5.3 Results and Discussion

The optimization methodology described in our previous paper (Bashir, Longtin-Martel, et al., 2022) was used to determine and improve the aerodynamic performance of the morphing leading-edge airfoil.

5.3.1 Optimization Results

The aerodynamic shape optimization was designed to maximize the lift-to-drag coefficient at different Mach numbers of 0.08, 0.1, and 0.15. The unsteady aerodynamic analysis of the morphing leading edge with its downward deflection and its influence on the stall angle of attack was then presented.

Table 5.1 Parameters of three different optimization algorithms

Black Widow Optimization Algorithm		**Genetic Algorithm**		**Particle Swarm Optimization**	
Spider Size	40	Population Size	40	Swarm Size	40
Generations	50	Generations	50	Iterations	50
Reproduction rate	0.6	Crossover	0.7	Cognitive factor (C1)	1.2
Cannibalism rate	0.44	Mutation	0.3	Social factor (C2)	1.2
Mutation rate	0.4				

Several separate CPUs were used to minimize the optimization process runtime for different flight cases with all three optimization algorithms. In addition, the optimization was performed to maximize the lift-to-drag ratio as the fitness objective.

The hybrid optimizer based on Particle Swarm Optimization (PSO) coupled with the Pattern Search algorithm was used for the UAS-S45 optimization to enhance the solution convergence and refinement. The PSO is based on a simplified social behavior study closely related to the swarming theory, with a solution set represented by particles that heuristically explore a search space. The efficiency of PSO concerning the efficiency of a genetic algorithm is due to its independence on parameters, namely crossovers and mutations; information is shared amongst

the population of particles to update the solution. The updated position of a particle depends on the best solution found by the single particle itself and by the best seen by the whole swarm. This way, the space is explored efficiently, and local minimums do not affect the optimization results.

Figure 5.5(a, b) show the pressure coefficient plots for an angle of attack of 2° and 6°, respectively, and a Mach number of 0.1. The morphed airfoil presents a smoother pressure peak at an angle of 2°, with an increased lift-to-drag ratio. It can be observed that a significant pressure variation occurred near the leading edge on the airfoil's upper side. The suction peak was progressively smoothed and redistributed from the reference airfoil to the optimized airfoil, which can be observed by forming a region of lower pressure on the morphing skin, slowly dissipating up to the mid chord. The pressure bump consecutive to the suction peak in the optimized airfoil was indicative and succeeded by a region providing for the total lift. The upper side pressure curve for the 6° angle of the attack shows the flow acceleration generating a separation bubble, which then attaches to the airfoil.

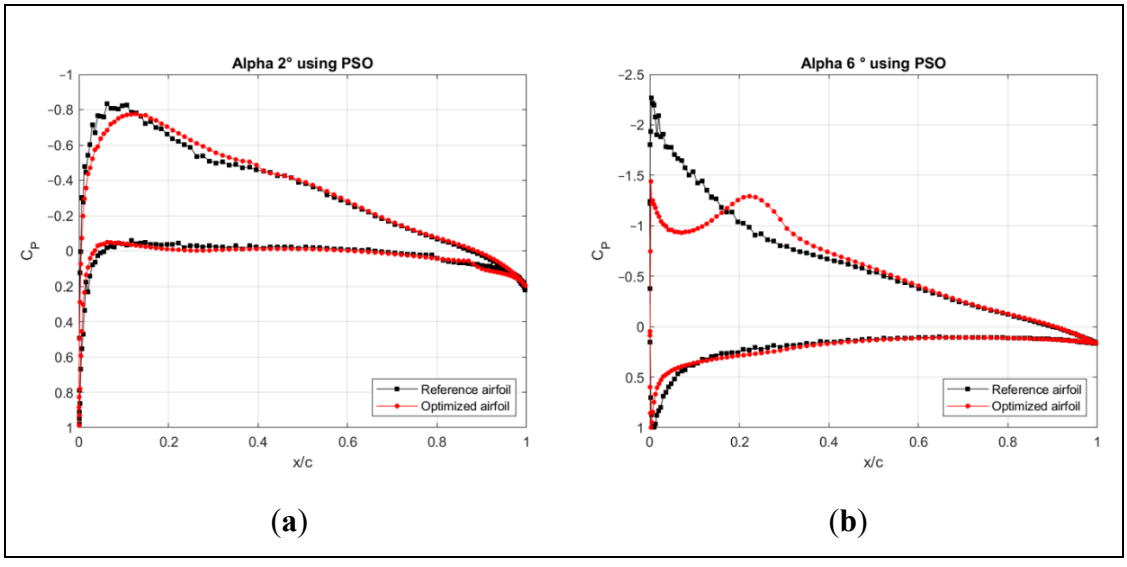

Figure 5.5 Cp distribution versus chord length using the PSO algorithm for the (a) angle of attack of 2° and (b) of 6°, compared to the reference airfoil

Genetic algorithms (G.A.s) can solve a wide variety of optimization problems, regardless of whether the fitness function is stable or non-stationary (changes over time), linear or nonlinear, continuous or discontinuous, or subject to random noise. Moreover, because a population's offspring operates independently, it can simultaneously explore the search space in various directions.

The pressure coefficients obtained by the G.A. are close to those obtained using a hybrid optimizer based on a PSO algorithm, as shown in Figure 5.6.

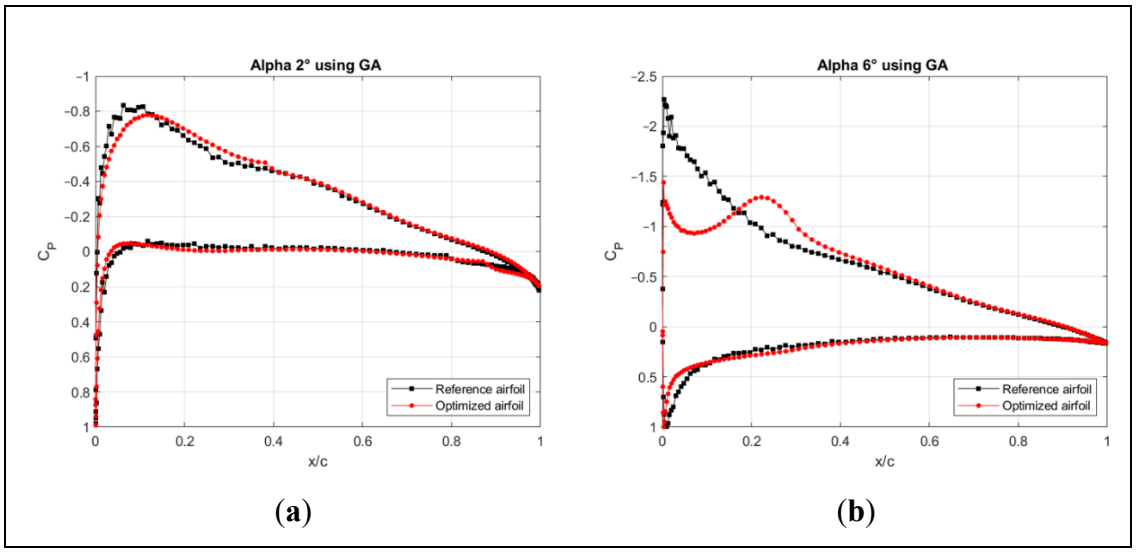

Figure 5.6 Cp distribution versus chord length using the GA algorithm for the (a) angle of attack of 2° and (b) of 6°, compared to the reference airfoil

The Black Widow Optimization (B.W.O.) algorithm is well-known for its different stages and implementations (Procreate, Cannibalism, and Mutation) at various parameters, including the procreating rate, cannibalism rate, and mutation rate. Figure 5.7 presents the pressure coefficient plots, showing that the morphing airfoil has a smoother pressure peak at 2° than at 6° and a better lift-to-drag ratio. On the upper surface of an airfoil, the main pressure variation occurred around the leading edge, where a reduced pressure area was formed on the morphing skin, which then gradually degraded up to mid-chord. Further results have been added in Annex I.

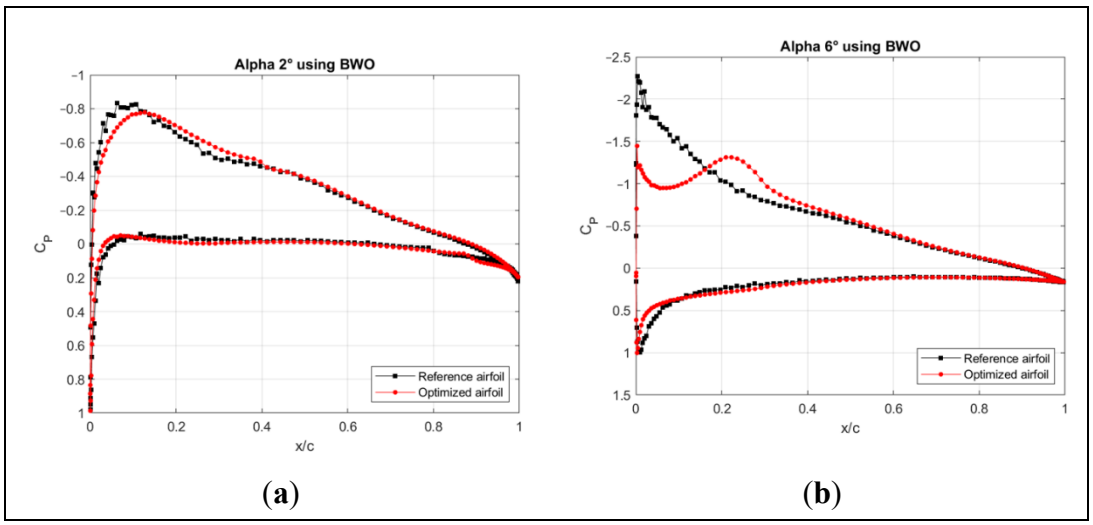

Figure 5.7 Cp distribution versus chord length using the BWO algorithm for the (a) angle of attack of 2° and (b) of 6°, compared to the reference airfoil.

The three optimization algorithms revealed that the B.W.O. converged quickly to the best optimal solution. Therefore, a B.W.O. algorithm-based method was used to investigate additional cases at different angles of attack and Mach numbers of 0.08, 0.1, and 0.15. The analysis was performed to better understand the optimization results at various flight conditions to determine its effectiveness. The lift-to-drag ratios at the three Mach numbers of 0.08, 0.1, and 0.15 and angles of attack from 0 to 10 in 2-degree increments are presented in Figure 5.8. At Mach 0.08, it is clear that the best improvements in efficiency are obtained at angles of attack of 4 to 6°. Similar trends (best performance) are noticed for Mach 0.10 and 0.15 and 6° angle of attack. Overall, the objective of maximizing the C_L/C_D ratio showed promising results for all angles of attack.

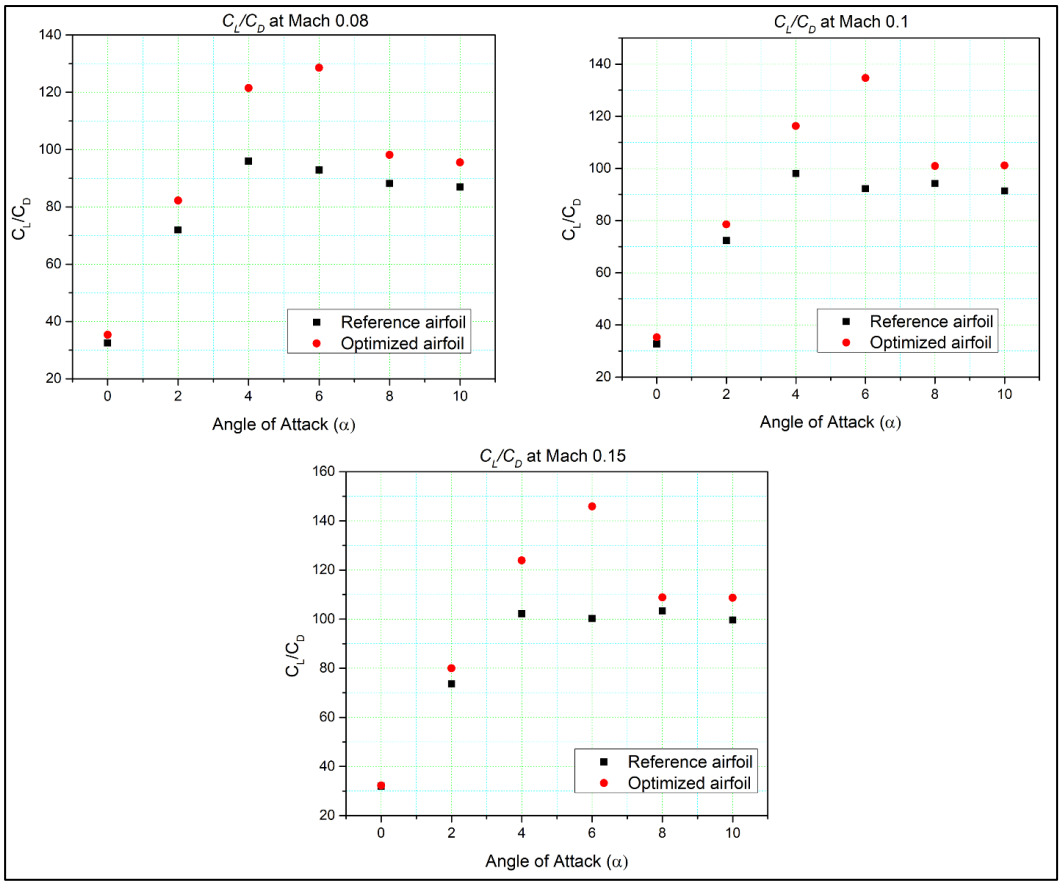

Figure 5.8 Comparison of CL/CD for the reference and optimized airfoils at different angles of attack and Mach numbers 0.08, 0.10, and 0.15. The lift-to-drag ratios at these three Mach numbers show that the best improvements in efficiency are obtained at angles of 4 to 6°

Figure 5.9a shows the convergence plots cost variation with the number of iterations obtained with these algorithms at the cruise flight condition. According to the convergence plot for cruise flight conditions at an angle of attack of 20 degrees, the GA requires 16 iterations to achieve a global minimum value of 0.01271, the PSO requires 15 iterations to achieve a global minimum value of 0.01270, and the B.W.O. requires only 14 iterations to reach the global minimum value of 0.012690. For the climb flight condition considered at a 6° angle of attack, both the G.A. and the PSO require 18 iterations to reach the global minimum values of 0.0074038 and 0.0074029, respectively, and the B.W.O. requires only 15 iterations to achieve a global minimum value of 0.007399, as shown in Figure 5.9b. Thus, the Black Widow Optimization algorithm proved superior to the other two.

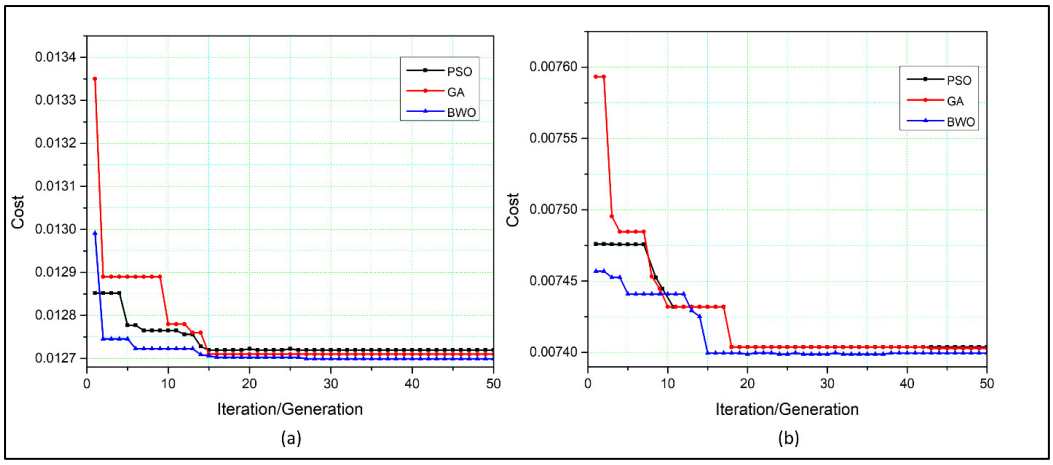

Figure 5.9 Evaluation of the cost for the B.W.O., the PSO, and the G.A. algorithms, (a) cruise condition and (b) climb condition

5.3.2 Unsteady Aerodynamic Results

The unsteady aerodynamic predictions may be more realistic than the steady morphed leading edge because the sudden changes in the flow behaviour of an airfoil can be obtained while the leading edge deflects downwards. Instantaneous aerodynamic coefficients and pressure distribution results can reveal the flow separation process and how the Laminar Separation Bubble (L.S.B.) moves over the airfoil during the morphing. This study used the methodology mentioned in Section 2.2. The turbulence model selection, the grid convergence for the mesh topology, and the grid size were all considered elements of the validation process.

5.3.2.1 Effects of Deflection on Morphing Leading Edge Aerodynamic

The effects of the leading-edge deflection at different angles of attack and time steps on the aerodynamics of the morphing airfoil are discussed. The impact of varying deflection rates (time steps) is analyzed until it reaches maximum deflection. The pressure contour with streamlines of the leading-edge morphing airfoil is shown in Figure 5.10. The pressure distribution shows the areas of low- and high pressure near the drooped leading edge. The flow around the leading edge shows the stagnation point that separates the flow between the upper and lower surfaces.

The Variable Morphing Leading-Edge (VMLE) of an airfoil is investigated at different angles of attack. The unsteady analysis of the morphing airfoil is performed by deflecting the airfoil's leading edge downwards with time at a morphing frequency of 2 Hz to provide further insights into the time-dependent lift and drag forces at different time steps. This study includes only the downward deflection of the leading edge. As mentioned in Section 2.2.3., UDF was used to morph the leading edge during the different time steps of the flow.

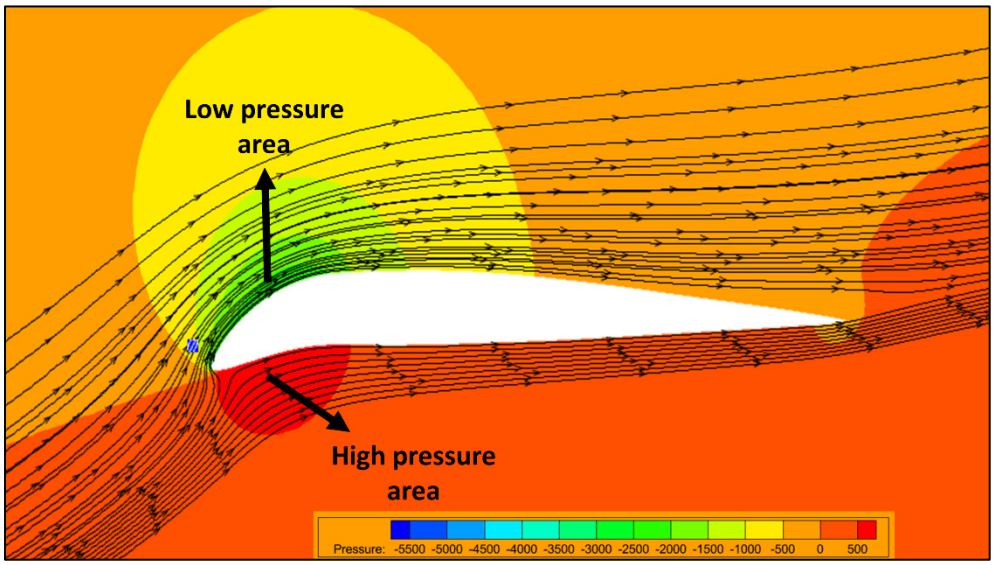

Figure 5.10 Pressure contour with streamlines of the morphing leading-edge airfoil

The steady aerodynamic analysis of the reference airfoil at 0° angle of attack is shown in Figure 5.11, with no flow separation over the airfoil surface. The reference airfoil was then subjected to transient analysis using the downward deflection of the airfoil's leading edge. The flow analysis is shown at different time steps. At t = 1.54 s, the leading-edge (L.E.) deflection rate did not cause any noticeable change in the flow behavior, as indicated by the corresponding pressure distribution. When the L.E. deflection increases at t = 1.635 s, no primary vortices are observed, and a slight pressure fluctuation is also noticed. Finally, at t = 1.74 s, the morphing ended, and the pressure distribution remained the same.

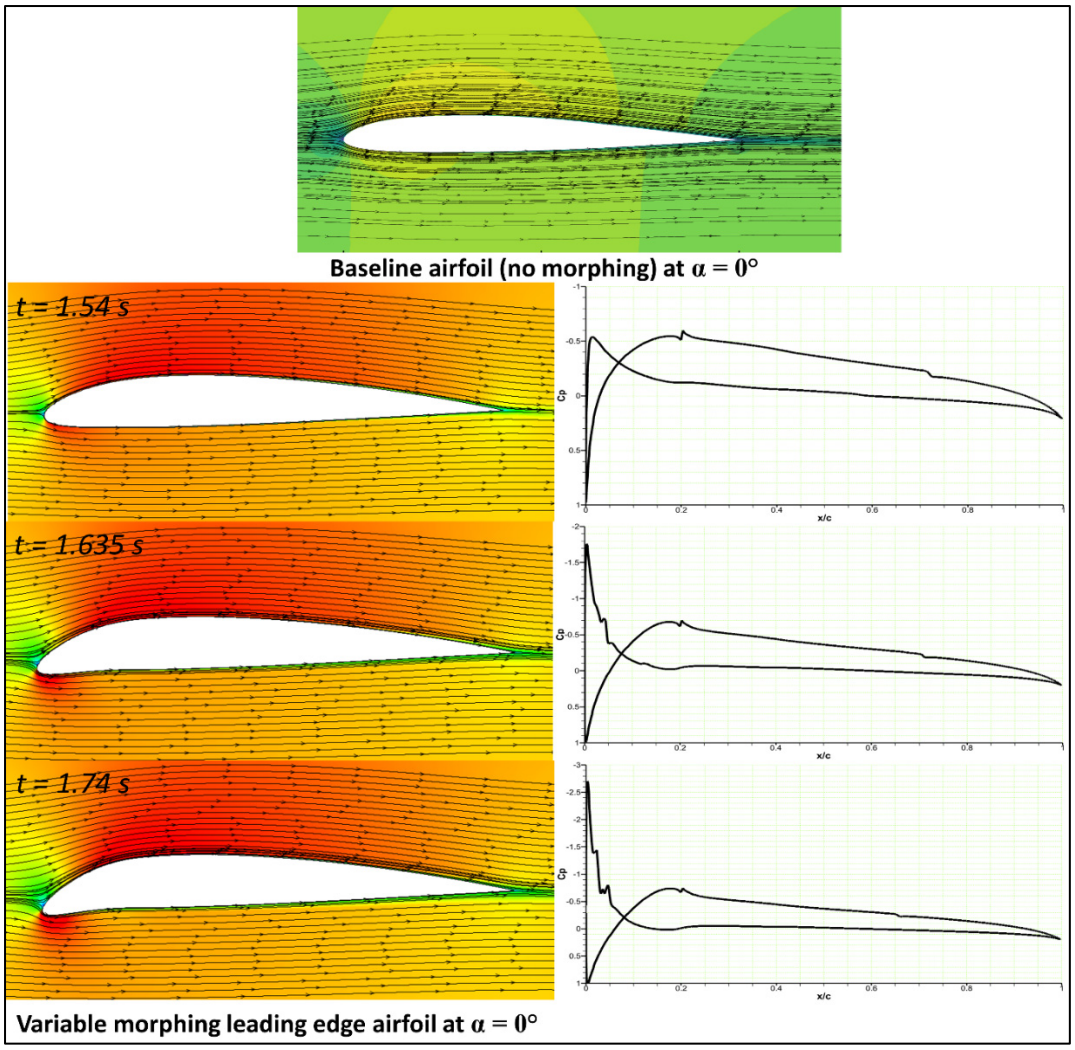

Figure 5.11 Streamline velocity contours at different time steps in a variable morphing leading edge and the Cp distribution at 0° angle of attack

The steady aerodynamic analysis of the reference airfoil at a 6° angle of attack is shown in Figure 5.12, where no flow separation was found over the airfoil surface. The downward deflection of the airfoil's leading-edge initiates at t = 1.50 s using the UDF, as mentioned in Section 2.2.3. The flow behaviour is shown at different time steps. At t = 1.54 s, the rate of leading-edge deflection did not cause any noticeable change in the flow behaviour, which can also be seen from the corresponding pressure distribution. Similarly, no flow separations were observed at the other time steps. Figure 5.12 shows that the leading-edge pressure reaches a peak value of $Cp = -1.6$ at t = 1.74 s.

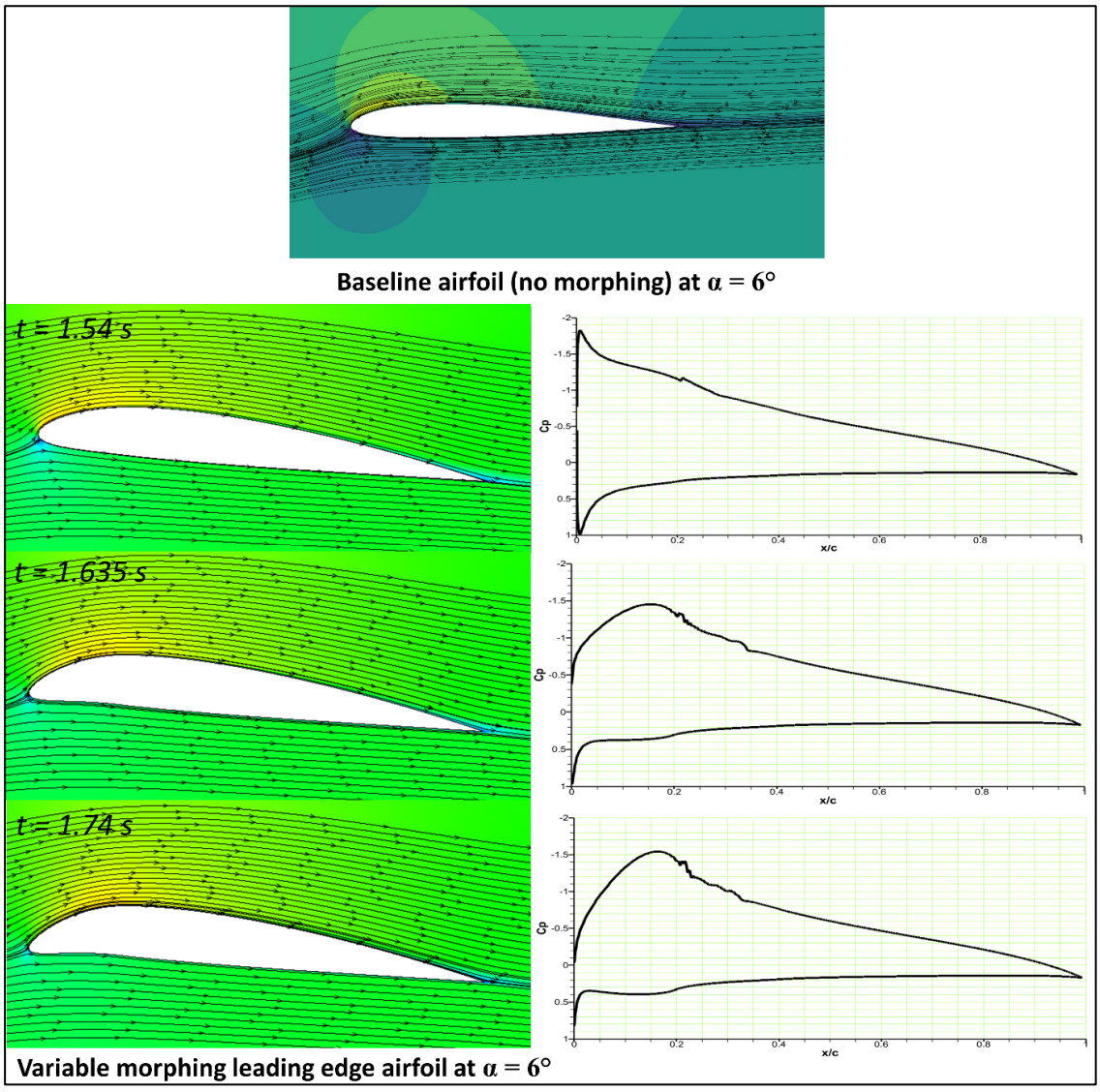

Figure 5.12 Streamline velocity contours at different time steps on a variable morphing leading edge and the Cp distribution at a 6° angle of attack

The large separation region at an attack angle of 18° for the baseline airfoil is in Figure 5.13. However, the droop nose leading edge airfoil at different leading-edge deflections shows that there is no significant flow separation or vortex and that the attached flow state is kept well within the large portion of the drooped airfoil. The flow streamlines indicate that a flow separation area is developed at the end of the trailing edge, and the corresponding pressure

coefficients suggest that the flow remains attached to the airfoil surface. The leading-edge suction values reach a peak of $Cp = -7.5$ at $t = 1.74$ s.

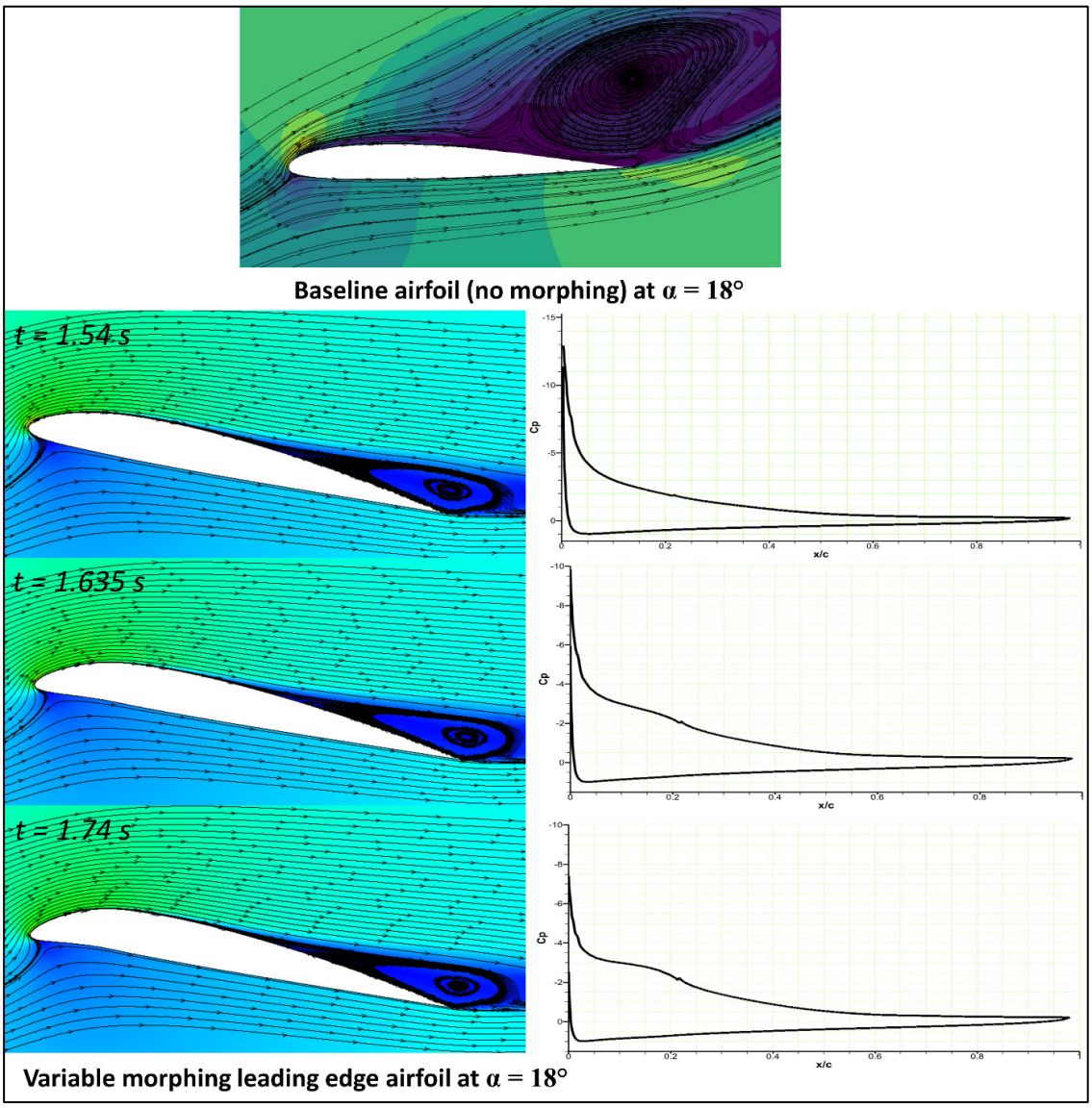

Figure 5.13 Streamline velocity contours at different time steps on a variable morphing leading edge and the Cp distribution at an angle of attack of 18°

Figure 5.14 depicts the flow separation area for the reference airfoil at an angle of attack of 22°. The trailing edge is not crucial in the initial vortex formation, especially at high angles of attack. However, it can improve the overall circulation around the airfoil by continuously

shedding counter-rotating vorticity into the wake. This increased circulation causes more vorticity accumulation near the leading edge, thus forming stronger vortices.

On the other hand, the droop nose deflection of the leading edge shows the trailing edge vortices at different stages; the influence of the trailing-edge flow may increase significantly when the primary vortex from the leading edge approaches the trailing edge. The development of primary and secondary leading-edge vortices is seen at t = 1.54 s; when the airfoil continues to droop at t = 1.635 s, the vortices start to reduce, and the flow begins to re-attach on the airfoil. The leading-edge deflection continues to increase until it reaches its maximum at t = 1.74 s. At the same time, the flow keeps re-attaching to the airfoil, and the trailing edge separation area remains small. However, it is essential to note that the flow separation area of the morphing airfoil remains much smaller than that of the reference airfoil. Therefore, the flow separation can be controlled using the variable morphing leading edge.

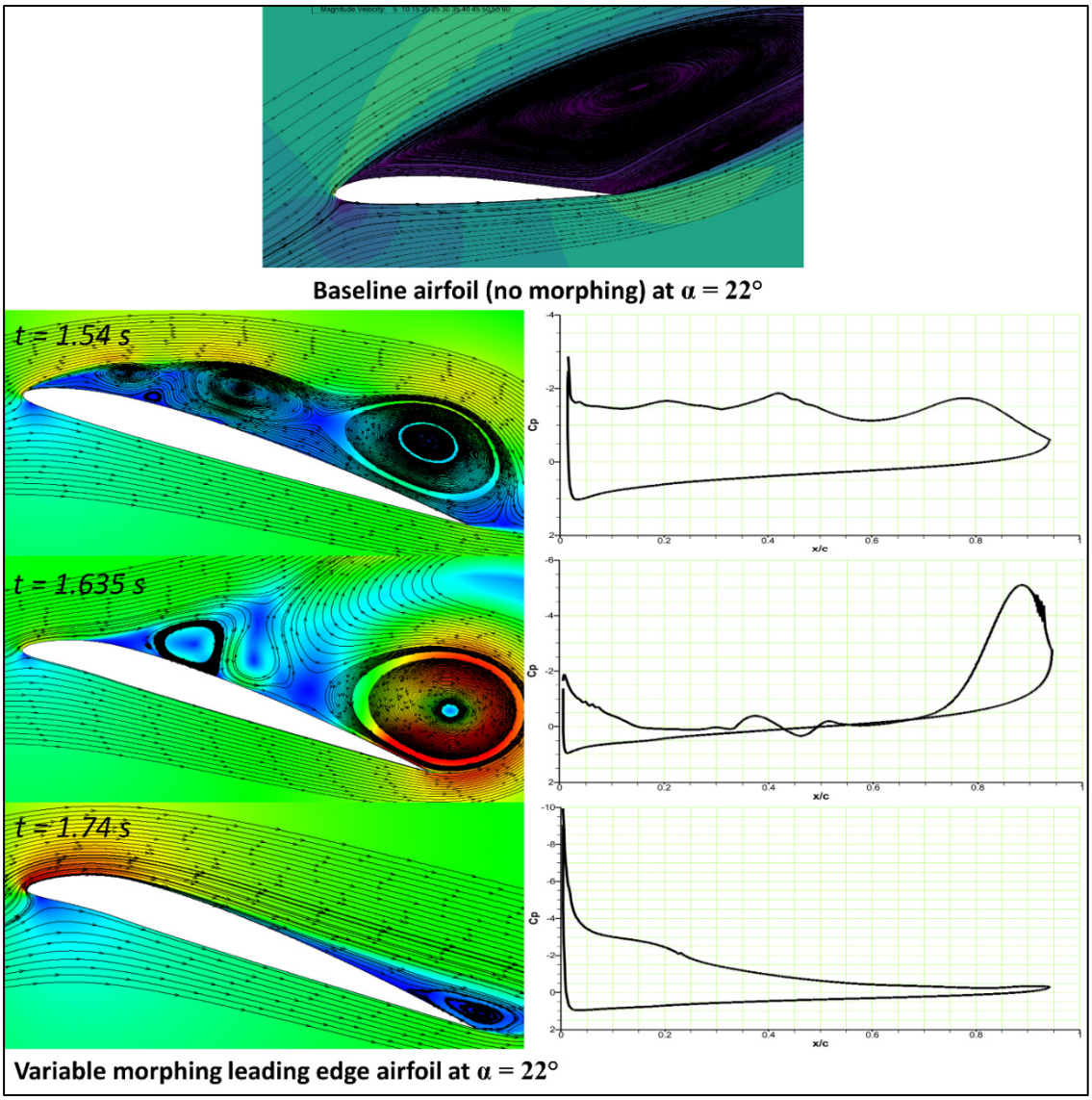

Figure 5.14 Streamline velocity contours at different time steps on a variable morphing leading edge and the Cp distribution at 22° angle of attack

Figure 5.15 compares the reference airfoil with the drooped morphing airfoil at an angle of attack of 24°. The flow remains fully separated on the reference airfoil, depicting the stall. For the VMLE morphing airfoil at t = 1.54 s, the vortices are majorly formed over the airfoil, and they continue to be seen at t = 1.635 s, where the flow separation area is smaller as compared to that of the reference airfoil. However, the flow separation reduces, and the flow is re-attached to the airfoil. Thus, it is found that the flow separation can be controlled using the variable morphing leading edge.

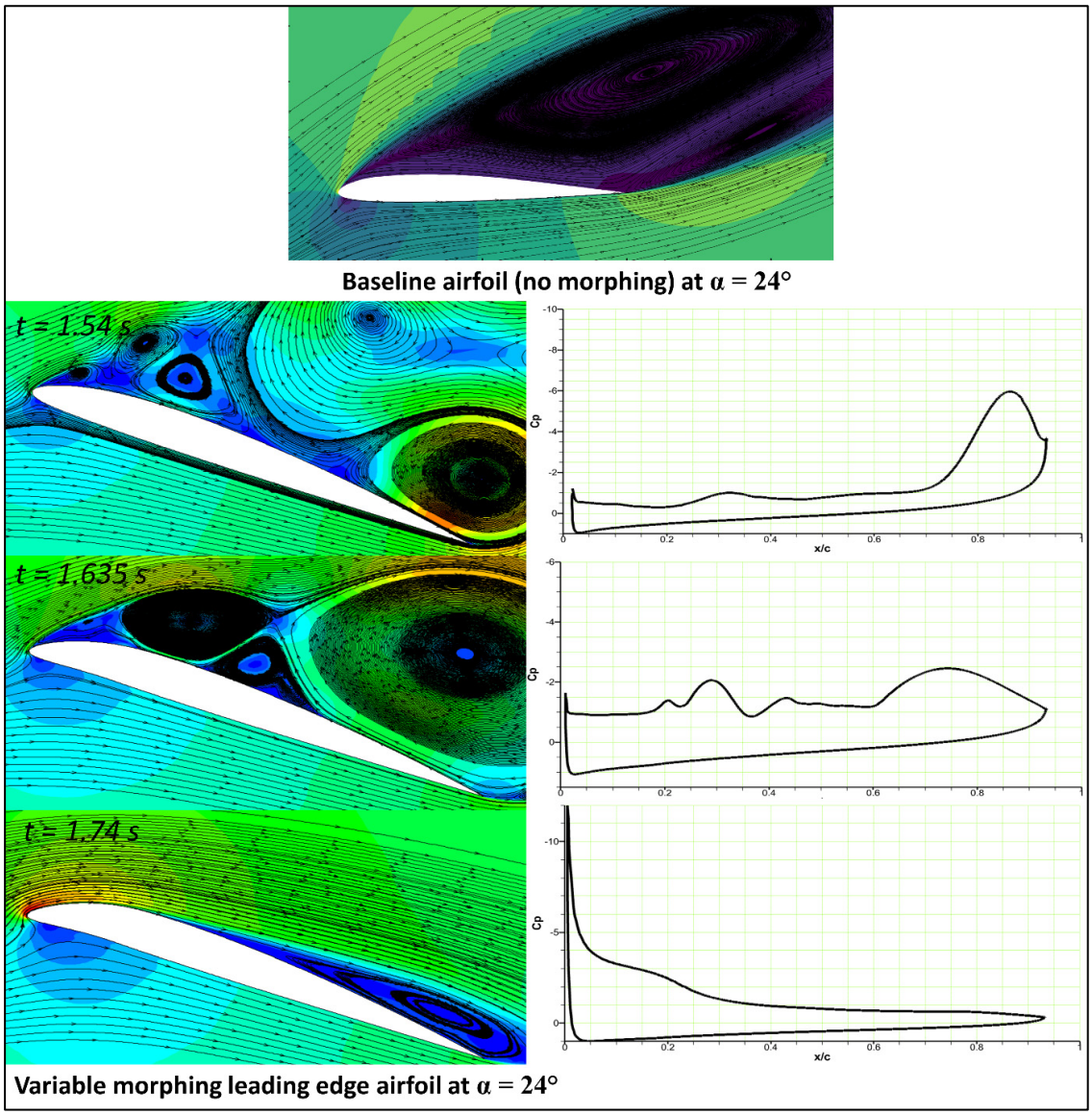

Figure 5.15 Streamlined velocity contours at time step of t = 0.53 s on a variable morphing leading edge and the Cp distribution at 24° angle of attack.

The understanding of the role of vorticity in the shear layer that forms at the interface between the outer flow and a separated flow zone close to the suction surface of the airfoil is desired to improve the flow separation prediction capabilities. Figure 5.16 shows the vorticity contours along with the flow development over a baseline airfoil (a) and a variable morphing edge airfoil (b) for different angles of attack and time steps during the morphing motion. At an 18° angle

of attack and t = 1.635 s, the separation is found at the trailing edge area of the airfoil. As the airfoil morphs, the vortex is smaller at t = 1.74 s. The reversed flow spreads from the trailing edge towards the leading edge for an airfoil at a 22° angle of attack and t = 1.635. The morphing continues till t = 1.74, and a considerable decrease in the vorticity magnitude can be seen. The same trend is found for the airfoil at a 24° angle of attack. This illustrates the gradual attachment of the boundary layer, with the separation point migrating from the leading edge to the trailing edge. The variable morphing leading edge action thus appears to dramatically improve the airfoil performance during the downstroke.

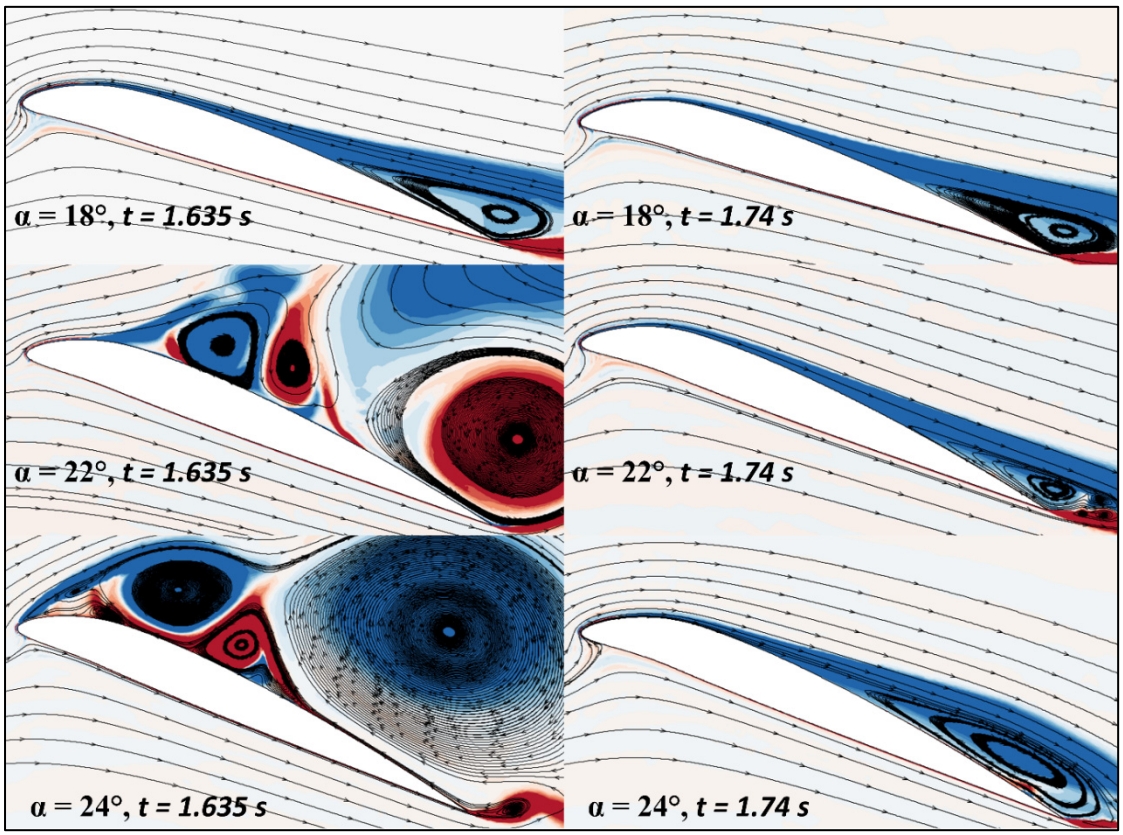

Figure 5.16 Vorticity contours with flow streamlines at different time steps and angles of attack (18°, 22°, and 24°)

With increasing Mach number, the mechanism of vortices shedding changes, as seen in Figure 5.17a–c, respectively. In these cases, the leading-edge morphing starts at t = 1.5 s, reaches maximum deflection at t = 1.74 s, and returns to its original position at t = 2 s. At Mach number

= 0.08, the leading-edge vortices are shifted towards the trailing edge but continue to fluctuate during the leading-edge morphing. As the Mach number increases to 0.1, the lift coefficient increases accordingly, and the flow re-attaches with the airfoil during t = 1.6 s to 1.74 s and attains the smooth lift coefficient distribution. At Mach number = 0.15, the flow structures become more coherent along with the peaks in the lift coefficients. With an increasing Reynolds number, leading-edge deflection has a more significant effect on the leading-edge separation.

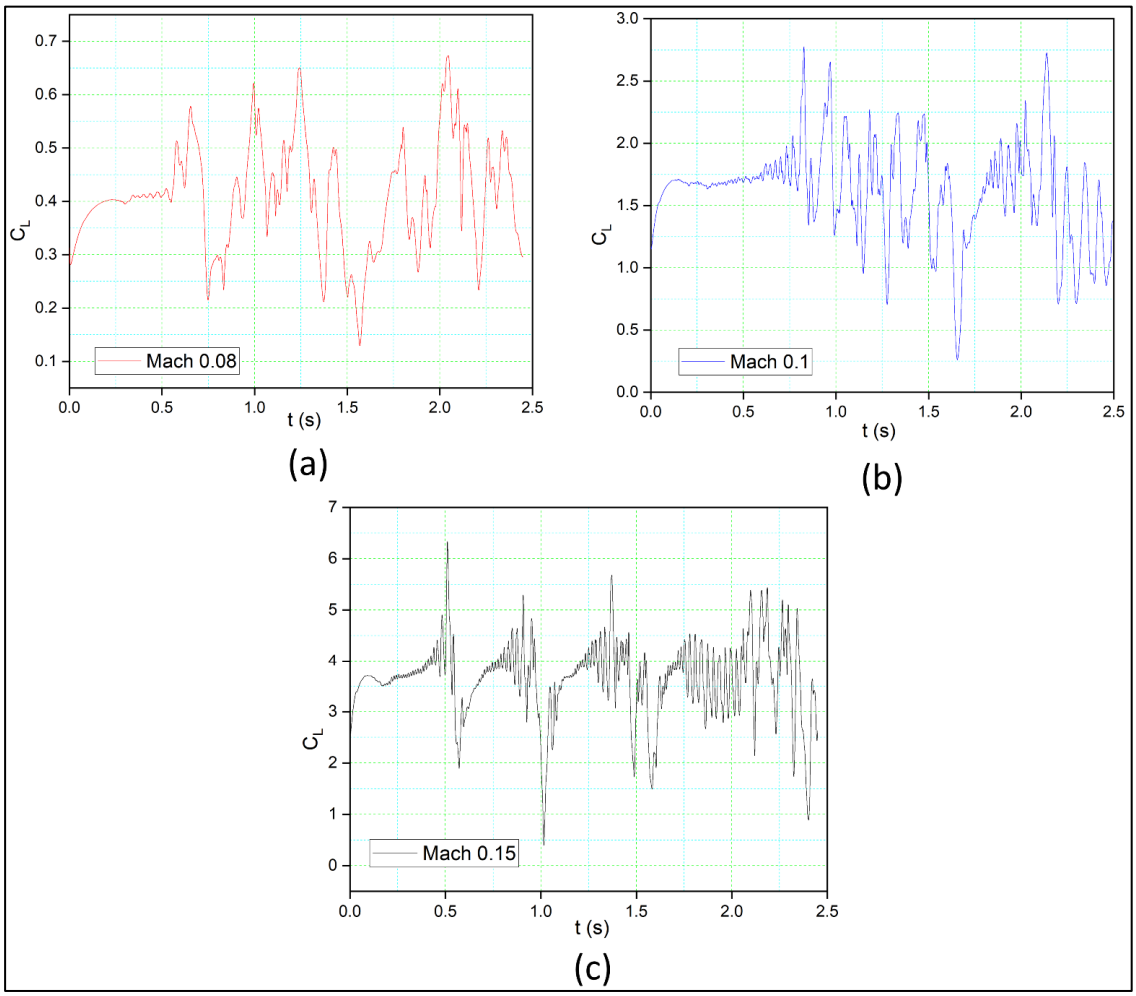

Figure 5.17 Aerodynamic lift coefficients for the morphing airfoil with time (s) at three different Mach numbers of (a) 0.08, (b) 0.1, and (c) 0.15

5.3.3 Preliminary Morphing Leading Edge Design

Numerous techniques involve reducing the weight, maximizing the lift effectiveness, and maximizing the buckling factor of an aircraft wing subject to aeroelastic and structural restrictions (Winyangkul et al., 2021), and studies for morphing skins have been developed, most of them are explained in (Chillara et al., 2020; Murugan et al., 2013; Thill et al., 2008). The UAS-S45 wing considered in this study has a span of 5.867 m and a mean chord of 0.53 m. A reference section of the wing with a span of 0.7 m was selected for the structural analysis in this paper, as shown in Figure 5.18.

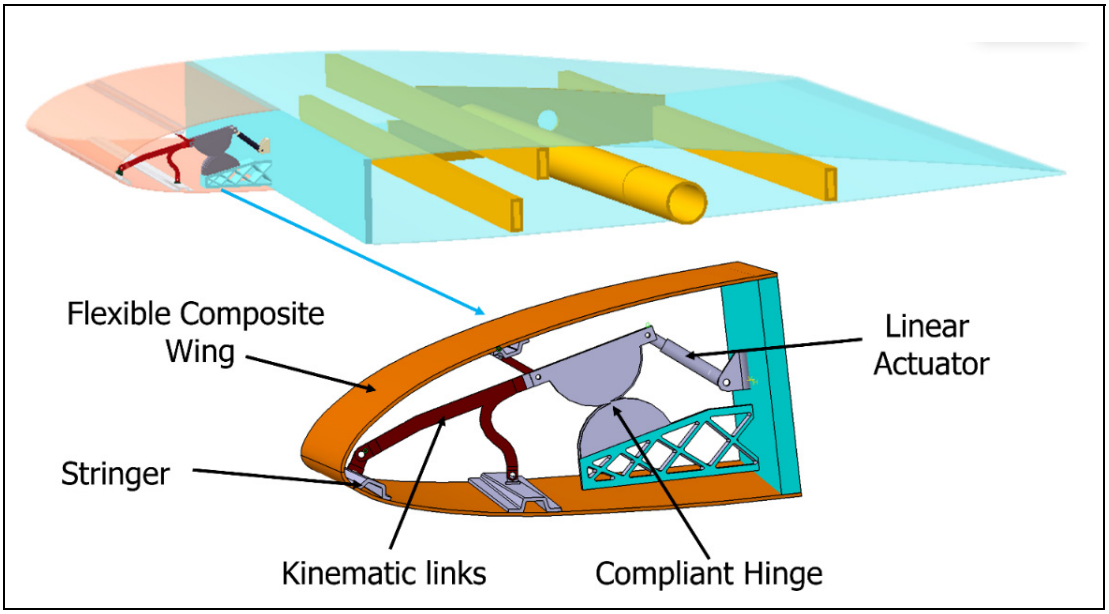

Figure 5.18 L.E. geometry at the reference section

5.3.3.1 Key Material Properties

The data manuals describe that the UAS-S45 wing is manufactured from S-glass, Kevlar, and carbon fibers. Due to the flexible nature of a morphing leading edge, carbon fiber and S-glass were selected to simulate its behaviour under the same conditions. The specifications of the materials used for UAV manufacturing and the mechanical properties are given in Table 5.2.

Table 5.2 Mechanical properties of Carbon/Epoxy S-Glass/Epoxy

Material Properties	Carbon/Epoxy	S-Glass/Epoxy
Young′s Modulus X direction (MPa)	59,160	50,000
Young′s Modulus Y direction (MPa)	59,160	8000
Young′s Modulus Z direction (MPa)	7500	8000
Shear Modulus X. Y. (MPa)	17,500	5000
Shear Modulus Y. Z. (MPa)	2700	3846.1
Poisson′s Ratio XY	0.004	0.3
Poisson′s Ratio YZ	0.3	0.4

5.3.3.2 Composite Material Modeling

Defining the mechanical properties of primary materials, such as the fabrics and ply type (s), including their failure criteria, is essential for composite materials modeling. The representation and ply layering in the laminate is shown by including the wing structure model shell elements. In the A.C.P. (Ansys Composite Pre-Post) module, the wing model is assigned the fabrics that can be designed along with other composite layers combined to form the completed laminated composite materials. By creating the composite fabric according to its thickness, a laminate is prepared by orienting all fabrics according to their assigned direction of 0/90/±45/90/0. One of the most challenging aspects during design configuration is the combination of various materials with different plies and orientations.

Three stringers reinforced the morphing wing skin on both the upper and lower skin panels to avoid deformations in areas far from the actuation mechanisms, which are oriented along the wingspan. The skin was made of two layers of fiberglass/epoxy and four layers of carbon fiber/epoxy laminate arranged in a symmetrical layup [0/90/±45/90/0] s 1.2 mm thick. The updated laminate in terms of the material layup and the orientation choices is shown in Figure 5.19.

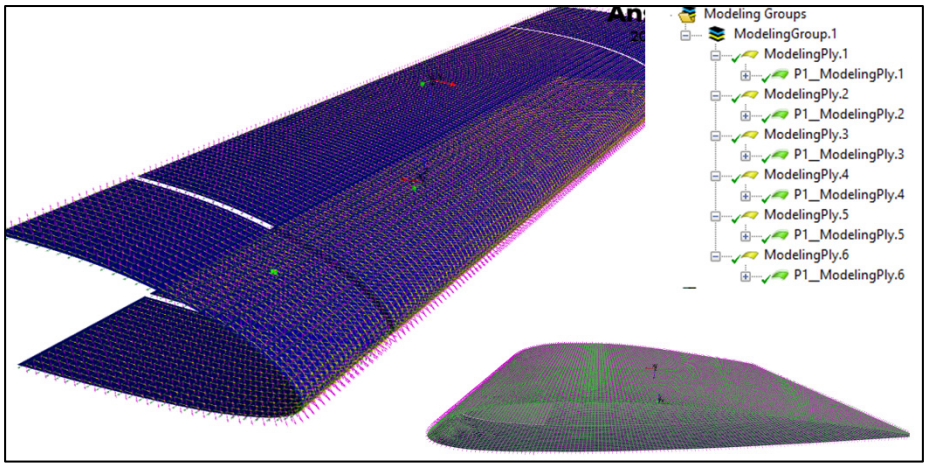

Figure 5.19 Modeling of the assigned laminated composite material components with the orientation direction

The accurate mechanical representation of a composite layup through simulation studies is a requirement for the design modeling process and manufacturing. Therefore, it is essential to integrate the numerical approach to the composite aspect of A.C.P. and the F.E. analysis of static structural analysis. In this study, the composite skin analysis considering the sensitivity analysis of different composite parameters such as the number of plies, fiber orientation, ply thickness, etc., can be done during the F.E. investigation. The integration of F.E. static structural and A.C.P. together was systematically linked by conveying the generated shell element model from A.C.P. (Pre-Processing) to the static structural model to push the analysis further and assess the composite Design in A.C.P. (Post-Processing). Hence, the results of the FE-ACP computational study analysis in the static structural analysis were evaluated from a composite point of view.

5.3.3.3 Static Structural Analysis

Static Structural Analysis was the next step, in which the deformations and stresses were analyzed. Figure 5.20a shows the total deformation contour in the structure due to the generated residual stresses. It revealed that the deformation occurred at a maximum of 5.09 mm for the layup. The red color indicates the critical values, whereas the dark blue indicates

the safest ones. Figure 5.20b shows the maximum stress that could be generated in the structure, 151.89 MPa. Similarly, Figure 5.20c shows the equivalent strain.

Fiber breakage, matrix cracking, and fiber pull-out are non-catastrophic failure modes in composites that can cause localized damage (Cantwell et al., 1991). Failures can occur at once or develop over time, making it challenging to observe composite failure. It is worth noting that Von Mises failure criteria can't be used for composite materials analysis because it is appropriate for only isotropic materials. Instead, Tsai-Hill, Tsai-Wu, or Tresca-based failure criteria must be used to obtain more realistic results. The materials consist of fibers and a matrix, each with different failure mechanisms. Failure is also influenced by the interface between the fibers and the resin, the ply stacking sequence, environmental conditions, etc. As a result, predicting failure in composites is a challenging task.

Inverse Reserve factor (I.R.F.) indicates failure margin, and higher I.R.F. values imply a "positive" margin to failure, whereas the lower values show a "negative margin." For example, I.R.F. non-critical values are 0 to1 while critical values are >1. Subsequently, the Inverse Reserve Factor (I.R.F.), used as a composite failure tool in this study, is shown in Figure 5.20d. For this model, the maximum value of I.R.F. found was 0.555. The failure load and mode prediction will also be analyzed using failure indicators such as the Maximum Stress and Tsai–Wu failure criterion.

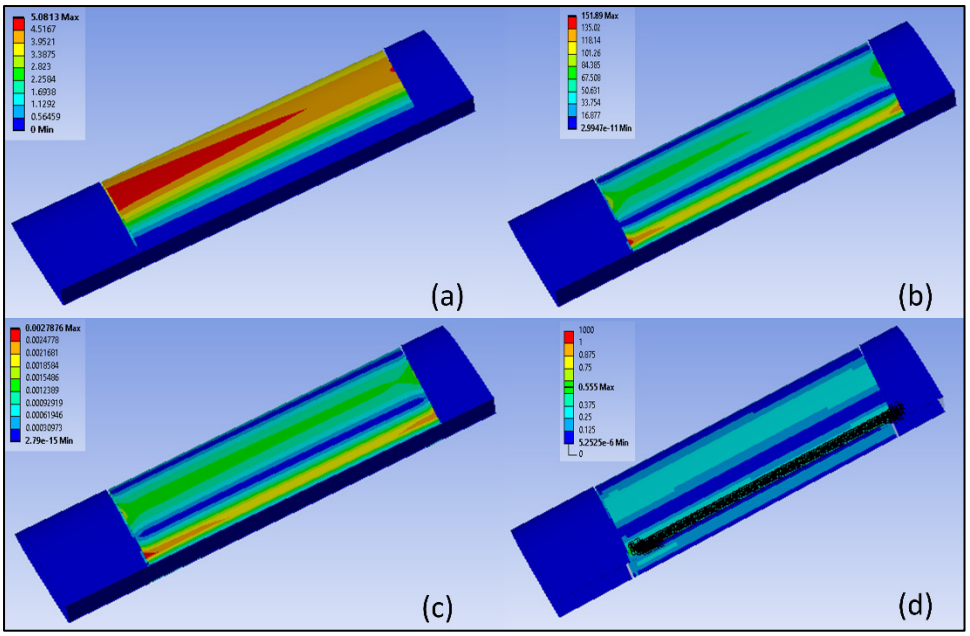

Figure 5.20 Leading Edge with glass fiber nose layup [0/90/±45/90/0]: (a) deformation, (b) equivalent stress, (c) equivalent strain, (d) Inverse Reserve Factor.

5.3.3.4 Preliminary Optimization Approach

In statistics, correlation or dependency illustrates the relationship between two or more variables. Correlation measures the degree of a linear relationship between two variables. The correlation coefficients commonly range from −1 to 1. For uncorrelated variables, the correlation coefficient is close to 0. Strongly correlated variables have a coefficient close to −1 or 1. The correlation coefficient remains positive if one variable increases with the other but increasing one variable while decreasing another result in a negative correlation coefficient. The correlation coefficient can anticipate the essential parameters that influence a model and are employed in practice for future model investigations.

The methods for calculating correlation coefficients are numerous, and several approaches can be found in the literature (Gideon, 2007; Wilcox et al., 2002). The Spearman correlation approach was utilized to discover the most correlated parameters in the morphing leading-edge wing model analysis. The correlation coefficient and variables can be analyzed in the

Correlation and Determination matrices. The main parameters of a correlation study are given in Table 5.3.

Table 5.3 Correlation Parameters

Thickness	
P20	Material thickness (ply thickness)
P19	Material thickness (Stack thickness)
Geometry	
P2	Ply Angle 1
P4	Ply Angle 2
P6	Ply Angle 3
P8	Ply Angle 4
P10	Ply Angle 5
P12	Ply Angle 6
Loads	
P47	Force X Component
P48	Force Y Component
P49	Pressure Magnitude
Failure criteria	
P53	Max. Stress Failure
P55	Tsai-Wu Failure

The sample size (N) significantly impacts the correlation; choosing a suitable sample size that provides a thorough correlation through convergence is essential. Based on the many cases analyzed, a sample size of 150 was implemented in this study.

The correlation and the determination matrices are presented in Figures 5.21 and 5.22, respectively. Their elements are employed as design factors for two failure criteria, the

maximum stress, and Tsai-Wu. The matrices have their most significant values near −1 and 1. The most relevant parameters have strong correlation coefficients, as their weight increases with sample size. The failure criteria have a strong linear association. The coefficients are dispersed throughout the matrix, indicating that a thorough matrix was supplied to identify essential parameters. These matrix results show that pressure magnitudes, ply angles, and ply thicknesses all impact the model and its Design.

Figure 5.21 shows a positive correlation between the Max-Stress failure criterion and the ply thickness and a positive coefficient of 0.4947 between the Tsai-Wu failure criterion and the pressure magnitude. Therefore, this study found the most vital connections between ply angles, ply thickness, and the failure criterion. This agrees with the composite Design and dimensioning practice where plies orientation is crucial to obtain the desired structural properties.

In addition, the maximum stress failure criterion significantly correlates with the pressure parameter (0.5149). Therefore, the failure mode at maximum stress is primarily related to the ply angles and thickness.

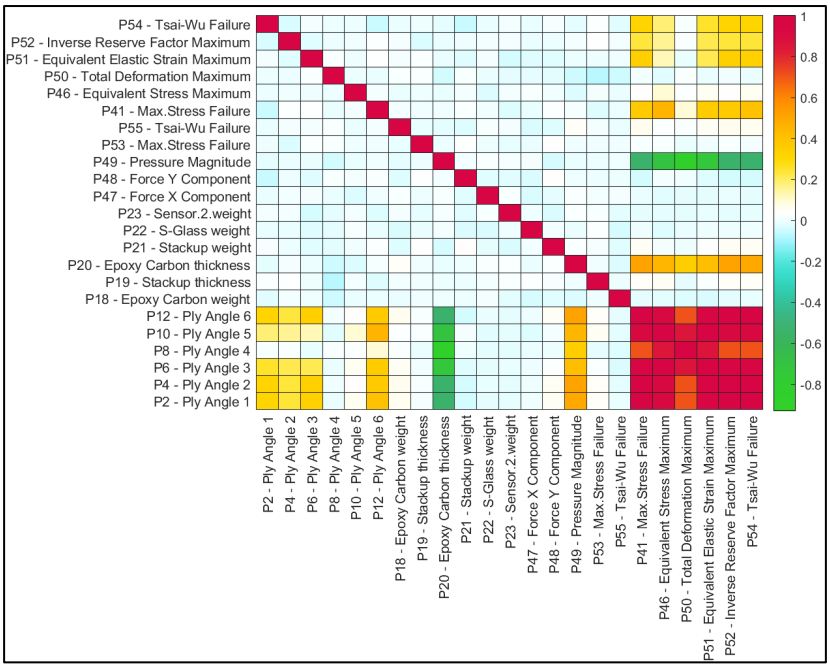

Figure 5.21 Parametric correlation matrix

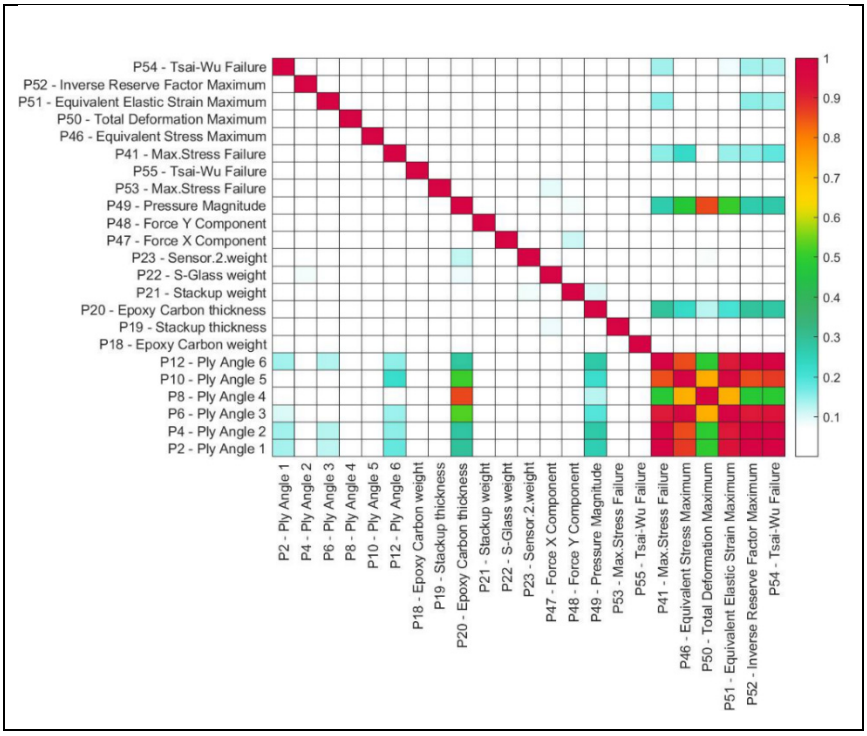

Figure 5.22 Parametric determination matrix

The sensitivity diagrams for the maximum stress and Tsai-Wu failures are shown in Figures 5.23 and 5.24, respectively. They indicate that the pressure, the ply angle, and the fiber thickness are the parameters that have the most substantial influence on the model's performance.

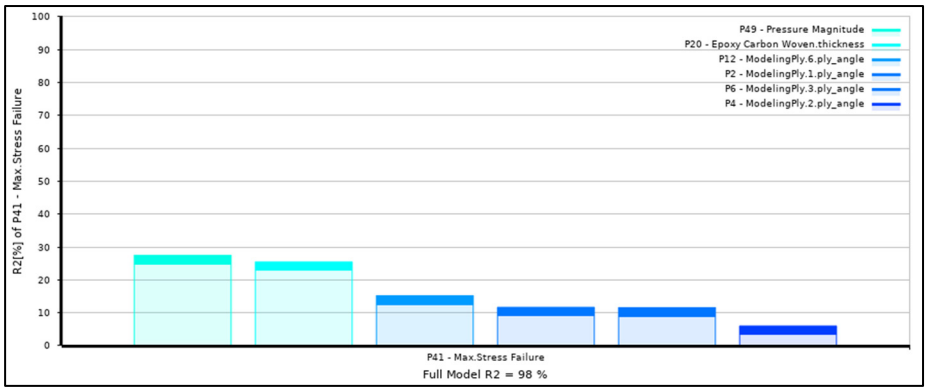

Figure 5.23 Sensitivities of max stress failure

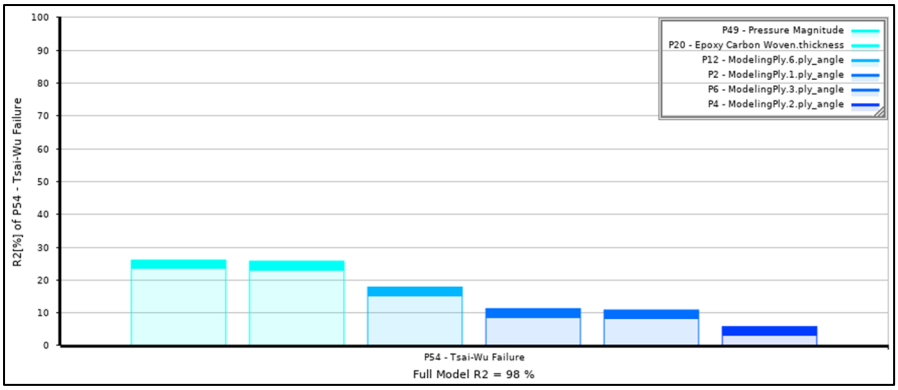

Figure 5.24 Sensitivities of Tsai-Wu failure

5.4 Conclusions

A Droop Nose Leading Edge Morphing airfoil, designed for the UAS-S45, is presented in this paper. Both aerodynamic and structural optimization was performed on the MLE airfoil. The impact of the optimization method selection for aerodynamic optimization was investigated by comparing three different optimization algorithms' results. The fitness function is the lift-to-drag ratio (L/D), which must be maximized. In addition, three other Mach numbers were used

in the optimization process: 0.08, 0.1, and 0.15, as well as the flight conditions of cruise and take-off. All these optimization algorithms consistently provided almost identical results, with lift-to-drag ratio changes of less than 0.03 % and airfoil geometries and pressure distributions that were very close to each other.

In addition, unsteady variable leading-edge morphing with a dynamic meshing scheme was performed to determine the flow behaviour of near-stall flow and use downward leading-edge deflection as a control mechanism. The numerical results showed that the variable morphing leading edge with continuous downward deflection of the leading edge increased the stall angle of attack. The variable morphing leading edge airfoil effectively reduces the flow separation and trailing edge vortices and decreases the static and dynamic stall over an airfoil. It is worth noting that a large separation region was found at an angle of attack of 18° for the reference airfoil. However, the variable morphing leading edge airfoil at different deflections showed no significant flow separation or vortex. The flow remained attached over a large part of the morphing airfoil.

A preliminary study of the Design and analysis of a morphing leading-edge structure for the UAS-S45 wing integrated with a set of internal actuation mechanisms was provided. The sensitive analysis is an effective solution to apply design optimization methods, such as “correlation,” to design the morphing leading edge. In addition, the parameters affecting the wing model were explored to enhance further optimization studies and predict future failures for all wing models. The wing model input parameters included the composite material qualities, ply angles, and the ply stacking sequences. With these settings, the A.C.P. process in Ansys software has defined, applied, and calculated each finite element’s failure criteria. The correlation and determination matrices were then computed using the parameter sets results by identifying the parameters with the highest correlation coefficients. These findings will be used to adapt the composite morphing leading edge for target droop nose optimization and, consequently, to design a demonstrator.

Future work will study the variable morphing leading edge at different frequencies and amplitudes. The interaction of leading-edge vortices with the trailing-edge vortices of the morphing airfoil will be highlighted by combining the oscillating airfoil with its morphing deflection. In addition, near-stall angles of attack should be explored at various frequencies to understand unsteady flow physics better and investigate options for delaying stall. This study will help to develop an improved optimization model for variable morphing leading edge that will employ an objective to delay the dynamic stall.

CHAPTER 6

NUMERICAL INVESTIGATION OF THE DYNAMIC STALL REDUCTION ON THE UAS-S45 AIRFOIL USING THE OPTIMIZED AIRFOIL METHOD

Musavir Bashir [a], Simon Longtin-Martel [b], Nicola Zonzini [c], Ruxandra Mihaela Botez [d], Alessandro Ceruti [e] and Tony Wong [f]

[a, b, d, f] Department of System Engineering, École de Technologie Supérieure, 1100 Notre-Dame West, Montréal, Québec, Canada H3C 1K3
[b, e] Department of Industrial Engineering, University of Bologna, Bologna, Italy Via Zamboni, 33, 40126 Bologna BO, Italy

Paper submitted for publication to *The Aeronautical Journal*, in October 2022

Résumé

Cet article étudie les effets des profils a bord d'attaque de type "Morphing Leading Edge (MLE) " et du bord de fuite de type "Morphing Trailing Edge (MTE) " optimisés sur les tourbillons de décrochage dynamique (DSV) pour un profil à tangage par le biais de simulations numériques. Dans la première étape de la méthodologie, l'optimisation du profil UAS-S45 a été réalisée à l'aide d'une optimisation de la déformation. Le modèle mathématique a utilisé la paramétrisation de Bézier-Parsec et l'algorithme d'optimisation de l'essaim de particules a été couplé à une recherche de traces dans le but de concevoir un profil aérodynamiquement efficace de l'UAS-S45. Le modèle de turbulence de transition $\gamma - Re_\theta$ a été appliqué premièrement pour prédire la transition de l'écoulement laminaire à turbulent. Le profil déformable a amélioré les performances aérodynamiques globales tout en retardant la séparation de la couche limite. Deuxièmement, l'analyse non-stationnaire du profil de l'UAS-S45 et de ses configurations de déformation a été effectuée et le champ d'écoulement non-stationnaire et les forces aérodynamiques ont été analysés au nombre de Reynolds de 2.4 x 10^6 et pour cinq fréquences réduites différentes k = 0.05, 0.08, 1.2, 1.6 et 2.0. Les variations des coefficients de portance (C_L), de traînée (C_D) et de moment (C_M) avec les angles d'attaque ont été calculés pour le profil déformable et ensuite comparés avec ceux du profil de référence. On

a constaté qu'une fréquence réduite plus élevée de 1.2 à 2 stabilisait le tourbillon du bord d'attaque qui fournissait sa variation de portance dans la phase de décrochage dynamique. Les coefficients de portance $(C_{L,max})$ et de traînée $(C_{D,max})$ maximums et les angles d'attaque de décrochage ont été évalués pour toutes les fréquences réduites étudiées. Les résultats numériques ont montré que le nouveau rayon de courbure du profil MLE peut minimiser le gradient de pression défavorable dans le sens du courant, empêcher une séparation significative de l'écoulement et supprimer la formation du DSV. En outre, il a été démontré que le profil déformable retardait l'angle d'attaque de décrochage de 14.26 % par rapport au profil de référence et que le $C_{L,max}$ du profil a augmenté de 2,49 à 3,04. Cependant, bien que le profil MTE ait augmenté le coefficient de portance global et le $C_{L,max}$, le décrochage dynamique n'a pas été contrôlé. Le comportement tourbillonnaire pendant la génération et le détachement du DSV a montré que le MTE peut modifier l'évolution des tourbillons et augmenter leur écoulement sur la couche de cisaillement du bord d'attaque en augmentant ainsi la circulation du DSV. La conclusion que l'on peut tirer de cette étude est que les profils aérodynamiques à bord d'attaque déformables de type "Droop Nose" ont le potentiel de contrôler le décrochage dynamique. Ces résultats contribuent à une meilleure compréhension de l'analyse de l'écoulement des profils déformables dans un écoulement non-stationnaire.

Abstract:

This paper investigates the effect of the optimized Morphing Leading Edge (MLE) and the Morphing Trailing Edge (MTE) on Dynamic Stall Vortices (DSV) for a pitching airfoil through numerical simulations. In the first stage of the methodology, the optimization of the UAS-S45 airfoil was performed using a morphing optimization framework. The mathematical model used Bezier-Parsec parametrization, and the Particle Swarm Optimization algorithm was coupled with a Pattern Search with the aim of designing an aerodynamically efficient UAS-45 airfoil. The $\gamma - Re_{\theta}$ transition turbulence model was firstly applied to predict the laminar to turbulent flow transition. The morphing airfoil increased the overall aerodynamic performances while delaying boundary layer separation. Secondly, the unsteady analysis of the UAS-S45 airfoil and its morphing configurations was carried out and the unsteady flow field

and aerodynamic forces were analyzed at the Reynolds number of 2.4 x 10^6 and five different reduced frequencies of k = 0.05, 0.08, 1.2, 1.6 and 2.0. The lift (C_L), drag (C_D) and moment (C_M) coefficients variations with the angle of attack of the reference and morphing airfoils were compared. It was found that a higher reduced frequencies of 1.2 to 2 stabilized the leading-edge vortex that provided its lift variation in the dynamic stall phase. The maximum lift $(C_{L,max})$ and drag ($C_{D,max}$) coefficients and the stall angles of attack are evaluated for all studied reduced frequencies. The numerical results have shown that the new radius of curvature of the MLE airfoil can minimize the streamwise adverse pressure gradient and prevent significant flow separation and suppress the formation of the DSV. Furthermore, it was shown that the morphing airfoil delayed the stall angle of attack by 14.26% with respect to the reference airfoil, and that the $C_{L,max}$ of the airfoil increased from 2.49 to 3.04. However, while the MTE airfoil was found to increase the overall lift coefficient and the $C_{L,max}$, it did not control the dynamic stall. Vorticity behavior during DSV generation and detachment has shown that the MTE can change the vortices' evolution and increase vorticity flux from the leading-edge shear layer, thus increasing DSV circulation. The conclusion that can be drawn from this study is that the fixed drooped morphing leading edge airfoils have the potential to control the dynamic stall. These findings contribute to a better understanding of the flow analysis of morphing airfoils in an unsteady flow.

6.1 Introduction

The increasing demand for air transportation has heightened environmental concerns and put a strain on the aircraft sector. Due to the unpredictability of fuel costs and growing environmental concerns, fuel efficiency has become a critical element in aircraft design. In 2020, the global aviation industry was predicted to surpass 40.3 million commercial flights, a 50% increase over the previous decade. The aviation industry's main objectives are to improve the quality and affordability of air transportation, to mitigate its environmental impact by reducing CO_2, NO_X, fossil fuels consumption, and noise emissions, and to address safety problems (ICAO, 2019). These goals have resulted in an increasing demand for novel research ideas aimed at developing more efficient and environmentally friendly aircraft. Moreover, all

the new studies dealing with the use of batteries for electric flight, new biofuels and hydrogen suggest the need for the increase of the aerodynamic efficiency in terms of energy to weight ratio. Aircraft configurations with higher efficiency could anticipate the batteries development level required for effective operations. Numerous investigations at the Research Laboratory in Active Controls, Avionics, and AeroServoElasticity (LARCASE) have explored potential ways for reducing aircraft fuel consumption and increasing the aerodynamic efficiency, including experimental investigations of morphing wing models (Bashir et al., 2021; Bashir, Longtin Martel, et al., 2022a, 2022b; R. Botez, 2018a; RM Botez et al., 2018; Ruxandra M Botez, 2022; Ruxandra Mihaela Botez et al., 2007; D Communier et al., 2019; Communier et al., 2020; David Communier et al., 2019; Félix Patrón et al., 2014; Hamy et al., 2016; Kuitche, Botez, et al., 2020a, 2020b). Figure 6.1 shows the Price-Païdoussis subsonic blow down wind tunnel used to carry out the LARCASE experimental studies.

Morphing can increase an aircraft's performance in terms of lift, drag, and noise by removing wing surface discontinuities and gaps (Arena et al., 2018; Ignazio Dimino et al., 2017; Kuitche et al., 2019; Kuitche, Botez, Viso, et al., 2020; Pecora, 2021), thus obtaining a smooth surface. Nowadays aircraft are designed to produce maximum aerodynamic performance (highest lift-to-drag ratio) within a flight envelope. Moreover, the maximum efficiency is not typically reached during the cruise because it requires a speed which is often too reduced, so that a trade-off between performances and operational needs must be defined. However, mission criteria vary continuously during flight phases, and an aircraft frequently flies in suboptimal conditions. Although typical aircraft are equipped with hinged lifting mechanisms and trailing edge surfaces to manage airflow, these aircraft may generate surface discontinuities and increase drag (Ameduri, Concilio, et al., 2018; Kintscher et al., 2011). These hinged surfaces have drawbacks in both their deployed and retracted states (Y. Li et al., 2013). If the high lifting surface is not aligned properly, it can induce noise, turbulence, and a turbulent boundary layer, thus increasing the drag. Moreover, also from a structural point of view, moving surfaces require complex mechanisms and in the case of the flaps usually only few deflection positions can be set by pilots in commercial aircraft. Many experts claim that laminarization technology can reduce drag and prevent flow separation (Abbas et al., 2013; Concilio et al., 2021; Giuliani

et al., 2022). The morphing leading edge device is a gapless flexible droop nose that undergoes a substantial shape and camber alteration. The actuation system can lie within the airfoil, thus avoiding the need for external mechanisms and fairings.

Figure 6.1 LARCASE Price-Païdoussis subsonic blow down wind tunnel

Unsteady aerodynamic analysis plays an important role in the process of conceptual morphing designs. Morphing optimization has revealed that optimized lift and drag coefficients can be obtained at different flight conditions. The effects of unsteady parameters such as oscillation amplitude, reduced frequency, Reynolds number and airfoil kinematics (deformation, variable thickness etc.) have been investigated by different researchers from the perspective of aerodynamic coefficients (Andersen et al., 2009; Wang et al., 2021; Zi, Daochun, Tong, et al., 2020; Zi, Daochun, Xiang, et al., 2020). Numerical studies were used to investigate morphing wing aerodynamic stall and to explore adaptive morphing trailing-edge wings, 1% drag reduction on-design and 5% off-design were obtained (Lyu et al., 2015). A hybrid RANS-LES technique was used to investigate the aerodynamic performance of an airfoil with a downward, statically morphing trailing-edge flap (TEF). Morphing enhanced lift-to-drag by 6%. (Abdessemed et al., 2022; Abdessemed et al., 2018b) Similar results were reported for the aerodynamic and aeroacoustics responses of an airfoil fitted with a harmonically morphing

Trailing Edge Flap (Abdessemed, Bouferrouk, et al., 2021). It is worth noting that a slight increase in efficiency impacts with a magnification factor the Maximum Take Off (MTO) mass of an aircraft by reducing in a significant way the fuel consumption. Moreover, RANS numerical simulations of a NACA0012 airfoil with a flexible trailing-edge showed that the morphing surface can delay the beginning of flow separation with the aim to achieve optimal aerodynamic performance (Jawahar et al., 2018; Kamliya Jawahar et al., 2017; Popov et al., 2008; Andrei V Popov, Lucian T Grigorie, Ruxandra Botez, Mahmoud Mamou, et al., 2010).

Dynamic stall is an aerodynamic phenomenon that occurs when the flow over the wings and aerodynamic bodies separates rapidly due to changes in relative freestream conditions. Dynamic stall is marked by increased flow-field unsteadiness, resulting in increased airframe vibration and reduced aerodynamic performance (Gupta et al., 2019; Wei et al., 2021). A thin reversed flow region forms at the trailing edge before dynamic stall. A reverse pressure gradient moves the reversed flow area to the leading edge, while the flow remains attached. The leading edge of the vortex produces a powerful suction. A Leading-Edge Vortex (LEV) progressively splits from the airfoil surface to generate a Dynamic Stall Vortex (DSV). The DSV develops near the trailing edge as the angle of attack increases, resulting in moment variations. For an increased angle of attack, the DSV separates from the trailing edge of the airfoil.

Numerous flow control devices have been developed to avoid flow separation and to mitigate dynamic stall effects. They can be classified as active, or passive based on their operational properties. Vortex generators, micro-tabs, and serrated trailing edges are all examples of passive control devices. Active control mechanisms include trailing-edge flaps and synthetic jets of fluids. The use of leading-edge slats (Balaji et al., 2006; Imamura et al., 2008), trailing-edge flaps (Gerontakos et al., 2006; T. Lee et al., 2011), synthetic jet/periodic excitation strategies (D Greenblatt et al., 2001; David Greenblatt et al., 2000; Traub et al., 2005), plasma actuators (Post et al., 2006), vortex generators (Heine et al., 2013), and dynamically morphing leading-edge (Sahin et al., 2003) has been studied. In the wind tunnel, a morphing wing was optimized in real time to delay the flow transition to the trailing edge (Andrei V Popov, Lucian

T Grigorie, Ruxandra Botez, Mahmood Mamou, et al., 2010). The upper surface of the morphing rectangular finite aspect ratio wing was designed using a flexible composite material, and it was further equipped with pressure sensors and two smart memory alloy actuators. The morphing wing was obtained to duplicate several optimal airfoils by modifying the two actuators' strokes automatically. It was demonstrated in this study that the optimization mechanism in the control software code allows the morphing wing to optimize its shape for various flight cases.

The use of a leading-edge slat device for dynamic stall control was investigated numerically using a two-dimensional Navier–Stokes solver for multi-element airfoils (Sahin et al., 2000). Another option is to use suction/blowing. Blowing slots were set at 10% and 70% of the chord to conduct a dynamic-stall control test. Sun and Sheikh numerically simulated dynamic-stall control with near-leading-edge tangential blowing (Seifert et al., 1999).

A deployable leading edge vortex generator was used in an active dynamic stall control approach (Le Pape et al., 2012). Wind tunnel studies have shown that the device delayed the static stall and reduced dynamic stall penalties. Three degrees were added to the static stall angle. The dynamic stall reduced the negative pitching moment peak by 60% [46]. Numerical studies evaluated the impact of the synthetic jet control on the unstable dynamic stall over a rotor airfoil (Qijun et al., 2017). It was shown that the jets were most efficient when the stall was located at the flow separation point. Adjusting jet angle and momentum coefficients had similar impacts on dynamic stall characteristics. When situated near the flow separation point, a modest jet angle offered the optimum control effects on airfoil aerodynamic forces. In the separated flow region, a medium-angle synthetic jet is more effective. Experimental investigations using plasma-based devices or other high-frequency actuation were carried out using employing high-fidelity wall-resolved large-eddy simulations (Visbal et al., 2018; Visbal et al., 2017).

The effects of the Trailing Edge Flap (TEF) flow control on helicopter rotor blade dynamic stall were explored in (Feszty et al., 2004). The authors found that the substantial negative

pitching moments and their related negative aerodynamic damping were caused by the trailing edge vortex: and its only upward flap deflections reduced aerodynamic damping. Another study examined the outcome of the Trailing Edge Flap TEF and Leading Edge Flap (LEF) on the dynamic loads generated by an oscillating airfoil (Gerontakos et al., 2007; T. Lee et al., 2009).

The study indicated that the downward LEF motion suppressed leading edge separation and eliminated the occurrence of the DSV, leading to a minor reduction in $C_{L,max}$ but a considerably improved post stall lift condition, compared with the baseline airfoil. The joint upward LEF and downward TEF control produced the largest $C_{L,max}$. Another investigation was carried out to study the effect of a TEF on dynamic stall of wind turbine blades (Samara et al., 2021). The TEF reduced lift and root bending moment by 26% and 24%, respectively. These results show how TEF reduced wind turbine blade loads changes. Another study analyzed the flow field around a helicopter blade in forward flight. (Karimian et al., 2021). The two-dimensional model incorporated forward flight speed, resulting in a time-variable airfoil flow speed. Therefore, phenomena such as shock wave near the leading-edge of airfoil, which is critical to dynamic stall formation, were modeled using more realistic flow conditions. This study examined airfoil nose drooping and showed that it reduces and alleviates dynamic stall. An airfoil can be drooped to eliminate shock wave from its leading edge, and therefore no dynamic stall will occur.

Therefore, the literature mentioned above has proven mainly those different methods can be implemented to control the dynamic stall of the pitching airfoil. In this paper, the attention is focused on the morphing airfoil deformations, which are done in the frame of one of the most promising methods available to control the dynamic stall. However, dynamic airfoil morphing phenomena imposes a significant amount of complexity in the structure and control systems of a morphing wing. Therefore, the first objective of this study is to obtain optimized airfoils for the Morphing Leading Edge (MLE) and the Morphing Trailing Edge (MTE) to enhance the overall aerodynamic performance. The obtained optimized airfoils are then evaluated to investigate the dynamic stall. To our knowledge, only a few numerical studies have used

optimized airfoils to model the dynamic stall phenomenon at a moderate Reynolds number turbulent flow regime. Transition SST model's ability to predict laminar, transitional and fully turbulent flow regimes will contribute to a better understanding of the flow physics of dynamic stall and its delay. The paper is structured as follows Section 2 describes the methodology developed to optimize the airfoil, Section 3 includes a discussion of the results obtained in Section 2. Finally, Section 4 describes the outcome of this study and future work that could be carried out to investigate the dynamic stall.

6.2 Methodology

6.2.1 Optimization Problem Definition

The MLE and MTE airfoils derived from the UAS-S45 aerodynamic shape have been obtained through an optimization by using an intelligent and iterative approach based on user-defined aerodynamics and constraints. In the aerodynamic technique used here, an objective function formulation was coupled with a geometrical shape parameterization model, an aerodynamic flow solver, and an optimization algorithm. All these mathematical tools have been combined together in order to find a solution. Different morphing airfoil shapes were obtained for improving the UAV's aerodynamic performance.

An optimization framework was developed for this study to allow the integration of airfoil generation via the direct manipulation of the airfoil shape variables while respecting to geometrical limitations. Figure 6.2 depicts the optimization approach structure, which includes a geometrical modelling block based on the Bezier-Parsec (BP) parameterization technique and an aerodynamic solver, namely the panel solver XFOIL. The Transition SST model's results are validated using a high-fidelity solver in Ansys Fluent, based on Reynolds-Averaged Navier–Stokes (RANS) equations. A hybrid optimizer is also utilized, which combines the Particle Swarm Optimization (PSO) method with the Pattern Search (PS) technique. The optimization procedure is presented in more details (Bashir et al., 2021).

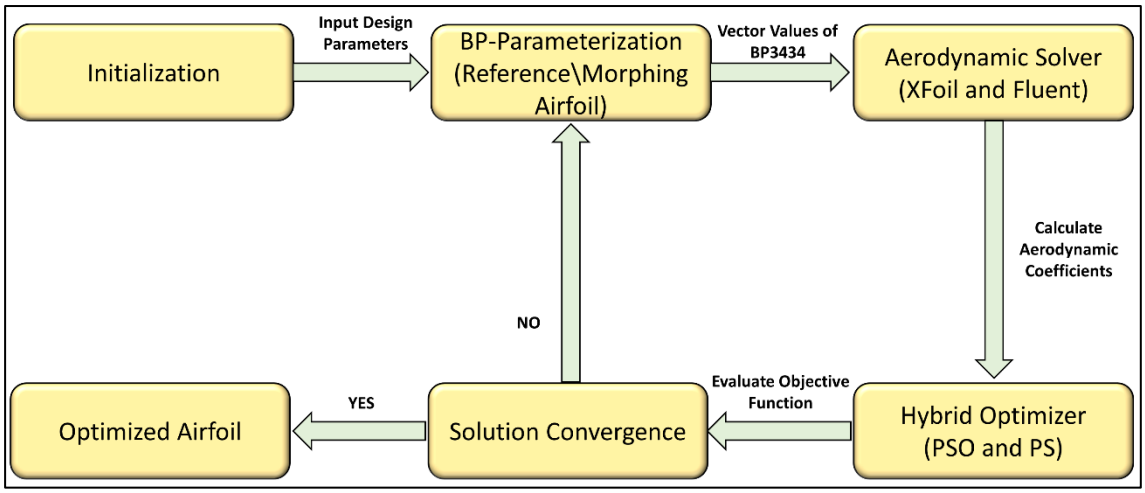

Figure 6.2 Schematics of the Optimization Procedure

The ability to search and obtain the best solution is demonstrated by designing an optimized airfoil derived from the UAS-S45 airfoil, with the goal of maximizing lift-to-drag ratio at cruise speed. For this design challenge, the following optimization function was constructed as shown in Equation 6.1:

$$Maximize\ f(x) = \frac{C_L}{C_D}(X); X\ \epsilon\ (airfoil\ set) \tag{6.1}$$

Such that

$$C_{Lmax} \geq C_{Lmax(baseline\ airfoil)}$$
$$X\ \in (airfoil\ set) \text{ such that Lb} \leq \text{X} \leq \text{Ub}$$

where N is the number of flight conditions for which the objective function is maximized.

The geometrical parameterization is one of the most important aspects of the airfoil shape optimization and design. By optimizing both the geometric and aerodynamic properties, the parameterized airfoil should have a small number of design variables. The number of design variables can be increased, which will take a long time and require high computing resources

(Manas Khurana et al., 2008a). There are numerous methods available for the shape parameterization of airfoils geometries. Some of the well-known methods are Discrete Points, Bezier or B-Spline, Free-Form Representation, and Cubic Spline Control Point Representation (Manas Khurana et al., 2008a; Trad et al., 2020). These methods have the disadvantages such as the method does not use airfoil parameters as design variables, requiring a large number of design variables than those of the airfoil parameters, and they frequently produce erroneous shapes for airfoil's leading and trailing edges. The main problem needed to solve is to find a mathematical description of the airfoil based on the positions of a limited set of points, whose positions are changed by the optimization algorithm.

The Bezier-PARSEC (BP) parameterization was developed by Derksen and Rogalsky, and describes Bezier curves using PARSEC parameterizations (Derksen et al., 2010). It is classified into BP3333 and BP3434. The BP3333 uses third-order Bezier curves for the airfoil camber and thickness, and its key advantages are of close relevance to airfoil aerodynamic parameters, fast optimization, continuity features low number of design variation, and avoidance of abrupt leading edges. Reduced degree of freedom prevents the parameterization of camber trailing edge airfoils. In the BP3434, third-order Bezier Curves define the camber and thickness of the airfoil's leading edge, whereas fourth-order Bezier curves define the trailing edge, as shown in Figure 6.3. When an airfoil's camber is negative along its chord, the BP3434 is more efficient than BP3333, and therefore the BP3434 type is implemented in this study.

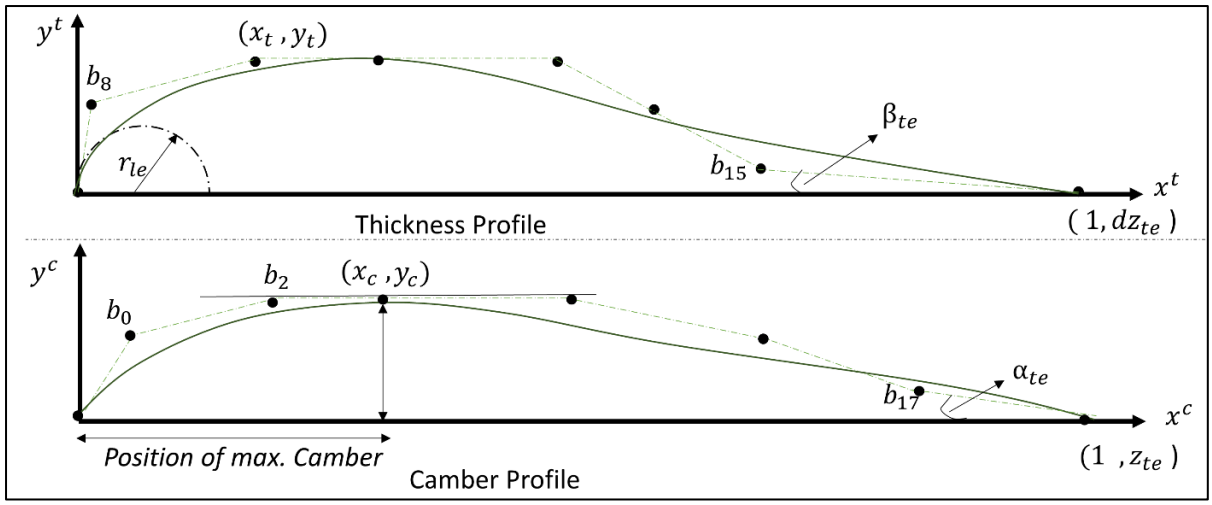

Figure 6.3 BP3434 parameterization scheme defining the Bezier airfoil curves

It is worth noting that Bezier curves are not defined by a set of interpolating points from which the curve passes through, but by a control polygon; the shape of the curve is managed by changing the positions of the points of the control polygon. For the UAS-S45 airfoil optimization, a hybrid optimizer based on the Particle Swarm Optimization (PSO) method combined with the Pattern Search algorithm was employed to improve the solution convergence and refinement. The PSO technique is based on the imitation of flock of birds or school of fish while searching for food, with solutions represented by particles that heuristically search a design space.

The hybrid optimization approach initially uses the PSO to optimize all variables. A second optimizer is then applied to the PSO's output due to small particles motion and their positions near optimized values or patterns. PSO is followed by Pattern Search optimization. The Pattern Search can identify a local optimum in a confined search region; the coupled use of PSO-PS provides better results than a single optimizer. One of the problems of heuristic optimization is the local minimum solution: such an algorithm can find a sub-optimal solution and not find the zones of the design space where the best solution lies. The optimization procedure generates a cost for every tested configuration by use of an objective function and a penalty function with the aim to remove non-realistic or non-feasible solutions from possible optimization results. Upper and lower bounds control the number of input variables. These

bounds ensure that the search space for both the PSO and the Pattern Search remain within them. During the PSO execution, if a particle is outside the search space constraints, its value is replaced by that of the within bound.

6.2.2 Unsteady Analysis using CFD Solver

For the pitching airfoil dynamic cases, the Reynolds number based on the airfoil chord length is Re = 2.4 x 10^6. During dynamic simulations, the airfoil undergoes a sinusoidal pitching motion, as shown in equation (6.2):

$$\alpha(t) = \alpha_m + \alpha_a \sin(\omega t) \tag{6.2}$$

The reduced frequency k is defined in equation (6.3):

$$k = \frac{\omega_p c}{2U_\infty} \tag{6.3}$$

where $\omega_p = 2\pi f$ is the circular frequency of motion, and α_m = 11◦ is the mean incidence angle, α_a = 15◦ is the amplitude, *f* is the airfoil oscillation frequency and *t* are time variable. Five reduced frequencies are considered in this research.

6.2.3 Computational Domain and Grid

The computational domain is 20c (20 times the length of the airfoil chord) upstream and 30c downstream of the airfoil pitch axis, while the inner circular region is 5c in diameter and centered at 0.25c aft of the leading edge. The mesh employs Sliding Mesh to obtain the airfoil pitching motion to avoid re-meshing, and to maintain cells quality. This work focusses on the pitching mode denoted by $\alpha(t) = 11 + 15\sin(\omega t)$ in which the airfoil enters a deep dynamic stall phase with considerable flow unsteadiness. Figure 6.4 shows the pitching axis

0.25c downstream of the chord line's leading edge. As already mentioned, based on the chord length and freestream velocity, the Reynolds number is 2.4 x 10^6.

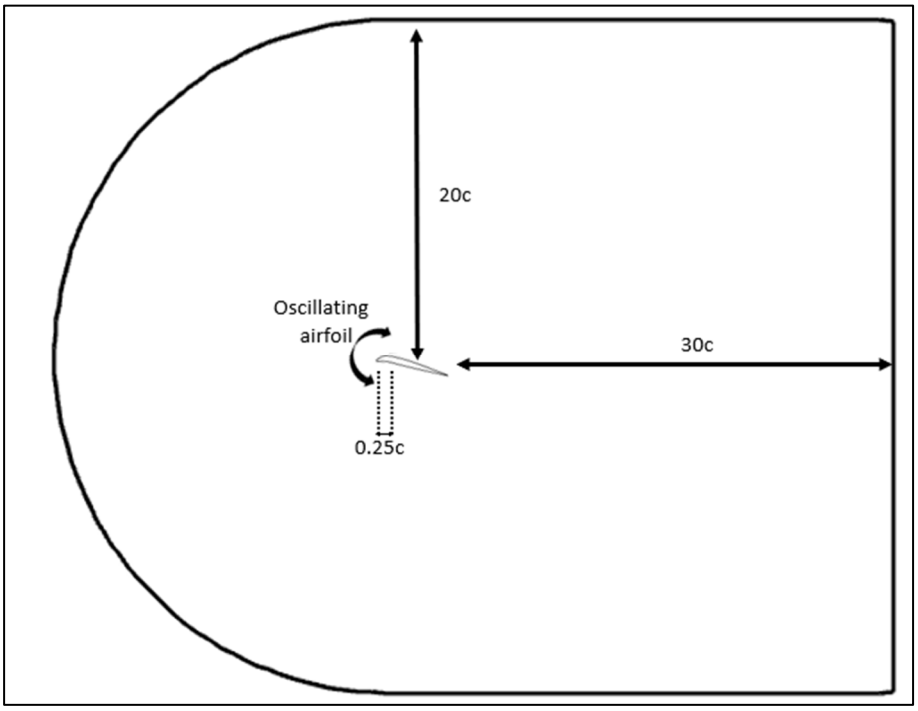

Figure 6.4 Computational domain with the pitching mode

One of the most important aspects in numerical simulations is the discretization of the computational domain. It is common practice to spend most of the time analyzing and studying the grid generation in order to find a grid-independent solution: a good trade-off between accuracy and computational effort must be found, which is most often addressed by a trial-and-error approach in which the numerical solution is compared with experimental data or analytical solutions. The mesh sensitivity analysis conducted after the initial validation process is detailed in the next section. The selection of a correct size and shape for the computational domain are crucial factors for the results quality, and they are strongly dependent on the aerodynamic characteristics, and on the type of the problem which is faced.

A Hybrid mesh made from a combination of structured and unstructured mesh was generated with ANSA, a multidisciplinary CAE pre-processor. It consists of a structured quadrilateral

layer mesh around the airfoil and an unstructured triangular mesh for the rest of the domain. Moreover, with the use of a blunt trailing edge it was possible to obtain O-shaped block layers around the airfoil and most importantly, to prevent instabilities of the solution induced by singular points located at the sharp corners of the trailing edge.

Figure 6.5 models the simulation domain with two mesh regions: i) the inner rotating grid, and ii) the outer stationary grid. The total number of elements in the grid is 103212, and the boundary region's first layer height is 0.006 mm with a bias factor of 1.08. The internal region has a minimum element length of 0.001 mm, a maximum length of 0.035 mm, and a bias factor of 1.08, while the external region has a minimum length of 0.035 mm, a maximum length of 0.6 mm and a bias factor of 1.08. The use of an internal circular domain allowed the mesh to move with the pitching airfoil without affecting the simulation's cell quality. High-quality quadrangular elements were used to refine the grid for its numerical stability in simulations, and mesh-independent results were obtained. Sliding Meshes were applied to the interfaces between the circular and external domains, thus designing non-matching nodes due to rotation, called 'hanging nodes': this improves the flow prediction near the walls. Since the nodes should have a constant position in their moving frame, no smoothing dynamic mesh approach was needed, and the quality remained the same.

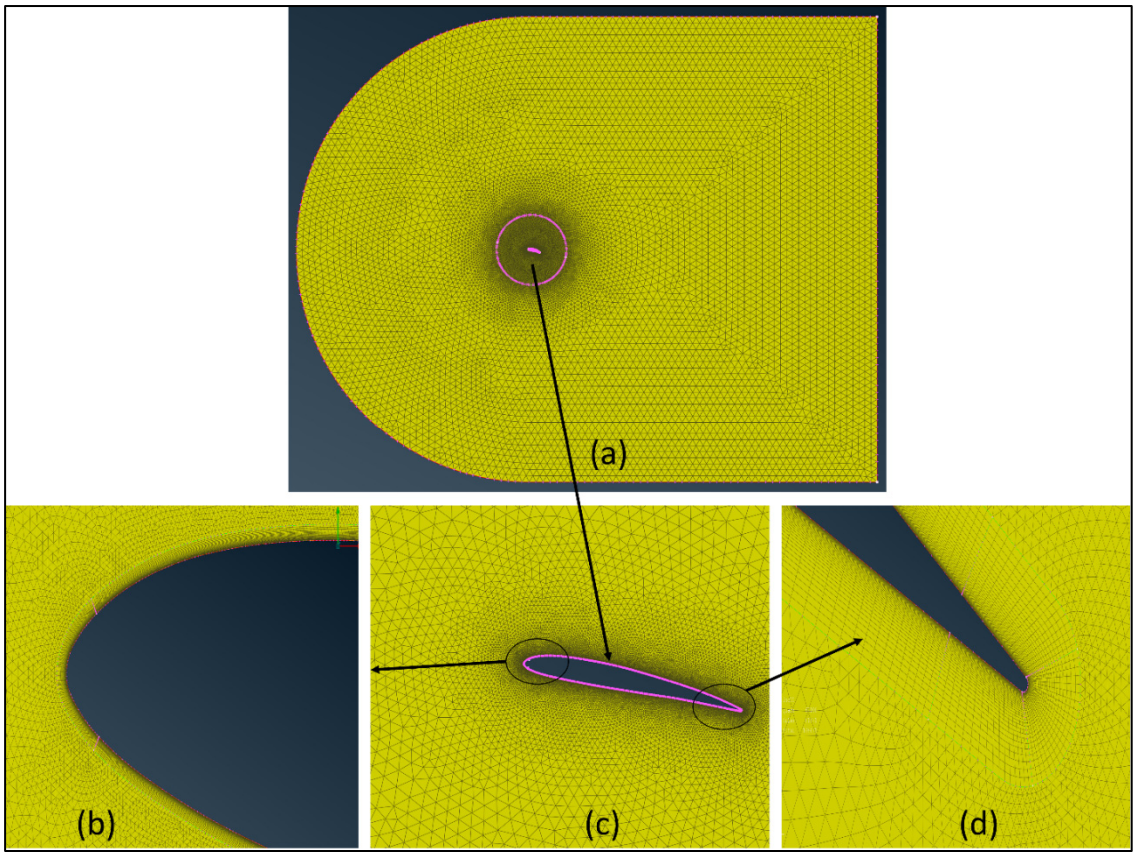

Figure 6.5 Mesh structure around the airfoil (a) mesh around the airfoil; (b) near the leading-edge, (c) near the airfoil, and (d) near the trailing-edge

The simulations were performed with a commercial CFD solver, called ANSYS Fluent. All scaled residuals were expected to decrease below $1x10^{6}$. The matching length of each time step was found to be below the sliding interface's minimum cell length to limit the interpolation error.

6.2.4 Validation of Results

Figure 6.6 shows the airfoils unsteady motion expressed by the lift coefficient for five pitching cycles. As soon as the lift coefficient reaches its greatest value, a sudden decrease is observed, thus depicting the beginning of the downstroke phase.

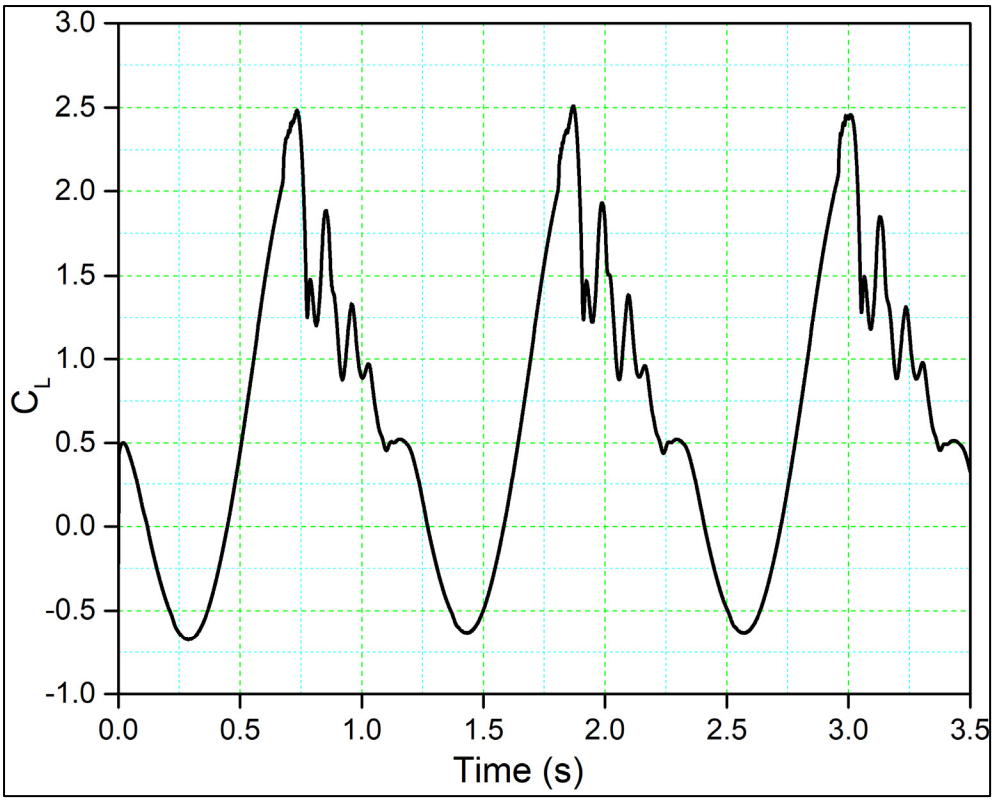

Figure 6.6 Lift coefficient variation with time for the pitch oscillating airfoil

Table 6.1 presents the properties of three different grid sizes which have been used for grid independency investigations. Figure 6.7 shows the lift coefficient versus the angle of attack for these three different grid sizes. Good correlation between each hysteresis loop is shown and the upstroke and downstroke also showed a good agreement. The lift coefficients for grid size 1 and grid size 2 are slightly different in the down-stroke phase, and the stall (the peak of the lift curve) has a slight variation. Additionally, the fluctuations in the lift coefficient for all the three grid sizes are similar in shape and magnitude. Similarly, very small discrepancies are visualized between grid size 3 and the other two grid sizes during the upstroke, while a small difference can be seen between the lift coefficients in the downstroke. The flow reattachment location for all grid sizes is the same. Therefore, grid size 2 was selected as the computational domain due to acceptable (medium size) cell count and results obtained.

Table 6.1 Grid properties of the three grid sizes for the grid-sensitivity analysis

Grid Size	Number of cells	Min length	Max length	Bias factor
1	62 626	0.001	0.06	1.12
2	103 212	0.001	0.035	1.08
3	206 038	0.001	0.02	1.05

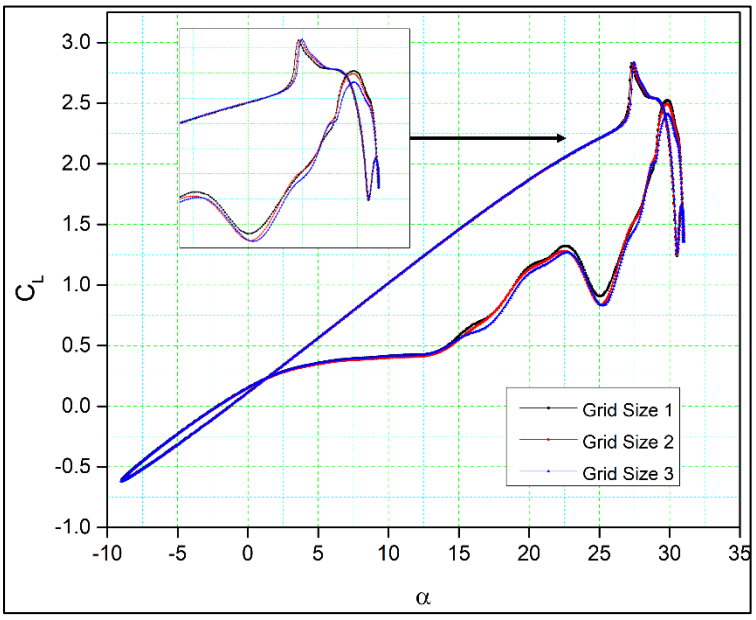

Figure 6.7 Comparisons of the numerical results for the lift coefficient versus the angle of attack for three different grid sizes

Figure 6.8 compares the model's computed lift and drag coefficients to their experimental values (MCALLISTER et al., 1978) and numerical data from previous literature (Correa, 2015). The first simulation example used as a reference the experiments of McAlister et al with Reynolds number 2.5 x10^6 and reduced frequency k = 0.10, from 5^0 to 25^0, with a mean incidence of 15^0, while the second simulation example used for benchmarking Correa et al.'s 2015 numerical data for the same settings.

The $SST\ k-\omega$ turbulence model can forecast the results' trend. The lift coefficient corresponds with its experimental value in the upstroke phase, but it predicts the stall differently than the experimental results. As the unsteady analysis is often dissipative, it

reduces the flow intensity and thus the kinetic energy. The numerical result is good, as it captures the load variation trend before the stall region. The ranges of differences in the peak noticed in the lift coefficient is small. The down-stroke variations are due to the extensive post-stall process, and hence discrepancy in the initial LEV prediction.

Figure 6.8 (b) illustrates the drag coefficient variation with angle of attack and a difference exists particularly when $\alpha > 12$, as the deep stall causes the drag to increase. The drag coefficient with angle of attack in Correa's numerical simulations is lower than the drag coefficient obtained in the other simulations. However, our numerical results of airfoil's maximum drag coefficient are lower than the experimental results due to large vortices on the airfoil surface and to the flow three dimensionality. These vortices occur because of the persistent flow separations at high angles of attack, which makes it difficult to effectively describe the viscous effects near the airfoil surface. The CFD simulations in our study also indicate a secondary LEV that contributes to the recovery of the lift and drag coefficients around the maximum angle of attack.

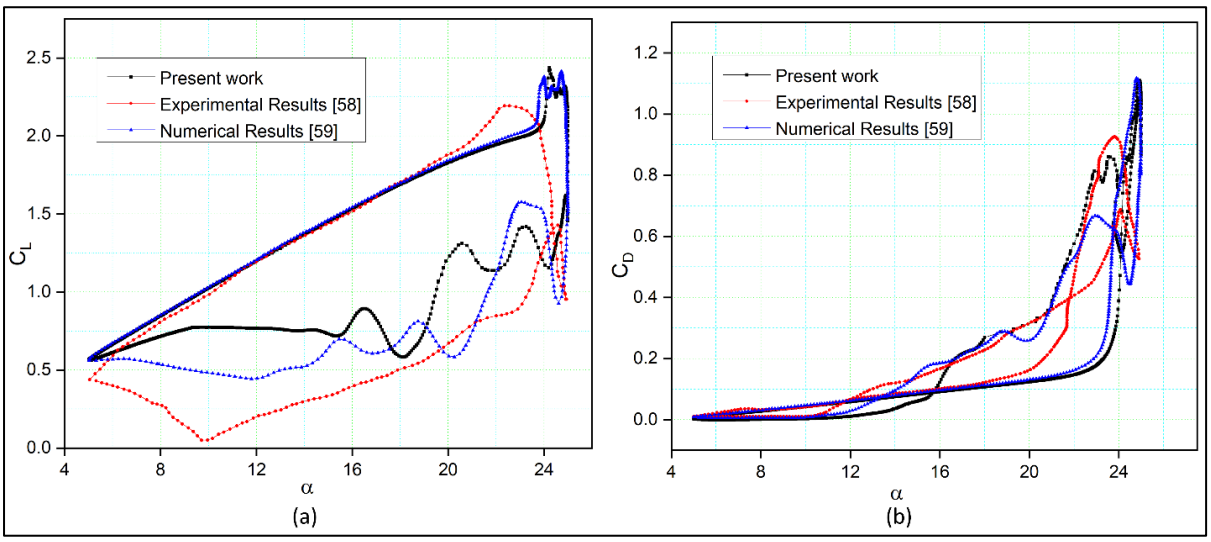

Figure 6.8 Comparison of our numerical results with experimental results obtained from previous wind tunnel tests [64] and numerical results [65]: (a) lift coefficient; (b) drag coefficient

6.3 Discussion of Results

The outcomes of the optimization procedure are expressed in terms of Morphing Leading Edge (MLE) and Morphing Trailing Edge (MTE) airfoil designs in the first part of this section. The findings of the unsteady flow analysis are presented in the second part of this section in order to better understand the Dynamic Stall Vortex (DSV) studies and the results of various airfoil configurations.

6.3.1 Optimization results

The aerodynamic optimization was obtained for the Morphing Leading Edge (MLE) and Morphing Trailing Edge (MTE) airfoils using the methodology presented in (Bashir et al., 2021). The study presents the leading edge and trailing edge optimization results of the S45 UAS' airfoil and will demonstrate the overall benefits of the morphing.

Figure 6.9 (a) indicates that the lift coefficients of the MLE airfoil are higher than those of the reference airfoil at Reynolds number = 2.4 x 10^6, where C_L is 1.57 and 1.65 for the MLE and the reference airfoil, respectively, thus representing a 5.09 % increase, and a static angle of attack increase of 3°. Figure 6.9 (b) shows the lift-to-drag ratio of the reference airfoil and the optimized airfoils and reveals a 3.8 % increase for $(\frac{C_L}{C_D})_{max}$ for MLE when compared to the reference airfoil.

Figure 6.9 (c) shows the pressure variations with the chord for MLE and reference airfoils. The MLE airfoil upper surface has the higher-pressure fluctuations than the reference airfoil. The chord-wise pressure distribution shows that the MLE optimized airfoil's cruise performance was improved by delaying the turbulent flow towards the trailing edge.

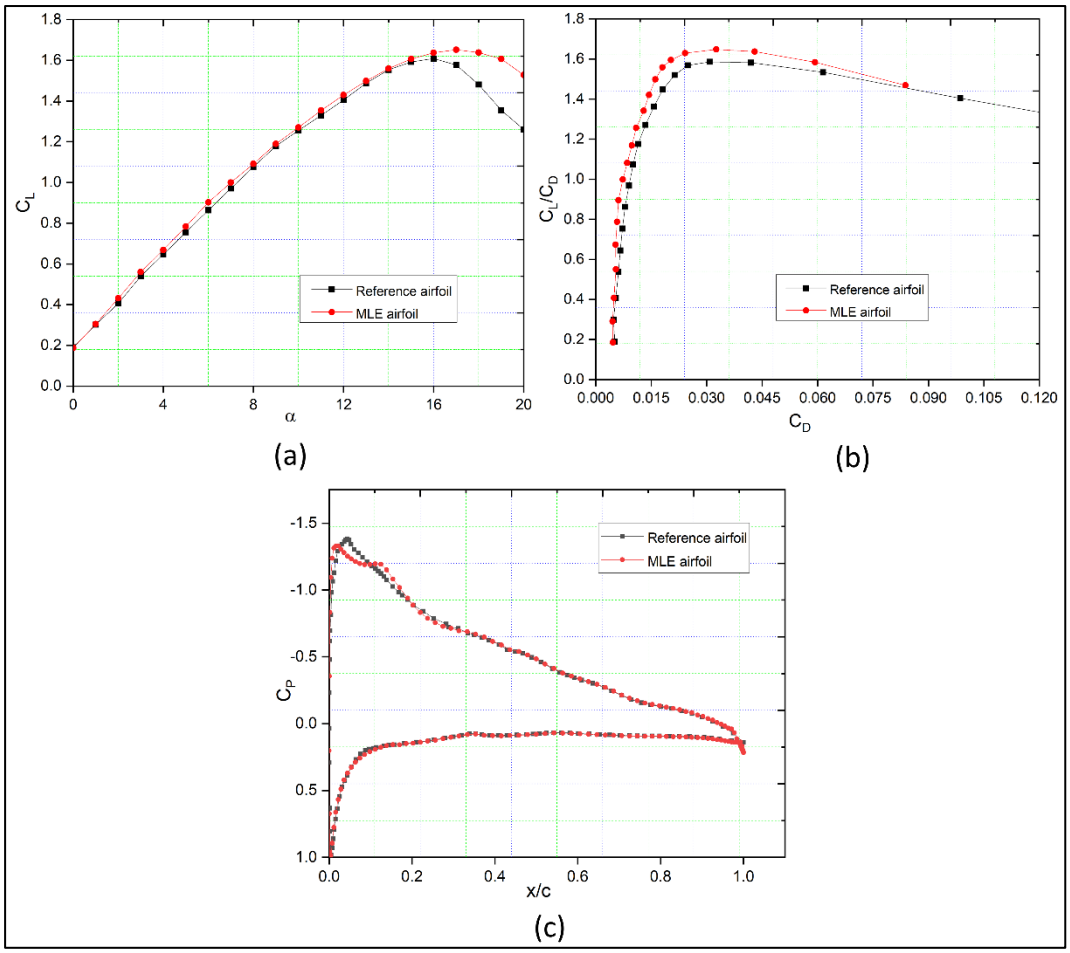

Figure 6.9 Comparison of aerodynamic coefficients: (a) CL, (b) CL vs CD ratio and (c) CP of the MLE versus the reference airfoil coefficients

Figure 6.10 (a) shows that the optimized airfoil has higher lift coefficients than the reference airfoil. The MTE lift coefficient was improved by maximum of 8.6% over the reference airfoil. In addition, the MTE airfoil stall angle increased by 2° with respect to the reference airfoil stall angle.

Figure 6.10 (b) shows the drag polar of the reference airfoil, and the optimized MTE airfoil. The morphing MTE airfoil has a higher $\frac{C_L}{C_D}$ ratio than the reference airfoil. Figure 6.10(c) shows the reference versus the MTE airfoil pressure coefficients at 10° angle of attack. The MTE airfoils have larger suction peaks than the reference airfoil.

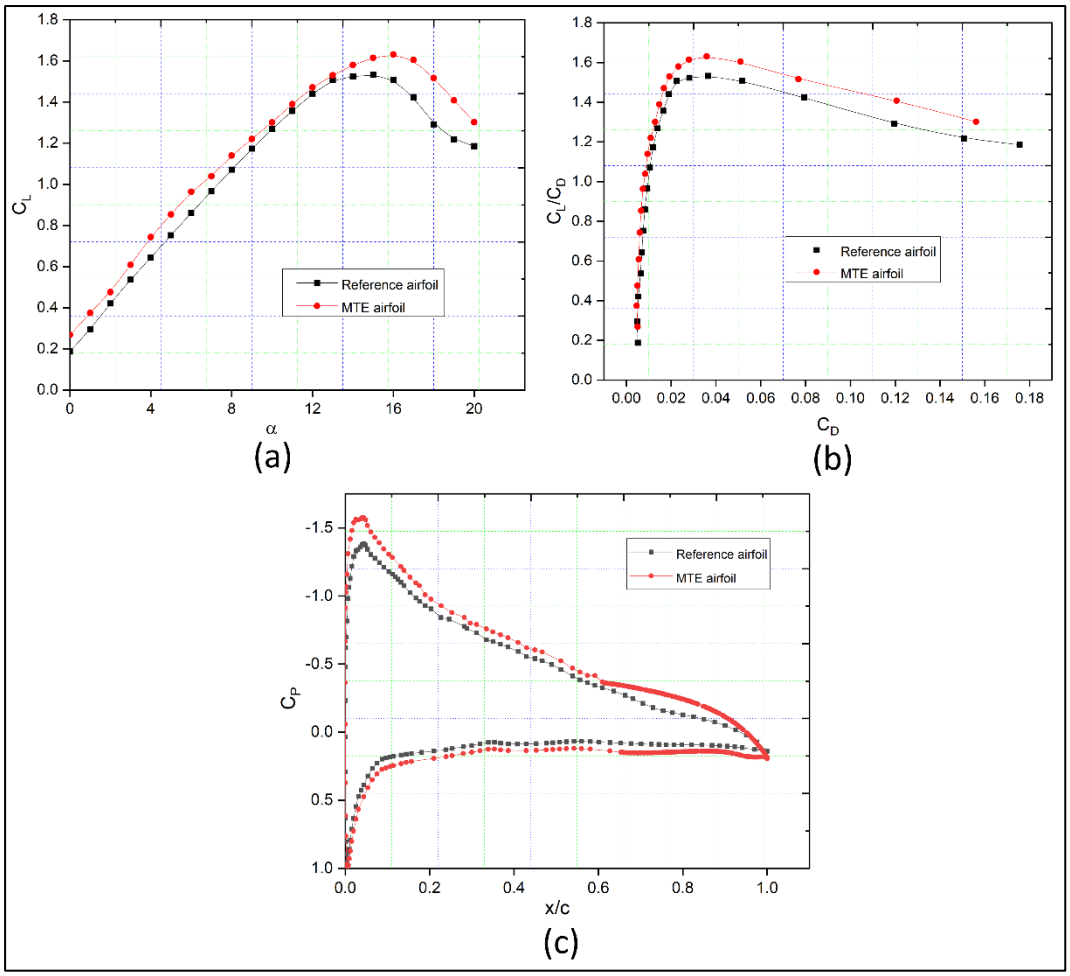

Figure 6.10 Comparison of aerodynamic coefficients: (a) CL, (b) CL vs CD ratio and (c) CP of the MLE versus the reference airfoil coefficients

Figure 6.11 presents the velocity contour with streamlines depicting the separation bubble on the reference airfoil at an angle of attack of 10°. The Laminar Separation Bubble (LSB) can be seen over the leading edge of an airfoil. The separation area was not visualized at lower angles of attack.

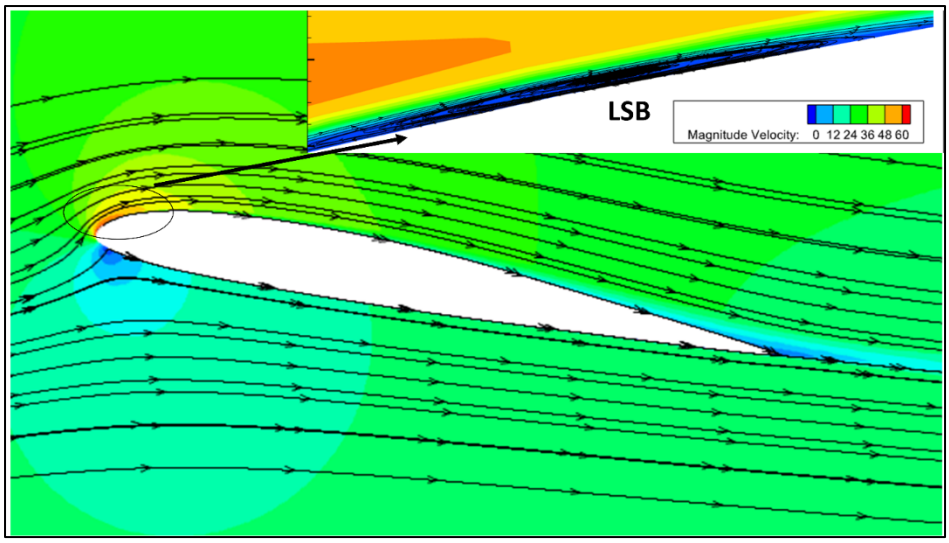

Figure 6.11 Velocity contour with streamlines at an angle of attack of 10°

Figure 6.12 shows the airfoil upper surface skin friction coefficient variation at angles of attack (AoA) of 2°, 6° and 10°. Figure 6.12 (a) depicts the airfoil lower surface skin friction coefficients by showing their way of increase with the incidence angle. The skin friction coefficient distribution on the upper surface of the airfoil shows that the transition position moves towards the leading edge gradually with the increase of the angle of attack. The skin friction coefficient curve at $\alpha = 10°$ shows an irregular variation, which is a typical trend for cases when flow separation exists. Figure 6.12 (b) shows the upper surface skin friction coefficients with their higher values at higher angles of attack by indicating the reduced shear velocity. In addition, the presence of flow separation is seen at 0.036c

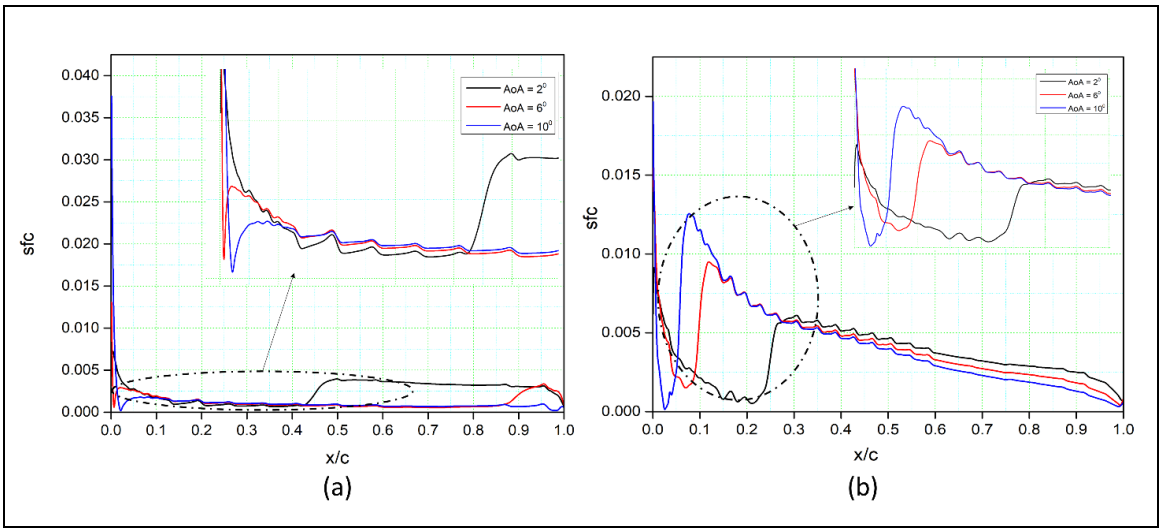

Figure 6.12 Skin friction coefficient variation with the chord location on the: (a) upper surface and (b) lower surface

6.3.2 Unsteady Aerodynamics Results

Unsteady numerical simulations of a sinusoidally pitching UAS-S45 airfoil and its morphing configurations will be studied. Airfoil pitching occurs at the quarter chord position. To analyze the dynamic stall, we demonstrate the occurrence of Leading-Edge Vortices (LEVs) over the UAS-S45 airfoil for different morphing airfoil configurations. Using this unsteady flow phenomena over the optimized airfoil configurations, the dynamic stall analysis will be presented.

6.3.2.1 Effect of reduced frequency on the UAS-S45 airfoil

Figure 6.13 presents a comparison of aerodynamic coefficients at different reduced frequencies for $\alpha(t) = \alpha_m + \alpha_a \sin(\omega t)$. The effect of the reduced frequency on the unsteady pitching airfoil motion is investigated by plotting the C_L versus the angle of attack for several reduced frequencies k = 0.05, 0.08, 0.12, 0.16, and 0.20 at Re = 2.4 x 10^6. As shown in Figure 6.13, $C_{L,max}$ increases with the reduced frequency values; from $C_{L,max}$= 2.43at k = 0.05, $C_{L,max}$= 2.49at k = 0.08, $C_{L,max}$= 2.54 at k = 0.12, $C_{L,max}$= 2.59at k = 0.16 and 2.64 at k = 0.20. A

greater k value broadens the hysteresis loops but does not affect the lift curve slope. Figure 6.13(b) shows a similar behavior for the drag coefficient, but k has a mixed influence ($C_{D,max}$). That is, increasing k changes $C_{D,max}$ from 1.17 at k = 0.05 to 1.45 at k = 0.2. Table 6.2 clearly shows the values of $C_{L,max}$ and $C_{D,max}$. Different types of vortices are generated at the trailing edge, as it can be seen from the downstroke. These vortices increase the lift force from the instant in which they are produced until their separation and shedding into the downstream wake. This process continues until the vortices are no longer present.

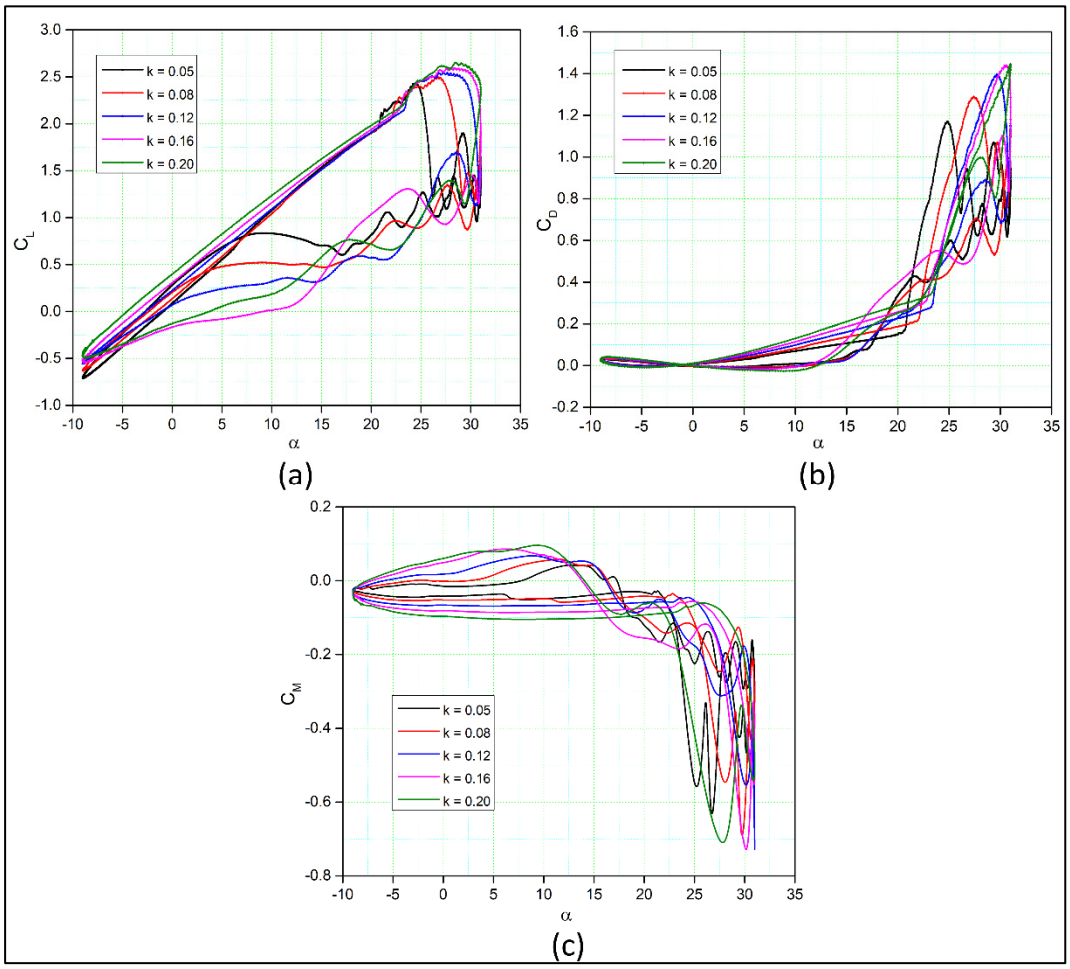

Figure 6.13 Aerodynamic coefficient hysteresis loops at different reduced frequencies for the variations of the (a) lift coefficient, (b) drag coefficient, and (c) pitching moment coefficient with the AoA

The vortex patterns at various instances of a dynamic stall cycle for k = 0.05 case are shown in Figure 6.14. Figure 6.14(a) depicts the upstroke LEVs in stall formation at four values of AoA. At α = 25.5°, the formation of fully developed primary LEV is visualized, along with the beginning of a secondary LEV. This phenomenon occurs as the incoming flow from the airfoil above the stagnation point enters the vortex. The fluid bypasses the vortex and enters the boundary layer at the trailing edge. However, the primary vortex rolls up under the action of the secondary vortices, which enter in the boundary layer. As the angle of attack increases, more high-energy flow enters in the primary vortex, thus increasing its size. The separation point advances towards the trailing edge as the vortex increases. Secondary and tertiary vortices are visualized in the last two portions of Figure 6.14(a).

At α = 27.3°, the flow on the bottom of the airfoil increases the size of the first trailing edge vortex. As the angle of attack increases to 28.8°, the separation point advances further behind the trailing edge, the mass of the fluid entering covers the entire airfoil, and the lift coefficient reaches its maximum. A part of the fluid enters as upstream vortices along the boundary layer, while the rest of it is transported downstream into the wake. A secondary trailing edge vortex appears, and large vortices confirm the dynamic stall occurrence.

Figure 6.14 (b) depicts the velocity contour in the downstroke phase. At α = 27.92°, the separation points travel behind the trailing edge, a vortex structure covers the entire airfoil from its leading edge to its trailing edge, and the lift coefficient increases. As the angle of attack reaches 20.42°, the bigger vortex reduces and starts to merge into the flow. The separation points travel upstream, and these vortices disappear at 13.91°. The vortex region is sucked into the boundary layer, and a part of it is transferred downstream into the wake. Eventually, the separation zones disappear, and the reattached flow occurs at the low angles of attack

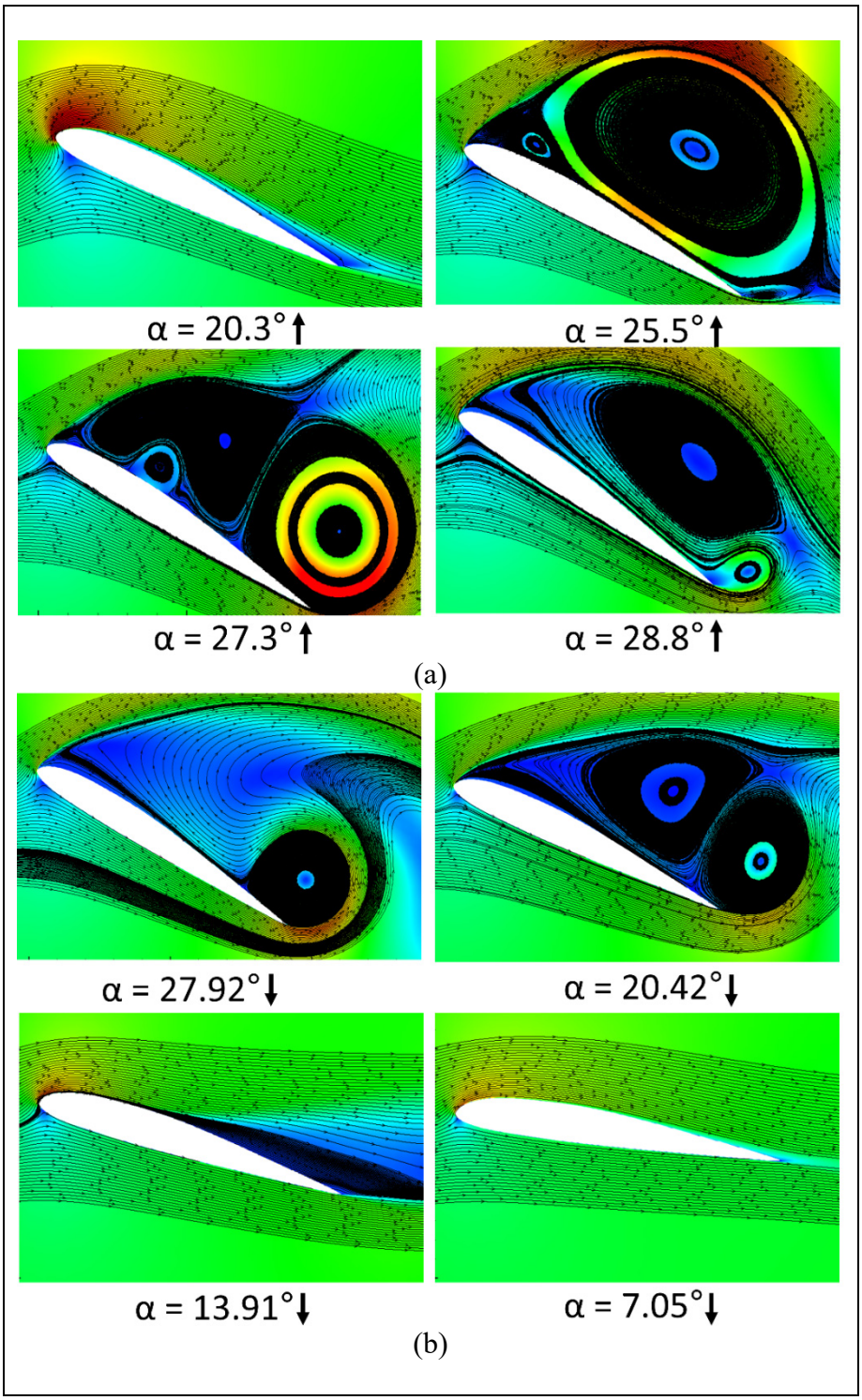

Figure 6.14 Velocity contour superimposed with flow at k = 0.05: (a) up-stroke cycle and (b) down-stroke cycle

Figure 6.15 reveals the stall development for up-stroke and down-stroke cycles of the airfoil for a higher reduced frequency of $k = 0.16$. In Figure 6.15 (a), at upstroke angle of attack of 20.3°, the flow evolves slowly and stays attached to the airfoil; the LSB is small and starts to form without a visible vortex. At 25.5°, the LEV evolves along the leading edge and continues to grow slowly. The increase of the angle of attack to 27.3° makes the LEV bigger and stronger. However, the dynamic stall can be seen at similar angles of attack, as it can be seen at $k = 0.05$ in Figure 6.14 (a).

Figure 6.15(b) shows the downstroke flow angles; multiple vortices are located over the airfoil at 27.92°, and the vortices merge and reduce in size at 20.42° and 13.91°. One important aspect is that the flow fails to fully reattach at higher reduced frequencies, which can also be seen in the downstroke cycle shown in Figure 6.14 (b).

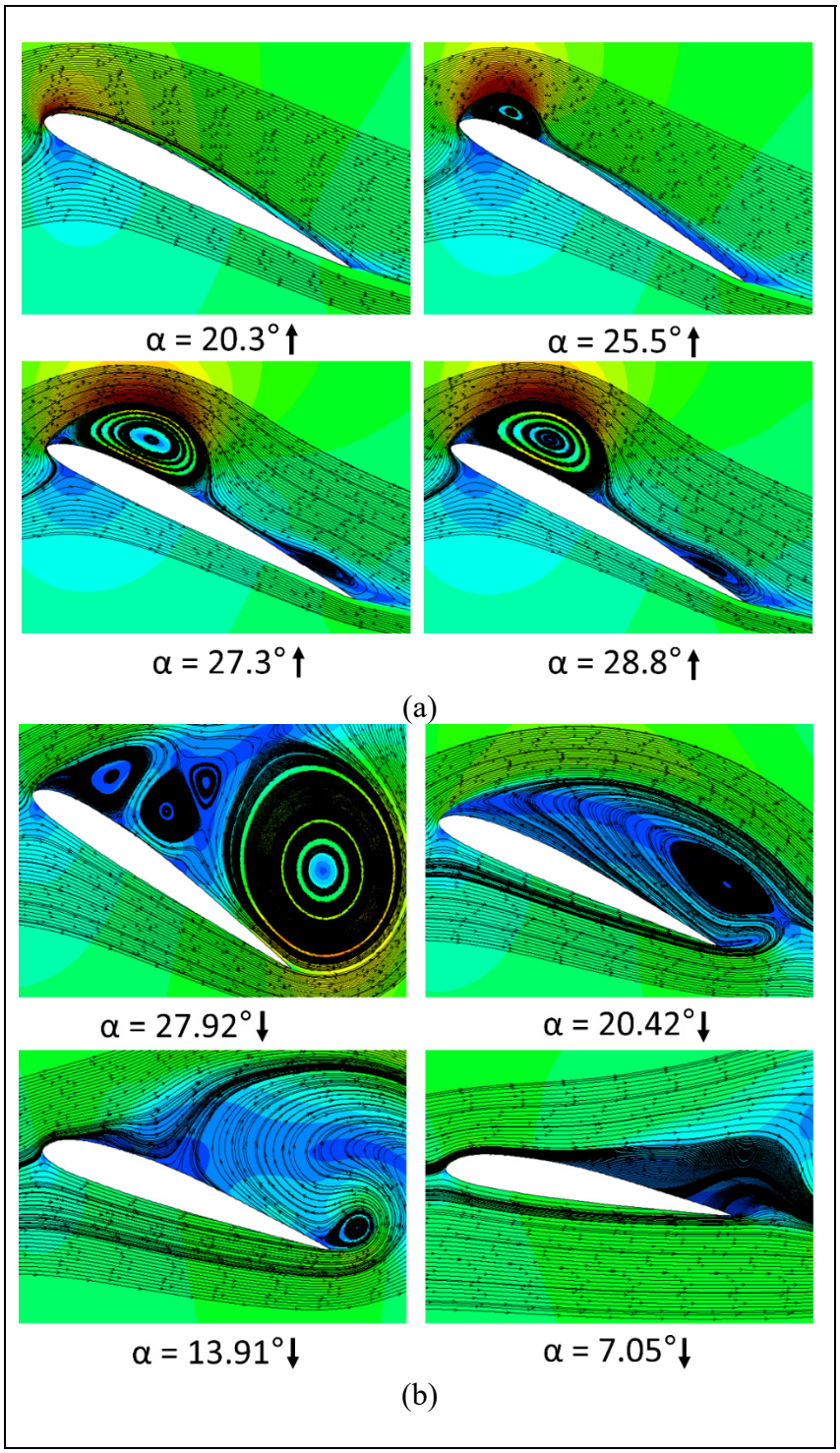

Figure 6.15 Velocity contour superimposed with flow at k = 0.16: (a) up-stroke cycle and (b) down-stroke cycle

Table 6.2 presents the results expressed in terms of aerodynamic parameters and stall features of an oscillating airfoil at different reduced frequencies. The values of the stall angle of attack ($\alpha_{ds}[°]$) reveal how reduced frequencies resulted in different dynamic stall angles. The stall angle increased from k = 0.05 to k = 0.20 by 4 degrees. It can be seen that the lift coefficient increases with the increasing reduced frequency. The lift coefficient of a pitching airfoil is higher than that of a static airfoil. Table 6.2 shows that the lift and drag coefficients variations during pitching motion at different reduced frequencies, and they increase at higher reduced frequencies.

Table 6.2 Airfoil performance parameters at different reduced frequencies

k	$C_{L,max}$	$\Delta C_{L,max}$	$\alpha_{ds}[°]$	$C_{D,max}$	$\Delta C_{D,max}$
0.05	2.43	1.09	24.41	1.17	0.7
0.08	2.49	1.15	26.70	1.29	0.82
0.12	2.54	1.2	27.18	1.39	0.92
0.16	2.59	1.25	28.01	1.44	0.97
0.20	2.64	1.3	28.50	1.45	0.98

Note: $C_{L,max}$= max dynamic lift coefficient; $C_{D,max}$ = max drag coefficient; α_{ds} = dynamic stall angle; $\Delta C_{L,max}$ = Max lift difference from steady state results;$\Delta C_{D,max}$= max drag coefficient difference from steady state results

6.3.2.2. Effect of the Morphing Leading Edge (MLE)

Figure 6.16 compares the aerodynamic coefficients of the morphing leading-edge airfoils to those of a reference airfoil with respect to the angle of attack over one complete cycle. Figure 6.16 (a) shows that morphing airfoils have both successfully increased $C_{L,max}$ value from 2.49 to 3.04. It is also clear that the morphing leading edge increased $C_{L,max}$, with the stall angle of attack increase. The main objective of the stall study is to delay or increase the stall angle, as stall angle of attack delay helps to maintain the airfoil lift coefficient even in the downstroke cycle. However, this result indicates that a strong vortex has been formed in the leading-edge of airfoil, which later results in dynamic stall.

Similarly, the drag coefficients are lower for the MLE airfoil for AoA lower than 30°, and the $C_{D,max}$ increases substantially at the peak angle with respect to the reference airfoil, as seen in Figure 6.16(b). Therefore, the drag coefficient of the MLE airfoil remains low for a large range of angles of attack. The MLE airfoil moment coefficient shows smaller C_M values with respect to those of the reference airfoil, as seen in Figure 6.16(c).

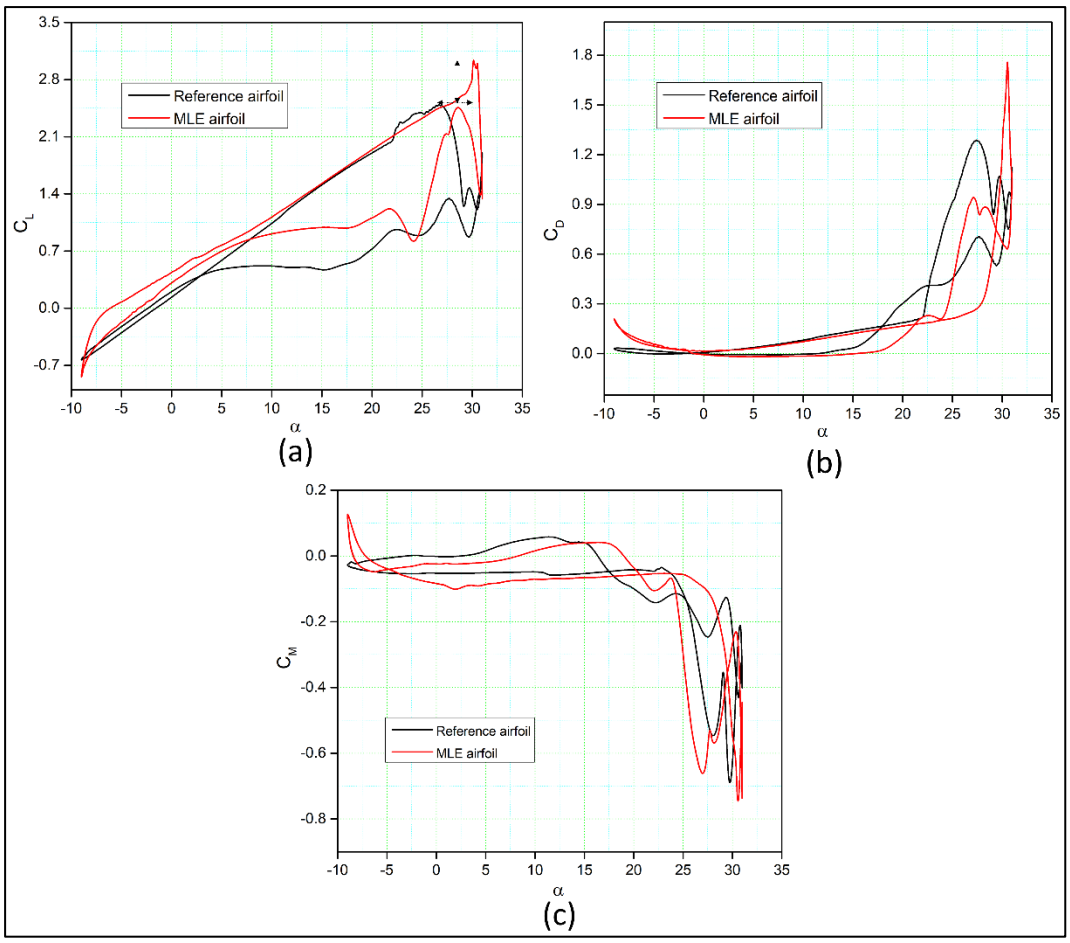

Figure 6.16 Aerodynamic coefficient hysteresis loops at k = 0.08: (a) lift coefficient, (b) drag coefficient, and (c) pitching moment coefficient

Figures 6.17(a) and 6.17(b) illustrate optimized MLE airfoil streamlines and Mach number contours. Figure 6.17(a) depicts the flow development at different upstroke angles of attack for the reference airfoil. The reference airfoil's primary LEV can be clearly seen at 25.5° angle

of attack. The clockwise vortex can also be seen near the trailing edge. As the angle of attack increases, the vortex size grows accordingly. The secondary and tertiary LEVs are also formed along with the primary LEV as the attack angle increases from 25.5° to 28.8°. The AoA increase results in more flow along the boundary layer by secondary and tertiary vortices, and a bigger trailing edge vortex at 29.8°and 31°.

In the case of an MLE airfoil, as seen in Figure 6.17 (b), the flow separation phenomenon is slow at low angles of attack, such as 25.5°, as the flow remains largely attached to the airfoil. By increasing the angle of attack to 28.8°, the leading-edge suction increases, and the LEV moves towards the trailing edge. The LEV also increases its size at 28.8°. This leading-edge vortex shedding is intensified by the formation of a small secondary vortex, which grows and breaks apart the main LEV. From 29.8° to 31°, the DSV is formed, which moves towards the trailing edge and increases the pitching moment coefficient.

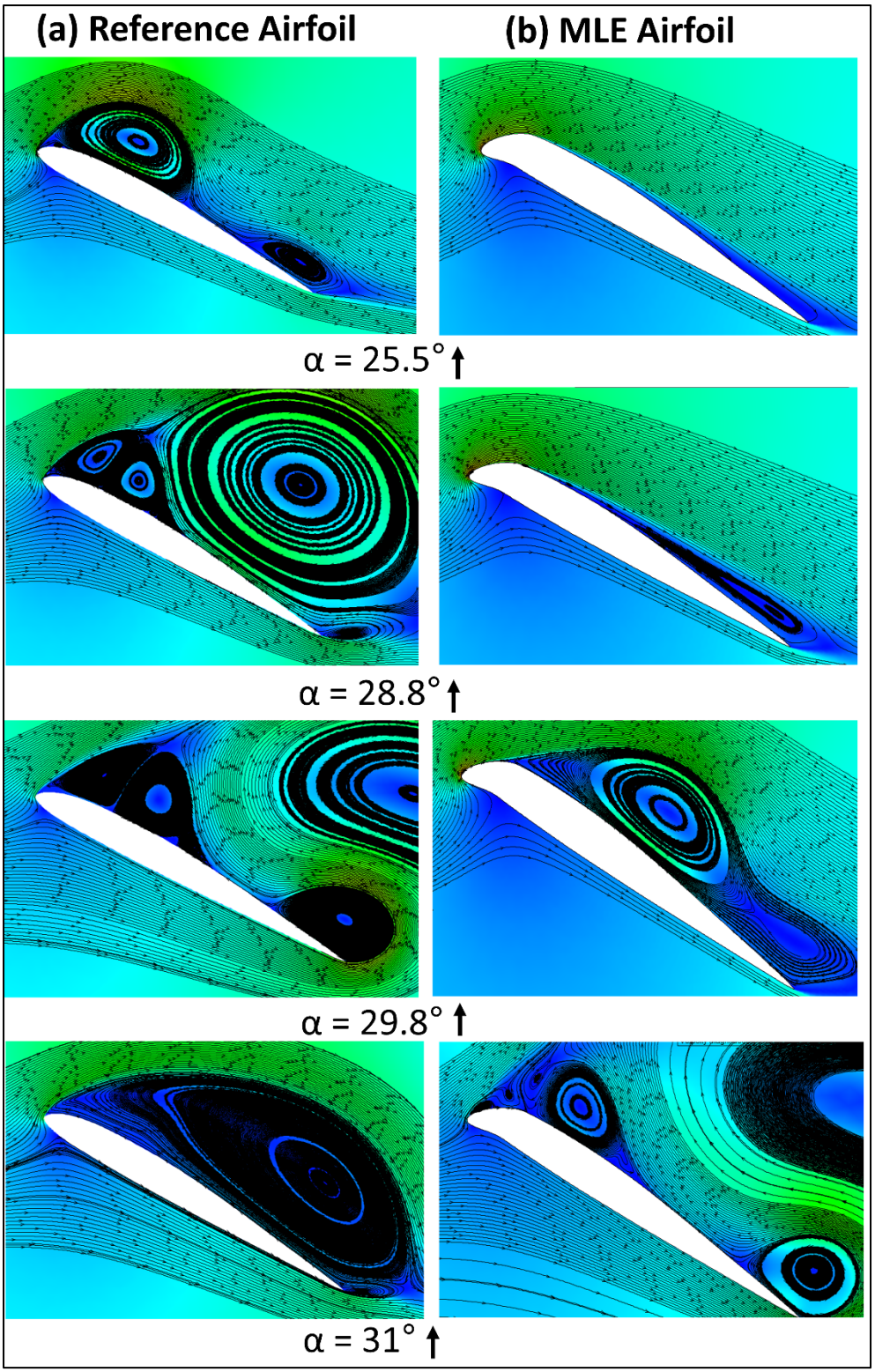

Figure 6.17 Velocity contour superimposed with flow at different values of α: (a) reference airfoil and (b) MLE airfoil

Large-scale vortical structures arise over the airfoil in the separated zone during the up-stroke motion by causing a ripple in the surface pressure distribution at $\alpha = 25.5°$, as seen in Figure 6.18(a). Figure 6.18 (b) shows the separated flow impact on the skin friction coefficient at x/c = 0.14 at $\alpha = 25.5°$. The flow reattaches at x/c = 0.24, and it remains then in its attached state. The flow acceleration around the leading-edge increases as the airfoil pitches up at $\alpha = 29.8°$, resulting in a larger peak suction and a stronger adverse pressure gradient across the laminar separation bubble. As shown in Figure 6.18 (c), the pressure coefficient is higher than -10 at $\alpha = 29.8°$, and the LEV formation can be clearly seen in the vicinity of the leading and trailing edges. The skin friction coefficients variations with the chord in Figure 6.18 (d) show that the flow separation is becoming bigger and is moving towards the trailing edge, accompanied by secondary and tertiary leading-edge vortices. The occurrence of the LEV is due to the increasing adverse pressure gradient, and then the dynamic stall vortex emerges and moves towards the trailing edge. As a result of the separation bubble occurrence, the skin friction coefficients show a large flow separation on the upper surface of the airfoil. Figure 6.18 (e) reveals that the negative pressure of the main vortex turns the flow from the pressure side of the airfoil at the trailing edge towards the suction side by generating a counter-rotating trailing edge vortex. As depicted in Figure 6.18 (f), the leading-edge vortex continues to flow along the airfoil surface by causing vortex shedding. Due to the shedding of the main leading-edge vortex, the lift coefficient begins to decrease.

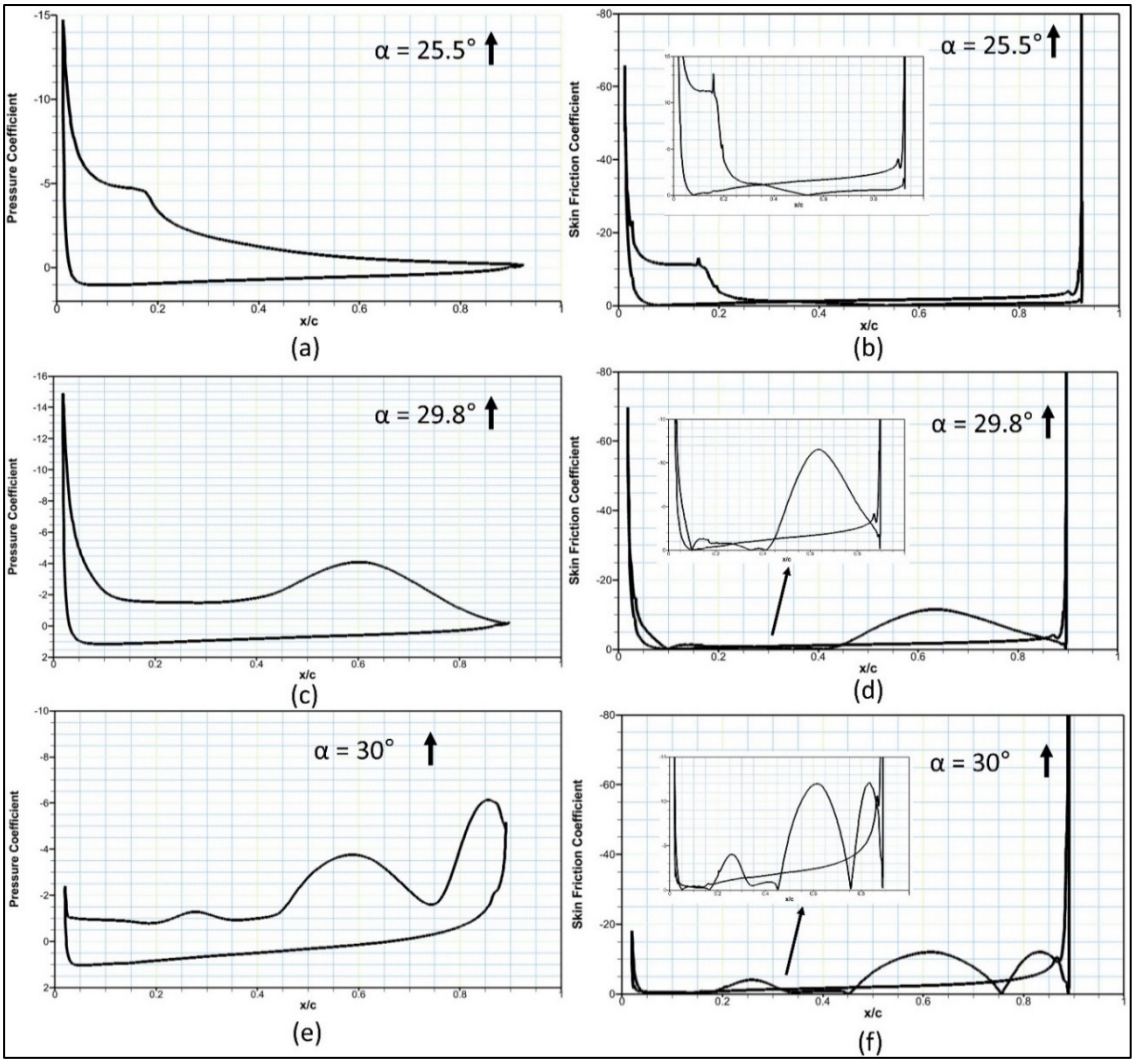

Figure 6.18 Computed pressure and skin friction coefficients for a MLE airfoil

Figure 6.19 illustrates the reference and optimized MLE airfoils' vorticity contours during one pitching cycle. Figure 6.19(a) shows the boundary layer attached to a shear layer at an attack angle of 25.5°. As the oscillating airfoil's angle of attack increases, reversed flow circulates from the trailing edge towards the leading edge (α = 29.8°) as seen in Figure 6.19(b). It shows a LEV that moves downstream along the airfoil surface, and results in increased vorticity forces. The vorticity sheds away from the trailing edge at α = 30.8° shown in Figure 6.19 (c). Figure 6.19(d) shows the MLE airfoil's vorticity at an angle of attack of 25.5°. Figure 6.19(e) shows that the MLE airfoils vorticity strength is less than the reference airfoil at an angle of attack of 29.8°. At the same time, a strong TEV is produced during the stall at 30.8°: this vortex

is quickly replaced by a secondary LEV that spans over the chord. Throughout the downstroke, alternating LEV and TEV creation and shedding causes force coefficient changes. The MLE airfoil also stalls, but at a smaller AoA than the reference airfoil.

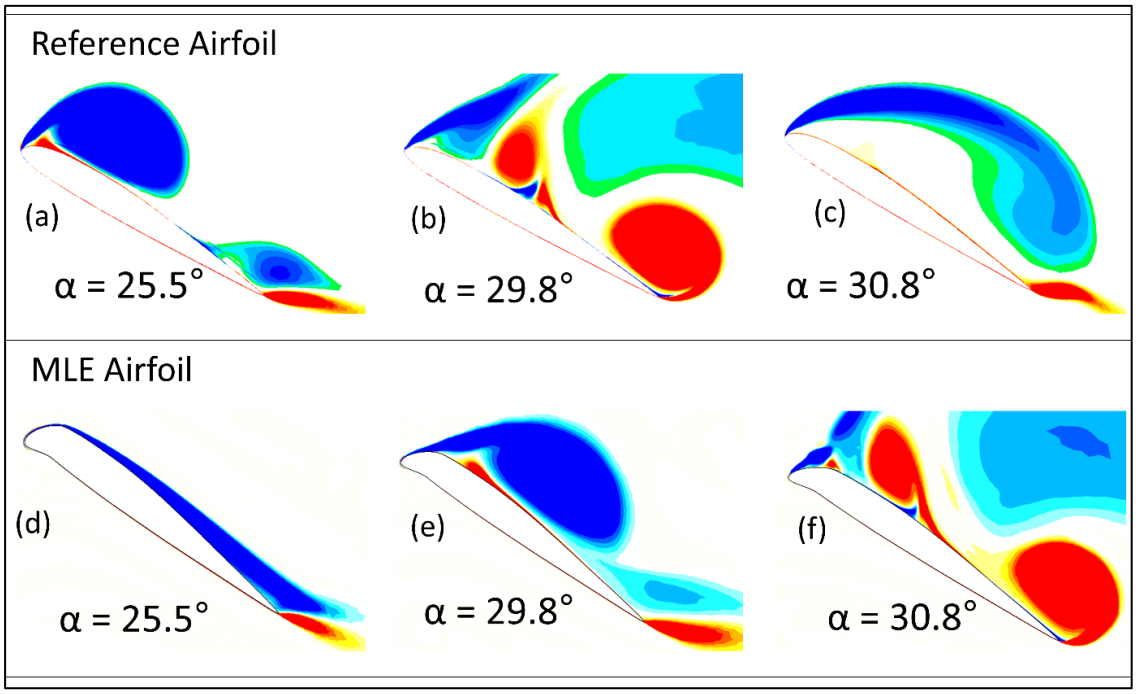

Figure 6.19 Comparison of vorticity contours of the reference airfoil with an MLE airfoil at different angles of attack

Table 6.3 shows the maximum aerodynamic lift and drag coefficients, and their stall angle variations values of the reference airfoil and of the MLE airfoil. It is worth noting that the maximum lift coefficient increased by 22.08% and the maximum drag coefficient increased by 57.31% for the MLE airfoil with respect to the to C_L of the reference airfoil. An increased delay in the stall angle of attack of 14.26% was achieved with the optimized MLE airfoil. Moreover, incremental values of $\Delta C_{L,max}$ and $\Delta C_{D,max}$ are provided for the MLE airfoil with respect to the static airfoil, in which the maximum lift coefficient of the MLE airfoil increased by 47.82% with respect to the reference airfoil maximum lift coefficient. The main objective of delaying the stall angle of attack was achieved, as it was delayed by 3.81° degrees.

Table 6.3 Comparison of airfoil performance parameters of the reference airfoil with those of the MLE airfoil

Airfoil	k	$C_{L,max}$	$\Delta C_{L,max}$	$\alpha_{ds}[°]$	$C_{D,max}$	$\Delta C_{D,max}$
Reference	0.08	2.49	1.15	26.70	1.29	0.82
MLE	0.08	3.04	1.17	30.51	1.76	1.29

Note: $C_{L,max}$= max dynamic lift coefficient; $C_{D,max}$ = max drag coefficient; α_{ds} = dynamic stall angle; $\Delta C_{L,max}$ = Max lift difference from steady state results;$\Delta C_{D,max}$= max drag coefficient difference from steady state results

6.3.2.3 Effect of the Morphing Trailing Edge (MTE)

Figures 6.20(a) and 6.20(b) illustrate the velocity contours with streamlines of an optimized MTE airfoil compared to those of the reference airfoil. Figure 6.20 (a) depicts the flow development over the reference airfoil for different angles of attack. At α = 25.5°, the flow remains attached to the airfoil with a LEV. A small clockwise vortex can also be seen near the trailing edge. Subsequently, the secondary and tertiary LEVs are produced starting from the leading edge, and the primary vortex size increases significantly as the airfoil pitches from 25.5° to 28.8°. The leading-edge suction results in the formation of a Leading-Edge Vortex (LEV) at 28.8°. This leading-edge vortex shedding is exacerbated by a tiny vortex formed at the leading edge, which increases from α = 29.8° and breaks from the main LEV. The LEV continues to increase and to spread over the airfoil, as seen at the AoA of 31°.

Figure 6.20 (b) shows that the MTE airfoil at 25.5° has a small trailing edge separation area. As the angle of attack increases to 28.8°, the LEV increases and advances towards the trailing edge. Due to the growing pressure gradient at α = 29.8°, the LEV bursts. It is evident that the trailing edge has resulted in an earlier stall formation than that of the reference airfoil.

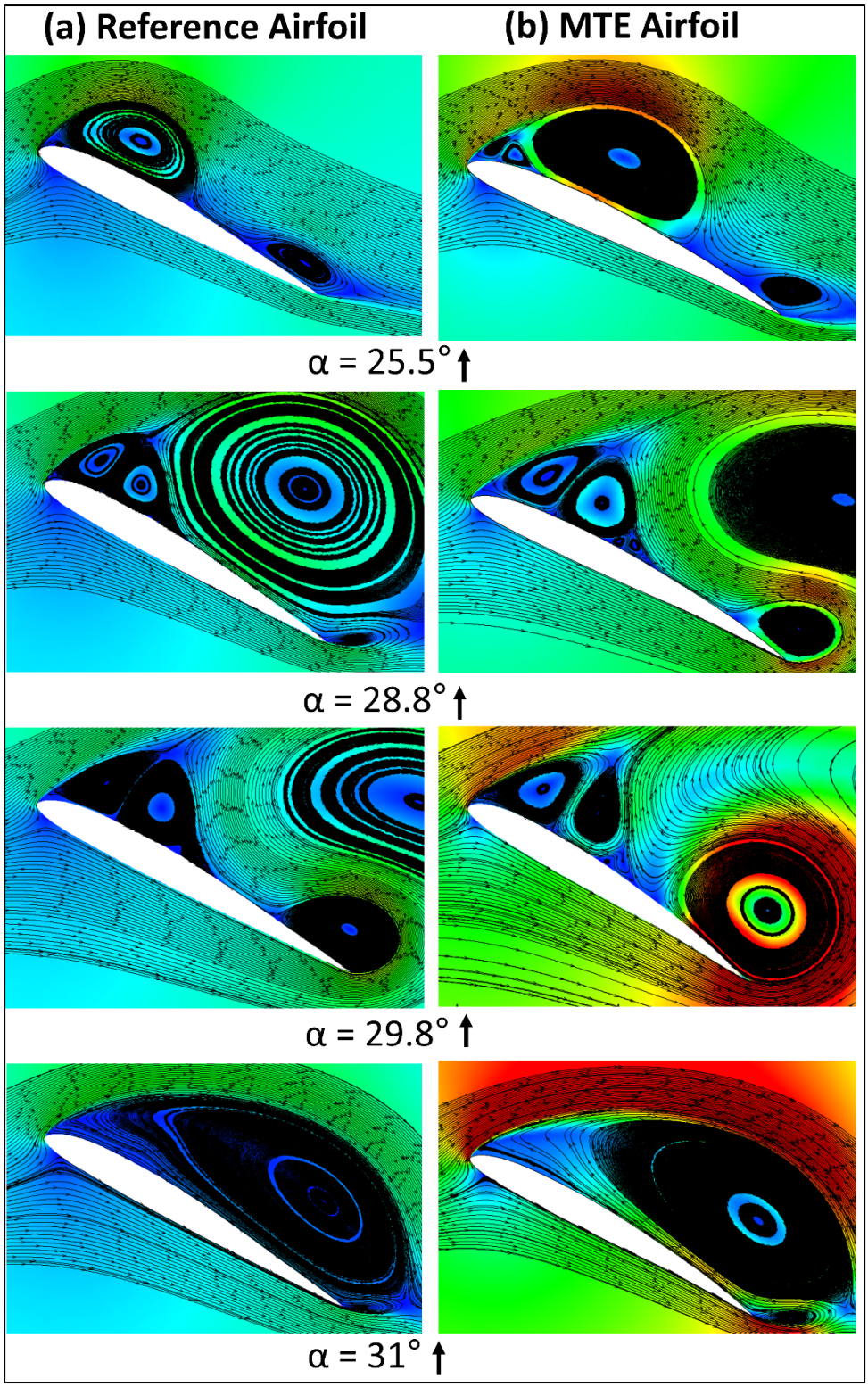

Figure 6.20 Velocity contour superimposed with flow at different values of AoA for the (a) reference airfoil and (b) MTE airfoil

Figure 6.21 shows how a complete cycle of angles of attack impacts the aerodynamic coefficients of airfoils equipped with a morphing trailing edge compared to the aerodynamic coefficients of the reference airfoil. In Figure 6.21 (a), the $C_{L,max}$ value increases from 2.49 to 2.67, while the morphing airfoil shows C_L increase throughout the full angle of attack cycle with respect to the reference airfoil. However, the stall angle of attack of MTE airfoil is slightly lower than that of the reference airfoil by 0.86°. The morphing airfoil has a lift drop similar to that of the reference airfoil during the downstroke, as expected. Figures 6.21(b) and (c) display the coefficients of drag and moment, respectively, of the two airfoils. Both $C_{D,max}$ and $C_{M,max}$ of the morphing airfoil are higher than those of the reference airfoil, with a maximum C_D increase of 5.42%.

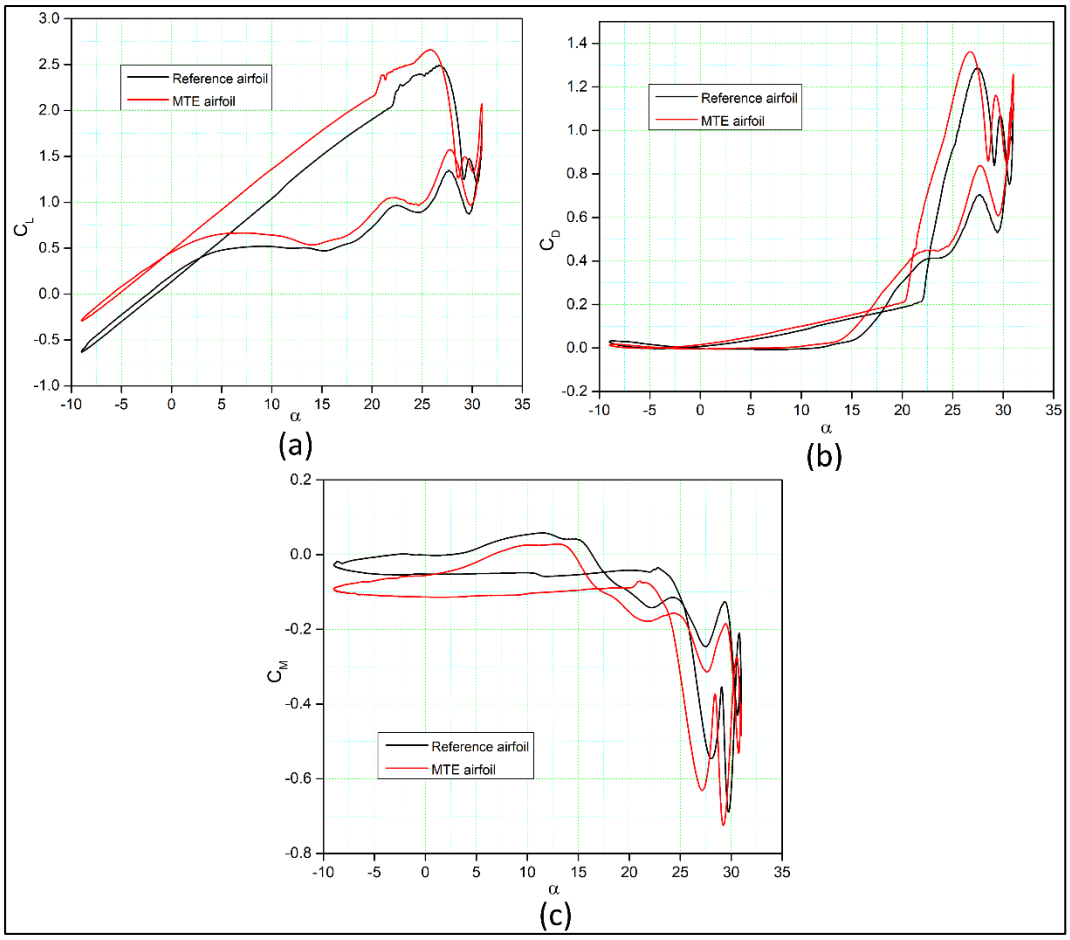

Figure 6.21 Aerodynamic coefficient hysteresis loops at k = 0.08: (a) lift coefficient, (b) drag coefficient; (c) pitching moment coefficient

Figure 6.22 (a) shows the pressure coefficient variations with the chord position $\frac{x}{c}$ at the angle of attack of 25.5°, with only very large scale vortical structures growing over the airfoil during up-stroke motion. This phenomenon results in smooth surface pressure contours. Figure 6.22 (b) shows the occurrence of the separated flow on the skin friction coefficient at $\frac{x}{c} = 0.8$ for an angle of attack of 25.5°. When the angle of attack further increases to 29.8° (Figure 6.22(c)), there is an increase in the leading-edge flow acceleration, resulting in a larger unfavorable pressure gradient, and resulting in a stall. Figure 6.22 (c) shows the pressure coefficient at 29.8°, thus indicating that the pressure coefficient has a smaller value than -4 , and it clearly indicates that the LEV is at x/c = 0.6. Flow separation inflates and moves towards the trailing edge with many secondary and tertiary leading-edge vortices (see Figure 6.22 (d)), and the

bubble breaks down due to the increased adverse pressure gradient. The dynamic stall vortex is formed while moving towards the trailing edge. A significant separation of the skin friction coefficient is caused by the stall occurrence. The flow from the airfoil's pressure side has a motion towards the suction side near the trailing edge, due to the negative pressure of the vortex causing a counter-rotating trailing edge vortex, as shown in Figure 6.22 (e) for the angle of attack of 30°. Figure 6.22 (f) shows vortex shedding as the leading-edge vortex moves over the airfoil surface. The leading-edge vortex dissipation causes a lift coefficient decrease.

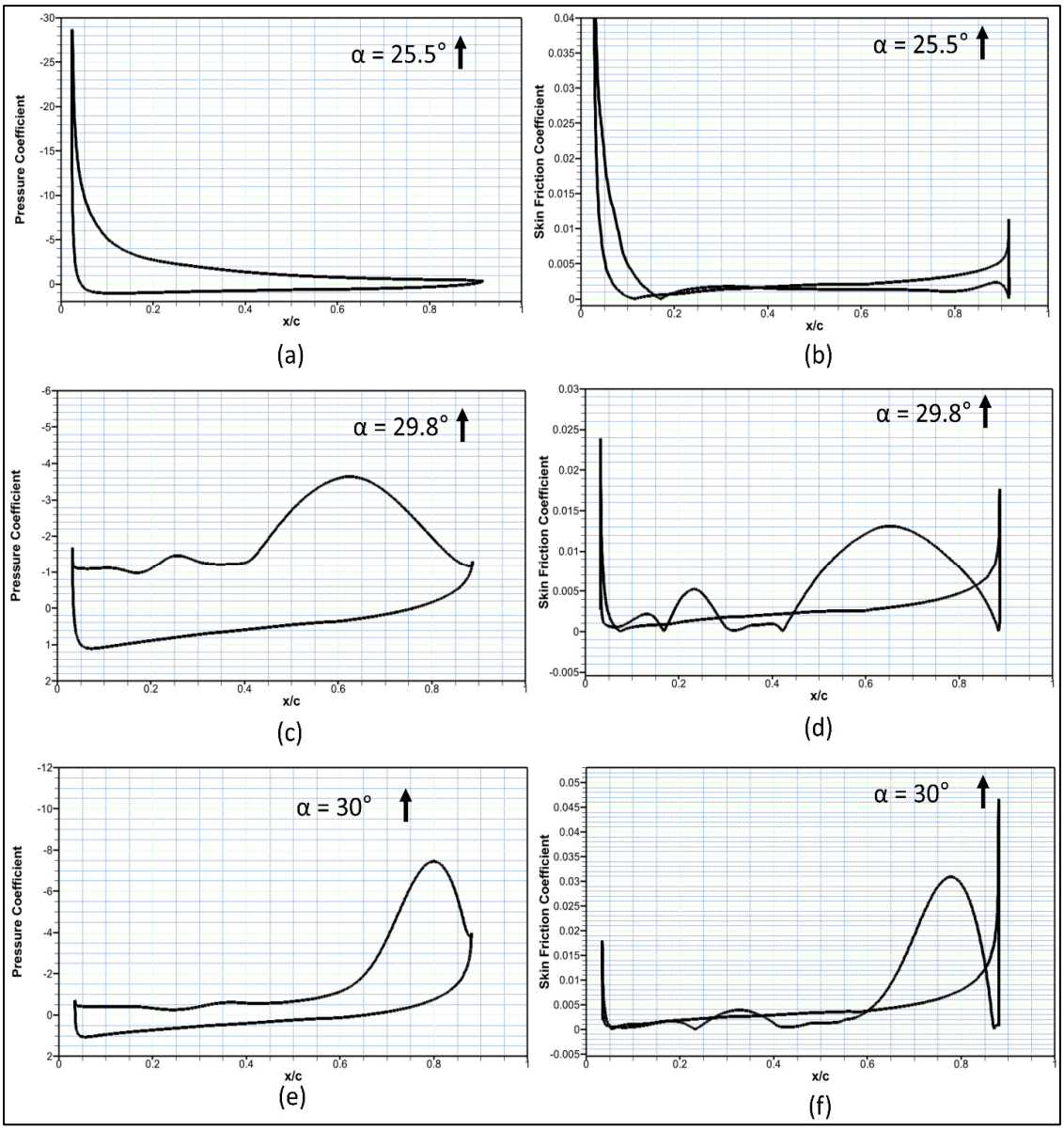

Figure 6.22 Computed pressure coefficient and skin friction coefficient for the MTE airfoil

Figure 6.23 shows the vorticity contours at different angles of attack during a pitching cycle for both the reference and the MTE airfoils. Figures 6.23 (a) and (d) reveal that the boundary layer separation takes place, and that the separation is more deepened for the MTE airfoil. The flow remains attached to the rest of the airfoil at angle of attack of 25.5°. When the angle of attack increases while the airfoil oscillates, a more reversed flow area occurs in the MTE airfoil

than the reference airfoil, moving from the trailing edge towards the leading edge as visualized at $\alpha = 29.8°$.

LEVs containing significant energy are created, and they migrate downstream on the airfoil surface, as seen in Figure 6.23(b), thus resulting in strong integral forces. These vortices structures are characterized by a stronger force coefficient curve slope, as displayed earlier in Figure 6.13.

The MTE airfoil also results in a much stronger vortex, as shown in Figure 6.23 (e), while a weaker TEV is produced at the critical angle of attack of 30.8° on the reference airfoil, as shown in Figure 6.23 (c). This TEV dissipates downstream where it is replaced by a secondary LEV, which spreads over most of the airfoil's chord span. Both LEVs and TEVs form and shed during the downstroke, causing significant force coefficient fluctuations. Using an MTE, the airfoil fully stalled and with a higher strength than the one observed in the reference airfoil.

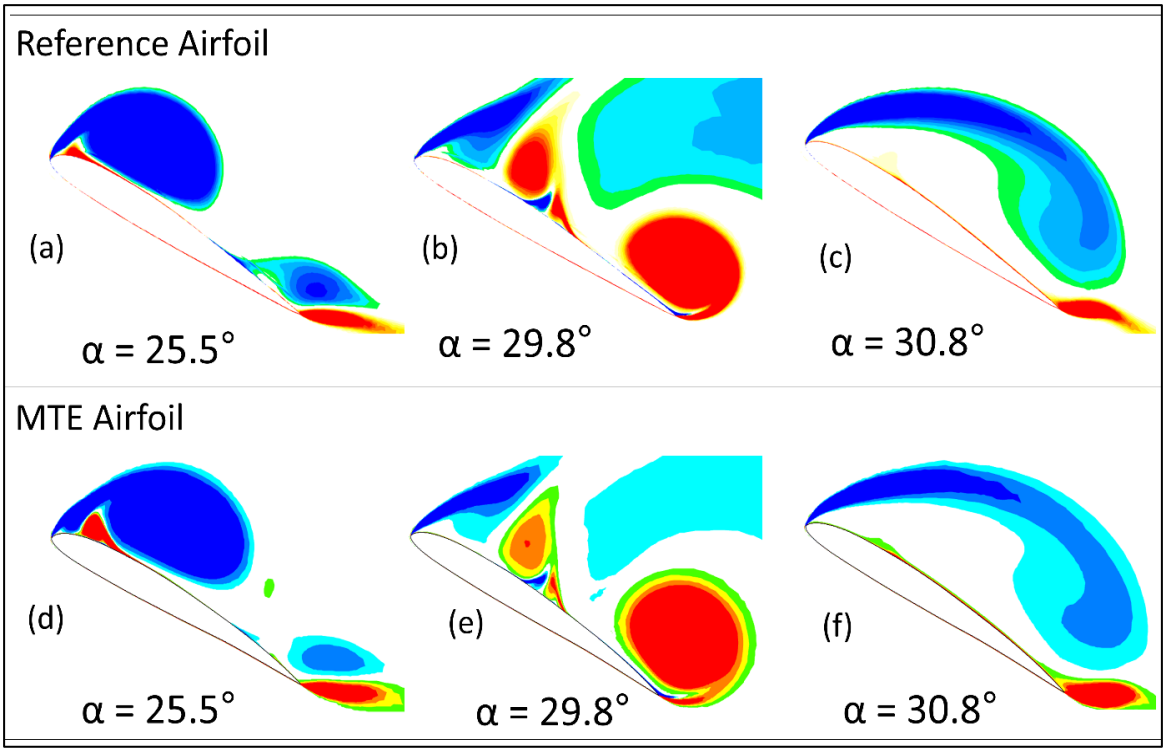

Figure 6.23 Comparison of vorticity contours of the reference airfoil with those of the MTE airfoil at different angles of attack

Table 6.4 presents the aerodynamic coefficients and stall characteristics of the reference airfoil and the MTE airfoil. The stall angle of attack was increased by1° for the MTE airfoil with respect to that of the reference airfoil. The maximum lift coefficient increased slightly by a maximum of 6.8%, and the maximum drag coefficient by 8.5%. The other results followed a similar trend, including the increase in maximum lift coefficient values of a pitching airfoil compared to a static airfoil.

Table 6.4 Comparison of airfoil performance parameters of the reference airfoil with the MTE airfoil

Airfoil	k	$C_{L,max}$	$\Delta C_{L,max}$	$\alpha_{ds}[°]$	$C_{D,max}$	$\Delta C_{D,max}$
Reference	0.08	2.49	1.15	26.70	1.29	0.82
MTE	0.08	2.67	1.32	25.84	1.36	0.89

Note: $C_{L,max}$= max dynamic lift coefficient; $C_{D,max}$ = max drag coefficient; α_{ds} = dynamic stall angle; $\Delta C_{L,max}$ = max lift difference from steady state results;$\Delta C_{D,max}$= max drag coefficient difference from steady state results

6.4 Conclusion

This paper investigated the effect of the optimized Morphing Leading Edge (MLE) and Morphing Trailing Edge (MTE) on the dynamic stall vortex (DSV) around a pitching airfoil through numerical simulations. Firstly, the optimization of the UAS-S45 airfoil was performed using a morphing optimization framework. This framework used Bezier-Parsec parametrization and the Particle Swarm Optimization coupled with the Pattern Search algorithm with the aim of designing an aerodynamically efficient S-45 airfoil. The $\gamma - Re_\theta$ transition turbulence model was applied to predict the laminar-turbulent flow transition region. Secondly, the study presented the unsteady analysis of the UAS-S45 airfoil and its morphing configurations. Finally, the unsteady flow field and the aerodynamic forces were analyzed at the Reynolds number of 2.4 x 10^6, and five different reduced frequencies. The lift (C_L), drag

(C_D) and moment (C_M) coefficients of the reference and the morphing airfoils were compared. Based on this study, the following conclusions were drawn:

The morphing airfoils improved the overall aerodynamic performance and delayed the boundary layer separation. The lift coefficients of the MLE airfoil compared to those of the reference airfoil have higher values, increasing from 1.57 to 1.65, which represented a 5.09% gain, while the static angle of attack increased, by 3°. An increase of 3.8% in the maximum $\frac{C_L}{C_D}$ was obtained for an MLE airfoil compared to the reference airfoil.

- The optimal shapes of MTE airfoil produced an increase of the lift coefficient with respect to the reference airfoil of up to almost 8.6%. In addition, an increase of 2° in the static stall angle was obtained for the MTE airfoil.
- The effect of the reduced frequency on the unsteady pitching motion was investigated by plotting the C_l versus the angle of attack for several reduced frequencies of k = 0.05, 0.08, 0.12, 0.16 and 0.20 at Re = 2.4 x 10^6. The $C_{L,max}$ increased with reduced frequency, from $C_{L,max}$= 2.43 at k = 0.05 to $C_{L,max}$= 2.64 at k = 0.12.
- The results showed a similar pattern for the drag coefficients values; however, 'k' had a mixed effect on the maximum drag coefficients ($C_{D,max}$). $C_{D,max}$ changed from 1.17 at k = 0.05 to 1.45 at k = 0.2 and from $C_{D,max}$ of 1.29 at k = 0.08 to 1.44 at k = 0.16 as 'k' increased. On the downstroke, numerous sorts of vortices were formed near the trailing edge. From the time of their separation and shedding into the downstream wake, these vortices increased the lift force.
- It was found that higher reduced frequency stabilized the leading-edge vortex (LEV) that provided its lift by reducing lift variation during the dynamic stall phase. High reduced frequency LEV stabilized the flow even when the airfoil was in the downstroke. The $C_{L,max}$, $C_{D,max}$ and stall angles of attack were calculated for all reduced frequencies.
- The numerical results have shown that the new radius of curvature of the MLE airfoil can minimize the streamwise adverse pressure gradient and prevent significant flow separation by delaying the Dynamic Stall Vortex (DSV) occurrence. Furthermore, it was shown that the morphing airfoil delayed the stall angle of attack with respect to the

stall of the reference airfoil by 14.26 %, and $C_{L,max}$ of the airfoil increased from 2.49 to 3.04.

- However, while the MTE airfoil was found to increase the overall lift coefficient and the $C_{l,max}$, it did not affect the dynamic stall. Vorticity behavior during DSV generation and separation has shown that the MTE can change vortices' evolution and increase vorticity strength from the leading-edge shear layer by increasing DSV flow.
-

Regarding future works, the LARCASE's Price-Padoussis subsonic wind tunnel will be used for further wind tunnel studies of the MLE and MTE airfoils. The findings are expected to clarify the flow physics, and hence to validate the findings of the morphing airfoil flow phenomena.

CHAPTER 7

FLOW CONTROL AROUND THE UAS-S45 PITCHING AIRFOIL USING A DYNAMICALLY MORPHING LEADING EDGE (DMLE): A NUMERICAL STUDY

Musavir Bashir [a], Nicola Zonzini [b], Ruxandra Mihaela Botez [c], Alessandro Ceruti [d] and Tony Wong [e]

[a, c, e] Department of System Engineering, École de Technologie Supérieure,
1100 Notre-Dame West, Montréal, Québec, Canada H3C 1K3
[b, d] Department of Industrial Engineering, University of Bologna, Bologna, Italy
Via Zamboni, 33, 40126 Bologna BO, Italy

Paper published in *Biomimetics*, January 2023.
DOI: https://doi.org/10.3390/biomimetics8010051

Résumé

Cet article étudie l'effet du bord d'attaque déformable dynamiquement (DMLE) sur la structure de l'écoulement et le comportement des tourbillons de décrochage dynamiques autour d'un profil en tangage de l'UAS-S45 dans le but de contrôler le décrochage dynamique. Une étude de paramétrage non-stationnaire a été développé pour modéliser le mouvement variable dans le temps du bord d'attaque. Le schéma a ensuite été intégré au solveur numérique Ansys-Fluent en développant une fonction définie par l'utilisateur (UDF) dans le but de dévier dynamiquement les limites du profil aérodynamique et de contrôler le maillage dynamique utilisé pour changer sa forme et l'adapter davantage. Les techniques de maillage dynamique et coulissant ont été utilisées pour simuler l'écoulement non-stationnaire autour du profil en tangage sinusoïdal de l'UAS-S45. Bien que le modèle de turbulence $\gamma - Re_\theta$ ait adéquatement capté les structures de l'écoulement des profils dynamiques associés aux formations de tourbillons sur le bord d'attaque pour une large gamme de nombres de Reynolds, deux études plus approfondies ont examinées ici: i) Tout d'abord, un profil oscillant avec le DMLE a été étudié; Le mouvement oscillation en tangage du profil et ses paramètres sont définis, tels que l'amplitude du nez de type "Droop Nose" (A_D) et le temps du début de la déformation (M_{ST}). Les effets de A_D et de M_{ST} sur les performances aérodynamiques ont été étudiés et trois cas d'amplitudes différentes ont été considérés, ii) Deuxièmement, le mouvement d'un DMLE

d’un profil pour différents angles d’attaque de décrochage a été étudié. Dans ce cas, le profil aérodynamique a été réglé à des angles d’attaque de décrochage plutôt que de l’osciller. Cette étude fournira la portance et la traînée transitoires à différentes fréquences de 0.5 Hz, 1 Hz, 2 Hz, 5 Hz et 10 Hz. Les résultats ont montré que le coefficient de portance du profil avait augmenté de 20.15 %, tandis qu’un retard de 16.58 % de l’angle de décrochage dynamique a été obtenu pour un profil oscillant avec le DMLE avec A_D = 0,01 et M_{ST} = 603 s, par rapport au profil aérodynamique de référence. De même, les coefficients de portance pour deux autres cas, où A_D = 0,05 et A_D = 0,0075, ont augmenté respectivement de 10.67 % et 11.46 % par rapport au profil de référence. De plus, il a été démontré que la déviation vers le bas du bord d’attaque augmentait l’angle d’attaque de décrochage et le moment de tangage avec le nez vers le bas. Enfin, il a été conclu que le nouveau rayon de courbure du profil DMLE minimisait le gradient de pression dans le sens du courant et empêchait une séparation significative de l'écoulement en retardant l'apparition du "Dynamic Stall Vortex (DSV)".

Abstract:

This paper investigated the effect of the Dynamically Morphing Leading Edge (DMLE) on the flow structure and behavior of vortices for dynamic stall around a pitching UAS-S45 airfoil with the aim to control the dynamic stall. The unsteady parametrization framework was developed specifically to model the morphing motion of the leading edge with time. This scheme was then integrated within the numerical solver by developing a User-Defined-Function (UDF), which served to dynamically deflect the airfoil boundaries and control the dynamic mesh algorithm used to deform and adapt the surrounding mesh. Both the dynamic and sliding mesh techniques were used to simulate unsteady flow across the sinusoidally pitching UAS-S45 airfoil. $\gamma - Re_\theta$ turbulence model is good for capturing the flow structures of dynamic airfoils associated with leading edge vortex formations for a wide range of Reynolds numbers. Two broader studies are considered: i) Firstly, the DMLE of an oscillating airfoil is investigated. In this part, the pitching-oscillation motion of an airfoil is defined and the parameters such as droop nose amplitude (A_D) and its starting time are evaluated. The effect of variation of A_D and starting time of morphing leading edge on the aerodynamic performance

will be studied, and three different amplitude cases are considered in this paper; ii) secondly, the DMLE of an airfoil at stall angles of attack is investigated. In this part, the analysis of the dynamically morphing leading edge is performed to provide further insights into the dynamic lift and drag forces during the motions at for pre-defined morphing frequencies of 1 Hz, 2 Hz, 5 Hz and 10 Hz, respectively. It was found that the DMLE of an oscillating airfoil at all the A_D values of 0.01, 0.005 and 0.075 and different morphing times respectively, lift coefficient for the airfoil increases almost linearly until 28°, after which a sudden surge in the C_l is observed as compared to the reference airfoil. In terms of drag coefficient, there is 17.70 % decrease in drag coefficient. It was found that the morphing airfoil delayed the stall angle of attack with respect to the stall of the reference airfoil by 11.63 %, and $C_{L,max}$ of the airfoil increased by 21.87 %. The numerical results have shown that the new radius of curvature of the DMLE airfoil can minimize the streamwise adverse pressure gradient and prevent significant flow separation by delaying the Dynamic Stall Vortex (DSV) occurrence.

7.1 Introduction

Modern Unmanned Aerial Vehicles (UAVs) have various advantages, including low operating costs, the ability to fly in risky conditions, and long flight endurance. UAVs are used for fire detection, search and rescue, wildlife monitoring, and security surveillance (Hassanalian et al., 2017; Jiménez López et al., 2019). The fixed-wing UAV plays an essential role in such missions due to its long endurance and high payload capacity. However, UAVs are designed for particular missions, indicating that they can perform well for these flight conditions; however, their performance is suboptimal for their multi-point flight envelope. In addition, during various flight conditions, UAVs might experience a sudden variation of the pitch attitude due to the necessity of performing extraordinary maneuvers or to unexpected external disturbances, such as vertical wind gusts. Consequently, an abrupt and sudden change in the angle of attack may develop non-linear unsteady aerodynamic effects such as dynamic stall on the aircraft.

Furthermore, UAVs are currently holding most of the market share (Research, September 07, 2021), and expect to contribute up to 20% of the global aviation market by 2037. Therefore,

designers are encouraged to develop breakthrough technology to meet the Green Aviation standards and reducing fuel consumption has become very important for the environment and air transportation. The challenges of meeting the demands for lower emissions and higher levels of air transport have increased the demand for new research ideas to produce more efficient and ecologically friendly aircraft.

Researchers have attempted to mimic bird flight to improve the aerodynamic performance of a broader flight envelope. However, such an attempt requires a high level of technology readiness, which allows it to be installed on UAVs because of safety and weight concerns (Andrei V Popov et al., 2010; Andrei Vladimir Popov et al., 2010). This possibility of meeting the desired aerodynamic efficiency by mimicking the bird flight is the new generation morphing wing technology. The early years of aeronautical research focused on biomimetic techniques based on flexible and highly deformable structures to mimic the ability of birds to adjust their shape to different flight cases. The Research Laboratory in Active Controls, Avionics, and AeroServoElasticity (LARCASE) team is studying several approaches for reducing fuel consumption (Bashir et al., 2021; Bashir, Longtin-Martel, Botez, et al., 2022; Bashir, Longtin-Martel, Zonzini, et al., 2022; Bashir, Longtin Martel, et al., 2022a, 2022b; R. Botez, 2018; R. Botez et al., 2018; Ruxandra M Botez, 2022; Ruxandra Mihaela Botez et al., 2007; Félix Patrón et al., 2014; Hamy et al., 2016), including the use of morphing wing technologies. Such as, the morphing leading edge prototype demonstrates the possibility of modifying the stall angle of the wing. It was shown that the stall angle of the wing was delayed using a downward deformation of leading edge (Communier et al., 2020; Communier et al., 2019). An experimental and numerical analysis was carried out for an UAS-S45 wing geometry with the aim to improve the laminar flow on the upper surface of the wing, between 10% and 70% of the chord (Oliviu Şugar Gabor et al., 2016; Koreanschi, Oliviu, et al., 2016; Koreanschi, Sugar-Gabor, et al., 2016). The morphing optimization considered different flight conditions, such as take-off, cruise, landing, stall, etc. It was shown that for all investigated cases, a significant transition improvement was obtained.

Traditional hinged lifting mechanisms and trailing edge surfaces control airflow aerodynamically, but they also increase drag (Kintscher et al., 2011). These hinged surfaces

have drawbacks in both deployed and retracted states (Li et al., 2013). When hinged surfaces are deployed, the gaps between the high-lifting surface and the wing can create noise, turbulence, and early transition. Retracted trailing edge hinges provide a turbulent boundary layer. Various techniques have been implemented recently to enhance aerodynamic efficiency. One such solution is the morphing wing technology, a promising state-of-the-art innovation (Arena et al., 2018; Dimino et al., 2017; Pecora, 2021). Several research programs have achieved significant results in the field of aircraft morphing (Ameduri et al., 2018; Concilio et al., 2021; Giuliani et al., 2022).

The use of morphing wing technology as a flow control technology has resulted in efficient aerodynamic designs (O Şugar Gabor et al., 2016; Gabor et al., 2014; Katam et al., 2005; Olivett et al., 2021). Dynamic stall control is especially significant because it occurs in all aerospace applications, such as on UAV's (Mathisen et al., 2021; Sekimoto et al., 2022), helicopter rotors (Liiva, 1969; Richez, 2018), wind turbines (Larsen et al., 2007; Zhu et al., 2021), military aircraft (Brandon, 1991; Nguyen et al., 2022), and others. Researchers have focused on tackling the dynamic stall phenomenon experienced by pitching oscillating airfoils for several years (Benton et al., 2019; Carr, 1988; McCroskey, 1981; McCroskey et al., 1976; Mulleners et al., 2013). Dynamic stall is caused by a rapidly pitched airfoil, wing, or turbine blade. The Leading-Edge Vortex (LEV) or Dynamic Stall Vortex (DSV) is a critical component of dynamic stall, as it increases the lift coefficient. However, this excess lift is lost when the vortex sheds into the wake, thus increasing drag and shifting the pitching moment. Since the discovery of dynamic stall, researchers have tried to understand its mechanics and to modify the LEV formation. Altering the LEV formation may increase an aircraft's operational envelope.

Numerous flow control devices have been developed to avoid flow separation and to mitigate dynamic stall effects. They can be classed into active and passive, based on their operational principles. Vortex generators, micro-tabs, and serrated trailing edges are all examples of passive control mechanisms, while active control mechanisms include trailing-edge flaps. synthetic jets, plasma actuators, etc. The use of leading-edge slats (Balaji et al., 2006; Imamura et al., 2008), trailing-edge flaps (Gerontakos et al., 2006; T. Lee et al., 2011), synthetic

jet/periodic excitations (D Greenblatt et al., 2001; David Greenblatt et al., 2000; Traub et al., 2005), plasma actuators (Post et al., 2006), vortex generators (Heine et al., 2013), and dynamically deformed leading edges (Sahin et al., 2003) to accomplish the flow control has been studied.

Several numerical studies have been carried out to investigate the aerodynamics of morphing wings and their stall properties. The Reynolds-Averaged Navier-Stokes (RANS) equations were used to analyze adaptive morphing trailing-edge wings, thus producing a drag reduction on-design of 1% and 5% off-design (Lyu et al., 2015). The lift-drag ratio increased by 6.5% for the morphing wing (Abdessemed et al., 2018b). The numerical simulations of a NACA0012 airfoil with a flexible trailing edge showed that the morphing surface could postpone the beginning of flow separation with the aim to achieve optimal aerodynamic performance (Jawahar et al., 2018; Kamliya Jawahar et al., 2017).

An active dynamic stall control technique with deployable LEV generators was developed in (Le Pape et al., 2012). For a dynamic stall flight, the active flow control would only be triggered on the retreating side of the blade to avoid increasing blade drag. The vortex generators performed very well in the wind tunnel, as they delayed the static stall and reduced the dynamic stall penalties. The static stall angle increased by 3 degrees, and the negative pitching moment peak was lowered by 60% for the dynamic stall.

The impact of synthetic jet control on the unstable dynamic stall over a rotor airfoil using numerical simulations was explored in (Qijun et al., 2017). The numerical findings indicated that the dual jet could significantly increase the control efficiency of the rotor airfoil's dynamic stall compared to the single jet. A high-frequency control method for dynamic stall mitigation that takes advantage of the natural instabilities of the laminar separation bubble (LSB) to delay the occurrence of Dynamic Stall Vortex (DSV) was proposed in (Visbal et al., 2018; Visbal et al., 2017) and merits further investigation. The effect of the trailing edge flap (TEF) on mitigating DSV-induced substantial negative pitching moments and negative aerodynamic damping was investigated in (Feszty et al., 2004). The authors hypothesized that the substantial negative pitching moments and related negative aerodynamic damping were caused by the TEV. The effect of the oscillating TEF on the dynamic loads generated by an airfoil was

evaluated (Gerontakos et al., 2007; T. Lee et al., 2009). The TEF motion did not affect the creation or separation of the DSV, but the TEF's deflection increased the airfoil's maximum lift.

A study investigating the effect of a TEF on the dynamic stall at high speeds for wind turbines was presented in (Samara et al., 2021). The TEF pitching impacts the load fluctuation loops. The trailing edge flap reduced cyclic variability by 26% in terms of root bending moment. These findings help in better understanding how TEFs reduce wind turbine blade load changes. Unsteady aerodynamic loads were applied on an airfoil by a TEF deflecting at various frequencies (Krzysiak et al., 2006). Phase delay between an airfoil angle of attack and the initial flap deflection was investigated. When the airfoil's angle of attack and TEF deflection both increased, the TEF oscillations increased the maximum lift coefficient.

A hybrid RANS-LES technique was used to investigate the airfoil morphing aerodynamic performance with a deflecting TEF (Abdessemed, Yao, et al., 2021; Abdessemed et al., 2018a). Morphing enhanced the lift-to-drag ratio by 6%. Similar type results were obtained for the aerodynamic and aero-acoustic responses of an airfoil fitted with a harmonically morphing TEF (Abdessemed, Bouferrouk, et al., 2021). Larger morphing TEF amplitudes increased Sound Pressure Levels (SPLs), and all morphing cases studied shifted the main tonal peak to a higher frequency that led to a 1.5 dB reduction in the predicted SPL.

A two-dimensional multi-element dynamic stall solver was investigated to demonstrate the leading edge slat's effectiveness in controlling dynamic stall (Bangalore et al., 1996). The major drawback of these slats was their high drag penalties associated with their use under off-design conditions. A retraction mechanism similar to that found on aircraft would be practically heavy and expensive.

Since the local shape of the airfoil leading-edge influences DSV production, changing the leading-edge shape is an efficient technique to reduce dynamic stall effects (Geissler et al., 1998). Active flow control based on a Variable Droop Leading-Edge (VDLE) device reduced local Mach number and improved pressure distribution near the leading edge, therefore postponing or eliminating dynamic stall without significant lift changes (Martin et al., 2003). The concept of a dynamically deforming leading edge was proposed, where the airfoil shape

was gradually changed, and the leading-edge radius increased as the airfoil pitched upwards (Chandrasekhara et al., 1998). Airfoils with large leading-edge radii tend to have mild adverse pressure gradients, as the local velocities are lower than those of a conventional airfoil. As the airfoil pitches downwards in the absence of a stall the airfoil returns to its original shape. In another study, the leading-edge droop was integrated on the Gurney flap to improve rotor airfoil dynamic stall and post stall (B.-s. Lee et al., 2005). The deflection of a 20° leading-edge droop with that of a 0.5% chord Gurney flap effectively delayed dynamic stall. The maximum lift coefficient increased, while the negative pitching moment decreased, and the lift-to-drag ratio increased with respect to reference designs.

The potential benefits of controlling and further delaying this nonlinear aerodynamic stall effect could be achieved by employing a Dynamically Morphing Leading Edge (DMLE). An in-depth understanding of the unsteady flow physics characterizing this class of morphing wings would be helpful. The DMLE concept as a comprehensive investigation of different parameters, such as the deflection frequency, the extent of deflection, and the morphing starting time, is barely found in the literature. This study aims to track the occurrence and development of an LEV and reduce the flow separation, and thereby avoiding the dynamic stall. The dynamic stall control with the DMLE on an oscillating UAS-S45 airfoil is evaluated using unsteady RANS equations. Two different studies and analyses are proposed and investigated.

7.2 Methodology

This study investigates the effect of a Dynamically Morphing Leading Edge (DMLE) on the dynamic stall of the UAS-S45 airfoil. The influence of the upward and downward airfoil deflections on the development process of the Dynamic Stall Vortex (DSV) is presented for the oscillating airfoil. To simulate the dynamic stall phenomenon, the pitching of the airfoil is governed by a time-dependent sinusoidal equation that guarantees a bounded time variation of the angle of attack. The pitching motion results in the generation of a periodic hysteresis cycle of the aerodynamic coefficients, including the lift, drag, and moment coefficients. The

following sinusoidal mode equation (1) governs the airfoil pitching motion about its ¼ chord position:

$$\alpha(t) = \alpha_m + \alpha_a \sin(\omega t) \tag{7.1}$$

where α_m = 11° is the mean incidence angle, α_a = 20° is the amplitude, ω is the angular velocity and t is the time.

The reduced frequency (k) is defined in equation (7.2):

$$k = \frac{\omega_p c}{2U_\infty} \tag{7.2}$$

where U_∞ is the freestream velocity and c is the airfoil chord length. A reduced frequency of k = 0.08 was chosen for the airfoil pitching motion and the Reynolds number based on the unit chord length and free-stream velocity of 35.5 m/s was set to 2.4×10^6.

7.2.1 Leading Edge Parametrization

The morphing leading edge geometry and its unsteady deformation must be defined in order to obtain the DMLE airfoil. These definitions require a parametrization technique that can accurately characterize the airfoil boundary/geometry. By using specific control parameters from the 4-digit NACA airfoil, it was possible to dynamically adjust the camber line of the targeted morphing region of the chord and to design a new airfoil shape that included the time variable in the parametrized equations of the trailing edge geometry (Abdessemed et al., 2017). However, due to the UAS-S45 airfoil asymmetry, it was impossible to directly adopt and converse the mathematical model of symmetric airfoil (Abdessemed et al., 2017). Therefore, a different concept was developed here for the asymmetric airfoils. The camber of an asymmetric airfoil determines its curvature and its type. Figure 7.1 shows the parameters considered in the leading-edge morphing model. The beginning of the morphing region is given by the parameter x_i, and the maximum displacement of the outermost leading-edge coordinate is given by W_{le}.

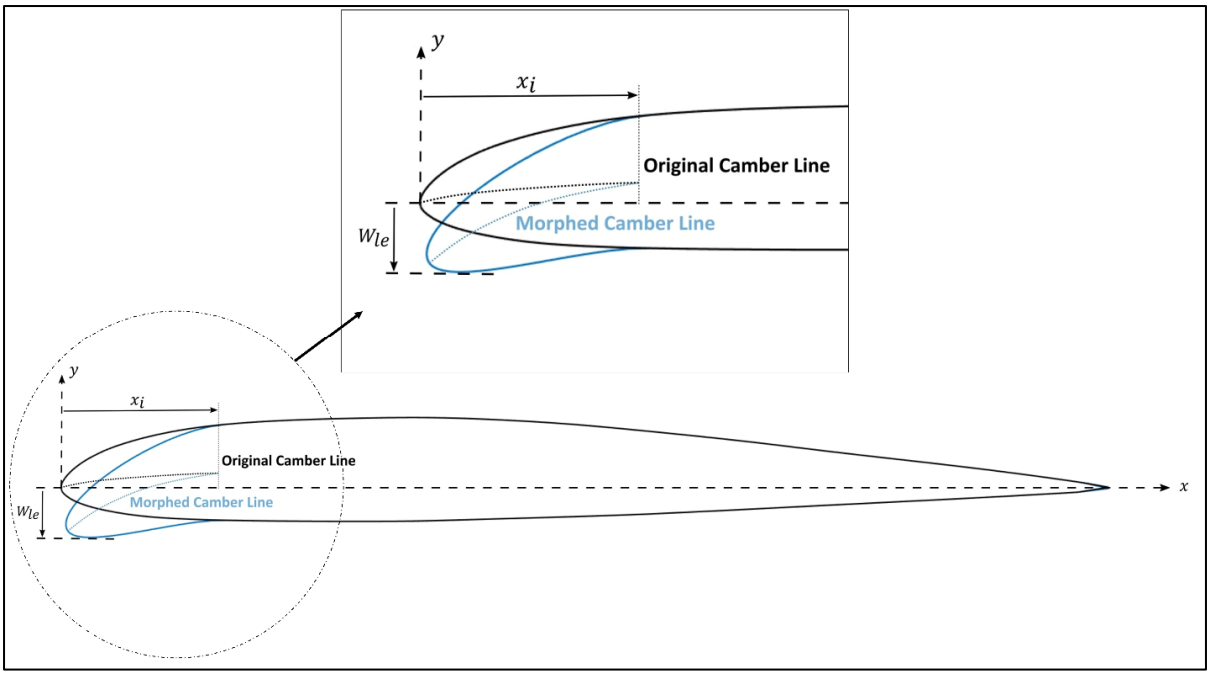

Figure 7.1 Geometrical definition of a variable camber line

The essential requirement for designing a DMLE framework is the development of the parametric equations for the camber line and the airfoil thickness distribution. These equations are developed for the asymmetric UAS-S45 airfoil model and are therefore used in the present study. The airfoil thickness distribution is given by equation (7.3).

$$\frac{y_t}{c} = \left(\frac{t}{c}\right)\left[a_0\sqrt{\frac{x}{c}} - a_1\left(\frac{x}{c}\right) - a_2\left(\frac{x}{c}\right)^2 + a_3\left(\frac{x}{c}\right)^3 - a_4\left(\frac{x}{c}\right)^4\right] \tag{7.3}$$

Depending on the considered airfoil portion (Leading-edge or Trailing edge) and on the chosen starting point of the morphing, it is possible to adopt one of the following equations (7.4) and (5):

$$\left.\begin{aligned}\frac{y_c}{c} &= \frac{M}{P^2}\left[2P\left(\frac{x}{c}\right) - \left(\frac{x}{c}\right)^2\right] \\ \frac{dy_c}{dx} &= \frac{2M}{P^2}\left[P - \left(\frac{x}{c}\right)\right]\end{aligned}\right\} \quad \left(\frac{x}{c}\right) < P \tag{7.4}$$

$$\left.\begin{aligned} \frac{y_c}{c} &= \frac{M}{(1-P)^2}\left[1-2P+2P\left(\frac{x}{c}\right)-\left(\frac{x}{c}\right)^2\right] \\ \frac{dy_c}{dx} &= \frac{2M}{(1-P)^2}\left(P-\left(\frac{x}{c}\right)\right) \end{aligned}\right\} \left(\frac{x}{c}\right) \geq P \tag{7.5}$$

where M is the maximum value of the percentage chord line, and P is the chordwise position of the maximum camber in 10's of the chord. For the definition of the camber line, since M and P for an asymmetric airfoil are not zero, the value of P serves to divide the camber line approximation into two separate equations in which both M and P appear.

After the definitions of the airfoil mean camber line equation, a second-order polynomial function is introduced to define the new camber line equation of the morphing airfoil portion. In order to obtain control of the maximum deflection of the leading edge, equation (7.6) is parametrized and defined as follows:

$$\frac{y_f}{c} = \begin{Bmatrix} \frac{y_f}{c} - W_{le}\frac{(x_i-\bar{x})^2}{x_i^2}, 0 \leq \bar{x} \leq x_i \\ 0, \qquad x_i \geq \bar{x} \end{Bmatrix} \tag{7.6}$$

where y_f is the final y-coordinate of the new morphing airfoil camber line, W_{le} is the value of the maximum deflection of the leading edge, and $\bar{x}$ is the x-coordinate of the selected control point. The maximum limit of leading-edge deflection was set to 0.05c and the airfoil was initially (x_i) set at baseline position.

To achieve a continuous deflection of the leading edge during transient flow simulations, the time variable must be introduced in the governing equations of the parameterization model. The parametrization equation was extended to include the time variable, while the parametrized camber line equation was modified with the aim to express the camber line as a function of time. The unsteady dynamic motion of the upper and lower surface airfoil coordinates is obtained by adding the thickness distribution to the time-dependent camber line equation. Moreover, the airfoil deflecting motion was designed to start from the baseline

configuration, then reach a maximum downward target position. It will then return to its initial baseline configuration, and a sinusoidal function has been chosen and further used. The parametrized time-dependent camber line is defined by the following equation:

$$\frac{y_f}{c} = \begin{Bmatrix} \frac{y_f}{c} - W_{LE}\sin(2\pi t f)\frac{(x_i - \bar{x})^2}{x_i^2}, 0 \le \bar{x} \le x_i \\ 0, \qquad x_i \ge \bar{x} \end{Bmatrix} \tag{7.7}$$

Where t is the time variable, and f is the deflection frequency parameter (cycles per second).

Five main parameters were determined to be of crucial importance for the airfoil morphing control: M, P, y_f, W_{le} and x_i. Figure 7.2 depicts some of these parameters.

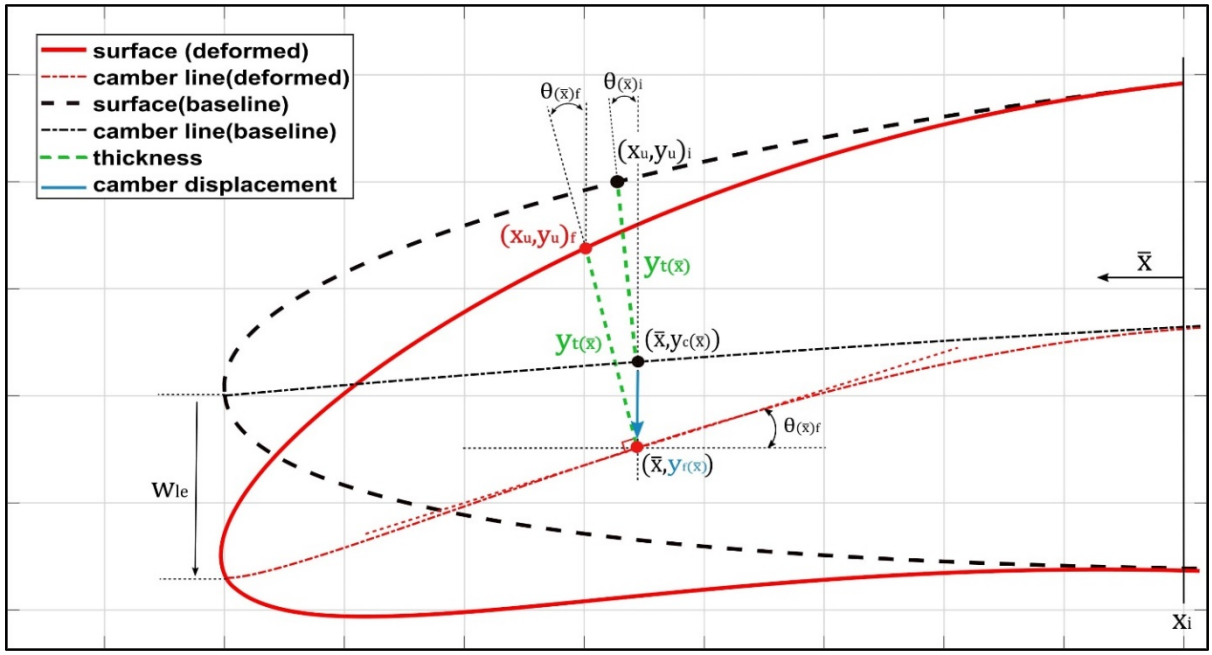

Figure 7.2 Numerical modeling of the camber line

7.2.2 Computational Domain and Grid

The size and shape of the computational domain affect the quality of results, which is also based on the geometry's aerodynamics. For the present aerodynamics scenario, the 2D computational domain is represented by a C-shaped grid with 20 times the chord length (20c) upstream and 30 times the chord length (30c) downstream. Such lengths were found to be large enough to ensure that the outer domain boundary conditions do not influence the airfoil flow and that they are small enough to keep the computing power in a reasonable range. In this study, both unstructured and structured hybrid meshes were considered, as illustrated in Figure 7.3, with a structured quadrilateral layer mesh near the airfoil and with an unstructured triangle mesh elsewhere. With a blunt trailing edge, it is possible to obtain O-shaped block layers surrounding the airfoil and thereby minimize any instabilities caused by sharp trailing-edge corners.

Wall condition parameter y^+ defines a dimensionless height of the first grid point measured from a wall, that is utilized to evaluate the 'near-wall' mesh requirements. To appropriately represent the near-wall mesh, a grid that meets a turbulence model's wall y^+requirements are obtained. In the current investigation, the $\gamma - Re_\theta$ turbulence model required that the first airfoil cells should be situated in the viscous sublayer; thus, a y^+ less than one was targeted.

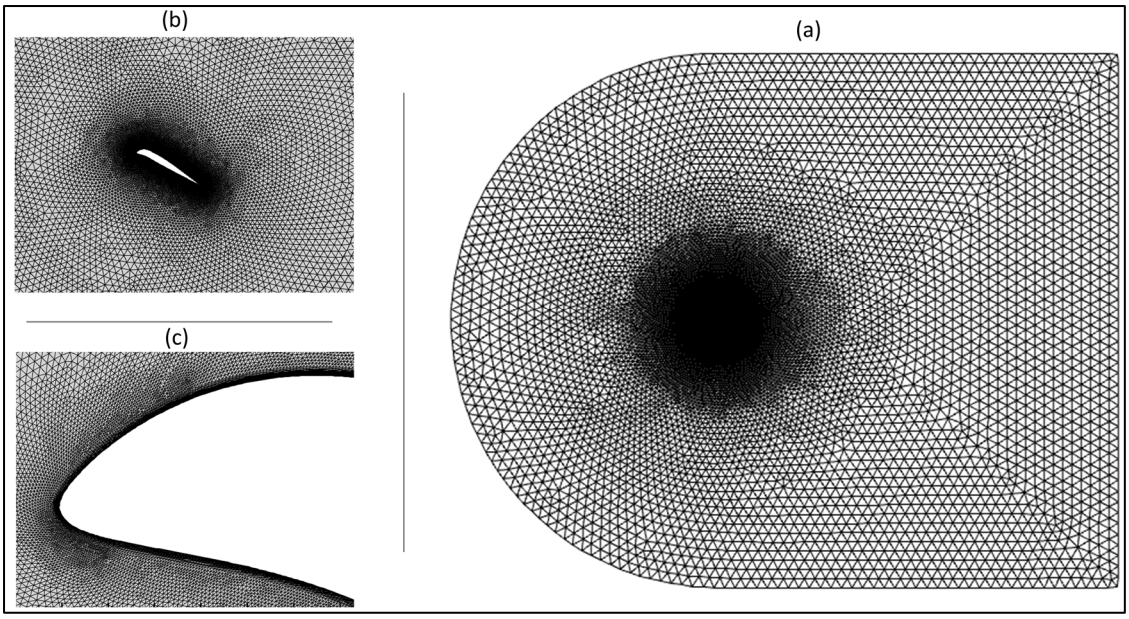

Figure 7.3 Computational domain with (a) hybrid mesh, (b) structured mesh around the airfoil, and (c) DMLE UAS-S45 airfoil mesh

7.2.3 Validation of Results

The time history variation of the lift coefficient illustrated in Figure 7.4 (a) displays a sudden stall after the maximum value of the lift coefficient (peak). Immediately afterward, a downstroke phase is characterized by the unsteady behavior of the flow. This trend qualitatively agrees with dynamic stall lift coefficient behavior. To better assess the simulation convergence, the lift coefficient and drag coefficients for nine pitching cycles are shown in Figure 7.4 and it shows that a very negligible difference is observed and the standard deviation between two successive pitching cycles was evaluated.

The outcome of this evaluation highlighted a little difference between the lift and drag coefficients between the successive pitching cycles. The difference between the force coefficients of the second cycle versus those of the rest of the cycles was negligible, approximately 0.01%. In addition, a maximum y^+ factor of 0.96 was found along the airfoil surface on the second pitching cycle, thus securing a correct first layer's height.

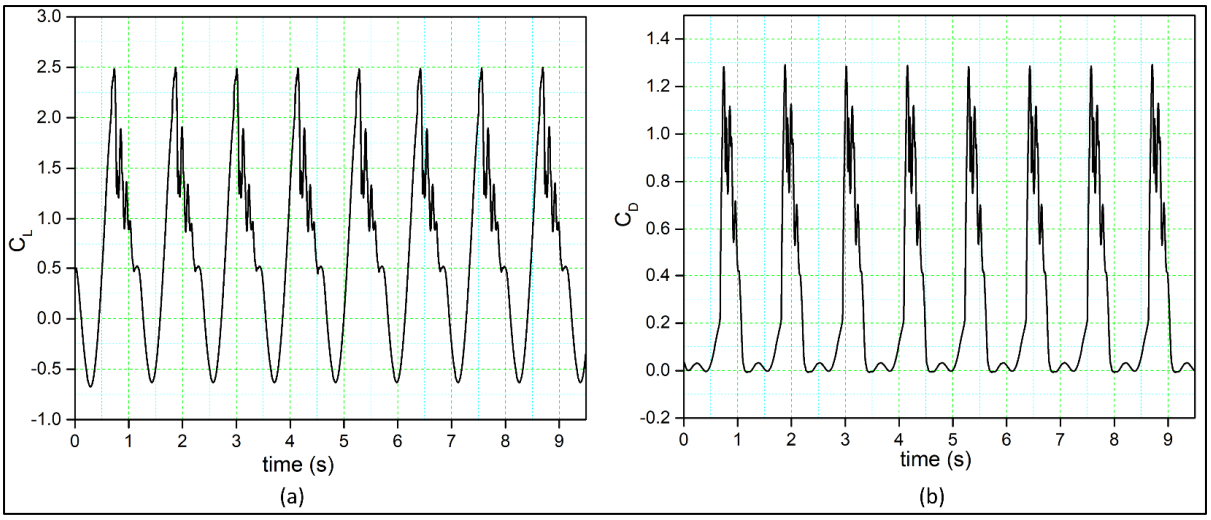

Figure 7.4 Time history of the; (a) lift coefficient and (b) drag coefficient

Table 7.1 presents the properties of three different grid sizes used for grid independency investigations. Figure 7.5 shows the lift coefficient variations with the angle of attack for these three grid sizes. There is a good correlation between these results. The lift coefficients obtained for grid size 1 and grid size 2 are slightly different in the downstroke phase, while their stall values (the peak of the lift curve) have a slight variation from each other. Additionally, the fluctuations in the lift coefficient for all three grid sizes are similar in shape and magnitude. Only very small lift coefficient discrepancies are visible between grid size 3 and the other two grid sizes during the upstroke, while a small difference can be seen between the lift coefficients in the downstroke. The flow reattachment location for all three grid sizes is the same. Therefore, grid size 2 was selected as the computational domain due to its acceptable (medium-sized) cell number and overall good results.

Table 7.1 Grid properties of the three grid sizes for the grid-sensitivity analysis

Grid Size	Number of cells	Min length	Max length	Bias factor
1	62 626	0.001	0.06	1.12
2	103 212	0.001	0.035	1.08
3	206 038	0.001	0.02	1.05

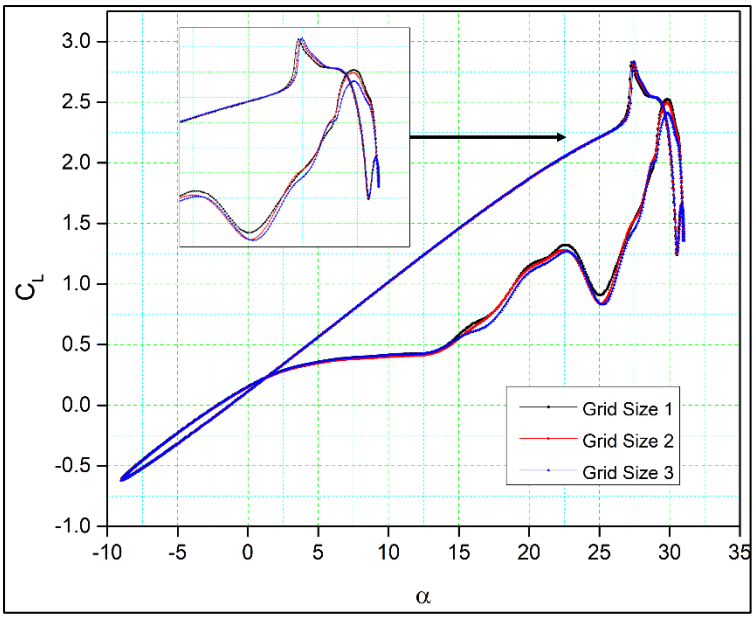

Figure 7.5 Comparisons of the numerical results for the lift coefficient versus the angle of attack for three different grid sizes

Figure 7.6 compares the NACA 0012 airfoil model's computed lift and drag coefficients to their experimental values (MCALLISTER et al., 1978) and numerical results from previous literature (Correa, 2015) for the Reynolds number 2.5 x10^6, the reduced frequency k = 0.10, and angles of attack of 5^0 to 25^0, with a mean incidence of 15^0 were validated while the second simulation used the numerical data from (Correa, 2015) for the same settings.

The $\gamma - Re_\theta$ turbulence model can forecast the results' trend. The lift coefficient corresponds to its experimental value in the upstroke phase, but it predicts the stall differently than its experimental value. As the unsteady analysis is often dissipative, it reduces the flow intensity and thus the kinetic energy. The numerical result is good, as it captures the load variation trend before the stall region. The range of differences in the peaks of the lift coefficient is small. The downstroke variations are due to the extensive post-stall process, and they result in a discrepancy in the initial LEV prediction.

Figure 7.6 (b) illustrates the drag coefficient variation with the angle of attack, revealing the notable difference when α > 12, as the deep stall causes the drag to increase. In numerical simulations (Correa, 2015), the drag coefficient with the angle of attack is lower than the drag

coefficient obtained in other simulations. However, our numerical results of an airfoil's maximum drag coefficient are lower than the experimental results due to large vortices on the airfoil surface and to the flow's three-dimensionality. These vortices occur because of the persistent flow separations at high angles of attack, which makes it difficult to effectively describe the viscous effects near the airfoil surface. The CFD simulations in our study also indicate a secondary LEV that contributes to the recovery of the lift and drag coefficients around the maximum angle of attack.

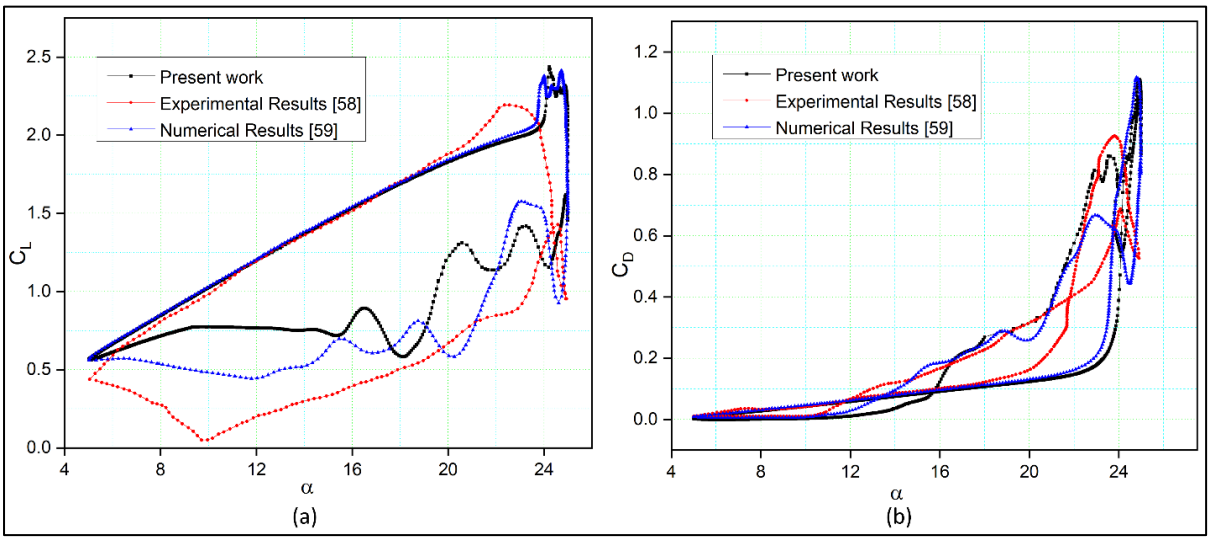

Figure 7.6 Comparison of our numerical results with experimental results obtained from wind tunnel tests (MCALLISTER et al., 1978) and numerical results (Correa, 2015): (a) lift coefficient; (b) drag coefficient variations with the angle of attack.

7.3 Discussion of Results

This study examines the unsteady aerodynamic characteristics obtained by the same oscillating baseline airfoil equipped with a variable morphing leading edge. Since an oscillating function controls the temporal deformation of the leading edge, a frequency parameter must be considered. The pitching-oscillation motion is invariably controlled by equation (1) where $\alpha_{mean} = 11°$, $\alpha_{amp} = 20°$ and a reduced frequency of $k = 0.08$. The operating Reynolds number used was 2.4×10^6 with a freestream velocity of $U_\infty = 35.5$ m/s and a turbulence intensity of Tu = 0.1%.

Two broader studies are considered i) The Dynamically Morphing Leading-Edge (DMLE) of an oscillating airfoil is investigated first. In this study, the pitching-oscillation motion of an airfoil is defined, and the parameters such as the droop nose amplitude (A_D), and the morphing starting time (M_{ST}) in terms of pitching angle are carefully chosen. The effects of the variation of A_D and of M_{ST} on the aerodynamic performance of the airfoil are studied, and three different amplitude cases considered are A_D = 0.01, 0.005, and 0.0075. Furthermore, the combinations of A_D and M_{ST} are evaluated with the aim to find optimal results; ii) The Dynamically Morphing Leading-Edge (DMLE) of an airfoil settled at stall angles of attack is investigated. In this case, the airfoil does not oscillate, but only the DMLE motion is studied at stall angles of attack. This analysis is performed to provide further insights into the transient lift and drag forces for the deflection frequencies of 1 Hz, 2 Hz, 5 Hz, and 10 Hz.

7.3.1 Results for Dynamically Morphing Leading-Edge of an Oscillating airfoil

The parameter A_D determines the deformation extent along the airfoil chord. The different airfoil deformations for different values of A_D are shown in Figure 7.7. These deformations indicate that the values of A_D vary with the angle of attack.

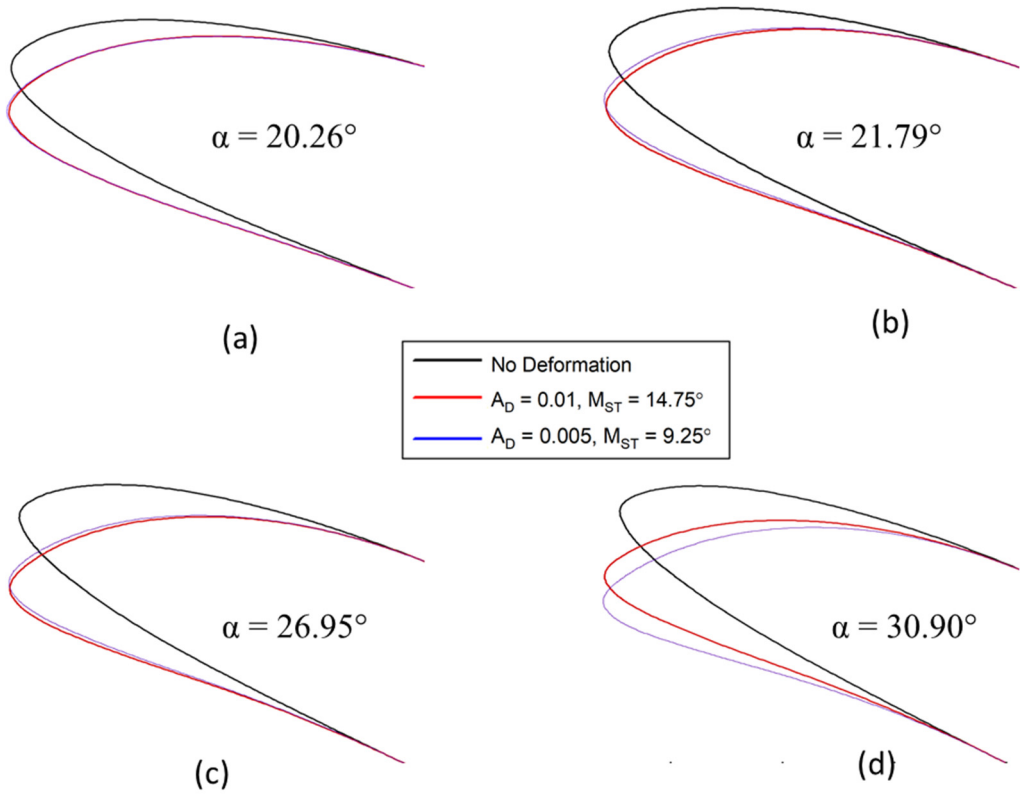

Figure 7.7 The reference airfoil in comparison to DMLE airfoils

Figure 7.8 compares the aerodynamic coefficients of the dynamically morphing leading-edge airfoils to those of a reference airfoil with respect to the angle of attack over one complete hysteresis cycle. Figure 7.8(a) shows that only the case with M_{ST} = 14.75° has successfully increased $C_{L,max}$ with respect to the reference airfoil. It is also clear that in this case, while the morphing leading edge has increased $C_{L,max}$, it also has delayed stall angle of attack. The main objective of this study is to delay or increase the stall angle since its delay helps to maintain favorable lift coefficient values even in the downstroke phase of the cycle. However, this result indicates that a strong vortex has been formed in the leading edge of the airfoil, which later results in the dynamic stall. Instead, for M_{ST} = 24.50°, both upstroke and downstroke motions exhibit a similar trend to the baseline oscillating airfoil. This behavior clearly shows the importance of choosing an adequate M_{ST} for the airfoil morphing deformation. In fact, by assuming an M_{ST} very close to the end of the upstroke would not allow the leading edge to deform sufficiently, thereby no major flow variation over an airfoil is observed.

For the M_{ST} = 14.75°, the lift coefficient increases almost linearly until 28°, after which an increase in the C_L is observed. As shown in the lift coefficient curves in Figure 7.8(a), the flow reattachment occurs early in the case of the reference (no deformation) airfoil, and for the airfoil with M_{ST} = 24.50°. In fact, at the angle of 28°, these two airfoils exhibit very low lift coefficient values due to the already separated leading edge vortex. Beneficial behavior, in terms of $C_{L,max}$ increase and a delay of α_{stall} delay is obtained if the deformation starts early by allowing the LEV to keep increasing on the suction side of the airfoil.

Similarly, the drag coefficients are lower for both DMLE airfoils at an angle of attack (AoA) smaller than 30°, and the $C_{D,max}$ increases substantially at the peak angle with respect to the reference airfoil only at M_{ST} = 14.75°, as seen in Figure 7.8(b). Therefore, the drag coefficient of the DMLE airfoil remains low for a large range of angles of attack. After its comparison with the reference airfoil that has no deformation, the airfoil at M_{ST} = 24.50° show similar behaviour. However, at M_{ST} = 14.75°, the DMLE is not very efficient in reducing the drag values at stall angles of attack.

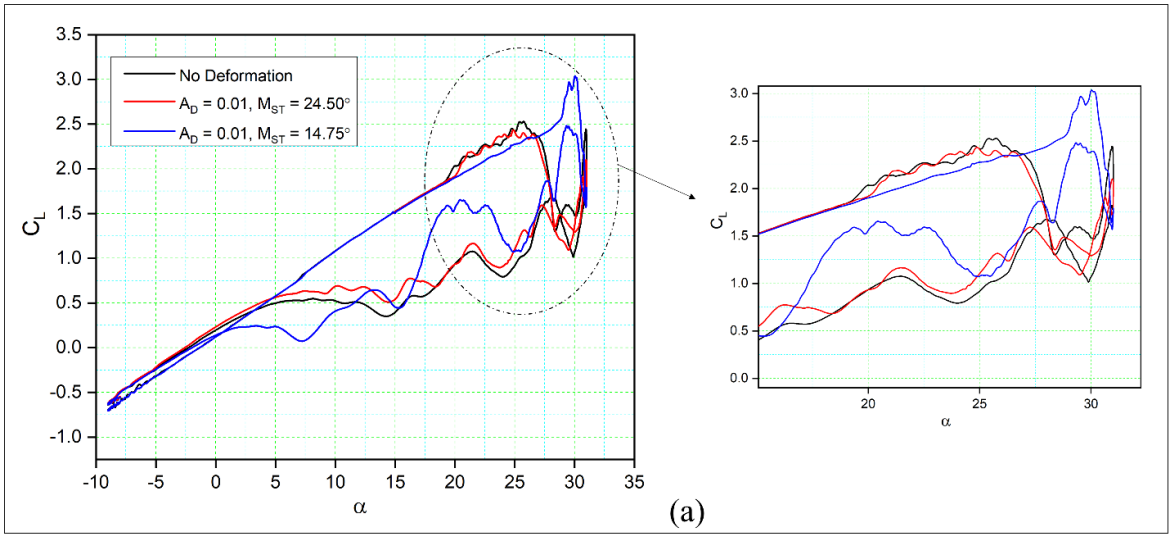

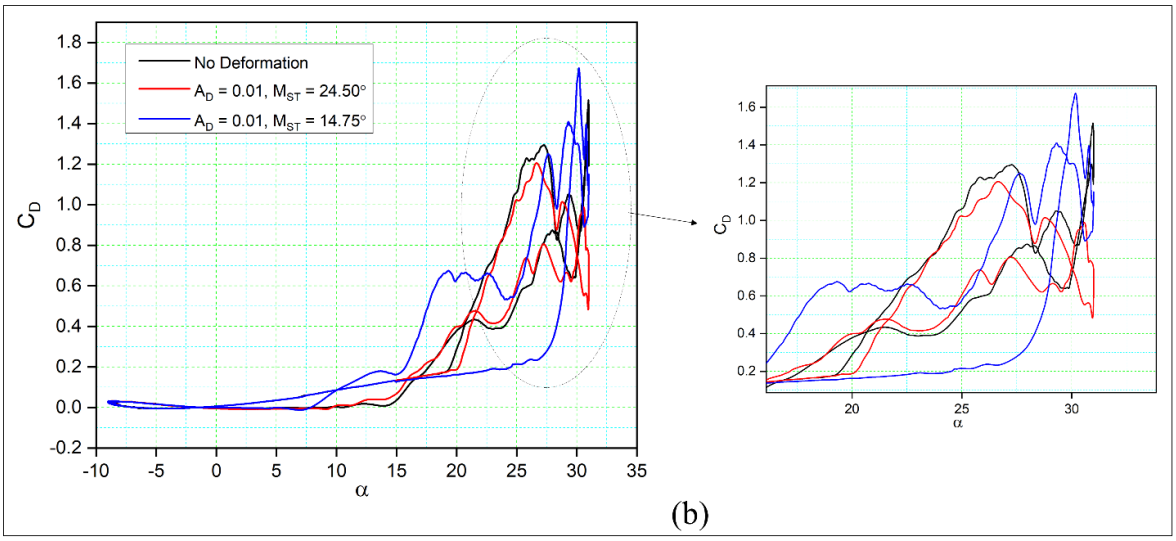

Figure 7.8. Hysteresis cycles for (a) the lift coefficient of DMLE airfoils and (b) the drag coefficient of DMLE airfoils in comparison to the reference (no deformation) airfoil

At an AoA = 21.79°, the reference airfoil develops a strong LEV, seen as a "bump" in the surface pressure distribution in Figure 7.9(a). When the angle of attack reaches an AoA = 26.95°, the LEV has increased in size and spread over a large part of the airfoil upper surface. There is a rapid reduction in the leading-edge suction peak due to the separation of the vortex. This shedding is accompanied by a large, abrupt decrease in the lift coefficient, as indicated in Figure 7.9(a).

For an airfoil with A_D = 0.01 and M_{ST} = 14.75°, no strong LEV is visible. In Figure 7.8 (a), at an upstroke an AoA = 20.3°, the flow evolves slowly and remains attached to the airfoil with a small LSB starting to form. At an AoA = 25.5°, the LEV develops along the leading edge and continues to grow slowly. The increase of the angle of attack to an AoA = 27.3° increases the LEV size.

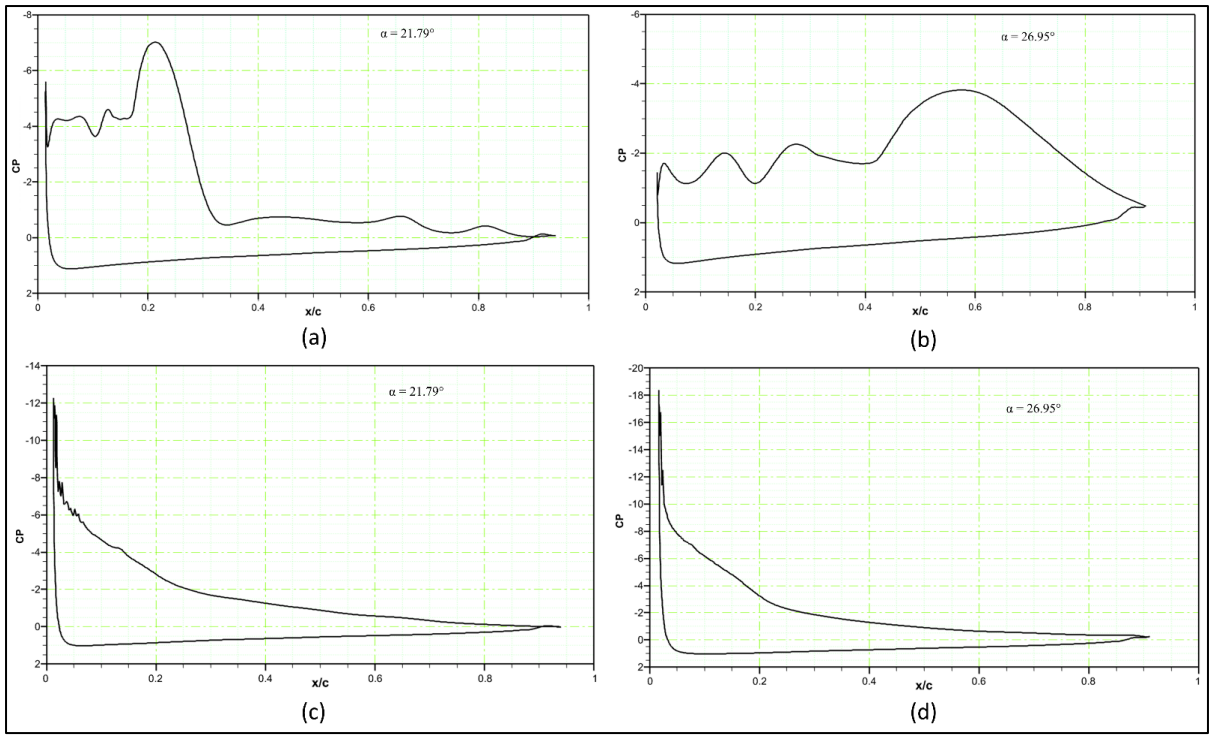

Figure 7.8 Pressure coefficients of the (a) reference airfoil at an AoA = 21.79°, (b) reference airfoil at an AoA = 26.95°, (c)the DMLE airfoil at an AoA = 21.79°, and (d) the DMLE airfoil at an AoA = 26.95°

Figure 7.10 compares the aerodynamic coefficients of two different M_{ST} cases of DMLE airfoils to those of a reference airfoil with respect to the angle of attack over one complete cycle. Low value of A_D (A_D = 0.005) and M_{ST} were chosen for these cases. Figure 7.10(a) shows that the DMLE airfoils both increased their $C_{L,max}$ values by 22.48% from 2.49 to 3.04 (case M_{ST} = 9.25°), and from 2.49 to 2.62 (case M_{ST} = 1.86°) with 5.22 %. It is also clear that the DMLE increased the $C_{L,max}$ with the increase in the stall angle of attack, that was one of the significant goals of this study, because of the fact that the stall angle of attack delay helps to maintain the airfoil lift coefficient value, even in the downstroke cycle. However, this result indicates that there is a strong flow separation once the downstroke starts.

As seen from Figure 7.10(a) where A_D = 0.005, compared to the previous cases where A_D = 0.01, the lift coefficient of the new DMLE airfoils increases slightly for high angles of attack. In both these cases, the lift coefficients are higher as the angle of attack increases, and therefore stall is delayed. As seen from the lift coefficients variation curves, the flow reattachment occurs

earlier for the reference airfoil and the DNLE airfoil with M_{ST} = 1.86°, which is the opposite behavior than that observed in the previous analysis for A_D = 0.01. In this case (M_{ST} = 1.86°), initiating the deformation early in the upstroke phase influences the flow field and thus results in a premature LEV separation.

Similarly, the drag coefficients are low for the DMLE with the M_{ST} = 1.86° for angles of attack smaller than 30° than the drag coefficients of the reference airfoil. However, the $C_{D,max}$ for the other case (M_{ST} = 9.25°) increases substantially for the same angles of attack with respect to the $C_{D,max}$ of the reference airfoil, as seen in Figure 7.10(b). The sudden $C_{D,max}$ increase of this latter case can be attributed to the corresponding increase in lift, developed as a consequence of the ongoing LEV. On the other hand, when compared with the reference airfoil, the M_{ST} = 1.86° case shows a smaller C_D trend. In this case, the DMLE is able to drastically reduce the drag over the entire pitching cycle.

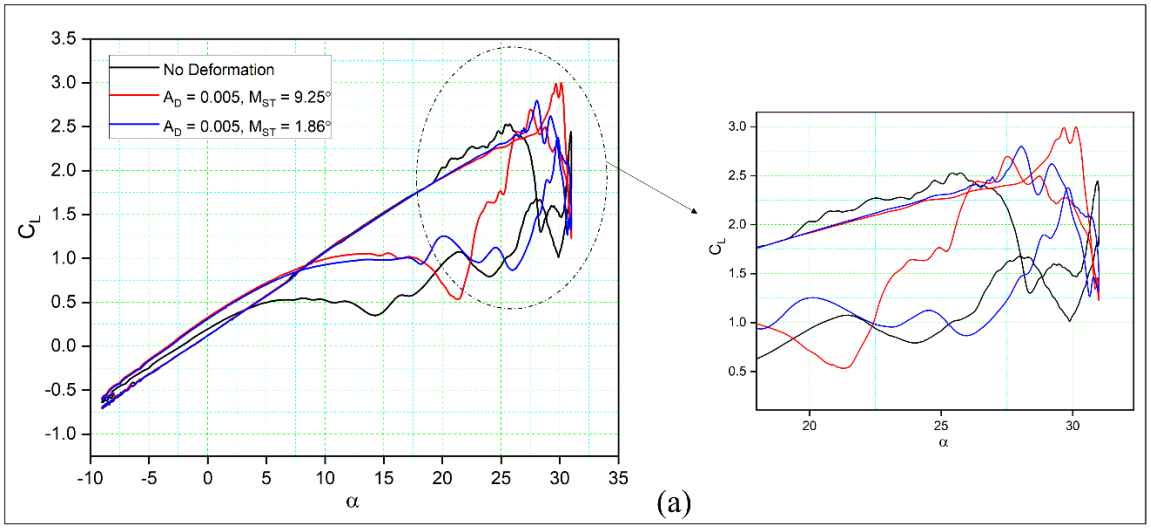

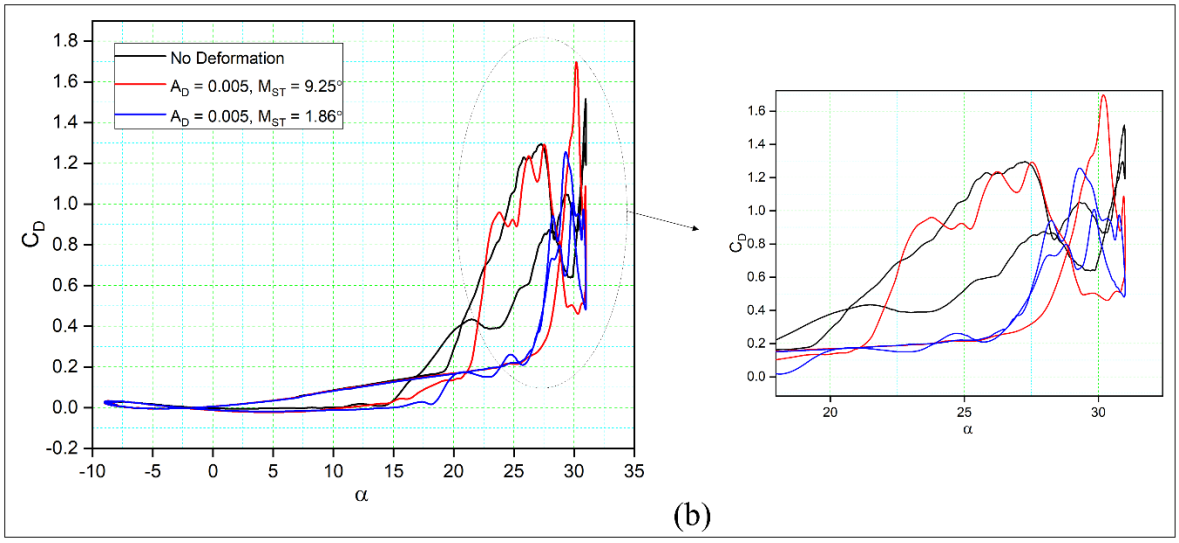

Figure 7.9 Hysteresis cycles for (a) Lift coefficient of DMLE airfoils (b) drag coefficient of DMLE airfoils in comparison to the reference airfoil

Similarly, it can be seen from Figure 7.11(a) that the maximum lift coefficient ($C_{L,max}$) of the DMLE airfoils increases slightly for high angles of attack. In addition, the flow reattachment for DMLE airfoils occurs earlier as the transition point moves from the trailing towards the leading edge. It thus appears that the DMLE airfoil performance increases during the downstroke. At an angle of attack of 10 degrees, the flow field attaches to both airfoils. The values of drag coefficients of DMLE airfoils at high angles of attack are lower than those of the reference airfoil, as shown in Figure 7.11(b).

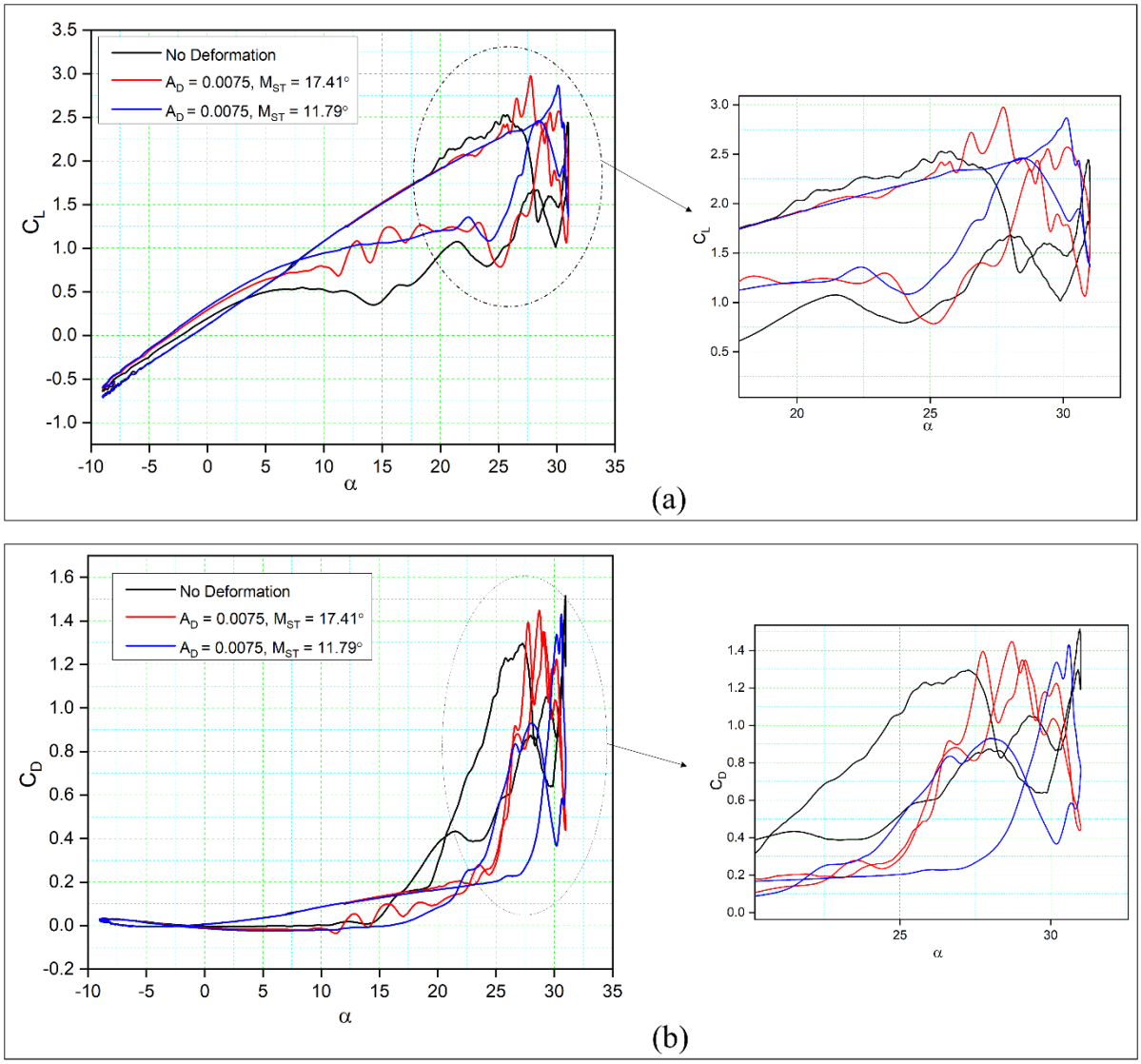

Figure 7.10 Hysteresis cycles for (a) the lift coefficients of DMLE airfoils and (b) the drag coefficients of DMLE airfoils in comparison to those of the reference (unmorphed) airfoil

Figure 7.12 (a) compares the aerodynamic coefficients for three different amplitudes (A_D) to those of a reference airfoil. It is clear that the different amplitudes result in higher C_L values for all the DMLE airfoils during the upstroke. At lower values of A_D (A_D = 0.01) and M_{ST} = 14.75°, the $C_{L,max}$ reaches 3.04, while the reference airfoil's $C_{L,max}$ is 2.53, showing a 20.15 % increase in $C_{L,max}$. However, the flow reattachment for this case of the DMLE airfoil is delayed compared to that of the reference airfoil during the downstroke. During the pitching

oscillation of the reference airfoil, the flow separation and stall occur at an angle of attack of 25°. However, with the droop deformation of the leading edge, the stall occurs at an angle of attack of 30°, thereby delaying the stall by 5°.

In the case when A_D = 0.005, slightly higher lift coefficients are found, as $C_{L,max}$ increased from 2.53 to 2.8, with a 10.67 % increase in comparison to the reference airfoil (Fig. 7.12(a)). As the value of A_D varies with the morphing time (M_{ST}), the main part of the droop deformation is closer to the leading-edge point. In case of A_D = 0.05, the stall angle is delayed 12% in comparison to the reference airfoil. In addition, the flow reattachment occurs earlier in this DMLE case.

With A_D = 0.0075, the lift coefficient of the DMLE airfoil increased by 11.46 % as compared to the reference airfoil, and the flow was also reattached earlier for the DMLE airfoil as compared to that of the reference airfoil. This DMLE airfoil also results in reduced drag coefficients as compared to the reference airfoil during both the upstroke and the downstroke cycles.

Similarly, Figure 7.12(b) shows the drag coefficients variations with the angle of attack of three DMLE airfoil cases (A_D = 0.01, 0.005 and 0.0075) in comparison to those of the reference airfoil. It is seen that the $C_{D,max}$ value is higher for the DMLE airfoil than the $C_{D,max}$ of the reference airfoil. In the downstroke, the C_D values are lower than those of the reference airfoil. This fact indicates that by controlling the DMLE airfoil deflection and the morphing starting time, the maximum aerodynamic coefficients can be improved accordingly. The LEVs are formed much earlier in the reference airfoil than in the DMLE airfoil, thus suggesting that the stall angle of attack delay helps to increase the airfoil lift coefficient, even in the downstroke cycle.

Therefore, it can be concluded that among the three droop amplitudes (A_D), A_D = 0.005 provides the best performance considering the overall aerodynamic efficiency. It is worth noting that the variation of the M_{ST} significantly affects the aerodynamic coefficient values. According to the definition of droop deformation, the droop rate varies with the time steps and therefore, the leading-edge shape also changes accordingly. This conclusion also reveals that

the M_{ST} should be studied along with A_D to further investigate and improve the overall DMLE performance gains.

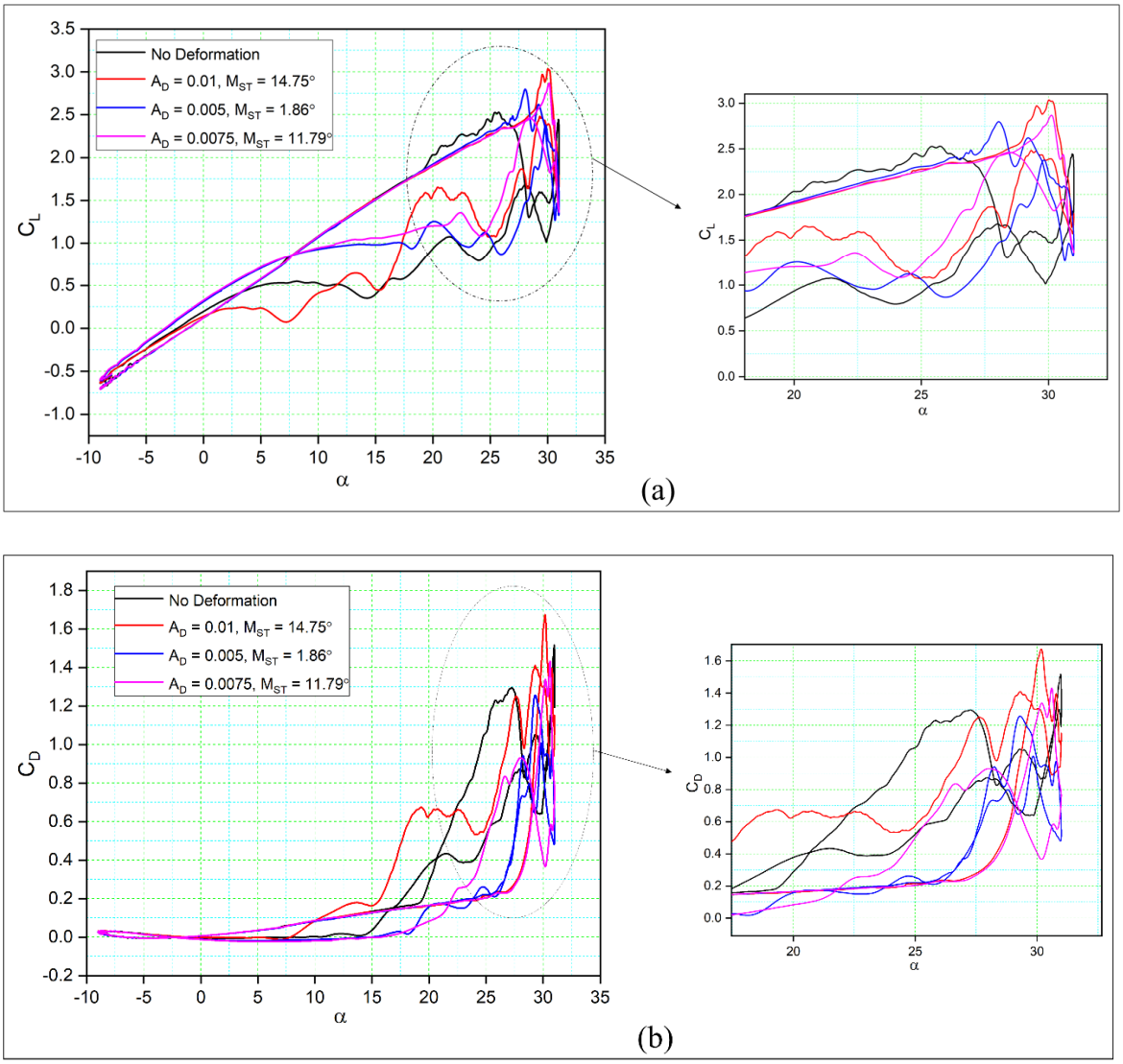

Figure 7.11 Hysteresis cycles for (a) the lift coefficients of DMLE airfoils and (b) the drag coefficients of DMLE airfoils compared to the reference airfoil

The reference airfoil's flow streamlines and velocity contours, and those of airfoils with A_D values of 0.01 and 0.005, are all shown in Figures 7.13(a), (b), and (c), respectively. Figure 7.13(a) shows the flow development for the reference airfoil at various upstroke angles of

attack. At 20.26°, the tiny LEV of the reference airfoil is seen. The vortex size increases as the angle of attack increases to 21.79°. Along with the primary LEV, secondary and tertiary LEVs are also formed. A Dynamic Stall Vortex (DSV) occurs as the angle of attack increases between 26.95° and 30.90°; thereby the flow increases through the boundary layer as secondary and tertiary vortices occur.

In the case of DMLE airfoils, as seen in Figure 7.13 (b), the flow separation phenomenon is not seen at low angles of attack, such as 20.26° and 21.79°, as the flow remains attached to the airfoil. At an angle of attack of 26.95°, the leading-edge suction increases, the LEV moves towards the trailing edge and the TEV has formed accordingly. Then the flow fully separates at an angle of attack of 30.90°. Figure 7.13 (c) shows the flow phenomena for the DMLE airfoil with $A_D = 0.005$ at different angles of attack. It shows similar behaviour as observed in the case with $A_D = 0.01$.

Therefore, it can be concluded that the DMLE airfoil cases with different deflection amplitudes improve aerodynamic efficiency ($C_{L,max}, C_{D,max}$) and delay the dynamic stall angle. The flow remained largely attached to the DMLE airfoils and the separation phenomena associated with a dynamic stall were reduced.

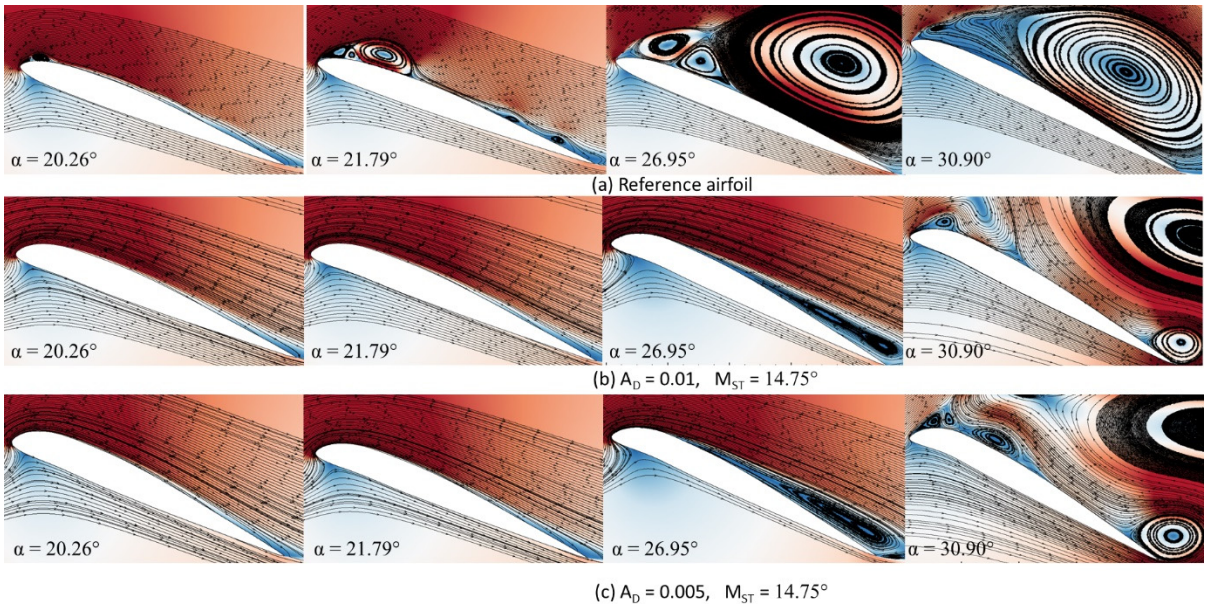

Figure 7.12 Velocity contours with flow streamlines for the (a) reference airfoil, (b) DMLE airfoil with $A_D = 0.01$ and (c) DMLE airfoil with $A_D = 0.005$

7.3.2 Results for Dynamically Morphing Leading Edge (DMLE) of a fixed airfoil

Figures 7.14 to 7.18 show the transient lift and drag coefficient for the DMLE airfoils at 5 different frequencies at an angle of attack of 22° degrees. This angle of attack was chosen because the flow is fully separated, and major vortices are formed at 22°. For all these simulation cases, the DMLE begins drooping at t = 1.5 s. The transient lift coefficient peaks increase as the leading edge keeps morphing dynamically. At low frequencies, such as 0.5 Hz, 1 Hz, and 2 Hz, the lift slope decreases when the DMLE airfoil begins its morphing until it reaches its maximum deflection. When the DMLE airfoil returns to its reference shape, the lift slope starts to increase again. As the DNLE deflects upwards, flow separation region increases. Lift coefficient peaks for 1 Hz and 2 Hz frequencies are mostly higher than 1 and their peak values are between 2.5 and 2.8. For 0.5 Hz, the lift coefficient values are below 1. Similarly, more lift coefficient peaks above the value of 2 are found at 2 Hz than at 1 Hz. As the frequencies increase to 5 and 10 Hz, the DMLE deflection results in a higher number of lift coefficients peaks above 1.5. The higher frequencies conduct to more transient flow than the lower frequencies, and therefore to large flow vortices on the airfoil.

In this study, the upward and downward deflection motions of the DMLE airfoil have shown that the downward deflection of the leading edge increased the stall angle of attack and the nose-down pitching moment. Furthermore, the larger the downward deflection angle, the better the lift-to-drag ratio of the DMLE airfoil will be at a small angle of attack. For the upward deflection, these results were reversed.

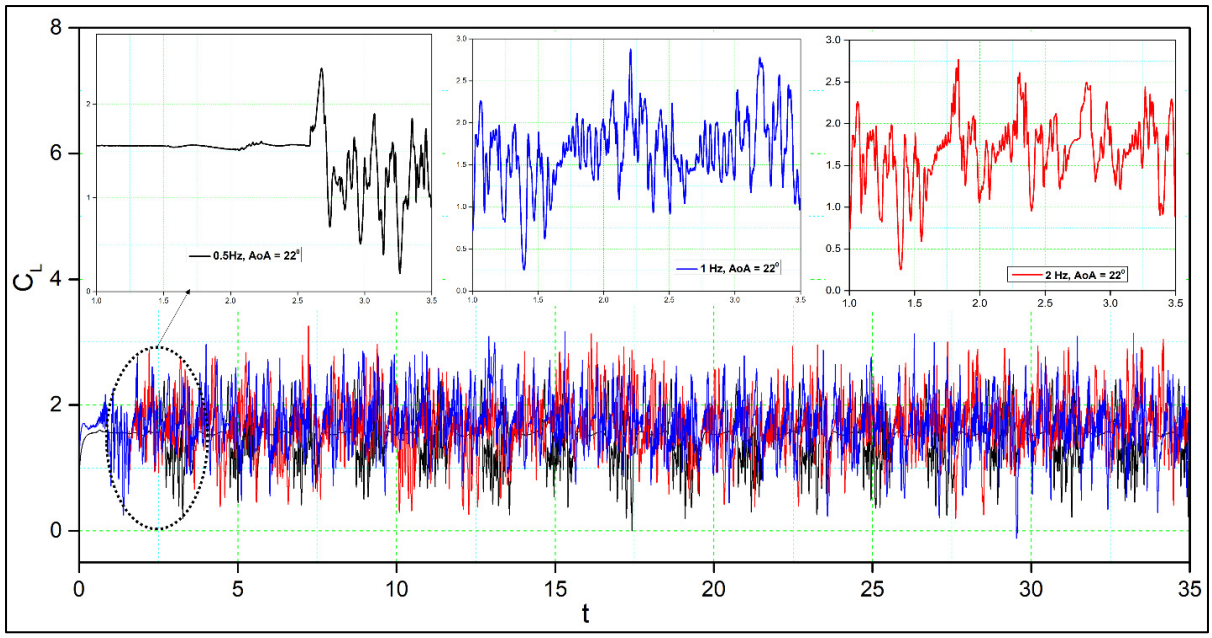

Figure 7.13 Transient lift coefficient responses to DMLE airfoil at 0.5 Hz, 1 Hz and 2 Hz

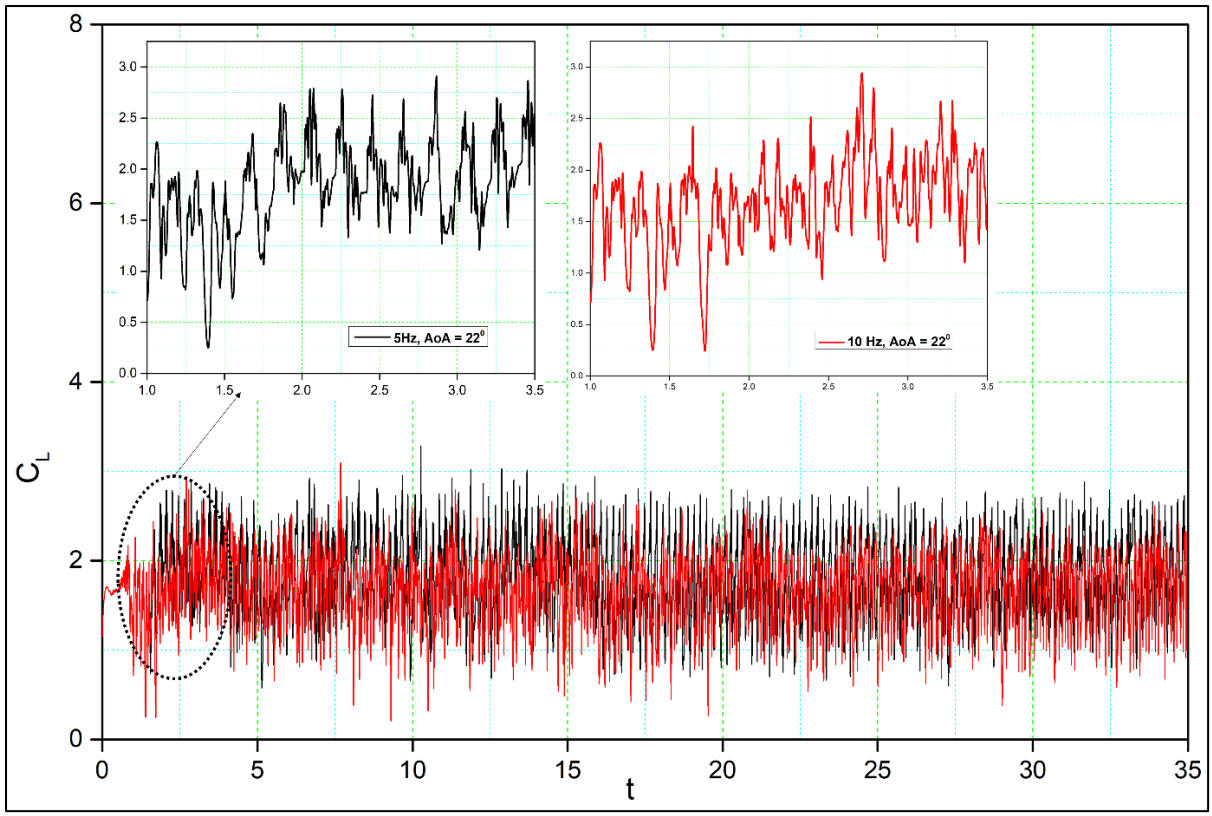

Figure 7.14 Transient lift coefficient responses to DMLE airfoil at 5 Hz and 10 Hz

The formation of unstable flow over an airfoil is greatly influenced by the development and shedding of vortices, which also have an impact on its aerodynamic characteristics. Analysis of the shedding vortices flow field properties variation in time-domain, however, is challenging. The discrete Fast Fourier Transform (FFT) algorithm is used to convert the aerodynamic coefficient from the time domain to the frequency domain. Based on the transient lift coefficient for the DMLE airfoil, the amplitude spectrum was estimated using the FFT algorithm; its frequency peak was caused by vortex shedding on the airfoil. Figures 7.16 shows that the frequency spectrum for a high angle of attack of 18° exhibits a denser and greater-amplitude frequency spectrum for different deflection frequencies. It is well known that the frequency de-creases with increasing angle of attack, thus indicating that the shedding period of vortices is increased.

For the DMLE airfoil, the oscillation curve is not periodic, and the lift coefficient curves are disordered, as seen in Fig. 7.14 and 7.15. The lift coefficient spectrum contains multiple deflection frequencies with different amplitudes, which demonstrates that the angle of attack shedding vortex has an aperiodic structure and that there are numerous vortices with various frequencies and comparable strengths. Similarly, intensity of vortices uses too much flow field energy in the disturbance that does not contribute too much to the lift coefficient, thus preventing it from increasing further.

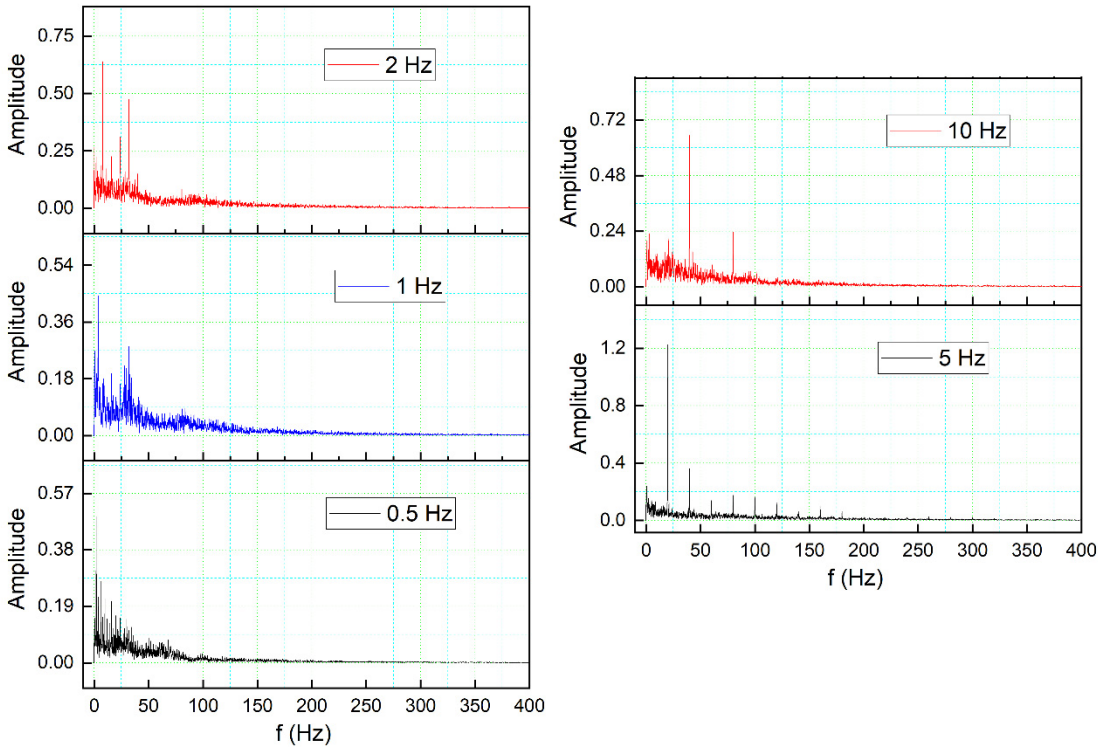

Figure 7.16. Lift coefficient transient responses for DMLE airfoil at 5 Hz and at 10 Hz

The transient drag response in Figures 7.17 and 7.18 shows nearly the same trend as the transient lift coefficient (Fig. 7.14 and 7.15). Initially, an overshoot is observed in the drag coefficient as the leading edge starts to morph at t = 1.5 s, and the amplitude of the drag is also proportional to the deflection frequency: high deflection frequencies cause large changes in the drag values. The reason for these large overshoots may be due to the sudden pressure changes over the leading edge of the airfoil. The downward deflection of the DMLE results in better aerodynamic efficiency.

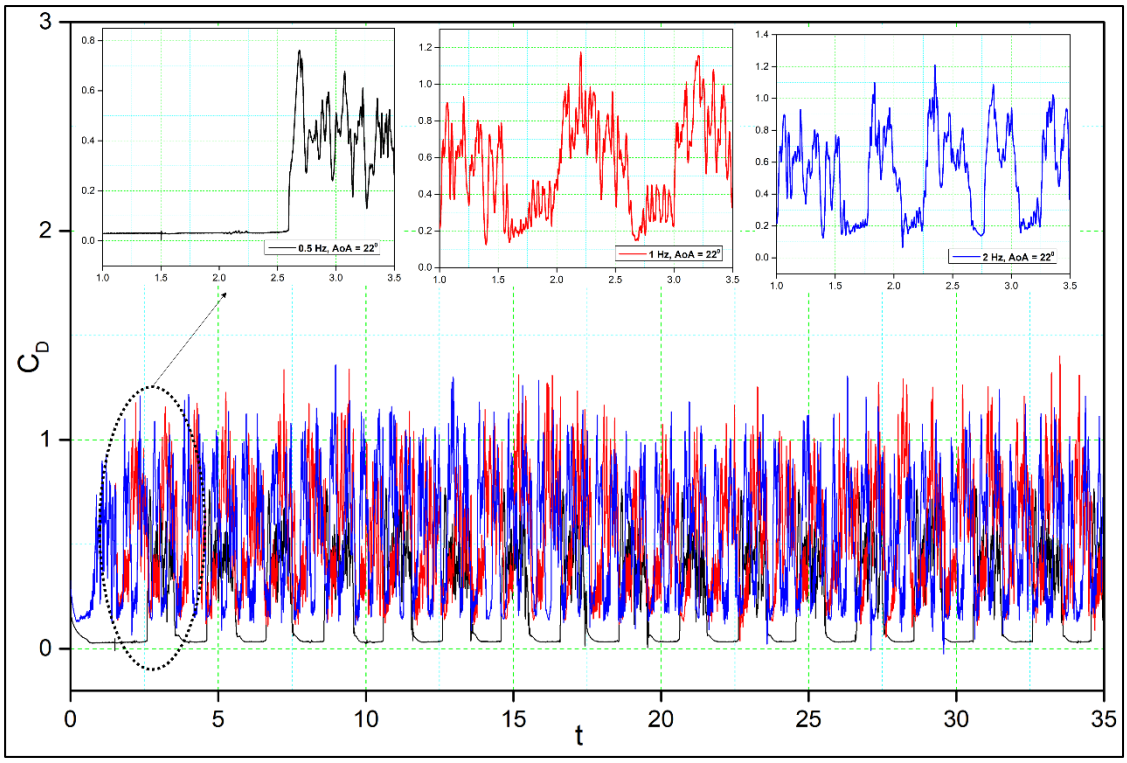

Figure 7.17 Transient drag coefficient responses to DMLE airfoil at 0.5 Hz, 1 Hz and 2 Hz

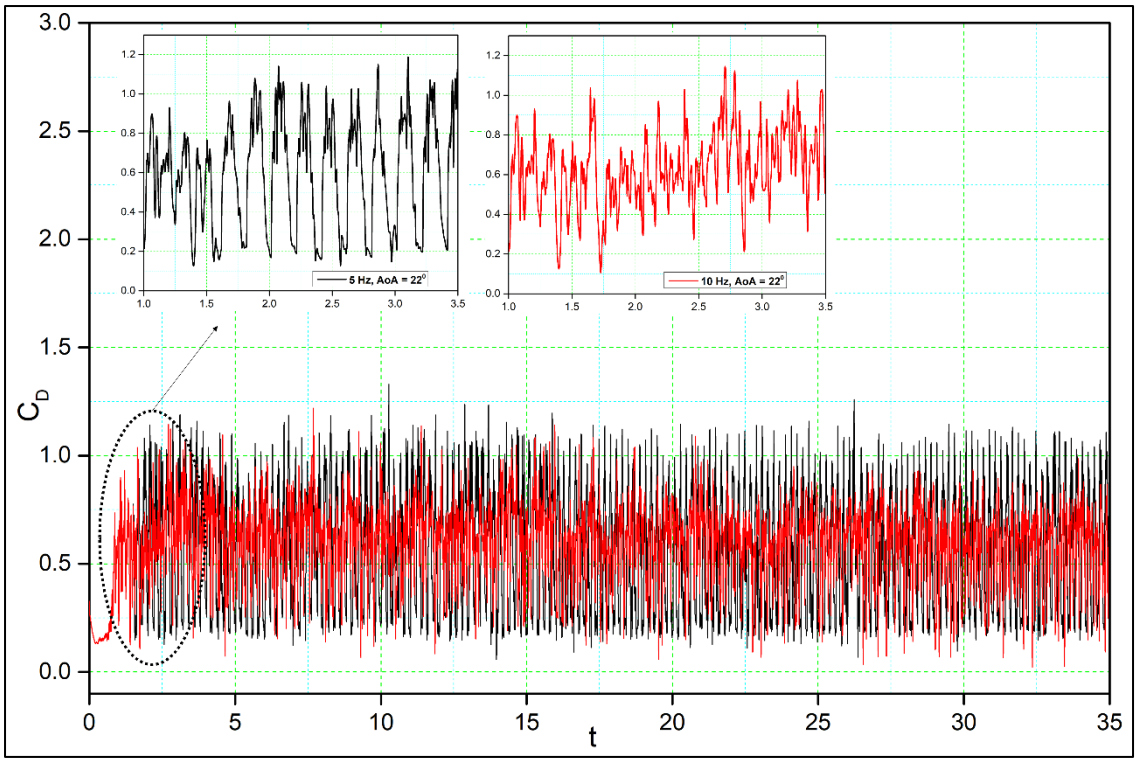

Figure 7.18 Transient drag coefficient responses to DMLE airfoil at 5 Hz and 10 Hz

The pressure coefficients of the DMLE airfoil at different frequencies are shown in Figures 7.19, 7.20, and 7.21. Figure 7.19 shows that at an angle of attack of 22° for the deflection frequency of 2 Hz and at the time, t = 1.41 s, the airfoil is already in a pre-stall condition, and has large LEVs over the airfoil; however, the flow remains attached to the DMLE airfoil. The flow is characterized by the presence of a large vortex near the trailing edge of an airfoil. The leading-edge morphing starts at t = 1.5 seconds and continues to deflect downwards until it reaches the maximum deflection at t = 1.71 s. It can be seen that at t = 1.625 s and t = 1.71 s, the flow remains largely attached to the airfoil, and does not have any significant LEVs over the surface. The leading edge starts to move upwards back to its original position while the pressure drops significantly, and a large trailing edge vortex separation can be seen at t = 2 s. The flow becomes stable again at t = 2.12 s and separates at t = 2.27 s. This process reveals that the downward deflection of the leading edge increases the flow stability and increases the stall angle of attack by delaying the formation of a Dynamic Stall Vortex (DSV).

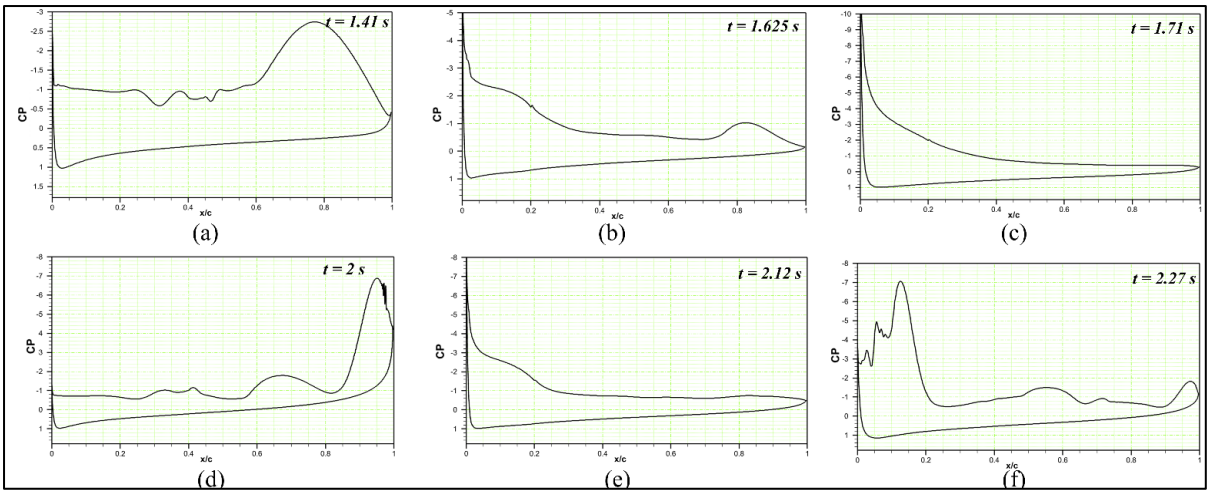

Figure 7.19 Pressure coefficient comparison of the reference airfoil with the DMLE airfoil at 22° AoA and time-steps for the morphing frequency of 2 Hz

At the deflection frequency of 5 Hz, the DMLE droops at a faster rate compared to its behavior at low frequencies such as 0.01 Hz and 0.005 Hz. Figure 7.20 (a) shows the chordwise pressure distribution at t = 1.41 s; LEVs can be observed over the airfoil. At t = 1.55 s, the leading-edge droops to the maximum value, and a large TEV can be seen over the airfoil (Fig 7.20(b)). When the leading edge starts to return to its original position, the flow stabilizes and reattaches with the airfoil, as seen at t = 1.6 s (Fig 7.20(c)). The flow takes more time to reattach to the airfoil at high frequencies as compared to the low-frequency deflections. The leading edge continues to deflect upwards, and the large LEV and flow separation can be seen at t = 1.645 s (Fig 7.20(d)). Similar type outcomes are obtained for the deflection frequency of 10 Hz, as shown in Figure 7.21 (a)-(d).

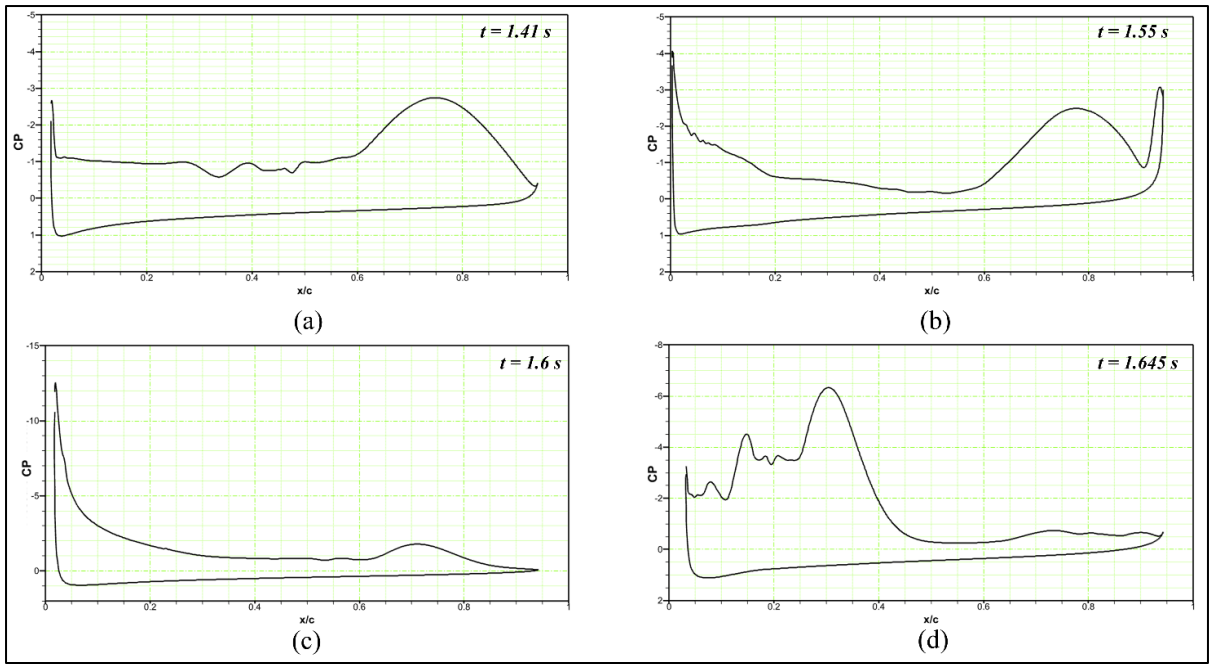

Figure 7.20 Pressure coefficient comparison of the reference airfoil with the DMLE airfoil at 22° AoA and time-steps for the morphing frequency of 5 Hz

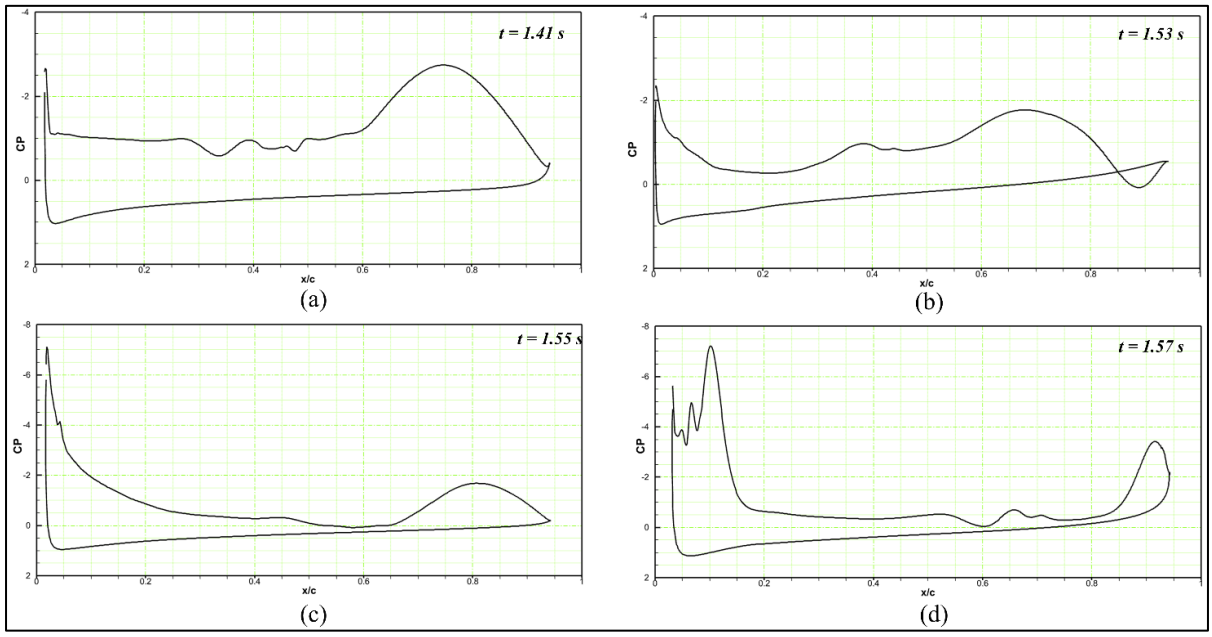

Figure 7.21 Pressure coefficient comparison of the reference airfoil with the DMLE airfoil at 22° AoA and time-steps for the morphing frequency of 10 Hz

To depict the vortices for the DMLE at the deflection frequency of 1 Hz and an angle of attack of 22° at different time steps, Figure 7.22 (a) shows that before the starting of morphing at t = 1.41 s, a series of vortices are observed over the airfoil, which may be expressed as their respective pressure distribution in Figure 7.22 (d). As the DMLE morphing starts at t = 1.5 s, the DMLE starts to droop, therefore the leading edge of the airfoil changes. Finally, at t = 1.625 s, the pressure distribution graph reveals that a reverse flow region arises and moves towards the trailing edge, as shown in Figures 7.22 (b) and (e). Keeping track of the vortices' formation, growth, and destruction and analyzing their magnitude is one of the important methods to evaluate the dynamic stall process. However, even with the best visual aids, flow circulation values can occasionally vary noticeably, independently of vortices sizes. Therefore, further data analysis, such as looking at pressure distributions at the wall and in the area around it, must be done.

The droop nose reaches its maximum deflection at t = 1.71 s, as shown in Figure 7.22(c), and it remains attached to the airfoil (Figure 7.22 (f)). Then, the airfoil returns to its original shape by deflecting the DMLE upwards. At t = 2 s, the vortices and a predominant flow-recirculating zone appear in the vicinity of the trailing edge region (Figure 7.23 (a) and (c)). As the airfoil deflects upwards, stronger LEVs are formed, as seen in Figures 7.23 (b) and (e). By observing the Spatio-temporal evolution of both LEVs, at t = 2.27 s (Figure 7.23 (c) and (f)), it is possible to understand how the fast-rolling up the mechanism of the trailing edge shear layer and the LEV keep growing due to the kinetic energy; this energy is supplied by the LEV gradient as a small counter-rotating vortex starts to form between the leading-edge and the LEV. In this full cycle process, it is evident that the flow remains attached to the airfoil when the DMLE is deflected downwards, and therefore, the DSV control can also be done by the droop nose morphing process.

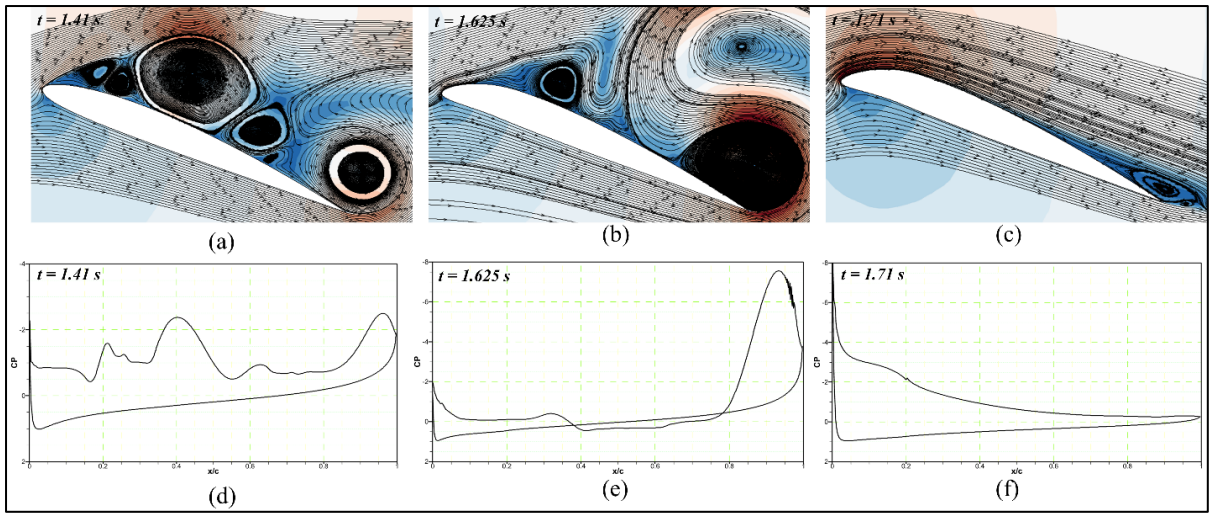

Figure 7.22 Velocity Streamline contours with Pressure coefficient of the reference airfoil with the DMLE airfoil at different time steps for downward deflection

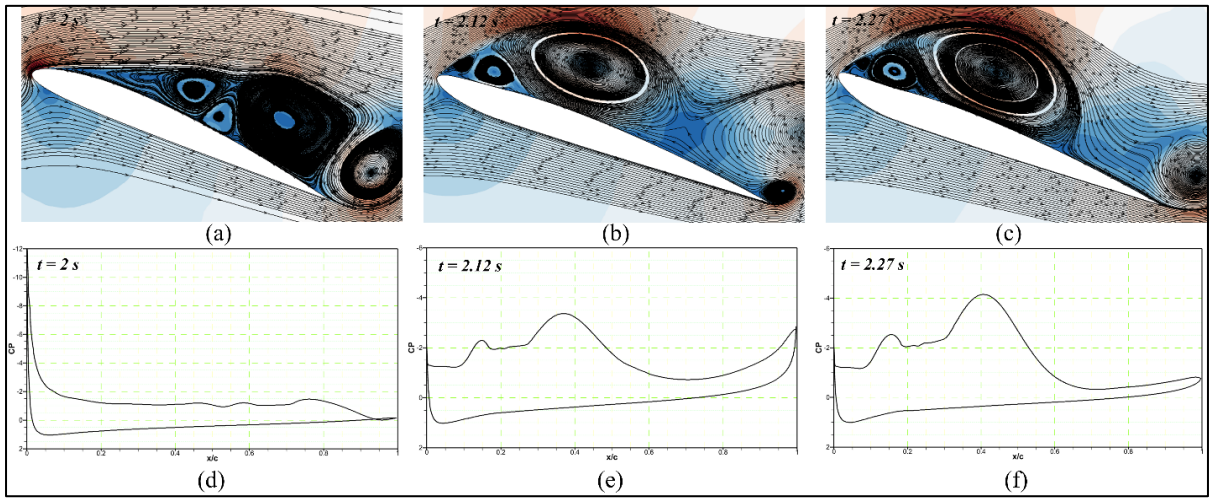

Figure 7.23 Velocity Streamline contours with Pressure coefficient of the reference airfoil with the DMLE airfoil at different time steps for upward deflection

7.4 Conclusion

This paper investigated the effect of the DMLE on the flow structure and behavior of vortices around a pitching UAS-S45 airfoil during the dynamic stall. The study focused on; 1) developing a framework to dynamically morph the leading edge of the S45 airfoil through a camber line deformation, and then 2) analyzing the aerodynamic performance in terms of

controlling the dynamic stall phenomenon. The framework was developed using an unsteady parametrization method from the UAS-S45 airfoil parametric equations, specifically adapted to obtain the morphing motion of the leading edge over time. This scheme was then integrated within the ANSYS Fluent solver by developing a User-Defined-Function (UDF) code to dynamically deflect the airfoil boundaries and control the dynamic mesh used for its deformation and adaption. The dynamic and sliding mesh techniques were used to simulate the unsteady flow across the sinusoidally pitching UAS-S45 airfoil. The $\gamma - Re_\theta$ turbulence model is used due to its ability to capture the flow structures of dynamic airfoils.

Two main studies were considered: i) Firstly, an investigation of the Dynamically Morphing Leading-Edge (DMLE) of an oscillating airfoil. In this study, the pitching-oscillation motion of an airfoil was defined, and its parameters, such as its droop nose amplitude and morphing starting time, were evaluated. The effects of both parameter variations of DMLE on the aerodynamic performance were studied, and three different amplitudes were considered; ii) Secondly, the DMLE of an airfoil at the stall angles of attack was investigated. The DMLE performance was analyzed to provide further insights into the dynamic lift and drag force variations at pre-defined deflection frequencies of 1 Hz, 2 Hz, 5 Hz, and 10 Hz. Some significant conclusions are outlined below:

- The unsteady aerodynamic parametrization method coupled with Laplace Diffusion dynamic mesh techniques gave good results. The mesh quality metrics were very well respected during the entire deformation process; hence, an accurate simulation process was confirmed by the validation of the results and mesh deformation schemes.

- For the DMLE of an oscillating airfoil, when A_D = 0.01 and M_{ST} = 14.75°, the lift coefficient increased by 20.15 %, while a 16.58 % delay in the dynamic stall angle was obtained compared to the reference airfoil. Similarly, the lift coefficients obtained for the two other cases, when A_D = 0.05 and A_D = 0.0075, increased by 10.67 % and 11.46 %, respectively, compared to the reference airfoil.

- The presence of an LEV was depicted in the case of the reference airfoil at the angle of attack of 21.97°, also seen as a “bump” in the surface pressure distribution. By the time the angle of attack reaches 26.95°, the LEV increased and spread over the large part of the airfoil. However, in the case of the DMLE airfoils with A_D = 0.01, 0.005, and 0075, no strong leading-edge vortex was observed for the same angles of attack of the reference airfoil.

- The numerical results have shown that the new radius of curvature of the DMLE airfoil can minimize the streamwise adverse pressure gradient, and further prevent significant flow separation by delaying the Dynamic Stall Vortex (DSV) occurrence. Furthermore, it was shown that the DMLE airfoil delayed the stall angle of attack with respect to the reference airfoil by 16.58 %.

- In the case of the DMLE of an airfoil at a given angle of attack, the lift slope decreases as the leading-edge morphing begins until it reaches the maximum deflection at low deflection frequencies. When the DMLE returns to its original position, the lift slope increases again. The leading edge deflects upwards, resulting in increased flow separation and high lift slopes. The DMLE repeats the cycle, and the same trend is followed by the lift and drag coefficients of the DMLE airfoil.

- The DMLE deflects rapidly at higher frequencies, such as 5 Hz and 10 Hz, resulting in increased lift coefficients. The higher frequencies lead to more transient flow; therefore, the flow remains separated from the airfoil. In this study, the upward and downward deflection motions of DMLE airfoils have shown that the downward deflection of the DMLE increases the stall angle of attack and the nose-down pitching moment. Furthermore, the larger was the downward deflection angle, the higher was the lift-to-drag of the morphing wing.

Regarding future works, the LARCASE's Price-Padoussis subsonic wind tunnel will be used for future wind tunnel studies of the DMLE airfoils. The findings are expected to clarify the

flow physics, and hence validate the findings of the unsteady flow behaviour of the DMLE airfoil.

CONCLUSION

Environmental and operational constraints have significantly influenced the design of modern aircraft and environmental issues, including noise and carbon emissions reduction that are gaining increasing importance in the development and use of commercial aircraft. In addition, fuel efficiency has also become a crucial component in aircraft design because of fuel costs unpredictability. The aviation industry has implemented various solutions to achieve these goals, such as smart material technology, laminar flow technology, and air traffic management technologies.

Morphing wing technology is a bio-inspired technology that enables an aircraft to modify its design configurations at different speeds and altitudes, and to optimize its performance over the entire flight envelope. Therefore, an aerodynamic and structural optimization for the UAS-S45 airfoil using morphing wing technology was performed at the Research Laboratory in Active Controls, Avionics, and AeroServoElasticity (LARCASE). This project presents the implementation and optimization of morphing technology on the Hydra Technologies UAS-S45 wing and optimize it for aerodynamic and structural performance improvements.

This research involves the investigation of the optimization framework, which included the optimization algorithm, airfoil parameterization methods, aerodynamic solver, and the coupling of these different tools. The impact of the metaheuristic selection of aerodynamic optimization results and computing time along with the results of different parameterization techniques in the optimization framework was studied. Furthermore, developing and applying the optimization approach and obtaining the solutions at the conceptual design phase will be a key design component rather than just an add-on later in the development cycle. Aerodynamically efficient wing design was obtained that consisted of a wing with a continuous camber variation with seamless trailing edge and leading-edge wing, that replaced the conventional discrete control surfaces, such as flaps, ailerons, or slats. This design enables smooth flow behavior over the wing, therefore shape morphing wing makes it possible to continuously fly at different flight conditions with optimal aerodynamic efficiency.

The parameterization methods, which are the Bezier-Parsec (BP), Class Shape Transformation (CST), and Makima methods, and the optimization algorithms, such as the Coupled Particle Swarm Optimization (PSO)-Pattern Search (PS), Genetic Algorithm, and Black Window Optimization (BWO) were evaluated. Several objective functions, such as drag minimization, lift-to-drag maximization, and aerodynamic endurance maximation were utilized to optimize the aerodynamic wing shape of the widely known UAS-S45. An aerodynamic solver was coupled with an in-house MATLAB-based optimization framework. The parameterization methods were integrated with the two-dimensional aerodynamic solver, XFoil, well-known for its rapid convergence and robustness, and a high-fidelity solver, the Transition ($\gamma-Re_\theta$) turbulence model was used to validate the optimization results.

Both the Bezier-Parsec (BP) and Class Shape Transformation (CST) techniques offer higher performance for aerodynamic optimization due to their close relationship with the airfoil parameters. The BP and CST parameters directly relate to the airfoil parameters, such as the leading and trailing edges of the camber line and the leading edge and trailing edge points related to the thickness distributions. These methods also have the ability to minimize the nonlinearity of the objective function and its related parameters. Typically, reducing the non-linear interaction of parameters by use of parameters more directly linked to the objective function will allow an optimizer to converge faster.

The optimization results revealed that MLE and MTE wings can be applied on the UAS-S45 to improve its aerodynamic performance at different flight conditions. Two-dimensional optimizations of the UAS-S45 airfoil with MLE and MTE technology were performed for various Mach numbers, Reynolds numbers, and an extensive range of angles of attack. The objectives used in the optimization framework to obtain the optimal wing airfoil shapes were the: 1) drag minimization; 2) lift-to-drag ratio maximization, and 3) aerodynamic endurance maximization. The results effectively met these objective functions using the MLE and MTE wing airfoil configurations. In addition, delaying the transition point at which the flow changed from laminar to turbulent led to a reduction in the airfoil's drag coefficient. Furthermore, both

morphing configurations gave very good results. Overall, morphing can potentially increase the maximum lift coefficient, delay the separation of the boundary layer, and increase the stall angle of attack.

The use of morphing wing technology as a flow control technology has resulted in efficient aerodynamic designs. Dynamic stall control is especially significant because it occurs in all aerospace applications. The need for dynamic stall control is crucial for UAVs and military aircraft, as it requires the highest level of maneuverability. Dynamic stall is caused by a rapidly pitching airfoil, wing, or turbine blade. The LEV or DSV is a critical component of dynamic stall, as it increases the lift coefficient. However, this excess lift is lost when the vortex sheds into the wake, thus increasing drag and shifting the pitching moment. Since the discovery of dynamic stall, researchers have tried to understand its mechanics and to modify the LEV formation. Altering the LEV formation may increase an aircraft's operational envelope, and its safety.

The design and implementation of the DMLE technology was investigated for different parameters, such as deflection frequency and amplitude, and the morphing starting time, and this design was not often found in the literature. In this work, the formation and development of LEV and flows separation were controlled, thus preventing the airfoil from experiencing dynamic stall. Systematic research was performed for dynamic stall control using DMLE technology on an oscillating UAS-S45 airfoil.

RECOMMENDATION FOR FUTURE WORK

Several recommendations can be made regarding the research presented in this thesis based on observations made during the two morphing wing projects of which this research was a part:

- Accurate aerodynamic solver calculations are essential in the optimization process. Since the optimization framework uses the nonlinear lifting line and vortex lattice methods, its methodology could use a high-fidelity CFD code instead of XFOIL.
- All three optimization methods explored here, the Genetic Algorithm, Particle Swarm Optimization and Black Widow Optimization (BWO), are metaheuristic algorithms. Gradient-based optimization algorithms should also be explored, and comparisons are made to determine their best choice.
- The structural optimization was performed on the DNLE; the wing box analysis needed high computational cost due to high number of mesh elements. Future studies should review the full morphing wing model for a better structural optimization study.
- Aerodynamic and structural optimization were performed separately due to high computational costs and number of design variables. We suggest investigating multi-objective aero-structural optimization to obtain optimized results.
- In the unsteady aerodynamic analysis of dynamic stall, a more extensive range of chordwise locations of the deflection, drooping amplitude, Reynolds numbers, and surface roughness would enrich the database of design knowledge for further improvements.

  The DMLE in deep dynamic stall regimes is highly influenced by interactions of vortical structures and turbulence features, therefore of the analysis using 3D unsteady flow modeling should be carried out. Since, turbulence is three-dimensional by definition, therefore, understanding unsteady flow physics affecting the dynamic pitching-morphing situation may be improved by using high fidelity and precision CFD methods, such as DES (Detached Eddy

Simulations) and LES (Large Eddy Simulations) to resolve turbulence's lowest scales.

- For a final validation of the morphing optimization study and unsteady aerodynamic results, experimental research should be conducted. Through wind tunnel testing, it will be possible to verify the accuracy and fidelity of the numerically produced results. Furthermore, with the support of instrumentations such as static pressure taps, total pressure rakes, Particle Image Velocimetry (PIV), and hot wire velocity probes, a complete representation of the flow physics of the morphing configurations.

ANNEX I

FURTHER RESULTS>

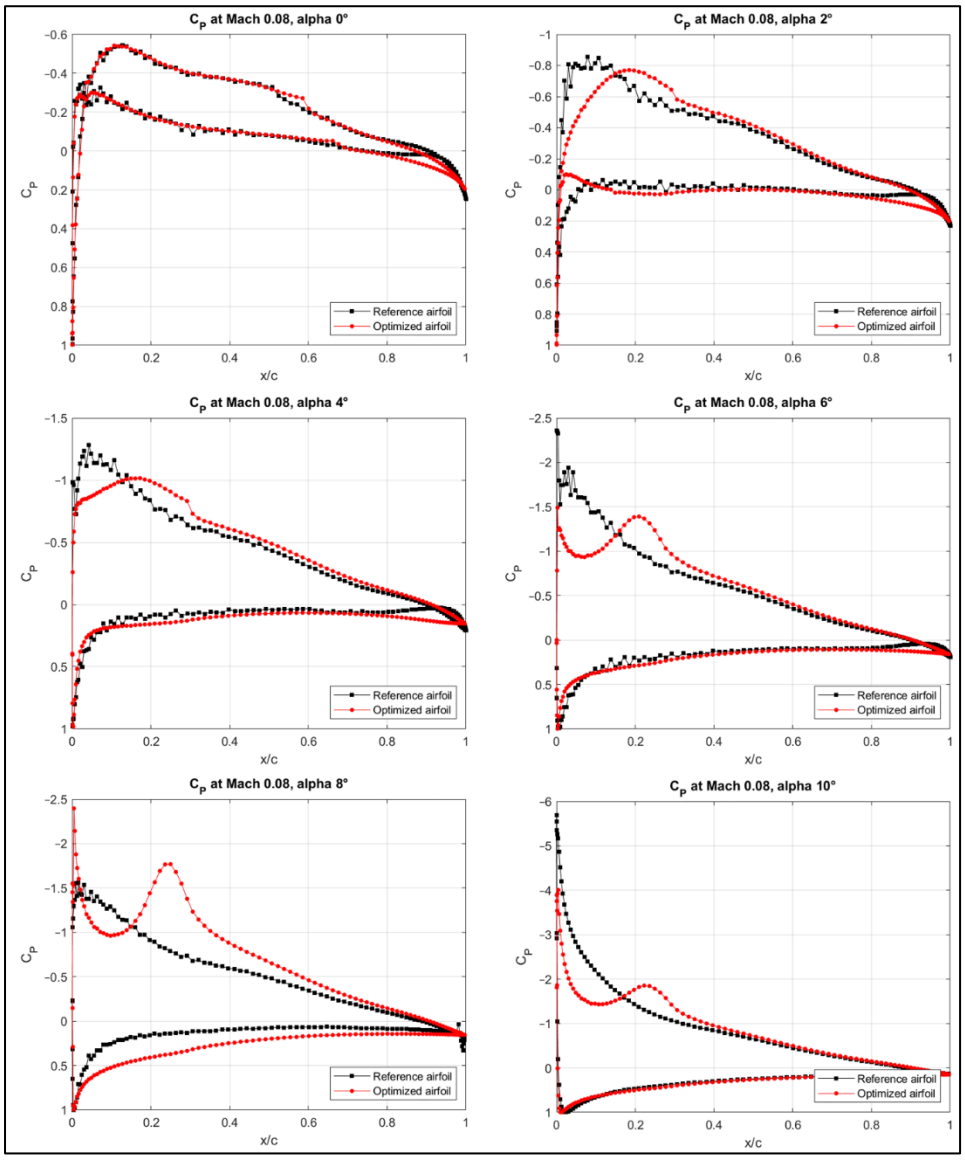

Figure AI-1 Cp distribution versus the chord obtained for the UAS-S45 optimized airfoil for M = 0.08

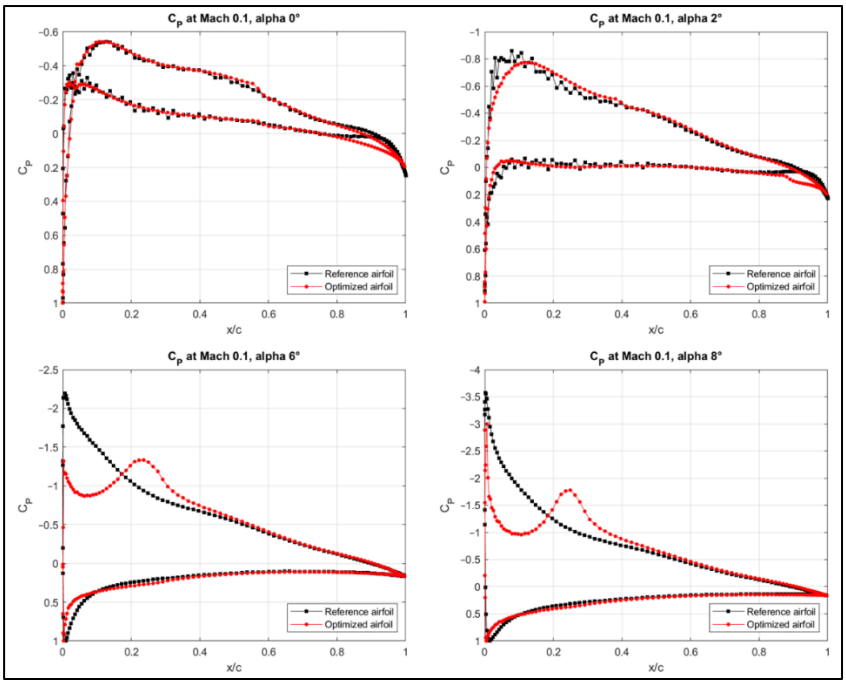

Figure AI-2 Cp distribution versus the chord obtained for the UAS-S45 optimized airfoil for M = 0.1

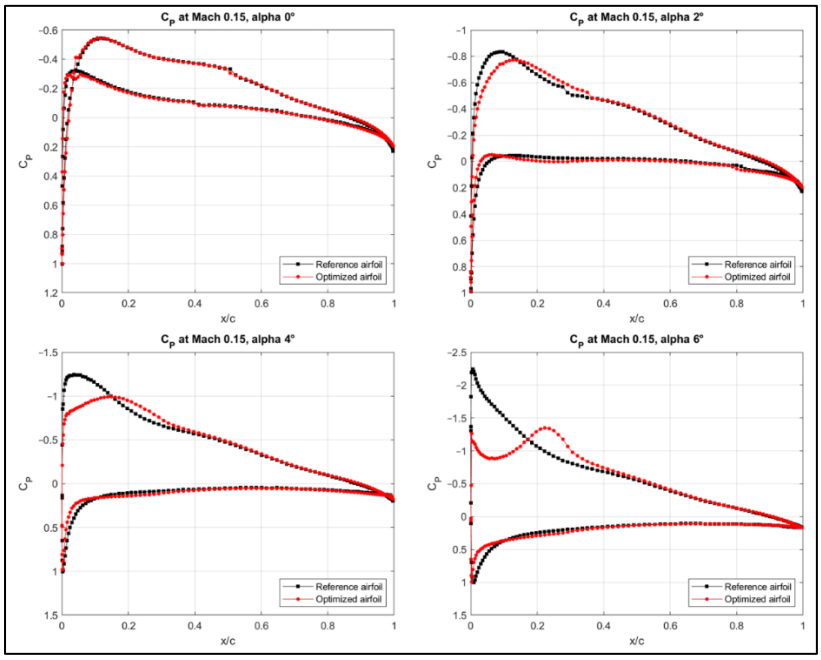

Figure AI-3 Cp distribution versus the chord obtained for the UAS-S45 optimized airfoil for M = 0.15

ANNEX II

DMLE CASES FOR DIFFERENT ANGLES OF ATTACK FOR DIFFERENT FREQUENCIES

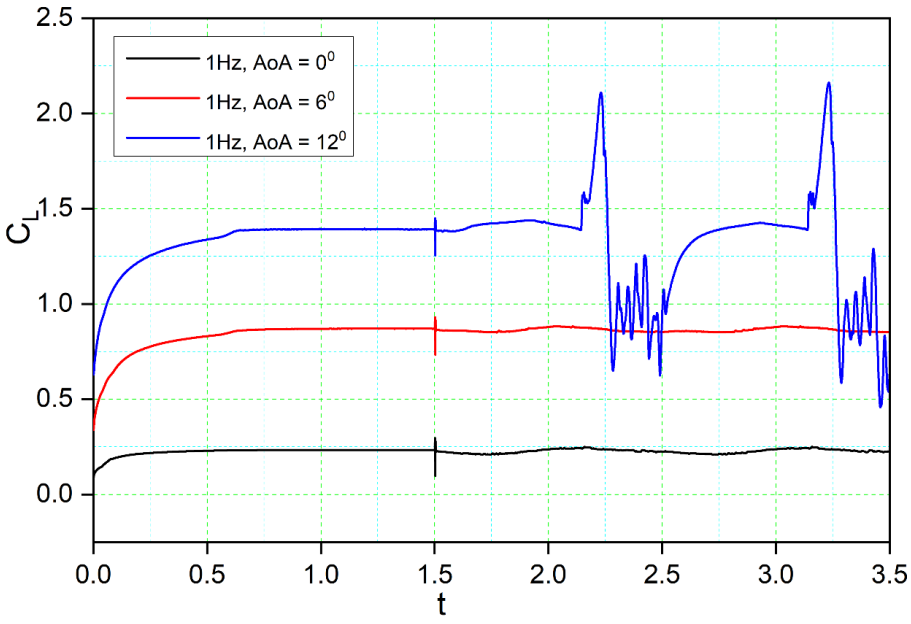

Figure AII-1. Lift Coefficient for DMLE case for different angles of attack For a Deflection Frequency of 1Hz

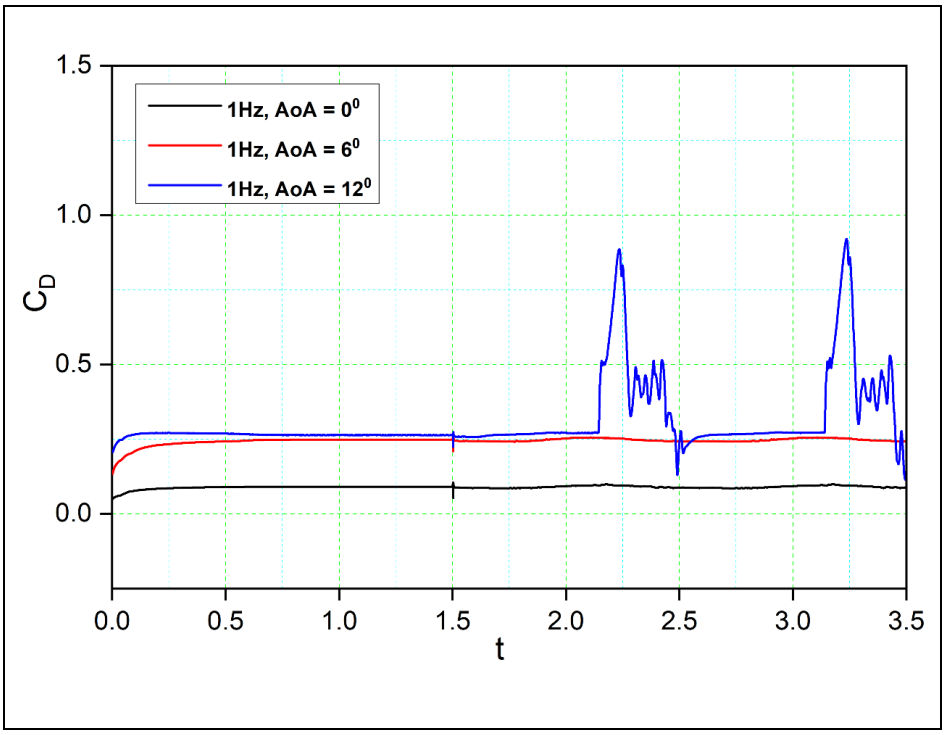

Figure AII-2 Drag Coefficient for DMLE case for different angles of attack for a Deflection Frequency of 1Hz

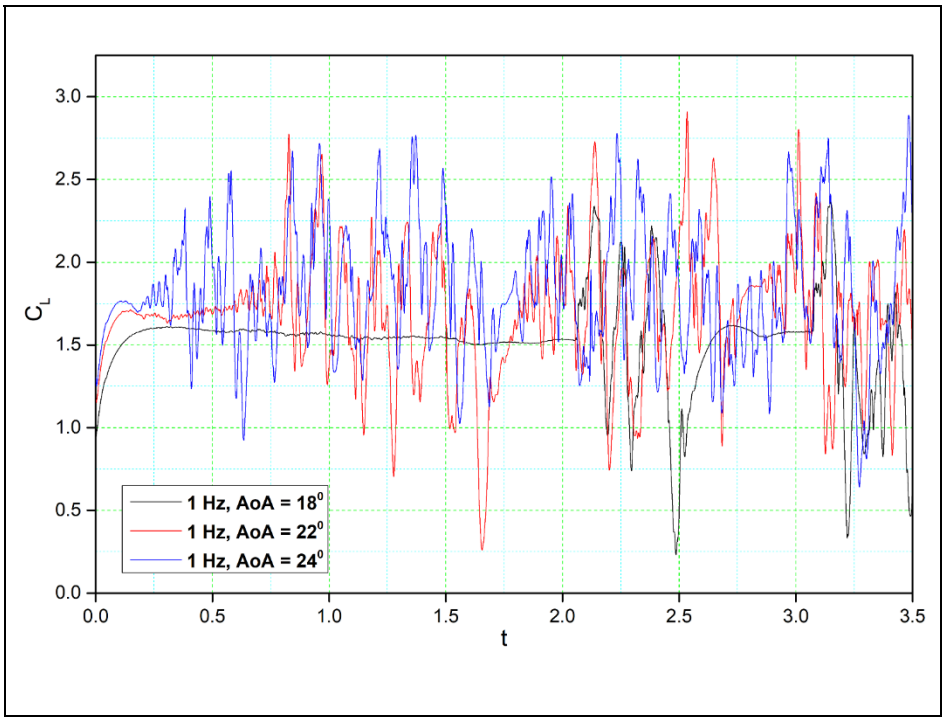

Figure AII-3 Lift Coefficient for DMLE case for different angles of attack for a Deflection Frequency of 1Hz

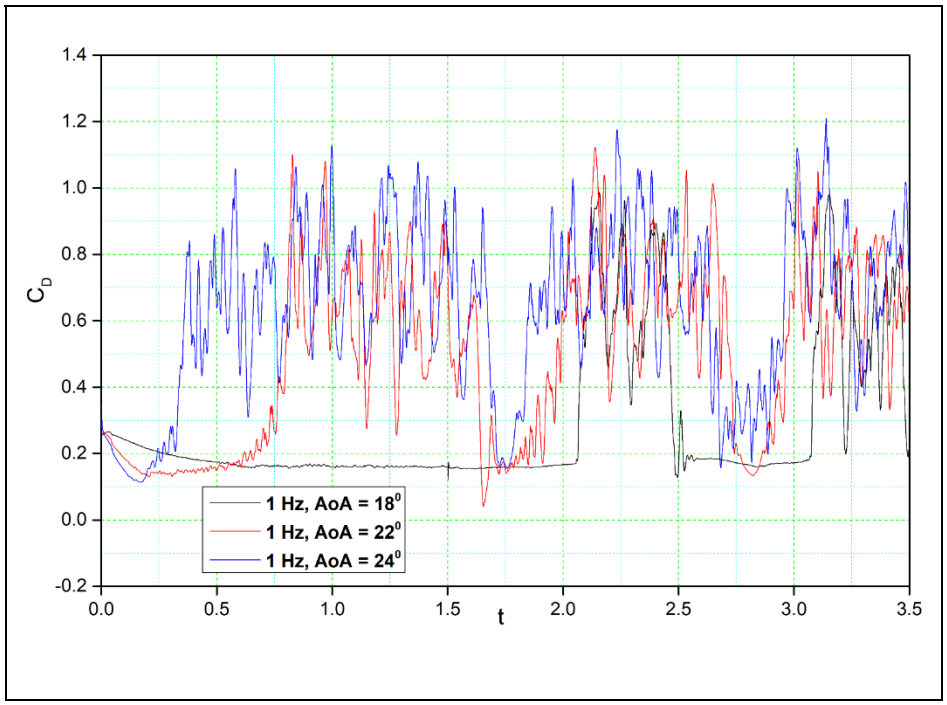

Figure AII-4 Drag Coefficient for DMLE case for different angles of attack for a Deflection Frequency of 1Hz

BIBLIOGRAPHY

Abbas, A., De Vicente, J., & Valero, E. (2013). Aerodynamic technologies to improve aircraft performance. *Aerospace Science and Technology, 28*(1), 100-132.

Abdessemed, C., Bouferrouk, A., & Yao, Y. (2021). Aerodynamic and aeroacoustic analysis of a harmonically morphing airfoil using dynamic meshing. Dans *Acoustics* (Vol. 3, pp. 177-199). Multidisciplinary Digital Publishing Institute.

Abdessemed, C., Bouferrouk, A., & Yao, Y. (2022). Effects of an Unsteady Morphing Wing with Seamless Side-Edge Transition on Aerodynamic Performance. *Energies, 15*(3), 1093.

Abdessemed, C., Yao, Y., & Bouferrouk, A. (2021). Near Stall Unsteady Flow Responses to Morphing Flap Deflections. *Fluids, 6*(5), 180.

Abdessemed, C., Yao, Y., Bouferrouk, A., & Narayan, P. (2018a). Aerodynamic analysis of a harmonically morphing flap using a hybrid turbulence model and dynamic meshing. Dans *2018 applied aerodynamics conference* (pp. 3813).

Abdessemed, C., Yao, Y., Bouferrouk, A., & Narayan, P. (2018b). Morphing airfoils analysis using dynamic meshing. *International Journal of Numerical Methods for Heat & Fluid Flow*.

Abdessemed, C., Yao, Y., Narayan, P., & Bouferrouk, A. (2017). Unsteady parametrization of a morphing wing design for improved aerodynamic performance.

Albuquerque, P. F. G. L. F. (2017). Mission-Based Multidisciplinary design optimization methodologies for unmanned aerial vehicles with morphing technologies.

Ameduri, S., & Concilio, A. (2020). Morphing wings review: aims, challenges, and current open issues of a technology. *Proceedings of the Institution of Mechanical Engineers, Part C: Journal of Mechanical Engineering Science*, 0954406220944423.

Ameduri, S., Concilio, A., Dimino, I., Pecora, R., & Ricci, S. (2018). AIRGREEN2-Clean Sky 2 Programme: Adaptive Wing Technology Maturation, Challenges and Perspectives. *Smart Materials, Adaptive Structures and Intelligent Systems, 51944*, V001T004A023.

Ameduri, S., Dimino, I., Pecora, R., & Ricci, S. (2018). AIRGREEN2-Clean Sky 2 Programme: Adaptive Wing Technology Maturation, Challenges and Perspectives. Dans *ASME 2018 Conference on Smart Materials, Adaptive Structures and Intelligent Systems*. American Society of Mechanical Engineers Digital Collection.

Ameduri, S., Galasso, B., Ciminello, M., & Concilio, A. (2020). Shape memory alloys compact actuators for aerodynamic surfaces twisting. Dans *AIAA Scitech 2020 Forum* (pp. 1299).

Andersen, P. B., Gaunaa, M., Bak, C., & Hansen, M. H. (2009). A dynamic stall model for airfoils with deformable trailing edges. *Wind Energy: An International Journal for Progress and Applications in Wind Power Conversion Technology, 12*(8), 734-751.

Arena, M., Chiatto, M., Amoroso, F., Pecora, R., & de Luca, L. (2018). Feasibility studies for the installation of Plasma Synthetic Jet Actuators on the skin of a morphing wing flap. Dans *Active and Passive Smart Structures and Integrated Systems XII* (Vol. 10595, pp. 131-139). SPIE.

Arena, M., Concilio, A., & Pecora, R. (2019). Aero-servo-elastic design of a morphing wing trailing edge system for enhanced cruise performance. *Aerospace Science and Technology, 86*, 215-235.

Arena, M., Nagel, C., Pecora, R., Schorsch, O., & Dimino, I. (2019). Static and Dynamic Performance of a Morphing Trailing Edge Concept with High-Damping Elastomeric Skin. *Aerospace, 6*(2), 22.

Arena, M., Palumbo, R., Pecora, R., Amoroso, F., Amendola, G., & Dimino, I. (2019). Flutter clearance investigation of camber-morphing aileron tailored for a regional aircraft. *Journal of Aerospace Engineering, 32*(2), 04018146.

Balaji, R., Bramkamp, F., Hesse, M., & Ballmann, J. (2006). Effect of flap and slat riggings on 2-D high-lift aerodynamics. *Journal of Aircraft, 43*(5), 1259-1271.

Bangalore, A., & Sankar, L. (1996). Numerical analysis of aerodynamic performance of rotors with leading edge slats. *Computational mechanics, 17*(5), 335-342.

Bar-Cohen, Y. (2006). Biomimetics—using nature to inspire human innovation. *Bioinspiration & biomimetics, 1*(1), P1.

Barbarino, S., Bilgen, O., Ajaj, R. M., Friswell, M. I., & Inman, D. J. (2011). A review of morphing aircraft. *Journal of intelligent material systems and structures, 22*(9), 823-877.

Bashir, M., Longtin-Martel, S., Botez, R. M., & Wong, T. (2021). Aerodynamic Design Optimization of a Morphing Leading Edge and Trailing Edge Airfoil–Application on the UAS-S45. *Applied Sciences, 11*(4), 1664.

Bashir, M., Longtin-Martel, S., Botez, R. M., & Wong, T. (2022). Optimization and Design of a Flexible Droop-Nose Leading-Edge Morphing Wing Based on a Novel Black Widow Optimization Algorithm—Part I. *Designs, 6*(1), 10.

Bashir, M., Longtin Martel, S., Botez, R. M., & Wong, T. (2022a). Aerodynamic Design and Performance Optimization of Camber Adaptive Winglet for the UAS-S45. Dans *AIAA SCITECH 2022 Forum* (pp. 1041).

Bashir, M., Longtin Martel, S., Botez, R. M., & Wong, T. (2022b). Aerodynamic Shape Optimization of Camber Morphing Airfoil based on Black Widow Optimization. Dans *AIAA SCITECH 2022 Forum* (pp. 2575).

Batina, J. T. (1991). Unsteady Euler algorithm with unstructured dynamic mesh for complex-aircraft aerodynamic analysis. *AIAA Journal, 29*(3), 327-333.

BBC News, Q. (2019). ATAG Beginner's Guide to Aviation Efficiency, the Intergovernmental Panel on Climate Change (IPCC).

Benton, S., & Visbal, M. (2019). The onset of dynamic stall at a high, transitional Reynolds number. *Journal of Fluid Mechanics, 861*, 860-885.

Berci, M., Gaskell, P. H., Hewson, R. W., & Toropov, V. V. (2013). A semi-analytical model for the combined aeroelastic behaviour and gust response of a flexible aerofoil. *Journal of Fluids and Structures, 38*, 3-21.

Boeing, A. C. (June 1973). Variable Camber Wing. *Second Progress Report, AD911543.*

Bonnema, K., & Smith, S. (1988). AFTI/F-111 mission adaptive wing flight research program. Dans *4th Flight Test Conference* (pp. 2118).

Botez, R. (2018a). Morphing wing, UAV and aircraft multidisciplinary studies at the Laboratory of Applied Research in Active Controls, Avionics and AeroServoElasticity LARCASE. *Aerospace Lab,* (14), 1-11.

Botez, R. (2018b). Morphing wing, UAV and aircraft multidisciplinary studies at the Laboratory of Applied Research in Active Controls, Avionics and AeroServoElasticity LARCASE.

Botez, R., Koreanschi, A., Sugar-Gabor, O., Tondji, Y., Guezguez, M., Kammegne, J., . . . Mamou, M. (2018). Numerical and experimental transition results evaluation for a morphing wing and aileron system. *The Aeronautical Journal, 122*(1251), 747-784.

Botez, R., Koreanschi, A., Sugar-Gabor, O., Mebarki, Y., Mamou, M., Tondji, Y., . . . Sandu, D. (2018). Numerical and experimental transition results evaluation for a morphing wing and aileron system. *The Aeronautical Journal, 122*(1251), 747-784.

Botez, R. M. (2022). Overview of Morphing Aircraft and Unmanned Aerial Systems Methodologies and Results–Application on the Cessna Citation X, CRJ-700, UAS-S4 and UAS-S45. Dans *AIAA SCITECH 2022 Forum* (pp. 1038).

Botez, R. M., Molaret, P., & Laurendeau, E. (2007). Laminar flow control on a research wing project presentation covering a three year period. Dans *Canadian aeronautics and space institute annual general meeting* (Vol. 2007).

Brandon, J. M. (1991). Dynamic stall effects and applications to high performance aircraft. *Aircraft Dynamics at High Angles of Attack: Ezperiments and Modelling*.

Buckley, H. P., Zhou, B. Y., & Zingg, D. W. (2010). Airfoil optimization using practical aerodynamic design requirements. *Journal of Aircraft, 47*(5), 1707-1719.

Burnazzi, M., & Radespiel, R. (2014). Assessment of leading-edge devices for stall delay on an airfoil with active circulation control. *CEAS Aeronautical Journal, 5*(4), 359-385.

Cantwell, W. J., & Morton, J. (1991). The impact resistance of composite materials—a review. *composites, 22*(5), 347-362.

Carossa, G. M., Ricci, S., De Gaspari, A., Liauzun, C., Dumont, A., & Steinbuch, M. (2016). Adaptive Trailing Edge: Specifications, Aerodynamics, and Exploitation. Dans *Smart Intelligent Aircraft Structures (SARISTU)* (pp. 143-158). Springer.

Carr, L. W. (1988). Progress in analysis and prediction of dynamic stall. *Journal of Aircraft, 25*(1), 6-17.

Carrier, G., Atinault, O., Dequand, S., Hantrais-Gervois, J., Liauzun, C., Paluch, B., . . . Toussaint, C. (2012). Investigation of a strut-braced wing configuration for future commercial transport. Dans *28th Congress of the International Council of the Aeronautical Sciences* (pp. 2012-2011). ICAS Bonn.

Champasak, P., Panagant, N., Pholdee, N., Vio, G. A., Bureerat, S., Yildiz, B. S., & Yıldız, A. R. (2022). Aircraft conceptual design using metaheuristic-based reliability optimisation. *Aerospace Science and Technology, 129*, 107803.

Chandrasekhara, M., Martin, P. B., & Tung, C. (2004). Compressible dynamic stall control using a variable droop leading edge airfoil. *Journal of Aircraft, 41*(4), 862-869.

Chandrasekhara, M., Wilder, M., & Carr, L. (1998). Unsteady stall control using dynamically deforming airfoils. *AIAA Journal, 36*(10), 1792-1800.

Chillara, V., & Dapino, M. (2020). Review of morphing laminated composites. *Applied Mechanics Reviews, 72*(1).

Chugh, T., Sun, C., Wang, H., & Jin, Y. (2020). Surrogate-assisted evolutionary optimization of large problems. Dans *High-Performance Simulation-Based Optimization* (pp. 165-187). Springer.

Communier, D., Botez, R., & Wong, T. (2019). Experimental validation of a new morphing trailing edge system using Price–Païdoussis wind tunnel tests. *Chinese Journal of Aeronautics, 32*(6), 1353-1366.

Communier, D., Botez, R. M., & Wong, T. (2020). Design and Validation of a New Morphing Camber System by Testing in the Price—Païdoussis Subsonic Wind Tunnel. *Aerospace, 7*(3), 23.

Communier, D., Le Besnerais, F., Botez, R. M., & Wong, T. (2019). Design, manufacturing, and testing of a new concept for a morphing leading edge using a subsonic blow down wind tunnel. *Biomimetics, 4*(4), 76.

Concilio, A., Dimino, I., & Pecora, R. (2021). SARISTU: Adaptive Trailing Edge Device (ATED) design process review. *Chinese Journal of Aeronautics, 34*(7), 187-210.

Cook, J. R., & Smith, M. J. (2014). Stability of Aeroelastic Airfoils with Camber Flexibility. *Journal of Aircraft, 51*(6), 2024-2027.

Correa, A. F. M. (2015). The Study of Dynamic Stall and URANS Capabilities on Modelling Pitching Airfoil Flows. *Masters Thesis, UNIVERSIDADE FEDERAL DE UBERLÂNDIA*.

Cummings, R. M., Morton, S. A., & Siegel, S. G. (2008). Numerical prediction and wind tunnel experiment for a pitching unmanned combat air vehicle. *Aerospace Science and Technology, 12*(5), 355-364.

Dancila, B., Botez, R., & Labour, D. (2013). Fuel burn prediction algorithm for cruise, constant speed and level flight segments. *The Aeronautical Journal, 117*(1191), 491-504.

De Gaspari, A., & Moens, F. (2019). Aerodynamic shape design and validation of an advanced high-lift device for a regional aircraft with morphing droop nose. *International Journal of Aerospace Engineering, 2019*.

DeCamp, R., & HARDY, R. (1981). Mission adaptive wing research programme. *Aircraft Engineering and Aerospace Technology, 53*(1), 10-11.

Decamp, R., & Hardy, R. (1984). Mission adaptive wing advanced research concepts. Dans *11th Atmospheric Flight Mechanics Conference* (pp. 2088).

Della Vecchia, P., Daniele, E., & D'Amato, E. (2014). An airfoil shape optimization technique coupling PARSEC parameterization and evolutionary algorithm. *Aerospace Science and Technology, 32*(1), 103-110.

Derksen, R., & Rogalsky, T. (2009). Optimum aerofoil parameterization for aerodynamic design. *Computer Aided Optimum Design in Engineering XI, 106*, 197-206.

Derksen, R., & Rogalsky, T. (2010). Bezier-PARSEC: An optimized aerofoil parameterization for design. *Advances in engineering software, 41*(7-8), 923-930.

Dimino, I., Lecce, L., & Pecora, R. (2017). *Morphing Wing Technologies: Large Commercial Aircraft and Civil Helicopters*. Butterworth-Heinemann.

Dimino, I., Pecora, R., & Arena, M. (2020). Aircraft morphing systems: elasticity of selected components and modelling issues. Dans *Active and Passive Smart Structures and Integrated Systems IX* (Vol. 11376, pp. 113760M). International Society for Optics and Photonics.

Drela, M. (1989). XFOIL: An analysis and design system for low Reynolds number airfoils. Dans *Low Reynolds number aerodynamics* (pp. 1-12). Springer.

Drela, M., & Youngren, H. (2015). XFOIL: Interactive program for the design and analysis of subsonic isolated airfoils.

Eguea, J. P., da Silva, G. P. G., & Catalano, F. M. (2020). Fuel efficiency improvement on a business jet using a camber morphing winglet concept. *Aerospace Science and Technology, 96*, 105542.

Elelwi, M., Kuitche, M., Botez, R., & Dao, T. (2020). Comparison and analyses of a variable span-morphing of the tapered wing with a varying sweep angle. *The Aeronautical Journal, 124*(1278), 1146-1169.

Félix Patrón, R. S., Berrou, Y., & Botez, R. (2014). Climb, cruise and descent 3D trajectory optimization algorithm for a flight management system. Dans *AIAA/3AF Aircraft Noise and Emissions Reduction Symposium* (pp. 3018).

Fereidooni, A., Marchwica, J., Leung, N., Mangione, J., & Wickramasinghe, V. (2021). Development of a hybrid (rigid-flexible) morphing leading edge equipped with bending and extending capabilities. *Journal of intelligent material systems and structures, 32*(9), 1024-1037.

Feszty, D., Gillies, E. A., & Vezza, M. (2004). Alleviation of airfoil dynamic stall moments via trailing-edge flap flow control. *AIAA Journal, 42*(1), 17-25.

Fincham, J., & Friswell, M. (2015). Aerodynamic optimisation of a camber morphing aerofoil. *Aerospace Science and Technology, 43*, 245-255.

Fortin, F. (2019). Shape optimization of a stretchable drooping leading edge. Dans *AIAA Scitech 2019 forum* (pp. 2352).

Frota, J. (2010). NACRE novel aircraft concepts. *The Aeronautical Journal, 114*(1156), 399-404.

Gamboa, P., Vale, J., Lau, F., & Suleman, A. (2009). Optimization of a morphing wing based on coupled aerodynamic and structural constraints. *AIAA Journal, 47*(9), 2087-2104.

Ganguli, R., & Rajagopal, S. (2009). Multidisciplinary design optimization of an UAV wing using kriging based multi-objective genetic algorithm. Dans *50th AIAA/ASME/ASCE/AHS/ASC Structures, Structural Dynamics, and Materials Conference 17th AIAA/ASME/AHS Adaptive Structures Conference 11th AIAA No* (pp. 2219).

Geissler, W., Sobieczky, H., Carr, L., Chandrasekhara, M., & Wilder, M. (1998). Compressible dynamic stall calculations incorporating transition modeling for variable geometry airfoils. Dans *36th AIAA Aerospace Sciences Meeting and Exhibit* (pp. 705).

Geng, F., Kalkman, I., Suiker, A., & Blocken, B. (2018). Sensitivity analysis of airfoil aerodynamics during pitching motion at a Reynolds number of 1.35× 105. *Journal of Wind Engineering and Industrial Aerodynamics, 183*, 315-332.

Gerhards, R., & Szodruch, J. (2001). Industrial Perspectives of Drag Reduction Technologies. Dans *Aerodynamic Drag Reduction Technologies* (pp. 259-266). Springer.

Gerontakos, P., & Lee, T. (2006). Dynamic stall flow control via a trailing-edge flap. *AIAA Journal, 44*(3), 469-480.

Gerontakos, P., & Lee, T. (2007). Trailing-edge flap control of dynamic pitching moment. *AIAA Journal, 45*(7), 1688-1694.

Gideon, R. A. (2007). The correlation coefficients. *Journal of Modern Applied Statistical Methods, 6*(2), 16.

Giuliani, M., Dimino, I., Ameduri, S., Pecora, R., & Concilio, A. (2022). Status and Perspectives of Commercial Aircraft Morphing. *Biomimetics, 7*(1), 11.

Gong, C., & Ma, B.-F. (2019). Aerodynamic evaluation of an unmanned aerial vehicle with variable sweep and span. *Proceedings of the Institution of Mechanical Engineers, Part G: Journal of Aerospace Engineering*, 0954410019836907.

Greenblatt, D., & Wygnanski, I. (2001). Dynamic stall control by periodic excitation, Part 1: NACA 0015 parametric study. *Journal of Aircraft, 38*(3), 430-438.

Greenblatt, D., & Wygnanski, I. J. (2000). The control of flow separation by periodic excitation. *Progress in Aerospace Sciences, 36*(7), 487-545.

Grigorie, T. L., Botez, R. M., Popov, A. V., Mamou, M., & Mébarki, Y. (2012). A hybrid fuzzy logic proportional-integral-derivative and conventional on-off controller for morphing wing actuation using shape memory alloy Part 1: Morphing system mechanisms and controller architecture design. *The Aeronautical Journal, 116*(1179), 433-449.

Gupta, R., & Ansell, P. J. (2019). Unsteady flow physics of airfoil dynamic stall. *AIAA Journal, 57*(1), 165-175.

Hamy, A., Murrieta-Mendoza, A., & Botez, R. (2016). Flight trajectory optimization to reduce fuel burn and polluting emissions using a performance database and ant colony optimization algorithm.

Hang, X., Su, W., Fei, Q., & Jiang, D. (2020). Analytical sensitivity analysis of flexible aircraft with the unsteady vortex-lattice aerodynamic theory. *Aerospace Science and Technology, 99*, 105612.

Harvey, C., & Inman, D. J. (2021). Aerodynamic efficiency of gliding birds vs comparable UAVs: a review. *Bioinspiration & biomimetics, 16*(3), 031001.

Hashimoto, A., Obayashi, S., & Jeong, S. (2014). Aerodynamic optimization of high-wing configuration for near future aircraft. Dans *10th AIAA multidisciplinary design optimization conference* (pp. 0291).

Hayyolalam, V., & Kazem, A. A. P. (2020). Black widow optimization algorithm: a novel meta-heuristic approach for solving engineering optimization problems. *Engineering Applications of Artificial Intelligence, 87*, 103249.

Heine, B., Mulleners, K., Joubert, G., & Raffel, M. (2013). Dynamic stall control by passive disturbance generators. *AIAA Journal, 51*(9), 2086-2097.

Hicken, J. (2009). *Efficient algorithms for future aircraft design: Contributions to aerodynamic shape optimization*.

Hicken, J. E. (2009). *Efficient algorithms for future aircraft design: Contributions to aerodynamic shape optimization*. University of Toronto Toronto, ON, Canada.

Hileman, D. J. I. (2022). Environment & Energy Research & Development Portfolio Overview. *Chief Scientific and Technical Advisor for Environment and Energy Office of Environment and Energy Federal Aviation Administration*.

ICAO. (2019). Aviation's contribution to climate change, Environmental report. *International Civil Aviation Organisation*. Repéré à http://www.icao.int/

Imamura, T., Enomoto, S., Yokokawa, Y., & Yamamoto, K. (2008). Three-dimensional unsteady flow computations around a conventional slat of high-lift devices. *AIAA Journal, 46*(5), 1045-1053.

Jameson, A., Shankaran, S., & Martinelli, L. (2008). Continuous adjoint method for unstructured grids. *AIAA journal, 46*(5), 1226-1239.

Jawahar, H. K., Ai, Q., & Azarpeyvand, M. (2018). Experimental and numerical investigation of aerodynamic performance for airfoils with morphed trailing edges. *Renewable Energy, 127*, 355-367.

Jiakun, H., Zhe, H., Fangbao, T., & Gang, C. (2021). Review on bio-inspired flight systems and bionic aerodynamics. *Chinese Journal of Aeronautics, 34*(7), 170-186.

Kamliya Jawahar, H., Ai, Q., & Azarpeyvand, M. (2017). Experimental and numerical investigation of aerodynamic performance of airfoils fitted with morphing trailing-edges. Dans *23rd AIAA/CEAS aeroacoustics conference* (pp. 3371).

Kao, J. Y., Clark, D. L., White, T., Reich, G. W., & Burton, S. (2019). Conceptual Multidisciplinary Design and Optimization of Morphing Aircraft. Dans *AIAA Scitech 2019 Forum* (pp. 0175).

Karimian, S., Aramian, S., & Abdolahifar, A. (2021). Numerical investigation of dynamic stall reduction on helicopter blade section in forward flight by an airfoil deformation method. *Journal of the Brazilian Society of Mechanical Sciences and Engineering, 43*(2), 1-17.

Katam, V., LeBeau, R., & Jacob, J. (2005). Simulation of separation control on a morphing wing with conformal camber. Dans *35th AIAA Fluid Dynamics Conference and Exhibit* (pp. 4880).

Khan, S., Grigorie, T., Botez, R., Mamou, M., & Mébarki, Y. (2020). Novel morphing wing actuator control-based Particle Swarm Optimisation. *The Aeronautical Journal, 124*(1271), 55-75.

Khurana, M. (2011). Development and application of an optimisation architecture with adaptive swarm algorithm for airfoil aerodynamic design.

Khurana, M., Winarto, H., & Sinha, A. (2008a). Airfoil geometry parameterization through shape optimizer and computational fluid dynamics. Dans *46th AIAA Aerospace Sciences Meeting and Exhibit* (pp. 295).

Khurana, M., Winarto, H., & Sinha, A. (2008b). Application of swarm approach and artificial neural networks for airfoil shape optimization. Dans *12th AIAA/ISSMO Multidisciplinary Analysis and Optimization Conference* (pp. 5954).

Kintscher, M., Wiedemann, M., Monner, H. P., Heintze, O., & Kühn, T. (2011). Design of a smart leading edge device for low speed wind tunnel tests in the European project SADE. *International Journal of Structural Integrity*.

König, J., & Hellstrom, T. (2010). The Clean Sky "Smart Fixed Wing Aircraft Integrated Technology Demonstrator": Technology targets and project status. Dans *Proceedings of the 27th International Congress of the Aeronautical Science* (Vol. 6, pp. 5101-5110). ICAS Stockholm, Sweden.

Koreanschi, A., Sugar-Gabor, O., Acotto, J., Brianchon, G., Portier, G., Botez, R. M., . . . Mebarki, Y. (2017a). Optimization and design of an aircraft's morphing wing-tip demonstrator for drag reduction at low speeds, Part II-Experimental validation using Infra-Red transition measurement from Wind Tunnel tests. *Chinese Journal of Aeronautics, 30*(1), 164-174.

Koreanschi, A., Sugar-Gabor, O., Acotto, J., Brianchon, G., Portier, G., Botez, R. M., . . . Mebarki, Y. (2017b). Optimization and design of an aircraft's morphing wing-tip demonstrator for drag reduction at low speed, Part I–Aerodynamic optimization using genetic, bee colony and gradient descent algorithms. *Chinese Journal of Aeronautics, 30*(1), 149-163.

Koreanschi, A., Oliviu, S. G., Acotto, J., Botez, R. M., Mamou, M., & Mebarki, Y. (2016). A genetic algorithm optimization method for a morphing wing tip demonstrator validated using infra red experimental data. Dans *34th AIAA applied aerodynamics conference* (pp. 4037).

Koreanschi, A., Sugar-Gabor, O., & Botez, R. M. (2016a). Drag optimisation of a wing equipped with a morphing upper surface. *The Aeronautical Journal, 120*(1225), 473.

Koreanschi, A., Sugar-Gabor, O., & Botez, R. M. (2016b). Numerical and experimental validation of a morphed wing geometry using Price-Païdoussis wind tunnel testing. *The Aeronautical Journal, 120*(1227), 757-795.

Kota, S., Ervin, G., Osborn, R., & Ormiston, R. (2008). Design and fabrication of an adaptive leading edge rotor blade. Dans *Annual Forum Proceedings-American Helicopter Society* (Vol. 64, pp. 2178). AMERICAN HELICOPTER SOCIETY, INC.

Kota, S., Osborn, R., Ervin, G., Maric, D., Flick, P., & Paul, D. (2009). Mission adaptive compliant wing–design, fabrication and flight test. Dans *RTO Applied Vehicle Technology Panel (AVT) Symposium* (pp. 18-11). RTO-MP-AVT-168, Evora, Portugal.

Krzysiak, A., & Narkiewicz, J. (2006). Aerodynamic loads on airfoil with trailing-edge flap pitching with different frequencies. *Journal of Aircraft, 43*(2), 407-418.

Kuitche, M. A. J., & Botez, R. M. (2019). Modeling novel methodologies for unmanned aerial systems–Applications to the UAS-S4 Ehecatl and the UAS-S45 Bálaam. *Chinese Journal of Aeronautics, 32*(1), 58-77.

Kuitche, M. A. J., Botez, R. M., Guillemin, A., & Communier, D. (2020a). Aerodynamic modelling of unmanned aerial system through nonlinear vortex lattice method, computational fluid dynamics and experimental validation-application to the uas-s45 bàlaam: Part 1. *INCAS Bulletin, 12*(1), 91-103.

Kuitche, M. A. J., Botez, R. M., Guillemin, A., & Communier, D. (2020b). Aerodynamic modelling of unmanned aerial system through nonlinear vortex lattice method, computational fluid dynamics and experimental validation-application to the UAS-S45 bàlaam: Part 2. *INCAS Bulletin, 12*(2), 99-115.

Kuitche, M. A. J., Botez, R. M., Viso, R., Maunand, J. C., & Moyao, O. C. (2020). Blade element momentum new methodology and wind tunnel test performance evaluation for the UAS-S45 Bàlaam propeller. *CEAS Aeronautical Journal, 11*(4), 937-953.

Kulfan, B. M. (2007). CST universal parametric geometry representation method with applications to supersonic aircraft. Dans *Fourth International Conference on Flow Dynamics Sendai International Center Sendai, Japan*.

Kulfan, B. M. (2010). Recent extensions and applications of the ‘CST’universal parametric geometry representation method. *The Aeronautical Journal, 114*(1153), 157-176.

Langtry, R., & Menter, F. (2005). Transition modeling for general CFD applications in aeronautics. Dans *43rd AIAA aerospace sciences meeting and exhibit* (pp. 522).

Larsen, J. W., Nielsen, S. R., & Krenk, S. (2007). Dynamic stall model for wind turbine airfoils. *Journal of Fluids and Structures, 23*(7), 959-982.

Le Pape, A., Costes, M., Richez, F., Joubert, G., David, F., & Deluc, J.-M. (2012). Dynamic stall control using deployable leading-edge vortex generators. *AIAA Journal, 50*(10), 2135-2145.

Lee, B.-s., Ye, K., Joo, W., & Lee, D.-H. (2005). Passive control of dynamic stall via nose droop with Gurney flap. Dans *43rd AIAA Aerospace Sciences Meeting and Exhibit* (pp. 1364).

Lee, D.-S., Gonzalez, L. F., Periaux, J., & Srinivas, K. (2008). Robust design optimisation using multi-objective evolutionary algorithms. *Computers & Fluids, 37*(5), 565-583.

Lee, T., & Gerontakos, P. (2009). Unsteady airfoil with dynamic leading-and trailing-edge flaps. *Journal of Aircraft, 46*(3), 1076-1081.

Lee, T., & Su, Y. (2011). Unsteady airfoil with a harmonically deflected trailing-edge flap. *Journal of Fluids and Structures, 27*(8), 1411-1424.

Li, D., Guo, S., & Xiang, J. (2013). Modeling and nonlinear aeroelastic analysis of a wing with morphing trailing edge. *Proceedings of the Institution of Mechanical Engineers, Part G: Journal of Aerospace Engineering, 227*(4), 619-631.

Li, D., Zhao, S., Da Ronch, A., Xiang, J., Drofelnik, J., Li, Y., . . . Monner, H. P. (2018). A review of modelling and analysis of morphing wings. *Progress in Aerospace Sciences, 100*, 46-62.

Li, Y., Wang, X., & Zhang, D. (2013). Control strategies for aircraft airframe noise reduction. *Chinese Journal of Aeronautics, 26*(2), 249-260.

Liauzun, C., Le Bihan, D., David, J.-M., Joly, D., & Paluch, B. (2018). Study of morphing winglet concepts aimed at improving load control and the aeroelastic behavior of civil transport aircraft. *Aerospace Lab,* (14), 1-15.

Liiva, J. (1969). Unsteady aerodynamic and stall effects on helicopter rotor blade airfoil sections. *Journal of Aircraft, 6*(1), 46-51.

Lyu, Z., Kenway, G. K., & Martins, J. R. (2014). Aerodynamic shape optimization investigations of the common research model wing benchmark. *AIAA journal, 53*(4), 968-985.

Lyu, Z., & Martins, J. R. (2015). Aerodynamic shape optimization of an adaptive morphing trailing-edge wing. *Journal of Aircraft, 52*(6), 1951-1970.

Magrini, A., & Benini, E. (2018). Aerodynamic optimization of a morphing leading edge airfoil with a constant arc length parameterization. *Journal of Aerospace Engineering, 31*(2), 04017093.

Magrini, A., Benini, E., Ponza, R., Wang, C., Khodaparast, H. H., Friswell, M. I., . . . Contell Asins, C. (2019). Comparison of constrained parameterisation strategies for aerodynamic optimisation of morphing leading edge airfoil. *Aerospace, 6*(3), 31.

Malik, S., Elaggan, E., & Dawson, P. J. (2021). Design, Analysis and Fabrication of Morphing Airfoil. Dans *AIAA Scitech 2021 Forum* (pp. 0352).

Marino, M., & Sabatini, R. (2014a). Advanced lightweight aircraft design configurations for green operations. Dans *Proceedings of the Practical Responses to Climate Change Conference, Melbourne, Australia* (pp. 207).

Marino, M., & Sabatini, R. (2014b). Advanced lightweight aircraft design configurations for green operations. Dans *Practical Responses to Climate Change Conference 2014* (pp. 207). Engineers Australia.

Martin, P., McAlister, K., Chandrasekhara, M., & Geissler, W. (2003). *Dynamic stall measurements and computations for a VR-12 airfoil with a variable droop leading edge*. NATIONAL AERONAUTICS AND SPACE ADMINISTRATION MOFFETT FIELD CA ROTORCRAFT ….

Martinelli, L., & Jameson, A. (2013). Computational aerodynamics: solvers and shape optimization. *Journal of Heat Transfer, 135*(1), 011002.

Mathisen, S., Gryte, K., Gros, S., & Johansen, T. A. (2021). Precision deep-stall landing of fixed-wing UAVs using nonlinear model predictive control. *Journal of Intelligent & Robotic Systems, 101*(1), 1-15.

Matsson, J. E. (2022). *An Introduction to ANSYS Fluent 2022*. Sdc Publications.

May, M., Arnold-Keifer, S., Landersheim, V., Laveuve, D., Asins, C. C., & Imbert, M. (2021). Bird strike resistance of a CFRP morphing leading edge. *Composites Part C: Open Access, 4*, 100115.

Mcallister, K., Carr, L., & Mccroskey, W. (1978). Dynamic Stall Experiments on the NACA 0012 Airfoil [Technical report No. 1100]: NASA.

McCroskey, W., & Philippe, J. (1975). Unsteady viscous flow on oscillating airfoils. *AIAA Journal, 13*(1), 71-79.

McCroskey, W. J. (1981). *The phenomenon of dynamic stall*.

McCroskey, W. J., Carr, L. W., & McAlister, K. W. (1976). Dynamic stall experiments on oscillating airfoils. *AIAA Journal, 14*(1), 57-63.

Moens, F. (2019). Augmented aircraft performance with the use of morphing technology for a turboprop regional aircraft wing. *Biomimetics, 4*(3), 64.

Monner, H., Breitbach, E., Bein, T., & Hanselka, H. (2000). Design aspects of the adaptive wing—the elastic trailing edge and the local spoiler bump. *The Aeronautical Journal, 104*(1032), 89-95.

Monner, H., Kintscher, M., Lorkowski, T., & Storm, S. (2009). Design of a smart droop nose as leading edge high lift system for transportation aircrafts. Dans *50th AIAA/ASME/ASCE/AHS/ASC Structures, Structural Dynamics, and Materials Conference 17th AIAA/ASME/AHS Adaptive Structures Conference 11th AIAA No* (pp. 2128).

Mulleners, K., & Raffel, M. (2013). Dynamic stall development. *Experiments in fluids, 54*(2), 1-9.

Murua, J., Palacios, R., & Peiró, J. (2010). Camber effects in the dynamic aeroelasticity of compliant airfoils. *Journal of Fluids and Structures, 26*(4), 527-543.

Murugan, S., & Friswell, M. (2013). Morphing wing flexible skins with curvilinear fiber composites. *Composite Structures, 99*, 69-75.

Murugan, S., Woods, B., & Friswell, M. (2015). Hierarchical modeling and optimization of camber morphing airfoil. *Aerospace Science and Technology, 42*, 31-38.

Nguyen, D. H., Lowenberg, M. H., & Neild, S. A. (2022). Analysing dynamic deep stall recovery using a nonlinear frequency approach. *Nonlinear Dynamics, 108*(2), 1179-1196.

Nonut, A., Kanokmedhakul, Y., Bureerat, S., Kumar, S., Tejani, G. G., Artrit, P., . . . Pholdee, N. (2022). A small fixed-wing UAV system identification using metaheuristics. *Cogent Engineering, 9*(1), 2114196.

Noviello, M. C., Dimino, I., Amoroso, F., & Pecora, R. (2019). Aeroelastic Assessments and Functional Hazard Analysis of a Regional Aircraft Equipped with Morphing Winglets. *Aerospace, 6*(10), 104.

Okrent, J. (2017). An Integrated Method for Airfoil Optimization.

Okrent, J. B. (2017). *An Integrated Method for Airfoil Optimization* (Lehigh University).

Olivett, A., Corrao, P., & Karami, M. A. (2021). Flow control and separation delay in morphing wing aircraft using traveling wave actuation. *Smart Materials and Structures, 30*(2), 025028.

Oliviu, S. G., Koreanschi, A., Botez, R. M., Mamou, M., & Mebarki, Y. (2016). Analysis of the aerodynamic performance of a morphing wing-tip demonstrator using a novel nonlinear vortex lattice method. Dans *34th AIAA applied aerodynamics conference* (pp. 4036).

Overton, J. (2019). Fact Sheet | The Growth in Greenhouse Gas Emissions from Commercial Aviation, Part 1 of a Series on Airlines and Climate Change. *Environmental and Energy Study Institute*.

Pantelakis, S., Horst, P., Kintscher, M., Wiedemann, M., Monner, H. P., Heintze, O., & Kühn, T. (2011). Design of a smart leading edge device for low speed wind tunnel tests in the European project SADE. *International Journal of Structural Integrity*.

Papadopoulos, M. (2016). *Smart Intelligent Aircraft Structures (SARISTU)*. Springer-Verlag Berlin Heidelberg.

Pecora, R. (2021). Morphing wing flaps for large civil aircraft: Evolution of a smart technology across the Clean Sky program. *Chinese Journal of Aeronautics, 34*(7), 13-28.

Pecora, R., Magnifico, M., Amoroso, F., & Monaco, E. (2014). Multi-parametric flutter analysis of a morphing wing trailing edge. *The Aeronautical Journal, 118*(1207), 1063-1078.

Peerlings, B. (2018). A review of aerodynamic flow models, solution methods and solvers and their applicability to aircraft conceptual design. *Delft University of Technology: Delft, The Netherlands*.

Pendleton, E. W., Bessette, D., Field, P. B., Miller, G. D., & Griffin, K. E. (2000). Active aeroelastic wing flight research program: technical program and model analytical development. *Journal of Aircraft, 37*(4), 554-561.

Perry III, B., Cole, S. R., & Miller, G. D. (1995). Summary of an active flexible wing program. *Journal of Aircraft, 32*(1), 10-15.

Perry, M., & Mueller, T. (1987). Leading-and trailing-edge flaps on a low Reynolds number airfoil. *Journal of Aircraft, 24*(9), 653-659.

Peter, F., Lammering, T., Risse, K., Franz, K., & Stumpf, E. (2013). Economic assessment of morphing leading edge systems in conceptual aircraft design. Dans *51st AIAA Aerospace Sciences Meeting including the New Horizons Forum and Aerospace Exposition* (pp. 145).

Popov, A. V., Botez, R. M., & Labib, M. (2008). Transition point detection from the surface pressure distribution for controller design. *Journal of Aircraft, 45*(1), 23-28.

Popov, A. V., Grigorie, L. T., Botez, R., Mamou, M., & Mebarki, Y. (2010). Closed-loop control validation of a morphing wing using wind tunnel tests. *Journal of Aircraft, 47*(4), 1309-1317.

Popov, A. V., Grigorie, L. T., Botez, R., Mamou, M., & Mébarki, Y. (2010). Real time morphing wing optimization validation using wind-tunnel tests. *Journal of Aircraft, 47*(4), 1346-1355.

Popov, A. V., Grigorie, T. L., Botez, R. M., Mébarki, Y., & Mamou, M. (2010). Modeling and testing of a morphing wing in open-loop architecture. *Journal of Aircraft, 47*(3), 917-923.

Post, M. L., & Corke, T. C. (2006). Separation control using plasma actuators: dynamic stall vortex control on oscillating airfoil. *AIAA Journal, 44*(12), 3125-3135.

Qijun, Z., Yiyang, M., & Guoqing, Z. (2017). Parametric analyses on dynamic stall control of rotor airfoil via synthetic jet. *Chinese Journal of Aeronautics, 30*(6), 1818-1834.

Ranasinghe, K., Guan, K., Gardi, A., & Sabatini, R. (2019). Review of advanced low-emission technologies for sustainable aviation. *Energy, 188*, 115945.

Richez, F. (2018). Analysis of dynamic stall mechanisms in helicopter rotor environment. *Journal of the American Helicopter Society, 63*(2), 1-11.

Saeed, A. S., Younes, A. B., Cai, C., & Cai, G. (2018). A survey of hybrid unmanned aerial vehicles. *Progress in Aerospace Sciences, 98*, 91-105.

Safari, A., Lemu, H. G., Jafari, S., & Assadi, M. (2013). A comparative analysis of nature-inspired optimization approaches to 2D geometric modelling for turbomachinery applications. *Mathematical Problems in Engineering, 2013*.

Sahin, M., & Sankar, L. N. (2000). Stall alleviation using a deformable leading edge concept. Dans *2000 IEEE Aerospace Conference. Proceedings (Cat. No. 00TH8484)* (Vol. 2, pp. 143-150). IEEE.

Sahin, M., Sankar, L. N., Chandrasekhara, M., & Tung, C. (2003). Dynamic stall alleviation using a deformable leading edge concept-a numerical study. *Journal of Aircraft, 40*(1), 77-85.

Samara, F., & Johnson, D. A. (2021). Deep dynamic stall and active aerodynamic modification on a S833 airfoil using pitching trailing edge flap. *Wind Engineering, 45*(4), 884-903.

Sanders, B., Crowe, R., & Garcia, E. (2004). Defense advanced research projects agency–Smart materials and structures demonstration program overview. *Journal of intelligent material systems and structures, 15*(4), 227-233.

Sankar, L. N., Sahin, M., & Gopal, N. (2000). Dynamic stall characteristics of drooped leading edge airfoils.

Sawyers, D. (2008). AWIATOR Project Perspectives: Passive Flow Control on Civil Aircraft Flaps Using Sub-Boundary Layer Vortex Generators. Dans *KATnet II Separation Control Workshop*.

Schweiger, J., Suleman, A., Kuzmina, S., & Chedrik, V. (2002). MDO concepts for an European research project on active aeroelastic aircraft. Dans *9th AIAA/ISSMO Symposium on Multidisciplinary Analysis and Optimization* (pp. 5403).

Sébastien, D., & Group, S. S. (2008). Toward ACARE 2020: innovative engine architectures to achieve the environmental goals? Dans *26th International Congress of The Aeronautical Sciences*.

Seifert, A., & Pack, L. (1999). Oscillatory excitation of unsteady compressible flows over airfoils at flight Reynolds numbers. Dans *37th Aerospace Sciences Meeting and Exhibit* (pp. 925).

Sekimoto, S., Kato, H., Fujii, K., & Yoneda, H. (2022). In-Flight Demonstration of Stall Improvement Using a Plasma Actuator for a Small Unmanned Aerial Vehicle. *Aerospace, 9*(3), 144.

Shmilovich, A., & Yadlin, Y. (2011). Flow control techniques for transport aircraft. *AIAA Journal, 49*(3), 489-502.

Shyy, W., Aono, H., Chimakurthi, S. K., Trizila, P., Kang, C.-K., Cesnik, C. E., & Liu, H. (2010). Recent progress in flapping wing aerodynamics and aeroelasticity. *Progress in Aerospace Sciences, 46*(7), 284-327.

Sinapius, M., Monner, H. P., Kintscher, M., & Riemenschneider, J. (2014). DLR's morphing wing activities within the European network. *Procedia Iutam, 10*, 416-426.

Skinner, S. N., & Zare-Behtash, H. (2018). State-of-the-art in aerodynamic shape optimisation methods. *Applied Soft Computing, 62*, 933-962.

Smith, J. W. (1992). *Variable-camber systems integration and operational performance of the AFTI/F-111 mission adaptive wing* (Vol. 4370). National Aeronautics and Space Administration, Office of Management ….

Sodja, J., Martinez, M. J., Simpson, J. C., & De Breuker, R. (2019). Experimental evaluation of a morphing leading edge concept. *Journal of intelligent material systems and structures, 30*(18-19), 2953-2969.

Stanewsky, E. (2001). Adaptive wing and flow control technology. *Progress in Aerospace Sciences, 37*(7), 583-667.

Su, W., & Song, W. (2019). A real-time hybrid aeroelastic simulation platform for flexible wings. *Aerospace Science and Technology, 95*, 105513.

Sugar-Gabor, O., Koreanschi, A., & Botez, R. (2016). Analysis of UAS-S4 Éhecatl aerodynamic performance improvement using several configurations of a morphing wing technology. *The Aeronautical Journal, 120*(1231), 1337-1364.

Sugar-Gabor, O., Koreanschi, A., & Botez, R. M. (2013). Optimization of an Unmanned Aerial System'wing using a flexible skin morphing wing. *SAE International Journal of Aerospace, 6*(1), 115-121.

Sugar-Gabor, O., Simon, A., Koreanschi, A., & Botez, R. (2014). Application of a morphing wing technology on hydra technologies unmanned aerial system UAS-S4. Dans *ASME International Mechanical Engineering Congress and Exposition* (Vol. 46421, pp. V001T001A037). American Society of Mechanical Engineers.

Sugar-Gabor, O., Simon, A., Koreanschi, A., & Botez, R. M. (2016). Aerodynamic performance improvement of the UAS-S4 Éhecatl morphing airfoil using novel optimization techniques. *Proceedings of the Institution of Mechanical Engineers, Part G: Journal of Aerospace Engineering, 230*(7), 1164-1180.

Suleman, A., Vale, J., Afonso, F., Lau, F., Ricci, S., De Gaspari, A., . . . Wales, C. (2014). Novel air vehicle configurations: from fluttering wings to morphing flight. Dans *World Congress on Computational Mechanics (WCCM XI)* (pp. 20-25). Barcelona.

Thill, C., Etches, J., Bond, I., Potter, K., & Weaver, P. (2008). Morphing skins. *The Aeronautical Journal, 112*(1129), 117-139.

Tian, X., & Li, J. (2019). A novel improved fruit fly optimization algorithm for aerodynamic shape design optimization. *Knowledge-Based Systems, 179*, 77-91.

Tianyuan, H., & Xiongqing, Y. (2009). Aerodynamic/stealthy/structural multidisciplinary design optimization of unmanned combat air vehicle. *Chinese Journal of Aeronautics, 22*(4), 380-386.

Trad, M. H., Segui, M., & Botez, R. M. (2020). Airfoils Generation Using Neural Networks, CST Curves and Aerodynamic Coefficients. Dans *AIAA AVIATION 2020 FORUM* (pp. 2773).

Traub, L. W., Miller, A., Rediniotis, O., Kim, K., Jayasuriya, S., & Jung, G. (2005). Effects of synthetic jets on large amplitude sinusoidal pitch motions. *Journal of Aircraft, 42*(1), 282-285.

Valasek, J. (2012). *Morphing aerospace vehicles and structures* (Vol. 57). John Wiley & Sons.

Van de Wal, H. (2010). Design of a wing with boundary layer suction. *Faculty of Aerospace Engineering, TU Delft*.

Visbal, M. R., & Benton, S. I. (2018). Exploration of high-frequency control of dynamic stall using large-eddy simulations. *AIAA Journal, 56*(8), 2974-2991.

Visbal, M. R., & Garmann, D. J. (2017). Numerical investigation of spanwise end effects on dynamic stall of a pitching NACA 0012 wing. Dans *55th AIAA aerospace sciences meeting* (pp. 1481).

Vu, P., Kelkar, A., & Whitmer, C. (2005). Investigation of the effects of stiffness on control power via a morphing wing technology. Dans *46th AIAA/ASME/ASCE/AHS/ASC Structures, Structural Dynamics and Materials Conference* (pp. 2039).

Wang, L., Feng, L.-H., Liang, Y., Chen, Y.-L., & Li, Z.-Y. (2021). Vortex control strategy for unsteady aerodynamic optimization of a plunging airfoil at a low Reynolds number. *Physics of Fluids, 33*(11), 117110.

Wei, B., Gao, Y., & Li, D. (2021). Physics of Dynamic Stall Vortex During Pitching Oscillation of Dynamic Airfoil. *International Journal of Aeronautical and Space Sciences, 22*(6), 1263-1277.

Wilcox, R. R., & Muska, J. (2002). Comparing correlation coefficients. *Communications in Statistics-Simulation and Computation, 31*(1), 49-59.

Winyangkul, S., Wansaseub, K., Sleesongsom, S., Panagant, N., Kumar, S., Bureerat, S., & Pholdee, N. (2021). Ground Structures-Based Topology Optimization of a Morphing Wing Using a Metaheuristic Algorithm. *Metals, 11*(8), 1311.

Wölcken, P. C., & Papadopoulos, M. (2015). *Smart intelligent aircraft structures (SARISTU): proceedings of the final project conference*. Springer.

Yu, Y., Zhigang, W., & Shuaishuai, L. (2021). Comparative study of two lay-up sequence dispositions for flexible skin design of morphing leading edge. *Chinese Journal of Aeronautics, 34*(7), 271-278.

Zhang, J., Shaw, A. D., Wang, C., Gu, H., Amoozgar, M., Friswell, M. I., & Woods, B. K. (2021). Aeroelastic model and analysis of an active camber morphing wing. *Aerospace Science and Technology*, 106534.

Zhang, J., & Xia, P. (2017). An improved PSO algorithm for parameter identification of nonlinear dynamic hysteretic models. *Journal of Sound and Vibration, 389*, 153-167.

Zhu, C., Qiu, Y., & Wang, T. (2021). Dynamic stall of the wind turbine airfoil and blade undergoing pitch oscillations: A comparative study. *Energy, 222*, 120004.

Zi, K., Daochun, L., Tong, S., Xiang, J., & Zhang, L. (2020). Aerodynamic characteristics of morphing wing with flexible leading-edge. *Chinese Journal of Aeronautics, 33*(10), 2610-2619.

Zi, K., Daochun, L., Xiang, J., & Cheng, C. (2020). Delaying stall of morphing wing by periodic trailing-edge deflection. *Chinese Journal of Aeronautics, 33*(2), 493-500.